# ELECTRIC DIPOLE MOMENTS OF HIGHLY EXCITED MOLECULAR VIBRATIONAL STATES

THÈSE N° 2867 (2003)

PRÉSENTÉE À LA FACULTÉ SCIENCES DE BASE

Institut de chimie moléculaire et biologique

SECTION DE CHIMIE ET GÉNIE CHIMIQUE

## ÉCOLE POLYTECHNIQUE FÉDÉRALE DE LAUSANNE

POUR L'OBTENTION DU GRADE DE DOCTEUR ÈS SCIENCES

PAR

# Patrice THEULÉ

DEA physique de la matière et du rayonnement, Université Grenoble I, France
ingénieur en physique, école nationale supérieure de physique de Grenoble, France
et de nationalité française

Lausanne, EPFL
2003

# Abstract

In this work, new spectroscopic techniques have been developed to measure electric dipole moments of highly excited rovibrational states of small polyatomic molecules in the gas phase.

These techniques make use of lasers and of microwave synthesizers. They enable one to measure the change on a molecular system caused by applying an external electric field, which is called Stark effect and from this, extract the dipole moment. The first technique, called microwave Stark spectroscopy, makes use of microwave-optical double resonance combined to either laser induced fluorescence or vibrational predissociation detection. The second approach, called Stark induced quantum beat spectroscopy, relies on the time evolution of a coherently prepared molecular wavepacket in an electric field, using either electronic photodissociation or laser induced fluorescence for detection. These techniques have been applied to $H_2CO$, HOCl, HDO, and $H_2O$ for whom the electric dipole moment have been measured for several highly excited rovibrational states of the ground electronic state.

Using these experimental measurements, the dependence of the dipole moment vector, both in orientation and in magnitude, on the vibrational excitation is discussed. Moreover the experimental data are used to test *ab initio* calculations potential energy and dipole moment surfaces and to establish critical benchmarks for future improvements.

Due to the rarity of dipole moment data for highly excited vibrational states and their central role in transition intensities, intermolecular forces and collisions, these measurements are of special importance for chemical and energy transfer processes in atmospheric sciences, combustion studies, planetology, or more generally in the whole quantitative spectroscopy field, where transitions intensities are at least as important as line frequency positions.

# Résumé

Au cours de ce travail, de nouvelles techniques spectroscopiques ont été développées afin de mesurer le moment dipolaire électrique de petites molécules polyatomiques en phase gazeuse dans des états rovibrationels très excités.

Ces techniques utilisent des lasers et des générateurs micro-ondes. Elles permettent de mesurer le changement induit par un champ électrique externe sur un système moléculaire, ou effet Stark, duquel est extrait le moment dipolaire. La première technique, ou spectroscopie Stark par micro-ondes, utilise une double résonance optique - micro-ondes combinée à une détection soit par fluorescence induite par laser, soit par prédissociation vibrationelle. La deuxième technique, ou spectroscopie par battements quantiques induits par effet Stark, repose sur l'évolution temporelle d'un paquet d'onde moléculaire cohérent soumis à l'effet d'un champ électrique externe; cette évolution étant détectée soit par photodissociation électronique, soit par fluorescence induite par laser. Le moment dipolaire est extrait de ces mesures d'effet Stark. Ces techniques ont été appliquées à $H_2CO$, $HOCl$, $HDO$, et $H_2O$, molécules pour lesquelles le moment dipolaire électrique a été mesuré pour plusieurs états rovibrationels excités de l'état électronique fondamental.

Les résultats expérimentaux permettent de discuter la dépendance du vecteur moment dipolaire, en orientation et en norme, avec l'excitation vibrationelle. De plus, les données expérimentales sont utilisées pour tester les calculs *ab initio* de surfaces d' énergie potentielle et de moment dipolaire, et pour établir des références strictes pour de futures améliorations de ces surfaces.

Les données de moment dipolaires pour les états vibrationles trés excités sont très rares et vu le rôle central du moment dipolaire pour les intensités de transition, les forces inter-moléculaires et les collisions, ces mesures sont d'une importance particulière pour l'étude des processus chimiques et de transfert d'énergie, en sciences atmosphériques, en combustion, en planétologie, ou plus généralement dans le domaine de la spectroscopie quantitative, où les intensités de transition sont au moins aussi importantes que la position en fréquence des raies.

# Acknowledgements

Je voudrais adresser mes sincères remerciements aux personnes que j'ai eu l'honneur et le plaisir de cotoyer au cours de ma thèse de doctorat à l' Ecole Polytechnique Fédérale de Lausanne, et qui ont contribué à la réussite de ce travail:

le Prof. Thomas Rizzo, pour m'avoir accepté dans son groupe, et pour toute l'aide qu'il m'a apportée dans la correction de ce manuscript,

le Dr. Andrea Callegari, pour son savoir ainsi que pour sa gentillesse et sa patience à m' enseigner la spectroscopie. Ce travail est essentiellement le fruit de son esprit pétillant,

le Prof. John Muenter, pour la collaboration fructueuse que nous avons eu, pour son savoir dans la spectroscopie micro-onde, pour sa patience à répondre par courrier électronique à mes questions, et pour sa bonne humeur lors de ses visites à Lausanne,

les Prof. Per Jensen, Prof. Frédéric Merkt, Prof. Hubert van den Bergh et Prof. Hubert Girault pour avoir accepté de faire partie de mon jury de thèse,

l'ensemble de mes collègues, présents ou anciens, au Laboratoire de Chimie Physique Moléculaire: Dr. Rainer Beck, Dr. Oleg Boiarkine, Richard Bossart, Andreas Braun, Christelle Cardon, Rachele Chianese, Marianne Dang, Thanh Tung Dang, Dr. Marcel Drabbels, Prof. Tino Gäumann, Anthi Kamariotis, Dr. Monika Kowalczyk, Dr. Joachim Makowe, Plinio Maroni, Sébastien Mercier, Antoine Milon, Dr. Dimitrios Papageorgopoulos , Mikhail Polianski, Dr. Julia Rebstein, Dr. David Rueda, Amanz Ruf, Marco Sacchi, Dr. Mathieu Schmid, and Roman Schmied, avec une mention spéciale pour mes colocataires Andreas Braun et Plinio Maroni,

les ateliers de mécaniques et d'électronique, pour toute l'aide technique qu'ils m'ont apportée durant la partie expérimentale de mon travail,

tous les amis que j'ai eus à Lausanne, ainsi que toute ma famille, pour leur soutien,

le système éducatif français, qui permet à chacun, quelle que soit son origine, d'avoir la possibilité d'accéder au doctorat.

# Contents

# Chapter 1

# Introduction

The electrical properties of molecules are of primarily importance for determining the behavior of matter. For example, a non uniform charge distribution may allow a molecule to absorb or emit light or to aggregate into a condensed phase. Electrical interactions are also important for understanding the shapes adopted by biological and synthetic macromolecules as well as the interactions between such molecules.

## 1.1 Electrical properties of molecules.

Molecular electrical properties reflect the degree to which the nuclei exert control over the electrons in a molecule, either by causing them to accumulate in particular regions, or by permitting them to respond more or less strongly to the effects of external fields.

The electric charge distribution operator in a molecule can be expanded in multiple-order tensor operators [1], the electric multipoles, as is illustrated schematically in Fig. 1.1. The field arising from an arbitrary finite charge distribution can be expressed as the superposition of the fields arising from a superposition of multipoles. The zero-order rank tensor, the monopole, is the overall electric charge of the molecule, which is zero for a neutral molecule, and non-zero for an ion. The second-order rank tensor, consists of two electric charges, $+q$ and $-q$, separated by a distance d. As is shown in Fig.1.2, this arrangement of charges is represented by a vector, the electric dipole moment vector $\vec{\mu}$, that points from the negative charge to the positive charge. We will follow this convention throughout this thesis. The magnitude of $\vec{\mu}$ is given by $\|\vec{\mu}\| = q.d$ . The magnitude of dipole moments are commonly reported in the non-SI unit debye D ($1D = 3.33564*10^{-30}\ C.m$). Dipole moments of small molecules are typically on the order of $1\ D$. Depending upon the level of description one desires and on the properties of the molecule considered, one uses the lowest non-zero terms of the charge distribution expansion. In some cases, particularly if a molecule has neither a net charge nor a dipole moment (as in the case
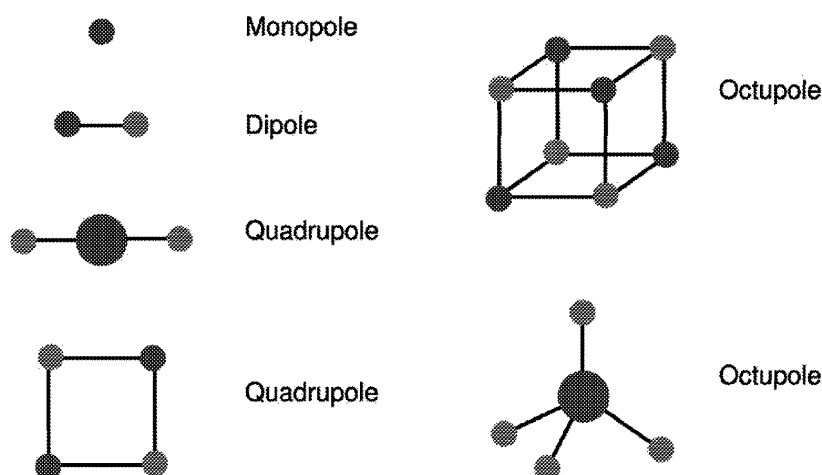
**Figure 1.1:** Typical charge arrays corresponding to electric multipoles. The dark and light tones correspond to charges of opposite sign. Adapted from Atkins [2].
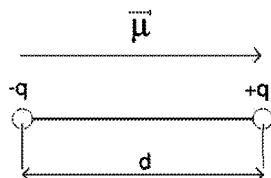


**Figure 1.2:** Convention for the dipole moment vector

of $CO_2$, for example) higher order terms in the multipole expansion, such as the quadrupole moment, become important. For a molecule such as $CH_4$, which has no charge, dipole or quadrupole moments, the octupole moment is used to characterize the charge distribution.

The present work is devoted to the study of the electric dipole moment vector of neutral gas phase small polyatomic molecules. A molecule is called polar if it has a permanent electric dipole moment. The electric dipole moment stems from the partial charges on the atoms in the molecule that arise from differences in electronegativity or other features of bonding. The more electronegative atom is normally the negative end of the dipole, but there are exceptions, particularly when antibonding orbitals are occupied, as in the case of a CO bond. Difference in atomic radii can also result in an imbalance of electron density because the enhanced charge density associated with the overlap regions lies closer to the nucleus of the smaller atom. Moreover symmetry criteria can determine that the dipole moment vector, or certain of its components, must be zero. For example a molecule belonging to a $D$ point group or to one of the cubic or icosahedral point groups is non-polar, and the permanent dipole moment of the polar water molecule cannot lie perpendicular to the $C_{2V}$ symmetry axis. To a rough approximation, the dipole moment of a polyatomic molecule can be resolved into contributions from the different bonds, and the different components can be vectorially added. Such a model is called a bond

dipole model [2].

Molecules can acquire an induced dipole moment in an electric field on account of the distortion the field causes in their electronic distributions and nuclear position. This induced moment, which is temporary and disappears as soon as the perturbing field is removed, is related to the strength of the applied electric field by the relation:

$$\vec{\mu^*} = \alpha\vec{\varepsilon} + \frac{1}{2}\beta\vec{\varepsilon}^{\,2} + ... \tag{1.1}$$

where $\alpha$ is the polarizability of the molecule, and $\beta$ the hyperpolarizability. Higher-order terms must be considered when the applied electric field is strong, as in a laser beam. As is illustrated in Fig.1.3, there are several contributions to the polarizability associated with different timescales of motion.
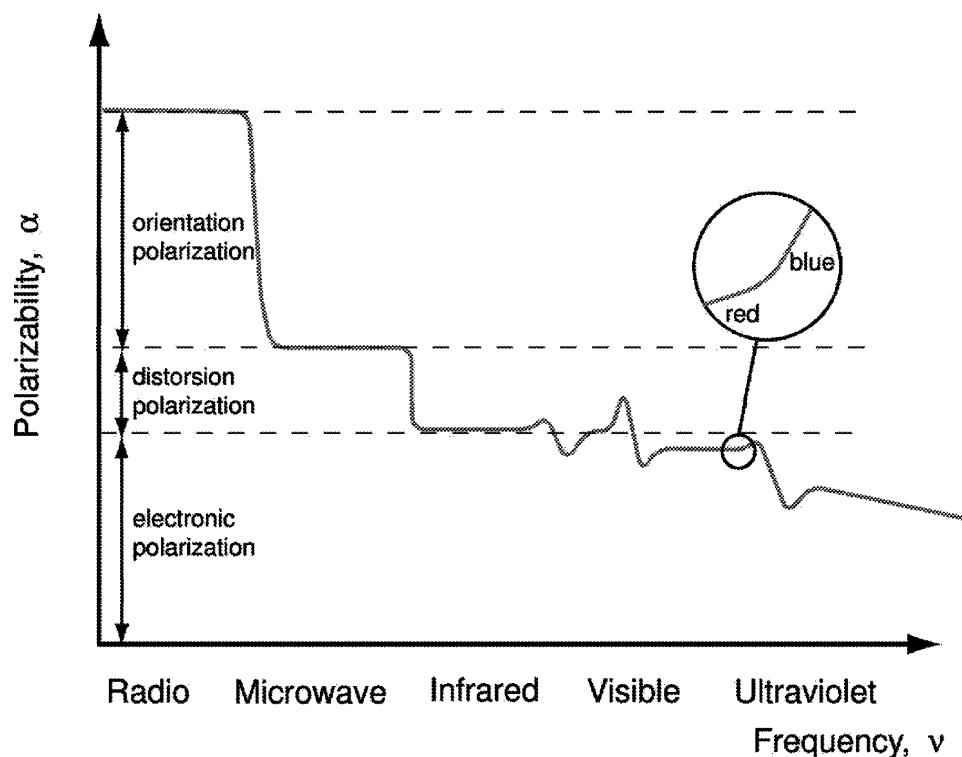


**Figure 1.3:** Variation of the polarizability with the frequency of the applied field. The inset shows the variation of the electronic polarizability in the visible region, near an electronic excitation of the molecule, as higher frequency light can distort the electronic distribution more strongly. Adapted from Atkins [2].

When the applied electric field changes direction too fast compared to the time scale on which the molecule can reorient, which is typically the free rotation timescale in the gas phase, the permanent dipole moment then makes no contribution to the polarization of the sample. The orientation polarization, which arises from the interaction of the field with the permanent dipole moment, is lost at such high frequency, typically in the microwave region. The next contribution to be lost as the electric field frequency is raised is the displacement polarization,

the polarization that arises from the distortion of the positions of the nuclei by the applied field. As the molecule is bent and stretched by the applied electric field, the dipole moment changes accordingly. The timescale for nuclear motion is approximately the inverse of the molecular vibrational frequency, so the polarization disappears in stages as the incident frequency rises above the frequency of a particular mode of vibration. At even higher frequency, in the visible region, only the electrons are mobile enough to respond to the rapidly changing direction of the applied field. The polarization that remains is now due entirely to the distortion of the electron distribution, and the surviving contribution to the molecular polarizability is called the electronic polarizability.

In the present study we will apply static electric fields, named Stark electric fields, and the polarizability will reflect the orientation of the molecule, the distortion of the nuclei and the electronic contributions to the polarization. We will also apply pulsed laser beams for which the oscillating electric field frequency is of the order of $10^{14}$ $Hz$, and the pulse duration 10 $ns$. Under these conditions the laser electromagnetic field can be seen to classically couple during a rovibrational transition to the molecule dipole moment.

## 1.2   Importance of the dipole moment in molecular physics

### Radiation-matter interaction

We describe the interaction of light with matter in a semi-classical manner–that is, the electromagnetic field is described classically, according to Maxwell equations, and the matter is described quantum mechanically. We consider the interaction of a matter particle of mass m, charge $q$, and spin $\vec{S}$, located at a distance $R$ from the center of a central potential $V(R)$, with an electromagnetic wave, propagating along the $y$ direction and described by its potential vector $\vec{A}(\vec{R}, t)$, which is related to the electric and magnetic fields by the relations:

$$\vec{E}(\vec{R}, t) = -\frac{\partial}{\partial t}\vec{A}(\vec{R}, t) = E\vec{e_z}cos(ky - \omega t) \tag{1.2}$$

$$\vec{B}(\vec{R}, t) = \nabla \times \vec{A}(\vec{R}, t) = B\vec{e_x}cos(ky - \omega t) \tag{1.3}$$

We can then write the radiation-matter Hamiltonian as [1]:

$$H = \frac{1}{2m}[\vec{P} - q\vec{A}(\vec{R}, t)]^2 + V(R) - \frac{q}{m}\vec{S} \cdot \vec{B}(\vec{R}, t) \tag{1.4}$$

or as

$$H = H_o + W_{DE}(t) + W_{DM}(t) + W_{QE}(t) + ... \tag{1.5}$$

with:

$$H_o = \frac{\vec{P}^2}{2m} + V(R) \tag{1.6}$$

$$W_{DE}(t) = -\vec{\mu}.\vec{E} = -qEZ\cos\omega t \tag{1.7}$$

$$W_{DM}(t) = -\frac{q}{2m}(L_x + 2S_x)B\cos\omega t \tag{1.8}$$

$$W_{QE}(t) = -\frac{q}{2mc}(YP_z + ZP_y)E\cos\omega t \tag{1.9}$$

where $H_o$ is the matter particle Hamiltonian, and the other terms represent the interaction of the light with the matter particle. This interaction Hamiltonian can be decomposed into the sum of $W_{DE}(t)$, the electric dipole interaction, $W_{DM}(t)$ the magnetic dipole interaction, and $W_{QE}(t)$ the electric quadrupole interaction, as well as other higher-order terms. $W_{DM}(t)$ and $W_{QE}(t)$ are of the same order of magnitude and much smaller than $W_{DE}(t)$. Thus, in the atomic or molecular physics domain, we can to a good level of approximation neglect terms other than the electric dipole moment Hamiltonian. We can consider that the primary interaction between matter and radiation considered in molecular physics is driven by the interaction of the first order charge distribution of the molecule, the molecular dipole moment, with the electric field of the light.

If we consider the intensity of a molecular transition in the same semi-classical approximation, assuming the molecules to be in thermal equilibrium at a temperature T, the integrated intensity for an electric dipole transition from an initial state with energy $E''$ to an final state with energy $E'$ is given by [3]:

$$I(f \leftarrow i) = \frac{8\pi^3 \aleph_A.\tilde{\nu}_{if}.\exp(-E''/k_BT)[1 - \exp(-hc.\tilde{\nu}_{if}/k_BT)]}{(4\pi\epsilon_0)3hcQ}.S(f \leftarrow i) \tag{1.10}$$

where $\tilde{\nu}_{if} = (E' - E'')/hc$ is the wavenumber of the transition, and $Q$ is the partition function given by

$$Q = \sum_w g_w \exp(-E_w/k_BT) \tag{1.11}$$

$g_w$ being the degeneracy of the state of energy $E_w$. The line strength $S$, of an electric dipole transition is given by:

$$S = \sum_{\phi'_{int},\phi''_{int}} \sum_{A=X,Y,Z} |\langle\phi'_{int}|\mu_A|\phi''_{int}\rangle|^2 \tag{1.12}$$

where $\phi'_{int}$ and $\phi''_{int}$ are eigenfunctions of the molecular Hamiltonian corresponding to the eigenvalues $E'$ and $E''$ respectively.

From this we can see that both the molecular energy eigenvalues, eigenfunctions and the molecular dipole moment is of fundamental importance when determining quantitatively how

much an electromagnetic wave is absorbed or emitted by a medium. The position of the energy levels is a subject widely treated by spectroscopy both experimentally and theoretically. However as we will see below, quantitative spectroscopy, which includes the accurate determination of the intensities, is very problematical despite its wide importance, mainly in atmospheric and astrophysical sciences as well as in combustion processes or trace detection.

## Optical properties

The concepts of dipole moment and polarizability also provide insight into optical properties of matter, such as the refractive index. The propagation of light through a medium can be imagined to occur by the incident light inducing an oscillating dipole moment, which then radiates light of the same frequency. The newly generated radiation is delayed slightly by this process, and thus it propagates more slowly through a medium than through vacuum. This property is expressed by the refractive index $n_r$ of the medium and is related to its polarizability $\alpha$, which in turn depends on the frequency of the light. Because higher frequency light can distort the electronic distribution more strongly as it can be seen in the inset of Fig.1.3, the refractive index is greater for blue light than red light, and this dependence on frequency of the polarizability is at the origin of the dispersion of white light by a prism.

Another important property related to the concepts of refractive index and polarizability is the optical activity which is the rotation of the plane of polarization of plane-polarized light. This arises when the polarizability is not the same in all directions in space.

## Intermolecular forces

Van der Waals forces are the interactions between molecules arising from the interaction of either permanent or induced dipole moments between molecules. These interactions have different physical origins. The permanent dipole moments of two polar molecules can interact with each other (dipole-dipole interactions), and for nearly freely rotating molecules this interaction scales as $\frac{C_1}{r^6}$. Moreover the dipole moment of a polar molecule can induce a dipole moment in a neighboring polarizable molecule. The induced dipole interacts with the permanent dipole of the first molecule, and the two are attracted together (dipole-induced-dipole interactions), which also scales as $\frac{C_2}{r^6}$. Even if both molecules are non-polar, the transient dipole moment that all molecules possess as a result of fluctuations in the instantaneous positions of the electrons allow them to attract one another. The transient dipole moment of one molecule can generate an electric field that polarizes another molecule to give an induced instantaneous dipole moment. The two dipoles then attract each other (induced-dipole-induced-dipole interactions). This type of interaction, which is also called dispersion interaction or London interaction, also scales as $\frac{C_3}{r^6}$.

The total attractive interaction between rotating molecules (considering only molecules that are unable to participate in hydrogen bond formation) is then the sum of the three van der Waals contributions discussed above, and if we neglect higher order multipole interactions, we can write this total attractive force as:

$$V = -\frac{C_6}{r^6} \qquad (1.13)$$

This attractive interaction is combined with repulsive interactions in a Lennard-Jones potential or an exp $-6$ potential (potential with an exponential repulsive term) to provide a simple model for the interaction of molecules, which is of primary interest in understanding collisions, condensation processes or weakly bound van der Waals complexes. Moreover, in more complex systems such as biomolecules, the folded shapes and intermolecular interactions are driven by the dipole moments of smaller units that are linking together.

One can therefore see that the dipole moment is of primary importance in the description of the interaction of electromagnetic radiation with matter as well as of matter itself.

## 1.3 Dipole moments of vibrationally excited molecular states

A significant fraction of chemical physics research focuses on the properties and dynamics of molecules far from equilibrium, as most molecules involved in chemical reactions are in excited rotational, vibrational or electronic states. Because such states have substantially different reactivity than ground state species, one must understand the molecular properties responsible for this reactivity. This necessitates developing techniques to measure the properties of molecules at chemically relevant energies.

The general qualitative behavior of dipole moments for the vast majority of excited vibrational states is easily summarized. Dipole moments change on the order of 1% with each increase in vibrational quantum number $v$, with moments of stretching states typically increasing for higher $v$ while those for bending states normally decreasing upon excitation. This behavior can be understood in terms of a bond moment model, where most bonds increase their polarity upon elongation near equilibrium geometries. The decrease of moments in bending states result from smaller projections of the vibrationally averaged bond moments on the molecular axes as the averaged bending angle is increasing and the molecule is opening. Molecules that generally obey these observations include HF [4], HCl[5], LiH [6], LiF[7], SiO[8], GeO[8], BaO [9], HCN [10, 11],OCS [12], $H_2O$[13, 14], $SO_2$[15], and $NH_3$[16]. Of all of the vibrational modes studied in this group, only two do not fit this simple picture: exciting the $C = S$ stretch in OCS[12] and the $C \equiv N$ stretch in HCN [11] decreases the dipole moments. Nevertheless, these cases can still

be described by a bond moment increase upon excitation that cancels a larger fraction of the dominant $C = O$ or $H - C$ bond moment, respectively.

For a diatomic molecule, this picture becomes quantitative by using vibrational wave functions to average the dipole moment over internal motions in order to get a perturbative dipole moment function. An obvious starting point is to use harmonic oscillator wave functions for the former together with a linear dipole moment function for the latter,

$$\mu = \mu_e + \frac{d\mu}{dR}(R - R_e) \tag{1.14}$$

This vibrational average gives the equilibrium dipole moment $\mu_e$ for the moment of any vibrational state, since the linear term averages to zero for an harmonic oscillator. The small vibrationally induced changes observed in dipole moments are consistent with the lack of vibrational dependence predicted by this model. Higher order terms in both the vibrational potential and the dipole moment function are needed to describe vibrationally induced changes in the dipole moment. Keeping terms in the dipole moment expansion up to second order gives:

$$\langle\mu\rangle_v = \mu_e + \frac{d\mu}{dR}\langle R - R_e\rangle_v + \frac{1}{2}\frac{d^2\mu}{dR^2}\langle(R - R_e)^2\rangle_v \tag{1.15}$$

where the angular brackets imply averaging over the $v^{th}$ vibrational wave function. Using Morse functions to evaluate the vibrational averages in Eq.1.15 yields the dipole moment in terms of conventional spectroscopic constants [17]:

$$\langle\mu\rangle_v = \mu_e + \frac{d\mu}{dR}\frac{3R_e\sqrt{\omega_e x_e B_e}}{\omega_e}\left(\nu_i + \frac{1}{2}\right) + \frac{d^2\mu}{dR^2}\frac{2R_e^2 B_e}{\omega_e}\left(\nu_i + \frac{1}{2}\right) \tag{1.16}$$

It is worth noting that the contributions arising from the anharmonicity and the quadratic term in the dipole function are typically comparable in magnitude and both result in linear contributions to the dipole moment change. This means that permanent dipole moment measurements cannot give independent values for first and second dipole derivatives. However, knowledge of the first derivative from infrared intensity data allows one to extract $\mu_e$ and $\frac{d^2\mu}{dR^2}$ from Stark data [4, 5].

Turning now to polyatomic molecules, the limited amount of dipole moment data for excited vibrational states exhibits nearly linear dependence on vibrational quantum numbers, and the perturbative dipole moment function can be written as:

$$\langle\mu\rangle_v = \mu_e + \sum_i^{3N-6} a_i(\nu_i + \frac{1}{2}) \tag{1.17}$$

As in the diatomic case, the coefficient of the terms linear in the vibrational quantum numbers ($a_i$ in the polyatomic case) depend upon first and second dipole derivatives as well as

upon cubic potential constants [18, 19, 20, 21]:

$$a_i = \frac{\partial^2 \mu}{\partial q_i^2} - \sum_j (1 + \delta_{ij}) \frac{k_{iij}}{\omega_j} \frac{\partial \mu}{\partial q_j} \qquad (1.18)$$

## 1.4   State-of-the-art in measuring dipole moments

Because of the importance of molecular dipole moments [22] as discussed above, substantial effort has been directed towards measuring them. The earliest technique for the determination of molecular electric dipole moments involved dielectric constant measurements of bulk matter [23]. This approach has the disadvantage of averaging over all thermally populated rovibrational states as well as naturally occurring isotopic species. Moreover these measurements are very sensitive to impurities and thus required extrapolation to infinite dilution.

However, the dependence of electronic structure upon vibrational and rotational degrees of freedom is of such importance for physical chemistry that substantial effort has been directed towards the measurements of electric dipole moments as a functional of rotational and vibrational quantum numbers.

With the advent of microwave spectroscopy in the late 1940's, accurate measurements of molecular dipole moments for specific rovibrational levels of a specified isotope became possible through analysis of the spectral shifts induced by an external electric field, which is called the Stark effect. This technique, which constitutes the most widely used and accurate method for direct measurements of electric dipole moment, is extensively described in Reference [24]. Microwave spectroscopy has enabled a remarkably precise determination of the electric dipole moment for molecules in their ground electronic state and in their ground vibrational state [25]. Studies of vibrationally excited systems with conventional microwave detection schemes, however, are limited to rovibrational levels that are thermally populated at room temperature. Thus, it is impossible to extend conventional techniques involving long path absorption cells to highly excited vibrational states. Thus, while a large number of dipole moments have been measured in vibrational ground states, much less data exist for vibrationally excited species.

Nevertheless, various experimental refinements have enabled a remarkably precise determination of the electric dipole moment for molecules in several excited vibrational states. The very sensitive technique of molecular beam electric resonance [26, 27] has permitted high precision dipole moments to be obtained for several vibrational states of several molecules, including both diatomics and polyatomics. Briefly, the experiment involves monitoring the intensity of a well-collimated beam of molecules after it has passed through two deflecting inhomogeneous field regions. Between these two regions, an oscillating field is applied. The spectrum appears as a change in the intensity of the beam as the frequency of the oscillating field is changed. The first non-uniform electrostatic electric field selects molecules in an $|J \ M_J\rangle$ molecular state. The

second non-uniform electrostatic electric field serves to analyze the molecular state after the molecule has been exposed to the spectroscopic radiation. The intensity of the molecular beam that passes through these three regions of the spectrometer is then monitored by a molecular beam detector. The occurrence of a transition between two states at a precise frequency due to the oscillating field is therefore observed by a change in the number of molecules detected. A Stark electric field shifts this transition frequency, and from this shift the electric dipole moment can be determined [26].

A direct extension of Stark effect microwave spectroscopy is laser Stark spectroscopy. In this technique, the Stark shift is measured for a rotation-vibration laser transition. This approach has extended dipole measurements to include overtone vibrations for several polyatomic species [28, 29, 30, 31, 32, 33, 34]. However extending Stark effect measurements to high energy states accessed by laser induced rotation-vibration transitions has been difficult, because Doppler widths of infrared and visible transitions are typically larger than the majority of available Stark splittings. Stark splittings produced by reasonable electric fields strengths ($\simeq 10\ kV/cm$) are small (a few tenths of wavenumbers) when compared to inhomogeneous Doppler broadening associated with electronic transition frequency (few $10000\ cm^{-1}$). For this reason, very little dipole moment data exist for excited electronic states using this method [35, 36, 37].

The development of microwave-optical double resonance experiments allowed more excited states dipole moments to be measured. In the most common microwave-optical double resonance experiments, microwave transitions occur in excited electronic states, detected by monitoring rotational transition induced changes in luminescence from the excited state [38]. Microwave-optical double resonance experiments observing rotational transitions in excited vibrational states of the ground electronic state use the optical photon (infrared or visible) to prepare molecules in the desired rovibrational state. While the microwave induced rotational transition can be detected by the change in absorption of the optical radiation it causes [39, 40, 11, 16, 41, 42], in some cases an independent detection step is required to detect the microwave transition. A number of options are available, including mass spectrometry [4, 5, 10, 15, 13], bolometry [43, 44], laser-induced fluorescence [45, 46, 47], multiphoton ionization [48, 49] and photo-fragment detection [50, 51].

In addition to the frequency domain techniques mentioned above, alternative time-domain techniques have been developed to measure both dipole moments of highly excited vibrational states of the ground electronic state [34, 52, 53] and dipole moments of electronically excited states [54, 55]. This approach, called quantum beat spectroscopy, is based on the creation of molecular coherences with one laser pulse and the measurement of their subsequent time evolution. A laser pulse excites a coherent superposition of eigenstates, called a wavepacket, and then the time dependence of the wavepacket is detected, either by fluorescence or laser induced fluorescence. This very accurate Doppler-free technique provides a viable method for

the systematic investigation of ground electronic state dipole moment functions over a wide range of vibrational and rotational excitation, but has the disadvantage of being difficult to implement, as it requires the use of several lasers and cannot be applied to all molecules (because of hyperfine structure or Franck-Condon overlap for example).

A widespread method to determine dipole moment for highly excited vibrational states consists in measuring the integrated intensity of a line and making use of Eq. 1.10 and Eq. 1.12 to derive the transition dipole moment associated with a transition between two levels [21]. This technique is relatively easy to carry out experimentally, but gives insight only into the transition dipole moment and not in the permanent dipole moment. Moreover, because of the difficulty in extracting the transition dipole moment from line intensities, due to noise on the baseline and on the lines, blended lines and difficulty in maintaining precisely the same experimental conditions during the spectrum acquisition, these measurements are not very precise. They have the advantage to be rather fast and easy to execute however.

Besides these different experimental methods, the development of *ab-initio* methods, together with the increase of computational power, allows one to calculate rather accurate Potential Energy Surfaces (PES) and Dipole Moment Surfaces (DMS)[56]. By fitting these surfaces one can derive a potential energy function and a dipole moment function [57]. The potential energy function is then used in the resolution of the Schrödinger equation to derive energy level positions and wavefunctions. Using an ab-initio PES, as far as the calculation method can be corrected by experimentally determined energy levels, it is possible to match experimental frequencies to a very high degree of accuracy [58]. This is not necessarily the case for region of the PES where there is no experimental data. This means that we can test and correct only the part of the surfaces experimentally accessible. Using the wavefunctions derived from the PES, along with the DMS, it is possible to calculate transition dipole moments and therefore predict line intensities and compare them with experimental line intensities [59, 56] to refine both PES and DMS. *Ab-initio* calculations have the advantage of being quite fast compared to experiment and able to access regions of the PES and DMS that are not accessible experimentally. Moreover, the use of these calculations is of great help in predicting and assigning experimental spectra. *Ab-initio* methods are refined by experimental input, both energy level positions and transition intensities, and improved to match better and better experimental data. The PES is optimized using the variational principle that is by making iterative refinements of the wavefunctions until the energy has converged to a desired accuracy. The wavefunctions obtained in this way are then used to compute the DMS data [58]. Since the variational principle allows more accurate determination of the energy than the wavefunction, it is easier to improve PES calculation method from experimental energy level positions and therefore the relative accuracy of the DMS data will be less than that of the energy [60]. Thus, variational methods that give comparable energies can produce quite different dipole moments [61, 62, 63]. Moreover, several difficulties,

such as treating the dynamical electron correlation, for example, could affect the dipole moment as well as the energy [60].

One does not need to make extensive measurements to calibrate a PES or DMS, only few experimental points are needed to compare and refine the calculation techniques. However, for high energy regions there exists much more energy level data than dipole moment data. Indeed dipole moment measurements for highly excited rovibrational states are extremely rare since these states at chemically relevant energy are difficult to access experimentally. These statements justify the need of accurate dipole moment measurements for highly excited rovibrational states to provide stringent tests and refinements for ab-initio DMS's.

## 1.5 Outline of the thesis

The goal of the present work is to use state-of-the-art laser and microwave techniques to avoid the experimental difficulties mentioned above to provide dipole moment measurements of highly excited vibrational states. Due to the rarity of dipole moment data for highly excited vibrational states, and to the importance of dipole moment for transition intensities, intermolecular forces and collisions, such measurements are extremely valuable, particularly for probing regions of the dipole moment surface at geometries far from equilibrium. These techniques are applied to $H_2CO$, HOCl, HDO, and $H_2O$ for which the electric dipole moment are measured for several highly excited rovibrational states of the ground electronic state. In terms of accuracy and insensitivity to sample conditions, the techniques used in this work are by far superior to other existing methods such as direct intensity measurements.

The outline of this thesis is as follows. Because of the central importance of the Stark effect in the techniques we used, Chapter 2 presents the theory behind this phenomenon and explains how one extracts dipole moment data from Stark splittings.

Chapter 3 and Chapter 4 present studies of dipole moments of vibrationally excited $H_2CO$ and HOCl respectively using frequency domain techniques. Here a pure microwave induced rotational transition is recorded in a highly excited vibrational state, and a Stark electric field shifts the frequency of this transition. In both molecules a first laser is used to populate the studied vibrational state (as there is no population at room temperature), and then the microwave rotational transition is made, originating from the previously laser populated rovibrational state. The microwave transition is detected by either Laser Induced Fluorescence (LIF), in the case of $H_2CO$, or photofragment spectroscopy, in the case of HOCl.

Chapter 5 describes an alternative way of measuring the Stark effect, using Stark induced quantum beat spectroscopy. This technique is a pump and probe technique, where a pump laser creates a coherent wavepacket that is later detected by a probe laser. A Stark electric field modulates the evolution of the wavepacket and allows determination of the Stark splitting. Applied

to $H_2O$ or its isotopic species HDO, electronic photodissociation followed by LIF detection of the OH or OD product fragments is used to detected the Stark induced quantum beats.

From the measurements made on these molecules, we discuss the evolution of the dipole moment vector, both in orientation and in magnitude, with vibrational excitation. For $H_2O$, the experimental data are compared to those determined from *ab initio* dipole moment and potential energy surfaces, and this comparison provides a correction method for these *ab initio* surfaces and establishes critical benchmarks for future improvements.

# References

[1] Claude Cohen-Tannoudji, Bernard Diu, and Franck Laloe. *Mécanique Quantique*, volume 2. Hermann, 1996.

[2] P. W. Atkins. *Physical Chemistry*. Oxford University Press, Oxford, Melbourne, Tokyo, sixth edition, 1999.

[3] Philip R. Bunker and Per Jensen. *Molecular Symmetry and Spectroscopy*. NRCC, Ottawa,Ont., second edition, 1998.

[4] S. M. Bass, R. L. Deleon, and J. S. Muenter. Stark, zeeman, and hyperfine properties of $v = 0$, $v = 1$, and the equilibrium configuration of hydrogen-fluoride. *Journal of Chemical Physics*, 86(8):4305–4312, 1987.

[5] E. W. Kaiser. Dipole moment and hyperfine parameters of $H(Cl - 35)$ and $D(Cl - 35)$. *Journal of Chemical Physics*, 53(5):1686, 1970.

[6] L. Wharton, W. Klemperer, and L. P. Gold. Preliminary values of some molecular constants of lithium hydride. *Journal of Chemical Physics*, 37(9):2149, 1962.

[7] L. Wharton, V. E. Derr, R. Strauch, L. P. Gold, J. J. Gallagher, and W. Klemperer. Microwave spectrum, spectroscopic constants, and electric dipole moment of Li6 F19. *Journal of Chemical Physics*, 38(5):1203, 1963.

[8] J. W. Raymonda, J. S. Muenter, and Klempere.Wa. Electric dipole moment of Sio and Geo. *Journal of Chemical Physics*, 52(7):3458, 1970.

[9] L. Wharton and W. Klemperer. Microwave spectrum of BaO. *Journal of Chemical Physics*, 38(11):2705, 1963.

[10] W. L. Ebenstein and J. S. Muenter. Dipole-moment and hyperfine properties of the ground-state and the $C - H$ excited vibrational-state of HCN. *Journal of Chemical Physics*, 80(9):3989–3991, 1984.

[11] R. L. Deleon and J. S. Muenter. The vibrational dipole-moment function of HCN. *Journal of Chemical Physics*, 80(9):3992–3999, 1984.

[12] L. S. Masukidi, J. G. Lahaye, and A. Fayt. Intracavity co laser stark spectroscopy of the $\nu_3$ band of carbonyl sulfide. *Journal of Molecular Spectroscopy*, 148(2):281–302, 1991.

[13] S. L. Shostak, W. L. Ebenstein, and J. S. Muenter. The dipole-moment of water .1. dipole-moments and hyperfine properties of $H_2O$ and HDO in the ground and excited vibrational-states. *Journal of Chemical Physics*, 94(9):5875–5882, 1991.

[14] S. L. Shostak and J. S. Muenter. The dipole moment of water .2. analysis of the vibrational dependence of the dipole moment in terms of a dipole moment function. *Journal of Chemical Physics*, 94(9):5883–5890, 1991.

[15] D. Patel, D. Margolese, and T. R. Dyke. Electric-dipole moment of $SO_2$ in ground and excited vibrational-states. *Journal of Chemical Physics*, 70(6):2740–2747, 1979.

[16] M. D. Marshall, K. C. Izgi, and J. S. Muenter. Ir-microwave double resonance studies of dipole moments in the $\nu_1$ and $\nu_3$ states of ammonia. *Journal of Chemical Physics*, 107(4):1037–1044, 1997.

[17] D.K. Hinderman and C. D. Cornwell. Vibrational corrections to nuclear-magnetic shielding and spin- rotation constants for hydrogen fluoride - shielding scale for $19f$. *Journal of Chemical Physics*, 48(9):4148, 1968.

[18] C. Secroun and P. Jouve. Mechanical anharmonicity contribution to absolute intensity of infrared-absorption bands of triatomic molecules $c_2v$. *Journal De Physique*, 32(11-1):871, 1971.

[19] A. Barbe, C. Secroun, and P. Jouve. Second-order anharmonic potential constants for isotopic molecules $S(16)O_2$ and $S(18)O_2$. *Journal De Physique*, 33(2-3):209, 1972.

[20] C. Secroun, A. Barbe, and P. Jouve. Higher-order vibration intensities of polyatomic-molecules - application to diatomic and bent $xy_2$ molecules. *Journal of Molecular Spectroscopy*, 45(1):1–9, 1973.

[21] C. Camy-Peyret and J. M. Flaud. *Vibration-rotation dipole moment operator for asymmetric rotors, Molecular Spectroscopy: Modern Research*, volume III, pages 69–110. Academic Press, Orlando, Fla., 1985.

[22] P. Debye. *The Dipole Moment and Chemical Structure*. Blackie & Sons Ltd., London, 1931.

[23] A.D. Buckingham. *Electric Moments in Molecules Physical Chemistry: an Advanced Treatise*. Academic Press, New York, 1970. chapter 8, pages 349-386.

[24] C.H. Townes and A.L. Schawlow. *Microwave Spectroscopy*. Dover Publications, New York, 1975.

[25] R.D. Nelson, D.R. Lide, and A. A. Maryott. Selected values of electric dipole moments for molecules in the gas phase. Technical report, Natl. Stand. Ref. Data Ser., U.S. National Bureau of Standard, Washington, 1967.

[26] T.R. Dyke and J.S. Muenter. The properties of molecules from molecular beam spectroscopy. In A.D. Buckingham, editor, *International Review of Science, Phys.Chem. II Molecular Structure and Properties*, volume II, pages 27–92. Butterwoths, London and Boston, 1971.

[27] B. Fabricant, D. Krieger, and J. S. Muenter. Molecular-beam electric resonance study of formaldehyde, thioformaldehyde, and ketene. *Journal of Chemical Physics*, 67(4):1576–1586, 1977.

[28] J. W. C. Johns and A. R. McKellar. Stark spectroscopy with CO laser - $\nu_2$ fundamentals of $H_2CO$ and $D_2CO$. *Journal of Molecular Spectroscopy*, 48(2):354–371, 1973.

[29] J. W. C. Johns and A. R. W. McKellar. Stark spectroscopy with CO laser - dipole-moment of $H_2CO$ in $v_2 = 2$ state. *Journal of Chemical Physics*, 63(4):1682–1685, 1975.

[30] M. Allegrini, J. W. C. Johns, and A. R. W. McKellar. Stark spectroscopy with *co* laser - $\nu_3$ fundamental band of $H_2CO$. *Journal of Molecular Spectroscopy*, 66(1):69–78, 1977.

[31] M. Allegrini, J. W. C. Johns, and A. R. W. McKellar. Study of coriolis-coupled $\nu_4$, $\nu_6$, and $\nu_3$ fundamental bands and $\nu_5$ -$\nu_6$ difference band of $H_2CO$ - measurement of dipole-moment for $\nu_5 = 1$. *Journal of Molecular Spectroscopy*, 67(1-3):476–495, 1977.

[32] K. Nakagawa, Y. Moriwaki, and T. Shimizu. Observation of the stark-effect in high-overtone band transitions of $NH_3$. *Optics Letters*, 14(10):488–490, 1989.

[33] J. A. Dodd, A. M. Smith, and W. Klemperer. Dipole-moments of highly excited vibrational-states of HCN. *Journal of Chemical Physics*, 88(1):15–19, 1988.

[34] P. H. Vaccaro, J. L. Kinsey, R. W. Field, and H. L. Dai. Electric-dipole moments of excited vibrational levels in the $\tilde{X}^1a_1$ state of formaldehyde by stimulated-emission spectroscopy. *Journal of Chemical Physics*, 78(6):3659–3664, 1983.

[35] D. E. Freeman and W. Klemperer. Electric dipole moment of $^1a_2$ electronic state of formaldehyde. *Journal of Chemical Physics*, 45(1):52, 1966.

[36] D. E. Freeman, J. R. Lombardi, and W. Klemperer. Electric dipole moment of lowest singlet $\pi'$ state of propynal. *Journal of Chemical Physics*, 45(1):58, 1966.

[37] D. E. Freeman and W. Klemperer. Dipole moments of excited electronic states of molecules $^1a_2$ state of formaldehyde. *Journal of Chemical Physics*, 40(2):604, 1964.

[38] T. Suzuki, S. Saito, and E. Hirota. Dipole-moments of $H_2CS$ in the $a^1a_2$ ($\nu = 0$) and $a^3a_2$ ($\nu_3 = 1$) states by modr spectroscopy. *Journal of Molecular Spectroscopy*, 111(1):54–61, 1985.

[39] K. Tanaka, A. Inayoshi, K. Kijima, and T. Tanaka. CO laser-microwave double-resonance spectroscopy of $H_2CO$ with intense stark field - precise measurement of dipole-moment in the ground and $\nu_2$ vibrational-states. *Journal of Molecular Spectroscopy*, 95(1):182–193, 1982.

[40] K. Tanaka, H. Ito, K. Harada, and T. Tanaka. $CO_2$ and CO laser microwave double-resonance spectroscopy of OCS - precise measurement of dipole-moment and polarizability anisotropy. *Journal of Chemical Physics*, 80(12):5893–5905, 1984.

[41] R. L. Deleon, P. H. Jones, and J. S. Muenter. Radio-frequency ir double-resonance spectroscopy using a color center laser. *Applied Optics*, 20(4):525–527, 1981.

[42] M. D. Marshall, K. C. Izgi, and J. S. Muenter. Ir-rf double resonance studies of dipole moments in the $v(1) + v(4)$ and $v(1) + v(5)$ states of acetylene-d. *Journal of Chemical Physics*, 105(18):7904–7909, 1996.

[43] J. C. Keske and B. H. Pate. Decoding the dynamical information embedded in highly mixed quantum states. *Annual Review of Physical Chemistry*, 51:323–353, 2000.

[44] E. R. T. Kerstel, K. K. Lehmann, J. E. Gambogi, X. Yang, and G. Scoles. The $\nu_1$ vibrational predissociation lifetime of $(HCN)_2$ determined from upperstate microwave-infrared double-resonance measurements. *Journal of Chemical Physics*, 99(11):8559–8570, 1993.

[45] K. C. Namiki, J. S. Robinson, and T. C. Steimle. A spectroscopic study of $CaOCH_3$ using the pump/probe microwave and the molecular beam optical stark techniques. *Journal of Chemical Physics*, 109(13):5283–5289, 1998.

[46] W. J. Childs. Overview of laser-radiofrequency double-resonance studies of atomic, molecular, and ionic beams. *Physics Reports-Review Section of Physics Letters*, 211(3):113–165, 1992.

[47] D. W. Callahan, A. Yokozeki, and J. S. Muenter. The polarizability anisotropy of $i-2$ from laser assisted molecular-beam spectroscopy. *Journal of Chemical Physics*, 72(9):4791–4794, 1980.

[48] H. Akagi, K. Yokoyama, and A. Yokoyama. Photodissociation of highly vibrationally excited $NH_3$ in the 5 $\nu_{N-H}$ region: Initial vibrational state dependence of N − H bond dissociation cross section. *Journal of Chemical Physics*, 118(8):3600–3611, 2003.

[49] A. Bach, J. M. Hutchison, R. J. Holiday, and F. F. Crim. Vibrational spectroscopy and photodissociation of jet-cooled ammonia. *Journal of Chemical Physics*, 116(12):4955–4961, 2002.

[50] J. S. Muenter, J. Rebstein, A. Callegari, and T. R. Rizzo. Photodissociation detection of microwave transitions in highly excited vibrational states. *Journal of Chemical Physics*, 111(8):3488–3493, 1999.

[51] A. Callegari, P. Theule, R. Schmied, T. R. Rizzo, and J. S. Muenter. The dipole moment of HOCl in $v_{OH} = 4$. *Journal of Molecular Spectroscopy*, submitted, 2003.

[52] P. Schmidt, H. Bitto, and J. R. Huber. Excited-state dipole-moments in a polyatomic molecule determined by stark quantum beat spectroscopy. *Journal of Chemical Physics*, 88(2):696–704, 1988.

[53] T. Walther, H. Bitto, and J. R. Huber. High-resolution quantum beat spectroscopy in the electronic ground-state of a polyatomic molecule by ir-uv pump-probe method. *Chemical Physics Letters*, 209(5-6):455–458, 1993.

[54] P. H. Vaccaro, A. Zabludoff, M. E. Carrerapatino, J. L. Kinsey, and R. W. Field. High-precision dipole-moments in $\tilde{A}^1a_2$ formaldehyde determined via stark quantum beat spectroscopy. *Journal of Chemical Physics*, 90(8):4150–4168, 1989.

[55] E. Hack, H. Bitto, and J. R. Huber. Stark quantum beat spectroscopy of polyatomic-molecules. *Zeitschrift Fur Physik D-Atoms Molecules and Clusters*, 18(1):33–44, 1991.

[56] G. Chambaud. Potential surfaces and spectroscopy. *Journal De Chimie Physique Et De Physico-Chimie Biologique*, 95(8):1892–1924, 1998.

[57] J. Tennyson, J. R. Henderson, and N. G. Fulton. *dvr3d* - for the fully pointwise calculation of ro-vibrational spectra of triatomic-molecules. *Computer Physics Communications*, 86(1-2):175–198, 1995.

[58] H. Partridge and D. W. Schwenke. The determination of an accurate isotope dependent potential energy surface for water from extensive ab initio calculations and experimental data. *Journal of Chemical Physics*, 106(11):4618–4639, 1997.

[59] B. Galabov, T. Dudev, S. Ilieva, and J. R. Durig. Creation of intensity theory in vibrational spectroscopy: Key role of ab initio quantum mechanical calculations. *International Journal of Quantum Chemistry*, 70(2):331–339, 1998.

[60] D. W. Schwenke and H. Partridge. Convergence testing of the analytic representation of an *ab initio* dipole moment function for water: Improved fitting yields improved intensities. *Journal of Chemical Physics*, 113(16):6592–6597, 2000.

[61] A. Halkier, W. Klopper, T. Helgaker, and P. Jorgensen. Basis-set convergence of the molecular electric dipole moment. *Journal of Chemical Physics*, 111(10):4424–4430, 1999.

[62] G. de Oliveira and C. E. Dykstra. Anomalous isotope effect in Ar − $H_2S$ versus the normal effect in Ne − $H_2S$. *Journal of Chemical Physics*, 110(1):289–295, 1999.

[63] H. G. Kjaergaard, K. J. Bezar, and K. A. Brooking. Calculation of dipole moment functions with density functional theory: application to vibrational band intensities. *Molecular Physics*, 96(7):1125–1138, 1999.

# Chapter 2

# Dipole moment measurement using the Stark effect

The term Stark effect refers to any change induced in the spectrum of a molecule or atom when it is subjected to an external electric field. The large Stark splitting afforded by molecules, in conjunction with high resolution made possible by microwave and lasers techniques, make the Stark effect an important spectroscopic probe for characterizing their properties. It is clearly the most sensitive and accurate technique available for the determination of molecular dipole moments.

It is useful at this point to examine the interaction of a molecular system, that is a collection of charges (nuclei and atoms), and an applied electric field. We will then see two techniques, using measurements in the frequency domain and in the time domain respectively, that make use of these electrical interactions to measure the dipole moment of molecules in excited vibrational states. Measuring the changes in spectra of vibrationally excited states of molecules induced by an external electric field poses the problem of the detection of those changes. A section of this chapter is dedicated to a survey of possible detection techniques for measuring electric field effects in highly vibrationally excited molecules.

## 2.1 Theory of the Stark effect

### 2.1.1 The Stark interaction Hamiltonian

Electrical interactions occur between the collection of charged particles constituting a molecule and an external electric field that exerts various forces and torques on the molecule. As explained in detail in Appendix A, the quantum mechanical operator, $\widehat{H}_{Stark}$, describing the interaction of a molecular electric dipole moment and an external electric field, can be formulated

19

as:

$$\widehat{H}_{Stark} = -\widehat{T}^1(\vec{\mu}) \cdot \widehat{T}^1(\vec{E}) = -\vec{\mu} \cdot \vec{E} \tag{2.1}$$

$$\text{or:} \quad \widehat{H}_{Stark} = -\mu E \cos\theta \tag{2.2}$$

where $\theta$ is the angle between the molecular dipole $\vec{\mu}$ and the electric field $\vec{E}$ lying along the $z$ axis. $\mu_Z = \mu \cos\theta$ is the $Z$ component of the dipole moment vector in the space-fixed system.

## 2.1.2 Stark effect for molecules

The discussion below about the Stark effect follows the treatment of Townes and Schallow [1]. Many of the details can be found in Appendix A.

**Stark effect for symmetric rotors**

We will use perturbation theory to evaluate the effect of an external electric field on the rotational motion of a symmetric rotor. We characterize symmetric rotor wave functions by the quantum numbers $J, K, M$ and $\alpha$, where $K$ and $M$ are the projections of the total angular momentum $J$ along the molecule-fixed and space-fixed z-axes respectively and $\alpha$ represents all the other quantum numbers of the system (e.g. associated vibrational and electronic degrees of freedom). Perturbation theory characterizes the energy of the molecule as the zeroth-order energy (i.e., that in the absence of the field) plus correction terms of successively higher order:

$$W(|\alpha JKM\rangle) = W^o(|\alpha JKM\rangle) + \Delta W_1 + \Delta W_2 + ... \tag{2.3}$$

If the external electric field direction defines the z-axis of the space-fixed system, the first-order correction gives (as developed in Appendix A):

$$\Delta W_1 = \langle \alpha JKM|\widehat{H}_{Stark}|\alpha JKM\rangle = \langle \alpha JKM| - \vec{\mu}.\vec{E}|\alpha JKM\rangle = -\mu(\alpha)E\frac{MK}{J(J+1)} \tag{2.4}$$

It is apparent that the derivation of Eq. 2.4 assumes an explicit separability of rotational motion from other (i.e., electronic and vibrational) degrees of freedom. Determining the quantity $\mu(\alpha)$, the dipole moment for a particular vibronic state in the vibronic molecule-fixed frame, is the object of this study.

It is very important at this point to understand that, as explained in Appendix A, the vibronic dipole moment $\mu(\alpha)$ is expressed in an Eckart frame averaged over a vibrational period of the studied vibronic state, and that its components are referred to this frame. This has an important consequence for line strength calculations since the intensity is proportional to the square of the transition dipole moment matrix element. As discussed in Ref. [2], the factorization of the intensity of a rovibrational transition into a purely vibrational parameter (i.e the vibrational band intensity) and a purely rotational factor (i.e. the Hönl-London factor) implies

that the dipole moment vector is referred to the Eckart internal axes.

The next level of approximation for the Stark effect (i.e., second-order perturbation theory) takes into account the small changes in the molecular wavefunction due to the field and is written:

$$\Delta W_2 = \sum_{n'} \frac{|\langle \alpha' J' K' M' | \mu_Z | \alpha J K M \rangle|^2 E^2}{W^0_{\alpha J K M} - W^0_{\alpha' J' K' M'}} \tag{2.5}$$

$$= (A_{JK} + B_{JK} M^2) E^2 \tag{2.6}$$

For a symmetric top molecule, the dipole moment matrix element is non-zero only if $\Delta J = 0, \pm 1$, $\Delta K = 0$, and $\Delta M = 0$, since $\mu_Z$ is always along the symmetry axis. The two states $|\alpha J K M\rangle$ and $|\alpha' J' K' M'\rangle$ are said to interact through the perturbation $\mu E \cos\theta$. This can be seen classically in terms of an induction process in which the external electrical field induces a moment in the molecule with which it can subsequently interact. The electric field distorts the distribution of electrons, polarizing the molecule and changing its energy [1], as discussed in Section 1.1. This second-order correction to the energy $\Delta W_2$ is usually much smaller than the first-order correction $\Delta W_1$. Still higher-order perturbation terms may be included in the Stark energy but in most cases they are very small.

In the absence of Stark splitting there are $2J + 1$ degenerate levels for each value of J corresponding to different values of $M$. The first-order Stark effect, when present, completely removes this degeneracy. The second-order Stark effect depends on $M^2$, and thus this term separates the levels into pairs of degenerate levels ($\pm M$) except for $M = 0$, which is non-degenerate.

## Stark effect for asymmetric rotors

Rotational levels of symmetric tops show a first-order Stark effect because levels with $K > 0$ are doubly degenerate as explained in Appendix A. In contrast, rotational levels of asymmetric rotors are non-degenerate and thus do not experience a first-order Stark effect. More generally,

---

[1] It is common to make the distinction between the second-order perturbation interaction between rovibronic levels described in Eq. 2.5 and the polarization induced by electronic or vibrational states. The electronic or vibrational polarization is expressed by the a polarizability tensor, a component of which is written, along one the axis of the molecule-fixed frame, as:

$$P_{xx} = 2 \sum_{n'} \frac{|\langle n' | \mu_Z | n \rangle|^2}{W_n - W_{n'}} \tag{2.7}$$

This polarizability tensor describes the polarization of the state $n$ by states $n'$, which can be other vibrational or electronic states. The contribution from the different rotational levels is not discriminated. The difference between the interaction between rovibronic levels as described in Eq. 2.5 and the interaction described by Eq. 2.7 is a matter of order of magnitude, since vibrational or electronic states are much further in energy than rotational states, and not of physical nature.

no electric multipole moments of odd order can exist in the absence of degeneracy. Thus, the Stark effect is only observed in asymmetric rotors in the second order perturbation theory corrections.

For the usual case in which there is no accidental near degeneracy, the Stark energy can be written as the sum of a number of terms containing matrix elements between rotational states, using the fact that the matrix elements are non zero for $\Delta M = 0$ and $\Delta J = 0, 1$:

$$\Delta W_{J\tau M} = \sum_{x=a,b,c} \sum_{\alpha'} \sum_{J'} \sum_{\tau' \neq \tau} \frac{\sum_M \sum_{M'} |\langle \alpha' J' \tau' M' | \mu_x | \alpha J \tau M \rangle|^2}{W^0_{\alpha J\tau} - W^0_{\alpha' J' \tau'}} E^2 \tag{2.8}$$

$$= \sum_{x=a,b,c} \mu_x^2 E^2 \sum_{\alpha'} \sum_{\tau' \neq \tau} \frac{\sum_M |\langle \alpha' J - 1\tau' M | \alpha J \tau M \rangle|^2}{W^0_{\alpha J\tau} - W^0_{\alpha' J - 1\tau'}} \tag{2.9}$$

$$+ \frac{\sum_M |\langle \alpha' J \tau' M | \alpha J \tau M \rangle|^2}{W^0_{\alpha J\tau} - W^0_{\alpha' J\tau'}} + \frac{\sum_M |\langle \alpha' J + 1\tau' M | \alpha J \tau M \rangle|^2}{W^0_{\alpha J\tau} - W^0_{\alpha' J+1\tau'}}$$

The indices $a, b$ and $c$ indicate the directions of the three axes of the molecule-fixed system [2], and $W^0_{\alpha J\tau}$ is the unperturbed energy of the rotational states $J_\tau$. We have factored out the dipole moment component $\mu_x$ along the molecule-fixed system axes, leaving only direction cosine matrix elements that can be evaluated using asymmetric rotor programs. To calculate the Stark shift of a state $|\alpha J\tau M\rangle$, one must consider its interaction with all the states $|\alpha' J - 1\tau' M\rangle$, $|\alpha' J\tau M\rangle, |\alpha' J + 1\tau' M\rangle$ in the energy region around it. States that are too far away in energy will not contribute significantly because of the denominator of each term, which contains the energy difference between the zeroth-order rotational state and the one shifting it via the Stark effect. The expression for the overall Stark shift can be condensed into

$$\Delta W_{J\tau M} = (A_{J\tau} + B_{J\tau}M^2)E^2 \tag{2.10}$$

where the matrix elements in Eq. 2.10 are combined into the constants A and B. These constants thus give the net shift of a given state by the collection of states that can interact through one or more of the appropriate matrix elements.

**Stark induced interaction of two nearby levels**

In the cases treated above it was assumed that the interaction between levels is weak, allowing the perturbation theory to be applied. If one considers two levels that are very close in energy, the energy due to the electric field induced interaction between the levels cannot be considered as a small perturbation, and perturbation theory does not apply. In this case one

---

[2] Eq. 2.8 is adapted from Ref. [1]. In this reference $a, b$ and $c$ are said to indicate the directions of the three principle axis of inertia. If this statement is valid for the equilibrium configuration, it does not hold anymore for vibrationally excited states. As discussed above, separating rotational from vibrational motion makes use of Eq. 25 of Appendix A, the so-called Eckart conditions, which define the Eckart frame. Therefore, the vibronic dipole moment of Eq. 2.8 is expressed in the Eckart frame.

must derive an exact solution. This situation typically occurs for slightly asymmetric rotors, and for l-type doublet levels of vibrationally excited linear molecules, where rotational levels can be very close. This applies as well for the case where there are accidentally two nearly degenerate levels.

An exact solution is therefore necessary to consider two neighboring zeroth-order levels, $\psi_1^0$ and $\psi_2^0$, strongly interacting through the operator $\hat{H}_{Stark} = -E\mu_Z = -E\mu\cos\theta$. After diagonalization of the total Hamiltonian, one gets the energies for the perturbed levels:

$$W_{1,2} = \frac{W_1^0 + W_2^0}{2} \pm \left[\left(\frac{W_1^0 - W_2^0}{2}\right)^2 + E^2\mu_{12}^2\right]^{1/2} \qquad (2.11)$$

$$\text{with} \qquad \mu_{12} = \langle\psi_1^0|\mu\cos\theta|\psi_2^0\rangle$$

We can consider two different cases, according to the strength of the interaction energy with respect to the energy separation of the two levels

$$\text{If} \quad E\mu_{12} \ll |W_1^0 - W_2^0| \quad \text{then} \quad W_1 = W_1^0 + \frac{E^2\mu_{12}^2}{W_1^0 - W_2^0} + ... \quad \text{and} \quad W_2 = W_2^0 - \frac{E^2\mu_{12}^2}{W_1^0 - W_2^0} + ... \qquad (2.12)$$

$$\text{If} \quad E\mu_{12} \gg |W_1^0 - W_2^0| \quad \text{then} \quad W_{1,2} = \frac{W_1^0 + W_2^0}{2} \pm E\mu_{12} + ... \qquad (2.13)$$

In the first case, Eq. 2.12, as the magnitude $E$ of the electric field increases, the Stark shift initially depends on $E^2$, as is typical for a second-order perturbation, although it is not necessarily small, depending upon the energy denominator. At higher electric field strength, the Stark shift becomes linearly dependent on $E$, as seen in Eq. 2.13, as would be expected from a first-order Stark of a symmetric top, since the two $K-$states are degenerate. Thus, for nearly degenerate levels, the Stark shift exhibits a transition from a second-order to a first-order Stark effect with increasing field strength. This case typically applies to a slightly asymmetric top, where pairs of the degenerate symmetric top energy levels are split by asymmetry. As they are non-degenerate, they cannot have a permanent electric dipole moment in the space-fixed frame, and the Stark effect is initially of second-order (induction process). Once the electric field is large enough to cause the mixing of states having opposite parity (_e.g._ the members of an asymmetry doublet), the Stark effect becomes linearly proportional to the electric field (see Appendix A for more details). Therefore the Stark shift for an asymmetric top shows a transition from a second-order to a first-order dependence on the electric field strength, depending on the magnitude of $\mu E$ with respect to $W_{J,\tau}^0 - W_{J,\tau'}^0$. At sufficiently high field, all the M-components of a single rotational state $W_{J,\tau}^0$, become equally spaced (see Eq. 2.13). If the asymmetry is small, dipole moment matrix elements $\mu_{12}$ can be approximated by those of a pure symmetric top as given by Eq. 2.4.

### 2.1.3 Relative intensities of Stark components

Having derived the expression of the Stark shift for all the M components of a rotational state, we must now calculate the relative intensity of transitions from one $|J\tau M\rangle$ state to another.

Consider a two-level system submitted to radiation during the time interval $t$. The Fermi golden rule [3, 4] gives a damped sine-squared dependence for the transition probability $P_{ij}$:

$$P_{ij}(\nu) = \frac{4\mu_{ij}^2 E^2}{4\mu_{ij}^2 E^2 + h^2(\nu_{ij} - \nu)^2} \cdot \sin^2\left[\sqrt{4\mu_{ij}^2 E^2 + h^2(\nu_{ij} - \nu)^2} \cdot \frac{t}{2\hbar}\right] \qquad (2.14)$$

where $\nu_{ij}$ is the resonant frequency, $E$ is the magnitude of the electric field of the radiation that induces the transition, and $\mu_{ij}$ is the transition dipole moment between levels $|i\rangle$ and $|j\rangle$.

The intensity is proportional to the square of the dipole moment matrix element. Having factored out the vibronic component of the dipole moment, $\mu_\alpha$ in Eq. 2.4 and Eq. 2.5, one can see that the intensity will be proportional to the square of the direction-cosine matrix elements. These matrix elements are derived for a symmetric top in Appendix A. The $M$ dependence of these matrix elements for an asymmetric rotor is the same as for a symmetric rotor. One can see this by considering that this dependence is roughly independent of $K$, and that the asymmetric rotor wavefunctions can be expanded in a basis of symmetric top wavefunctions of the same $J$ and $M$, but different $K$. Thus, the $M$ dependence of these matrix elements for an asymmetric rotor is the same as for a symmetric rotor. The two levels involved in a rotational transition are $(2J + 1)$ degenerate, and the lineshape and intensity of a rotational transition is given by Eq. 2.14. When an electric field is applied, the spatial degeneracy is lifted. The $\Delta M = 0$ selections rules of Appendix A allows $2J + 1$ two-level transitions for which the intensity and lineshape are given by Eq. 2.14.

### 2.1.4 Stark effect when hyperfine structure is present

One usually considers the nuclei of a molecule as point charges of infinite mass. In reality, a nucleus should be considered as a charge distribution in motion with a nuclear spin angular momentum $\vec{I}$ that can couple with the total electronic angular momentum $\vec{J}$ to give the total angular momentum $\vec{F} = \vec{J} + \vec{I}$. The perturbation of the rovibronic energy levels of a molecule induced by this coupling is called hyperfine structure. Most of the time the inhomogeneity of the charge distribution inside the nucleus, represented at the lowest order by the electric quadrupole moment $Q$ is small, making it difficult to observe the splitting of the energy levels arising from this hyperfine effect. In this case, the treatment of Stark effect presented above is perfectly valid. However, if one or more nuclei have a large electric quadrupole moment, one must take into account the coupling between the nuclear spin $\vec{I}$ and the electronic angular momentum $\vec{J}$. This coupling can be characterized into three regimes.

In the limit of a weak electric field, the Stark energy is considerably less than the hyperfine energy. The molecular state is satisfactorily specified by the quantum numbers $I$, $J$, $F$, and $M_F$. $M_J$ is no longer a good quantum number. Each hyperfine level is then split by the Stark effect into various components by an amount that is small compared with the hyperfine splitting. The first-order correction to the energy is given by Ref. [1]:

$$\Delta W_{FJKIM_F} = -\frac{\mu K \left[J(J+1) + F(F+1) - I(I+1)\right] M_F E}{2J(J+1)F(F+1)} \tag{2.15}$$

In the limit of high electric field, the Stark energy is much larger than the hyperfine energy. In this case, the molecule is made to precess so violently by the electric field that the nuclear orientation cannot follow the motion. When this occurs, $\vec{I}$ and $\vec{J}$ are decoupled, and $F$ and $M_F$ are no longer good quantum numbers, since $\vec{I}+\vec{J}$ is no longer fixed. The good quantum numbers are $I$, $J$, $M_I$ and $M_J$ and the Stark splitting is identical with that obtained when no hyperfine structure is present. The hyperfine structure splits each $M$ level by an amount that is much smaller than the Stark levels. If the Stark energy is large compared with the hyperfine energy but small compared with the rotational energy, the hyperfine splitting is given by Ref. [1]:

$$\Delta W_{JKIM_J M_I} = \frac{eqQ}{4I(2I-1)(2J-1)(2J+3)} \left[\frac{3K^2}{J(J+1)} - 1\right] \left[3M_I^2 - I(I+1)\right] \left[3M_J^2 - J(J+1)\right] \tag{2.16}$$

where $eqQ$ is the quadrupole coupling constant.

In an intermediate regime, the Stark and hyperfine energies, and hence splittings, are comparable in magnitude. In this case $M_J$, $M_F$ and $F$ are no longer good quantum numbers. The wavefunctions in this intermediate regime are combinations of wavefunctions appropriate for the weak or strong field regimes. Calculation of wavefunctions, energy levels and relative intensities in this regime is complex [1].

### 2.1.5 Contribution of rotation to the dipole moment

In the above development, we have considered dipole moment matrix elements for rovibronic states $\langle \alpha' J' \tau' M' | \mu_Z | \alpha J \tau M \rangle$, and we assumed an implicit factorization $\langle \alpha' | \mu_Z | \alpha \rangle \langle J' \tau' M' | J \tau M \rangle$, where $\langle \alpha' | \mu_Z | \alpha \rangle$ is the dipole moment characteristic of a particular vibronic state. This allowed us to derive all the above expressions using direction-cosine matrix elements.

At the level of accuracy needed for high resolution spectroscopy, however, the molecular Hamiltonian is not truly separable into electronic, vibrational and rotational degrees of freedom. This is nevertheless done with recourse to several approximations and transformation of the molecular Hamiltonian [5, 6]. Using these approximations when deriving the vibronic dipole moment, there still remains a J dependence to the dipole moment [7] due to the centrifugal distortion of the molecule. An exact derivation of the vibrational and rotational dependence of

the dipole moment operator for asymmetric rotors can be found in Ref. [8]. The space-fixed $Z$ vibronic component $\mu_Z^\nu$ of the dipole moment is given by [8]:

$$\mu_Z^\nu = \sum_\alpha \varphi_\alpha \mu_\alpha^\nu + \sum_{\alpha,\beta,\gamma} \frac{1}{2}\{\varphi_\alpha, J_\beta J_\gamma\} \, {}^{\alpha,\beta\gamma}_{(2)}\tilde{M} \tag{2.17}$$

$$ {}^{\alpha,\beta\gamma}_{(2)}\tilde{M} = \Theta_\alpha^{\beta\gamma} + C_\alpha^{\beta\gamma} \tag{2.18}$$

$$\Theta_\alpha^{\beta\gamma} = -\sum_m \frac{B_m^{\beta\gamma\,\alpha}}{\omega_m}\,\mu_m \tag{2.19}$$

$$ {}^\alpha\mu_m = \frac{\partial \mu_\alpha}{\partial Q_m} \tag{2.20}$$

$$C_\alpha^{\beta\gamma} = s_{111}\sum_\delta \epsilon_{\beta\gamma\delta}(\delta_{\alpha\beta}^\beta \mu_e - \delta_{\alpha\beta}^\gamma \mu_e) \tag{2.21}$$

$$B_m^{\beta\gamma} = -\frac{\hbar^3}{2(hc)^{3/2}}\frac{(\partial I_{\beta\gamma}/\partial Q_a)_e}{I_\beta I_\gamma \omega_m^{1/2}} \tag{2.22}$$

where the second term of Eq. 2.17 expresses the rotational contribution to the dipole moment operator ($\{A, B\}$ is the anti-commutator of $A$ and $B$). This rotational contribution can be decomposed into two terms, as seen in Eq. 2.18, where $\Theta_\alpha^{\beta\gamma}$ is the coefficient of Watson and $C_\alpha^{\beta\gamma}$ is the term arising from the rotational contact transformation introduced by Clough et al.[9]. The indices $\alpha, \beta, \gamma$ denote the principal inertial axis, $\omega_m$ and $Q_m$ are the vibrational frequency and the dimensionless normal coordinate of the mode $m$ respectively, $I$ is the moment of inertia tensor, $\delta$ the Kronecker symbol, $\epsilon$ the asymmetric tensor and $\varphi_\alpha$ the direction cosine between the axis $Z$ and $\alpha$. $s_{111}$ is the term of the contact transformation used to reduce the quartic centrifugal terms of the molecular Hamiltonian [5].

## 2.2  Experimental techniques used for measuring Stark splittings.

We saw in last section that Stark splittings and shifts are directly related to the dipole moment of the molecule. If one can measure these Stark splittings for two levels $a$ and $b$, one can extract the dipole moments of those levels.

We used several techniques to measure the dipole moments of highly excited states. All these techniques can be decomposed into three elementary steps:

1. The excitation/state-selection step:

   Highly excited rovibrational states are not populated at room temperature. Population must be transferred selectively to these excited states using either overtone excitation or stimulated emission pumping. Overtone excitation limits the nature of the excited rovibrational levels for which one can measure the dipole moment to light atom stretch

overtones (typically OH, CH stretches). Stimulated emission pumping makes it is possible to access vibrational states of different nature than light atom stretch, but the pump step (see Section 3.2.6) must be to a Franck-Condon active mode.

2. The Stark splitting measurement:

We will distinguish between frequency and time domain techniques of measuring Stark splittings. The frequency domain technique is based on microwave spectroscopy. We will measure the shift induced by the Stark field on a microwave induced transition between two rotational states $a$ and $b$ within an excited vibrational state. The time domain technique is based on Stark induced quantum beat spectroscopy. A coherent wavepacket is created as a superposition of the two stationary eigenstates $a$ and $b$. The wavepacket evolves differently in time as it is submitted to a Stark field.

3. The detection step:

Both the microwave induced pure rotational transition in the excited vibrational state and the time evolution of the wavepacket must be detected. We use one of three techniques for this step: laser induced fluorescence, vibrational predissociation and electronic photodissociation.
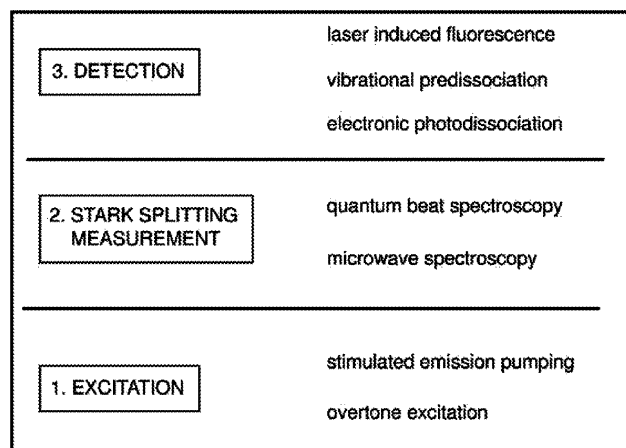


**Figure 2.1:** A measurement of the dipole moment of a highly excited vibrational state can be decomposed in three elementary steps. Different techniques can be used to perform each step. An experiment is a choice of combination of these techniques.

Overtone excitation [10] has been used in all our experiments for the state-selection step (step 1) and will be not described any further. Steps 2 (Stark microwave spectroscopy and Stark induced quantum beat spectroscopy) and 3 are described in more detail below. The different experiments implemented in this work are different combinations in the range of possibilities, summarized in Fig. 2.1, for the three successive steps.

## 2.2.1 Frequency domain measurements of Stark splittings: Stark microwave spectroscopy.

As seen above, applying an external electric field splits and shifts the levels of the molecule and hence modifies its spectrum in a manner that depends upon the dipole moment. This can be applied to measuring the dipole moment of an excited vibrational state.

Once a rovibrational state $a$ have been selected and populated (step 1), one can use a microwave source to induce a pure rotational transition between two rovibrational states $a$ and $b$ within the same excited vibrational state. Upon applying an external Stark electric field, both level $a$ and $b$ are split into their different M-components and shifted according to the expressions reported in Section 2.1.2. From the amount the microwave transition is shifted, one can extract the dipole moment of the excited vibrational state.

For the sake of clarity, it is useful to consider as an example an experiment we performed on $H_2CO$ (this experiment will be discussed in much more detail in Chapter 3). Briefly, a microwave transition is made between the $1_{11}$ and $1_{10}$ rotational levels in the $5_2$ vibrational level, as displayed in Fig. 2.2. Applying a Stark field shifts the center transition frequency. Fig. 2.3 displays the shift of the center transition frequency as a function of the Stark voltage.
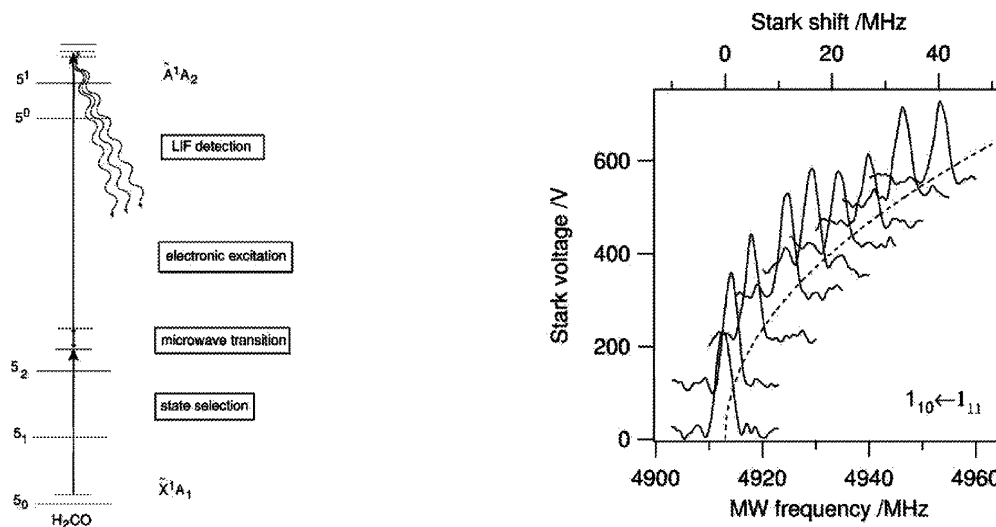


**Figure 2.2:** Stark effect detection using LIF on $H_2CO$. A first laser pulse populates a single rovibrational state with 2 quanta of CH stretch, and a second laser pulse probes the population transferred by the microwave to the first excited electronic state, that fluoresces to the ground electronic state.

**Figure 2.3:** Quadratic Stark effect in $H_2CO$. The frequency of the microwave transition $1_{11} \leftrightarrow 1_{10}$, in the vibrational level of $H_2CO$ with 2 quanta in the asymmetric C-H stretch mode, is shifted under the effect of a Stark field. In this case the Stark shift depends on the square of the electric field.

According to Eq. 2.10, the Stark shift is quadratic with respect to the electric field. Fitting the experimental Stark shift of Fig. 2.3 with Eq. 2.10 enables us to determine the value of the

dipole moment for the $5_2$ vibrational state of $H_2CO$.

## 2.2.2 Time domain measurement of Stark splittings: Stark induced quantum beat spectroscopy.

The quantum beat principle relies on the interference effect between different indistinguishable paths in a pump-probe experiment. A polarized pump laser pulse excites molecules from an initial state $|i\rangle$ to at least two intermediate excited states $|e\rangle$ creating a coherent superposition, or wavepacket, of several excited states $|e\rangle$. After a fixed time delay, a polarized probe pulse induces a transition from the superposition of excited states $|J_e \ M_e\rangle$ to the final states $|f\rangle$. Fig. 2.4 gives a scheme of the quantum beat technique principle and Fig. 2.5 provides an example of a quantum beat experiment made on $H_2O$. In this example the initial states $|i\rangle$ are $|J_i \ M_i\rangle$ M-rotational states of the ground vibrational state, the excited states $|e\rangle$ are $|J_e \ M_e\rangle$ M-rotational states of the vibrational state with 4 quanta of OH stretch and the final states $|f\rangle$ are $|J_f \ M_f\rangle$ are M-rotational states of a dissociative excited electronic state. This example will be discussed in more details in Chapter 5.
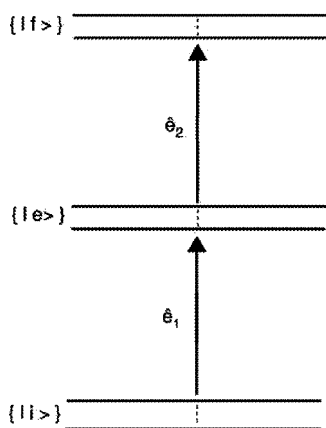


**Figure 2.4:** Scheme of the double-resonance stark induced quantum beat technique.
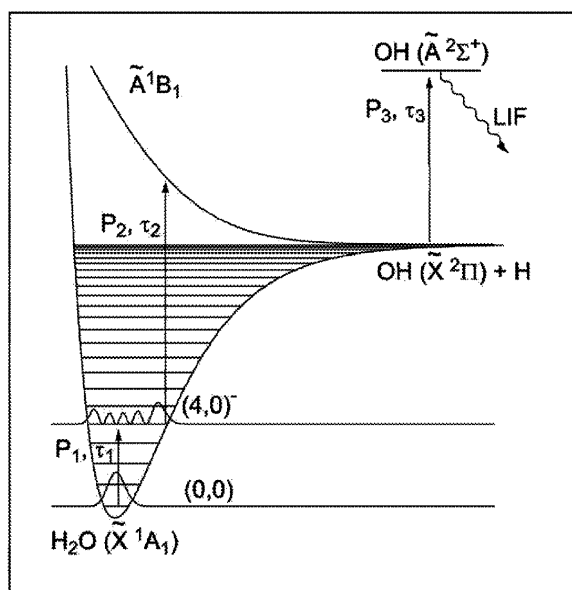
**Figure 2.5:** Stark effect detection using electronic photodissociation for $v_{OH} = 4$ of water. A first laser populates a rovibrational state with 4 quanta in the OH stretch. A second laser brings the molecule to a purely repulsive electronic state. A third laser probes by LIF the OH fragments.

The orientation of the pump laser polarization with respect to an external electric field controls the preparation of the coherent superposition of several $|J_e \ M_e\rangle$ from a single $|J_i \ M_i\rangle$. For example a laser polarized parallel to the electric field will gives $\Delta M = 0$ selection rules,

and a laser polarized perpendicular to the electric field will gives $\Delta M = \pm 1$ selection rules. A detailed formulation of the quantum beat phenomenon is given in Appendix B, where a simple expression is derived for the time dependence of the amount of molecules transferred to the final states,

$$N_f(t) \propto \sum_{M_e} \sum_{M_e'} P^{pump}_{M_e M_e'} P^{probe}_{M_e' M_e} \exp\left[-i\left(\omega_{M_e} - \omega_{M_e'}\right)t\right] \tag{2.23}$$

with the scalar quantities $P^{pump}_{M_e M_e'}$ and $P^{probe}_{M_e' M_e}$ that depends both on the quantum numbers of the initial, intermediate, and final states and on the polarizations of the pump and probe radiation. $\omega_{M_e}$ and $\omega_{M_e'}$ are the angular frequencies of the states $|J_e\ M_e\rangle$ and $|J_e\ M_e'\rangle$ respectively. According to the derivation proposed in Appendix B, the amount of population of molecules transferred to the final states as a function of time $N_f(t)$ is a superposition of oscillating signals each one of them having a phase $\left(\omega_{M_e} - \omega_{M_e'}\right)t$, and a normalized magnitude of oscillation given by the contrast $P$ which depends on the polarization of the pump and probe radiation and on the quantum numbers of the states involved. This contrast gives the theoretical depth of the beats. A table of the contrast is given in Appendix B for a linearly polarized pump-probe scheme and for different sets of initial, intermediate and final states [3]. It is convenient to choose $J_e = 1$ intermediate levels and lasers polarized at $45^o$ with respect to the external field (in the case of a second order Stark effect) in order to have a single beat between $M_e = 0$ and $|M_e| = 1$ states. However more complex beat patterns can be considered following this treatment.

If we fix the origin of time at $t = t_{pump} = 0$, Eq. 2.23 gives the amount of molecules transferred at time $t = t_{probe} - t_{pump}$, and the frequencies of the oscillations are given by the energy differences $\hbar\left(\omega_{M_e} - \omega_{M_e'}\right)$ which are related to the external Stark electric field which defines the quantization axis. The wavepacket is a coherent superposition of stationary eigenstates with the same total angular momentum $J$, and different values of projection $M$ on the space-fixed laboratory frame, and as such a superposition of $M$-states, it is spatially orientated. Since a superposition of eigenstates is non-stationary, the phase of the wavepacket, or its spatial orientation, changes both as a function of the time and of the amplitude of the electric field.

An alternative of viewing this, as displayed in Fig. 2.6, is to see a wavepacket created at $t = 0$ with a particular initial spatial orientation, and evolving with phases $\left(\omega_{M_e} - \omega_{M_e'}\right)t$ during a period of time $t_{probe} - t_{pump}$. At time $t = t_{probe}$, the spatial orientation of the wavepacket is probed by a linearly polarized laser. If we take pump and probe lasers with parallel polarizations, for an integer number of periods (or at $t_{probe} - t_{pump} = 0$), the maximum population of final molecules is achieved for $(P, R)$, $(R, P)$, $(P, P)$, $(R, R)$ or $(Q, Q)$ pump/probe transitions, and the minimum is achieved for a $(Q, P)$, $(Q, R)$, $(P, Q)$, $(R, Q)$ pump/probe transitions, since

---

[3] In this table, the set of the different initial, intermediate, and final states are indicated by the initial state $J_i$ and into parenthesis the type ($P$, $Q$ or $R$) of rotational transitions involved in the pump/probe sequence. For example, $J = 0$ $(R, P)$ indicates an initial state $J_i = 0$, $J_e = 1$ and $J_f = 0$.

for a $Q$ branch transition the transition moment lies along $\vec{J}$, while for $P$ and $R$ branch transitions the transition moment lies in a plane perpendicular to $\vec{J}$. Since the energy separation $\hbar\left(\omega_{M_e} - \omega_{M'_e}\right)$ is determined by the Stark effect, as explained in section 2.1.2, this can be classically seen as the field exerting a torque on the molecular wavepacket, making it precess during the time interval $t_{probe} - t_{pump}$. The spatial orientation at time $t = t_{pump}$ determines the overlap with the probe radiation polarization, and thus the transition moment of the probe transition. The evolution of the wavepacket can be measured by probing it at different $t = t_{probe}$,
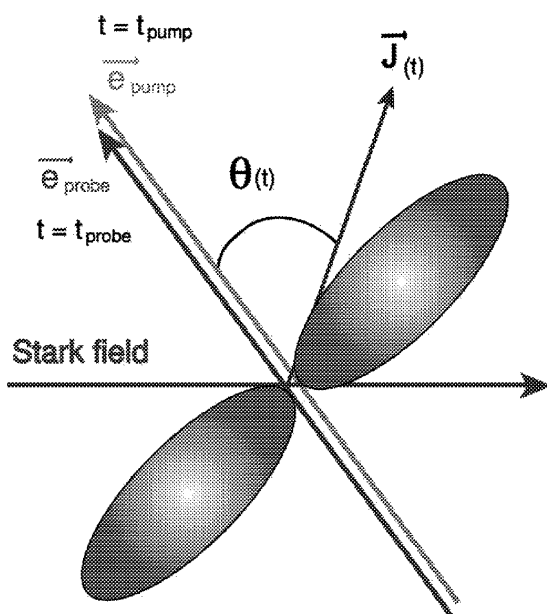


**Figure 2.6:** Pump-probe experiments and temporal evolution of the wavepacket. At $t = t_{pump}$, the polarized pump radiation, $\vec{e}_{pump}$ creates the wavepacket of the $M_e$ intermediate excited states (represented as an angular momentum wavefunction, in grey ). The spatial orientation $J(t)$ of the wavepacket makes an angle $\theta(t)$ with the polarization $\vec{e}_{probe}$ of the probe radiation that transfers the wavepacket to the final states. At $t = t_{probe}$, $\theta = \theta_{(probe)}$ . The temporal evolution $\theta(t)$ of the wavepacket is driven by the Stark electric field.

and so measuring $N_f\left(t_{probe}\right)$. This time domain method has been applied, for dipole moment or nuclear quadrupole constant measurements (see Ref. [11] for a review) although up to this point not for highly vibrationally excited states. An equivalent method consists in changing the phase $\left(\omega_{M_e} - \omega_{M'_e}\right)t_{probe}$ by changing the energy difference $\left(\omega_{M_e} - \omega_{M'_e}\right)$, which is related to the Stark electric field and to the molecular dipole moment, at a fixed time $(t_{probe})$, and thus measuring $N_f\left(E_{Stark}\right)$, which is in practice more convenient to carry out experimentally. The quantity $\left(\omega_{M_e} - \omega_{M'_e}\right)$, and thus the dipole moment, is extracted from the measurement of the period of the beat oscillations. Fig.2.7 gives an example of quantum beats on the water molecule. The line shape of the oscillations can be approximated by a sine with a phase $\left(\omega_{M_e} - \omega_{M'_e}\right)t$, since only the phase is of interest for us. To take into account limitations of actual experiments we will write the more general expressions of Eq. 2.24 and Eq. 2.25 for a first-order and second-order

quantum beats line shape respectively.

$$S(E)^{(1)} = (k - 1 - k_2 E)[1 + k_3 sin(2\pi C^{(1)} Et + \phi)] \qquad (2.24)$$

$$S(E)^{(2)} = (k - 1 - k_2 E^2)[1 + k_3 sin(2\pi C^{(2)} E^2 t + \phi)] \qquad (2.25)$$

In these expressions, the coefficients $C^{(1)}$ and $C^{(2)}$ are respectively called first and second-order Stark coefficients. They are respectively related to $-\mu(\alpha)\frac{K}{J(J+1)}$ of Eq. 2.4 and to $B_{JK}$ of Eq. 2.5. $C^{(1)}$ and $C^{(2)}$ have units of $Hz(v/cm)^{-1}$ and $Hz(v/cm)^{-2}$ respectively. This is a very
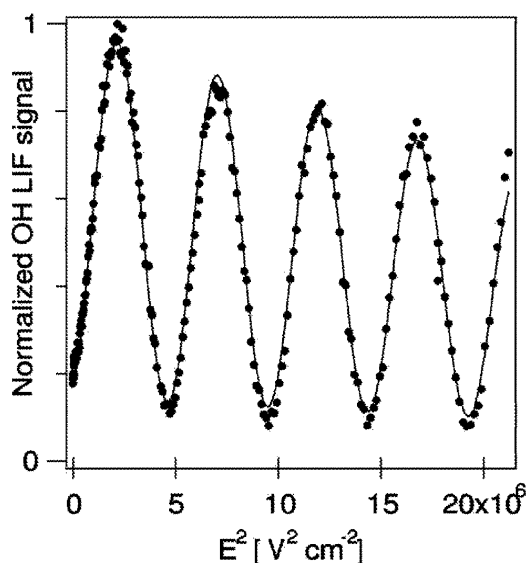


**Figure 2.7:** Quantum beat spectrum for the wavepacket which is the superposition of the $M$ states of the $1_{1\,0}$ rotational state of the $v_{OH} = 4$ vibrational state of $H_2O$. The orientation of the wavepacket is related to the LIF of OH fragments, as shown in Fig. 2.5. Scanning the Stark electric field changes the orientation of the wavepacket at $t = t_{probe}$ and thus modulates the LIF. The period of these oscillation is related to the dipole moment of this vibrational state.

powerful method to measure small energy level splittings below the limits imposed by Doppler broadening and finite laser linewidth, giving us access to the molecular properties responsible for the splittings.

Once we have populated the final states $J_f$, the transferred population $N_f$ must be detected by a means that can keep the coherence between the $M_f$ states. This will be the subject of section 2.2.3.

## 2.2.3 Spectroscopic techniques for detecting Stark effect

Both techniques of measurement of the Stark effect, either in the frequency or in the time domain, rely on initially populating a single rovibrational state. After some time delay, the population of this rovibrational state has been modified, either because a microwave radiation transferred its population to another rovibrational state, or because the coherent superposition

of the M-states wavepacket has evolved with time. The information on the dipole moment is extracted from the modification of this change of population under the effect of an electric field, and this population change must be detected spectroscopically (step 3). In the following section we will consider the various possibilities for completing step 3.

For the frequency domain technique, a microwave transition induces a pure rotational transition, transferring population between states $a$ and $b$. One must subsequently detect the transferred population. For the time domain technique, the coherent wavepacket evolves in time until it is detected by a delayed probe laser. We have used several different techniques for detecting the population of the final state.

## Detection using laser induced fluorescence (LIF).

If a fluorescent electronic state is easily accessible with a laser, and if the non-radiative decay (_via_ internal conversion, inter-system crossing, or collisions) is not too fast and the fluorescence lifetime not too long (with respect to the transit-time of the molecules in front of the photomultiplier), laser induced fluorescence detection is a sensitive method for detecting molecules in vibrationally excited states. In part of the work performed for this thesis, this LIF method was applied to $H_2CO$, as shown in the energy level diagram of Fig. 2.8.

This is a straightforward method if there is a bound electronic state at a wavelength easy to generate. However, the transition we use to probe must have an appreciable Franck-Condon factor. Since we start from vibrational states with quanta in light atoms stretch modes (OH, CH, NH) which are generally not Franck-Condon active in electronic transitions, we probed them by exciting vibronic states with the same number of quanta in these modes.

## Detection using vibrational predissociation

If no fluorescing electronic state is easily available, another way of detecting the population of the final state of the Stark measurement is to use a laser pulse to transfer the molecules to a vibrational state above the dissociation limit of the ground electronic state. The unimolecular dissociation fragments are then probed by using a third laser to induce an electronic transition and recording the fluorescence with a photomultiplier. This solution has been used for HOCl [12] to study the vibrational state with 4 quanta in the OH stretch mode, as shown in Fig. 2.9.

This is a powerful method, as it is applicable to all molecules that can be dissociated by vibrational overtone excitation. However, the dissociation must be fast compared to the time that the molecules fly out of the region of the laser overlap and the region observed by the PMT. Moreover, the products are distributed among several rovibrational states and since we probe only one product state at a time, we loose the population in the other states. This requires choosing the rovibrational state of the product corresponding to the main dissociation channel
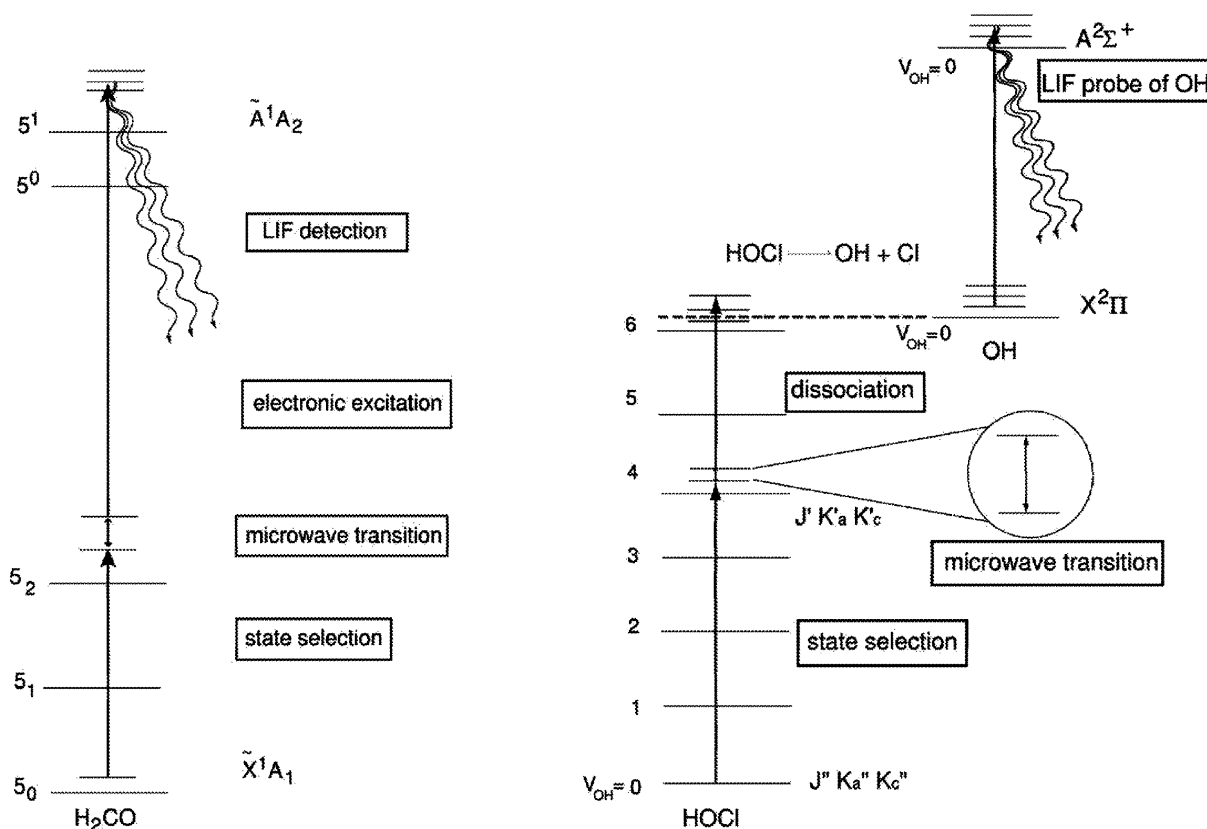
**Figure 2.8:** Stark effect detection using LIF on $H_2CO$. A first laser pulse populates a single rovibrational state with 2 quanta of CH stretch, and a second laser pulse probes either the population transferred by the microwave or the coherent wavepacket to the first excited electronic state, that fluoresces to the ground electronic state.

**Figure 2.9:** Stark effect detection using vibrational predissociation for $\nu_{OH} = 4$ of HOCl. A first laser pulse populates a rovibrational state with 4 quanta of OH stretch. Microwave radiation then induces a pure rotational transition between two rotational of this excited vibrational state. A second laser pulse makes a vibrational overtone transition to a dissociative rovibrational state, and a third laser probes the OH fragments by LIF.

of the excited parent molecule created in the second step. Thus, the sensitivity of this approach is reduced by the fractional product population that one can detect at one time.

## Detection using electronic photodissociation

Electronic photodissociation can be also used to probe the amplitude of a coherent wavepacket by transferring it to a purely repulsive electronic state (*i.e.* an excited electronic surface with no dissociation barrier). In this case, the molecule is likely to dissociate on a picosecond or even femtosecond time scale, and we can probe as previously the dissociation products by LIF, with the same limitations related to the distribution over various dissociation channels. This method has been applied to $H_2O$ and HDO as schematically illustrated in Fig. 2.5.

However electronic photodissociation cannot be used to detect the population transfer induced by a microwave radiation between two excited rovibrational states. The electronic transition that dissociates the molecule is not rotationally resolved and all the rovibrational states with sufficient energy can reach the electronic continuum. Therefore it is not possible to determine the difference of population between the two excited rovibrational states since the populations of both of them are transferred to the electronic state continuum [4].

## 2.3  Summary

We showed in this section that the Stark effect has different expressions, linear or quadratic with the electric field, for the different types of rotors, and that correction terms due to the hyperfine structure or to the centrifugal distortion must be added to be able to extract the dipole moment value from the Stark shift. Two different methods have been used to measure the Stark shift of vibrationnally excited levels of the ground electronic state, one using a microwave-induced pure rotational transition, and the other one quantum beats of a coherent wavepacket. We also described several methods that we have used to detect the change in the molecular system induced by the Stark electric field. Subsequent chapters will describe in details how these approaches have been implemented.

## References

[1] C.H. Townes and A.L. Schawlow. *Microwave Spectroscopy.* Dover Publications, New York, 1975.

[2] C. R. Lesueur, S. Miller, J. Tennyson, and B. T. Sutcliffe. On the use of variational wave-functions in calculating vibrational band intensities. *Molecular Physics,* 76(5):1147–1156, 1992.

[3] Claude Cohen-Tannoudji, Bernard Diu, and Franck Laloe. *Mécanique Quantique,* volume 2. Hermann, 1996.

[4] N.F. Ramsey. *Molecular Beams.* Oxford University Press, New York, 1956.

[5] M.R. Aliev and J.K.G. Watson. *High-order effects in the vibration-rotation spectra of semi-rigid molecules, Molecular Spectroscopy: Modern Research,* volume III, pages 2–67. Academic Press, Orlando, Fla., 1985.

---

[4] This statement is not strictly correct since we are using polarized lasers. The efficiency with which the population of the rovibrational state is transferred to the repulsive electronic state is thus $J$ dependent as explained in Appendix B. It may be possible to detect a microwave induced population transfer between two different rovibrational states.

[6] H. Meyer. The molecular hamiltonian. *Annual Review of Physical Chemistry*, 53:141–172, 2002.

[7] T. R. Dyke and J. S. Muenter. Electric dipole-moments of low j states of $H_2O$ and $D_2O$. *Journal of Chemical Physics*, 59(6):3125–3127, 1973.

[8] C. Camy-Peyret and J. M. Flaud. *Vibration-rotation dipole moment operator for asymmetric rotors, Molecular Spectroscopy: Modern Research*, volume III, pages 69–110. Academic Press, Orlando, Fla., 1985.

[9] S. A. Clough, Y. Beers, G. P. Klein, and L. S. Rothman. Dipole-moment of water from stark measurements of $H_2O$, HDO, and $D_2O$. *Journal of Chemical Physics*, 59(5):2254–2259, 1973.

[10] F. F. Crim. Vibrationally mediated photodissociation - exploring excited- state surfaces and controlling decomposition pathways. *Annual Review of Physical Chemistry*, 44:397–428, 1993.

[11] R. T. Carter and J. R. Huber. Quantum beat spectroscopy in chemistry. *Chemical Society Reviews*, 29(5):305–314, 2000.

[12] A. Callegari and T. R. Rizzo. State-to-state unimolecular reaction dynamics of highly vibrationally excited molecules. *Chemical Society Reviews*, 30(4):214–225, 2001.

# Chapter 3

# Fluorescence detected microwave spectroscopy of rovibrationally excited $H_2CO$.

This chapter describes experiments in which we measure dipole moments of single rovibrational states of $H_2CO$. As explained in Chapter 2, a single rovibrational state is populated with a laser transition, a cw microwave source induces a pure rotational transition from a rovibrational state to another rovibrational state and the microwave transition is detected by LIF.

## 3.1 Motivation.

Formaldehyde has played a key role in the current understanding of the spectroscopy, photochemistry, and photophysics of polyatomic molecules. The large body of work on this molecule, both experimental and theoretical, makes it a uniquely valuable system for quantum-state resolved studies of non radiative electronic transitions, of vibrational motions in highly excited states, and of photofragmentation dynamics. Useful reviews can be found in Ref [1] and Ref. [2]. Moreover, a dozen dipole moments are known for $H_2CO$ (see Table 14 of Ref. [1]). For all these reasons $H_2CO$ is a good starting point to apply the fluorescence detected microwave technique to measure dipole moment of highly excited vibrational states. Normal modes of $H_2CO$ are represented in Fig.3.1 [1].

---

[1] A common way of noting vibronic states is to indicate by a subscript the number of quanta in the corresponding vibrational mode (e.g. $5_2$ means $n_5 = 2$ in the $\tilde{X}^1 A_1$ ground electronic state), whereas a superscript indicates the number of quanta in the corresponding vibrational mode in the $\tilde{A}^1 A_2$ excited electronic state (e.g. $5^2$ means $n_5 = 2$ in the $\tilde{A}^1 A_2$, or $S_1$, electronic state). This notation can be combined with the $J_{K_a K_c}$ rotational state notation to label a rovibronic state, as for example $5^2 1_{11}$.
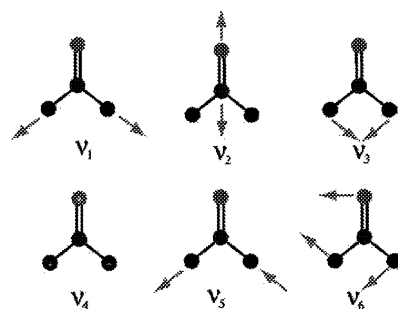
Figure 3.1: The six normal modes of $H_2CO$.

## 3.2 Experimental procedure

### 3.2.1 Experimental set-up

We used the experimental sequence shown in Fig. 3.2 to measure the dipole moment of ground electronic state $5_2$ for example. The experimental set-up is shown in Fig. 3.3 and Fig. 3.4.

Infrared laser pulses are used to populate a single rotational state within the excited $5_2$
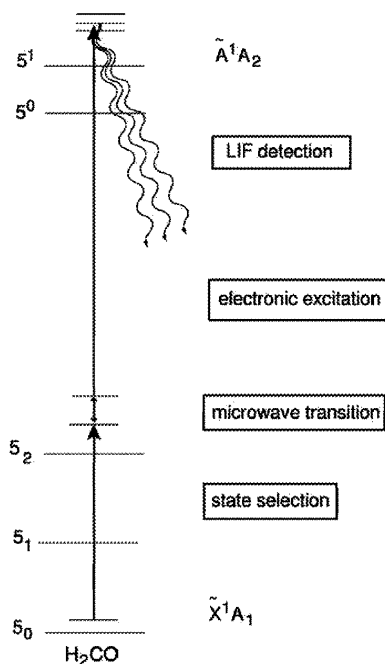


Figure 3.2: Experimental energy level diagram for LIF detected microwave-optical double resonance. A first laser pulse populates a single rovibrational state with 2 quanta of CH stretch, and a second laser pulse transfers the population to the first excited electronic state, that fluoresces on the ground electronic state. The LIF is recorded.

vibrational level of $H_2CO$, that is the state with two quanta in the asymmetric CH stretch mode. They are generated by difference frequency mixing the output of Nd:YAG pumped dye

laser with single mode Nd:YAG radiation at 1.064 $\mu m$ in a $LiNbO_3$ crystal, to produce between 1 and 5 $mJ$/pulse of IR radiation. The dye laser normally has a linewidth of 0.15 $cm^{-1}$, but this can be reduced to 0.02 $cm^{-1}$ by inserting an etalon inside the oscillator. This linewidth is largely preserved after mixing in the crystal.

To detect the overtone transition we used a vibronic transition in the $\tilde{A}^1A_2 \leftarrow \tilde{X}^2A_1$ electronic band [2]. Laser radiation for electronic transition is produced by frequency doubling another Nd:YAG pumped dye laser in KDP. Both lasers are calibrated on atomic transitions using an Ar-Ne optogalvanic lamp. The optogalvanic lamp is also used to calibrate a wavemeter that is in turned used for frequent frequency checks of the laser wavelengths. The microwave source is a Hewlett-Packard model $83751A$ frequency synthesizer, which covers the range from 2 $GHz$ to 20 $GHz$. An active $DBS2640 \times 218$ frequency doubler-amplifier extends the range to $40GHz$. The two (IR and UV) laser beams counter-propagate inside a quasi-static cell (described in Fig. 3.4). Perpendicular to these beams, an $f/1$ lens collects H$_2$CO $\tilde{A}^1A_2$ fluorescence and images it onto a photomultiplier tube ($EMI\ 9235QB$).

Laser timing, wavelength scanning, and signal acquisition are accomplished through CA-MAC modules interfaced to a PC, and a Labview program enables automatic data acquisition, as well as control of the frequencies and timing of the two lasers and microwave source. The microwave synthesizer is connected to the data acquisition computer by two TTL logic lines. One logic level is used to gate the microwave power, so that microwave radiation is present and absent during alternate laser pulses. The difference between signals from alternate pulses allows background subtraction. The second logic level is used to step the microwave frequency in preset increments. To acquire a microwave spectrum, the lasers are tuned to the desired frequencies and the initial microwave frequency, frequency increment, and power level of the synthesizer are set manually. The computer then averages the background subtracted LIF signal for a fixed number of laser shots (typically 20, 40 or 60) and steps the microwave frequency. The frequency increment is typically 0.1 MHz per data point. The signal and background are averaged for ten laser shots, and then subtracted.

We used an aluminum body cell with stainless steel baffle arms to reduce the amount of scattered light from the lasers. The cell body has outside dimensions of approximately $100 \times 100 \times 180\ mm$, and it is continuously evacuated by a rotary vane pump (of about 65 $m^3/h$) in order to maintain a pressure of about 15 to 20 $mtorr$ while slowly flowing sample through it. A 100 $mm$ $O.D.\emptyset$ flange located at the bottom of the cell provides vacuum feedthroughs for microwave radiation and dc Stark voltages and supports the Stark electrodes. The Stark

---

[2]It is standard to use a compact notation for vibronic transitions where the ground electronic state initial vibrational state is indicated as subscript, and the excited electronic state final vibrational state as superscript. For example, $4_0^1 5_2^0$ stands for the vibronic transition $\tilde{A}^1A_2\ 4^1 5^0 \leftarrow \tilde{X}^1A_1\ 4_0 5_2$.

We will also combine the rotational transition notation $\tilde{A}^1A_2\ 4^1 5^0\ 2_{11} \leftarrow \tilde{X}^1A_1\ 4_0 5_2\ 2_{02}$ to the previous notation to label a rovibronic transition.
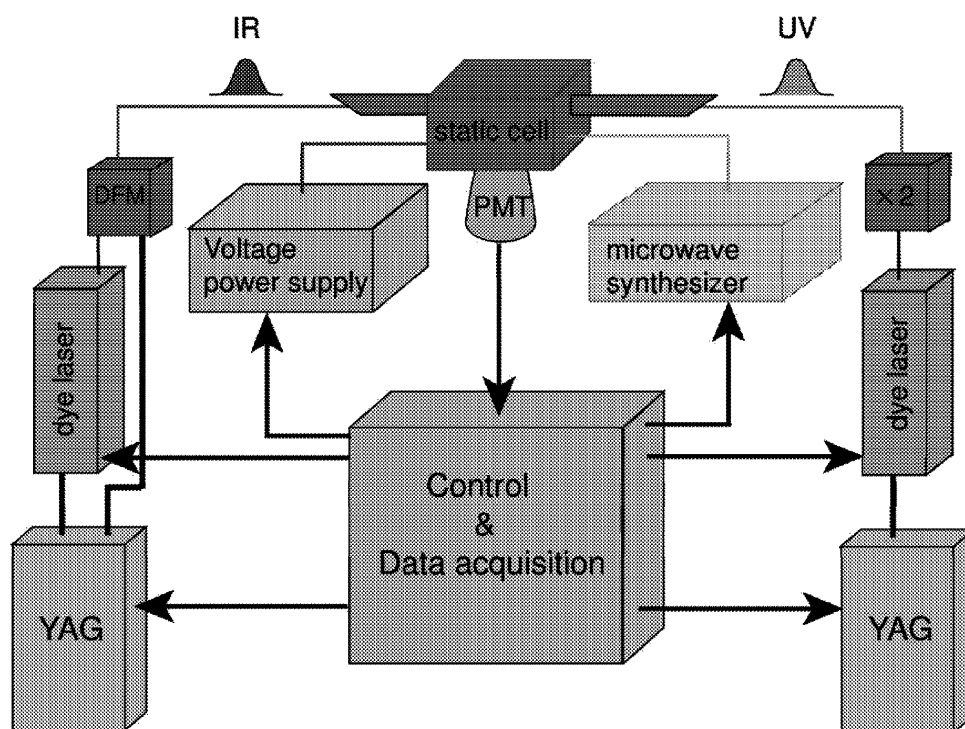
**Figure 3.3:** Schematic view of the experimental set-up used on $H_2CO$. Two $Nd : YAG$ pumped dye lasers counterpropagate inside a static cell of $H_2CO$. Microwave radiation is brought into the cell and a Stark voltage is applied to a pair of electrodes. A PMT records the fluorescence inside the cell. CAMAC modules interfaced to a PC controls the lasers, the microwave synthesizer, the voltage and the data acquisition.
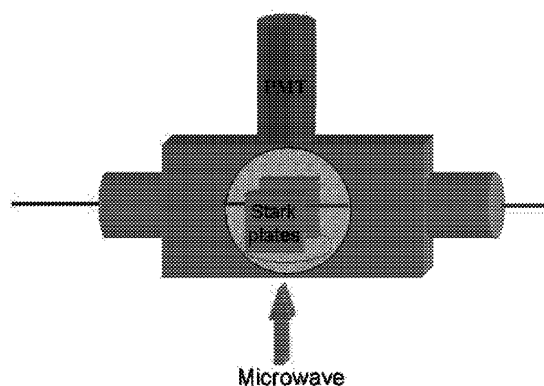


**Figure 3.4:** Detail of the experimental set-up: inside the cell. Lasers are crossing parallel to the Stark electrodes. The microwave radiation is introduced between the electrodes, and a photomultiplier tube collects the fluorescence in the vertical direction.

voltage is produced using a Fluke 410B power supply.

The microwave signal is brought into the cell with 3.58 $mm$ $OD$ hermetically sealed semi-rigid coaxial cable that goes through a swagelok connector on the bottom flange of the cell. Inside the cell this cable is connected to an antenna positioned immediately below the Stark

electrodes. The Stark electrodes consist of $60 \times 40 \times 4$ *mm* anodized and rounded aluminium plates, separated by 10 *mm* and supported by precision machined teflon blocks. The outer part of the coaxial cable and one electrode are grounded. A mylar sheet electrically isolates the waveguide from the electrodes (so as not to destroy the synthesizer and the doubler-amplifier in case of discharge between the Stark electrodes) and provides an hermetic isolation from the leaks that could occur from the coaxial cable. The waveguide orientation generates a plane polarized microwave $E$-field parallel to the dc field giving $\Delta M = 0$ selection rules. The fact that we use a metallic cell along with several metallic pieces as Stark electrodes means that there will be microwave interference effects and standing waves, and we have no information about such interference patterns. Moreover the coupling between the inner part of the coaxial cable (the antenna) and the electrode at the Stark voltage, is frequency dependent. Both of these effects could affect the intensity of the microwave radiation in the volume from which signal is collected.

The H$_2$CO gas sample has been synthesized by pyrolisis of paraformaldehyde (Aldrich) polymer in a bath of polyethylene glycol. After the pyrolisis, we carry out two fractional distillations in a vacuum line and condense H$_2$CO in a liquid nitrogen trap, which allows us to use the pure monomer gas sample in our cell. We have also simply pyrolized paraformaldehyde and flowed the entire mixture through the cell, which gives similar results, and thus in most cases we have proceeded in this manner.

## 3.2.2 Stark measurements in the $\tilde{X}^1A_1$ $5_2$ level of H$_2$CO.

For the $5_2$ level of H$_2$CO, which is the first overtone of the asymmetric C-H stretch mode, the IR $a$-type transition used for the initial state preparation step (refer to Fig. 3.2) corresponds to $\tilde{X}$ $5_2$ $1_{11}$ $\leftarrow$ $\tilde{X}$ $0_0$ $2_{12}$; the microwave $a$-type transition in the second step is between $1_{11}$ and $1_{10}$ rotational levels in the $5_2$ vibrational level, and the $b$-type electronic transition used in the third step to detect the microwave transition is $\tilde{A}$ $4^1$ $1_{01}$ $\leftarrow$ $\tilde{X}$ $5_2$ $1_{10}$. The $4_0^1 5_2^0$ vibronic transition used in the detection step is not the one with the largest Franck-Condon factor. The $5_2^1$ transition, which is stronger, was first used, but the laser dye used to generate this frequency, $LDS698$, degrades too quickly. We then tried the $2_0^1 5_2^1$ transition using $LDS751$ dye, but if we block the IR laser, a signal is observed originating from the UV laser alone. We then changed the detection step to the $4_0^1 5_2^0$ vibronic transition at $\simeq$ 780 *nm* using a mixture of $LDS765$ and $LDS821$ laser dye, which produces 47.5 mJ/pulse at this wavelength.

Since there is no spectroscopic information in the literature for the $5_2$ vibrational level, and since we need rotational constants at a sufficient accuracy to be able to find the microwave transitions in the vibrationally excited state, a photoacoustic spectrum of the $5_2$ band was taken, as shown in Fig. 3.5.

In order to assign this photoacoustic spectrum, we took a series of IR-UV double resonance
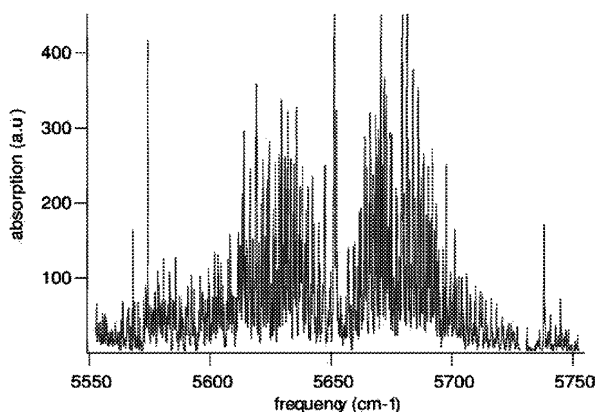
**Figure 3.5:** Photoacoustic spectrum of the $5_2$ vibrational band of $H_2CO$. A dye laser is passed through a photoacoustic cell. When the laser is in resonance with a rovibrational transition of the $5_2$ band, an acoustic signal is recorded with a microphone inside the cell.

spectra since the fewer and cleaner lines of these double resonance spectra are more easily assigned than those of the photoacoustic spectrum. The IR laser makes the $\tilde{X}\ 5_2 \leftarrow \tilde{X}\ 0_0$ transition and the UV laser the $4_0^1 5_2^0$ vibronic transition. The fluorescence from the upper vibronic state $\tilde{A}\ 4^1$ is collected. For each spectrum, the UV laser is kept at a fixed frequency on an unassigned $4_0^1 5_2^0$ rovibronic transition, and the IR laser is scanned. Figure 3.6 displays several of these double resonance spectra. Since the energy levels positions of the ground vibrational state are precisely known, it is straightforward to assign from the IR laser scans, both the first and the second laser transitions. Therefore we can determine the energy levels position of the intermediate $5_2$ vibrational level and thus its rotational constants. The rotational constants are
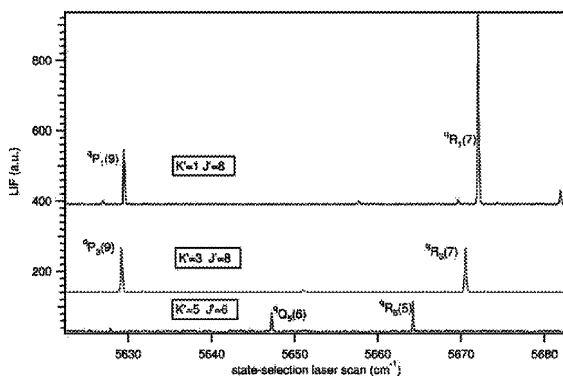


**Figure 3.6:** Double resonance spectra of $5_2$ of $H_2CO$. The detection laser frequency is fixed and the state-selection is scanned. The $J'_{K'}$ states denote the intermediate rotational state in the $5_2$ vibrational state. It is derived from the $P$, $Q$, $R$ lines spacings, which represent ground vibrational state energy differences.

then refined by fitting the photoacoustic spectrum. The final rotational constants are used to make an estimation of the desired $5_2$ $1_{10}$ $\leftarrow$ $5_2$ $1_{11}$ microwave transition frequency.

This microwave transition is found to occur at 4912.65(2) $MHz$, as shown in Fig. 3.7. The 300 $ns$ delay between the infrared state-selection pulse and the UV detection pulse, which fixes the microwave transition time, limits the theoretical FWMH line width to 3 $MHz$. Both the flight time of molecules through the laser beams and collisional dephasing further shorten the microwave transition time, resulting in a slightly broader line shape. For this reason the pressure is also optimized to give the best microwave signal, being careful to avoid arcing at high values of the Stark electric field. The microwave transition displayed in Fig.3.7 exhibits a characteristic two-level system Rabi resonance line shape.
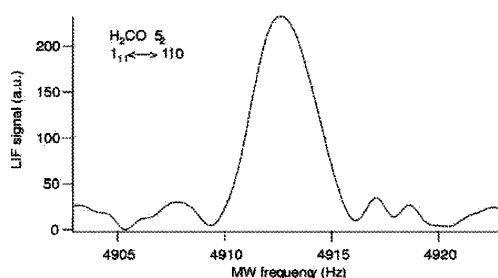


**Figure 3.7:** Microwave transition between the rotational states $1_{11}$ $\leftrightarrow$ $1_{10}$ of the $5_2$ vibrational state of $H_2CO$. When the microwave frequency is resonant with the $1_{11}$ $\leftrightarrow$ $1_{10}$ transition, a LIF signal is observed at the photomultiplier tube. We thus observe the LIF as a function of the microwave frequency. The sinc lineshape of the LIF signal is typical of a two-level system transition which exhibit Rabi oscillations.

As shown in Fig. 3.8, this microwave transition was then recorded for a series of different Stark voltages. Fig. 3.8 displays the shift of the center transition frequency as a function of the Stark voltage for the $1_{11}$ $\leftrightarrow$ $1_{10}$ transition within the $5_2$ vibrational state.

### 3.2.3 Stark measurements in the $\tilde{X}^1A_1$ $1_1$ level of $H_2CO$.

A pure rotational transition was also recorded between levels $1_{10}$ and $1_{11}$ of the $1_1$ vibrational level of formaldehyde (i.e., the state with one quantum in the C-H symmetric stretch), by using the IR $a$-type transition $\tilde{X}$ $1_1$ $1_{1\,0}$ $\leftarrow$ $\tilde{X}$ $1_0$ $2_{1\,1}$ for state preparation and the UV $b$-type transition $\tilde{A}$ $4^1$ $1_{01}$ $\leftarrow$ $\tilde{X}$ $1_1$ $1_{11}$ for detection of the microwave transition. The frequency for exciting the former transition was generated by difference frequency mixing the Nd:YAG pumped dye laser, using $LDS821$ dye, with the single mode Nd:YAG radiation at 1.064 $\mu m$ in a $LiNbO_3$ crystal. This produces IR radiation at about 2780 $cm^{-1}$ ($3.6\mu m$) that was aligned through the cell and superimposed with the UV radiation using a pyroelectric detector. The UV radiation was generated by frequency doubling a Nd:YAG pumped dye laser, using $LDS765$
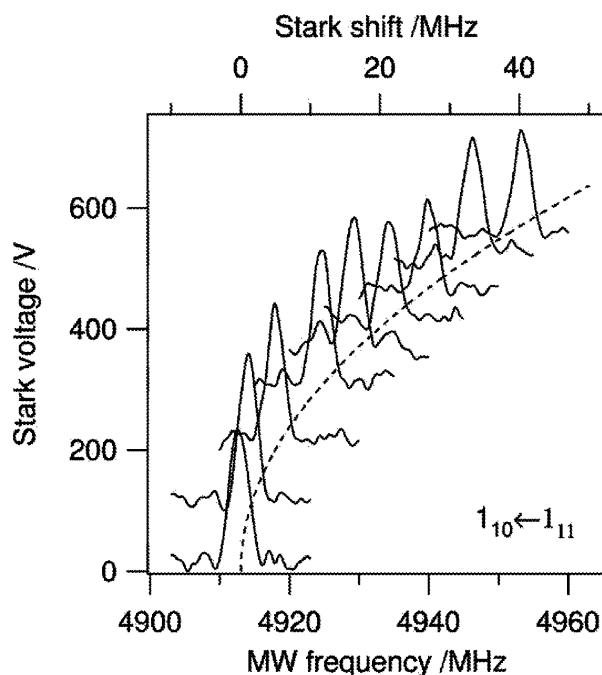
**Figure 3.8:** Quadratic Stark effect in $J = 1$ of $H_2CO$. The frequency of the microwave induced pure rotational transition $1_{11} \leftrightarrow 1_{10}$ in the $5_2$ vibrational level of $H_2CO$ is shifted by the Stark voltage. The Stark shift is proportional to the square of the Stark voltage, which is typical of the Stark effect in an asymmetric top.

dye, in a KDP crystal. The infrared transitions for $5_1$ are taken from Ref. [3] and the UV transitions are calculated from Ref. [4]. The microwave transition $1_1$ $1_{11}$ $\leftarrow$ $1_1$ $1_{10}$ was found at $4,945.52(3)$ $MHz$, and its Stark shift was recorded for different voltages as previously to get the dipole moment of $1_1$ .

### 3.2.4  $5_1$ of $H_2CO$ and the calibration of the Stark electric field.

Calibrating the Stark electric field is a very important issue for the accuracy of the measurement. The electric field has different sources of uncertainties: the non-linearity of the power supply, the inhomogeneity of the Stark electric field between the two electrodes arising from imperfect parallelism of the electrodes, electric field gradients and edge effects, and uncertainty on the spacing between the electrodes. To calibrate the power supply, we use a Hewlett-Packard 3456A digital voltmeter and a high-voltage probe previously calibrated on a highly stable power supply (Standford Research Systems PS350/5000V-25W, 0.05% accuracy ). The electrode spacing is measured with high precision gauge blocks. This calibration gives a relatively good precision to our measurements but does not reflect potential systematic errors associated with electric field calibration. To guarantee that small vibrationally induced changes in dipole moments can be accurately compared with measurements from different laboratories,

it is very useful to combine our measured Stark coefficient to the dipole moment of $5_1$ which is known from Ref. [5] to be 2.2841(47) $D$. Toward this end, we recorded a pure rotational transition between the $1_{11}$ and $1_{10}$ rotational levels in the $5_1$ level, and measured the Stark coefficients for this transition. We therefore have a second calibration of our Stark electric field.

An additional and independent calibration of the electrode spacing has been made on a OCS transition at Rochester University. This third calibration gives an agreement within 0.1% with the first calibration made using the dipole moment the $5_1$ level of H$_2$CO and is within the limit of uncertainty of the second calibration made using the gauge blocks.

## 3.2.5   Higher J transition in the $5_2$ level of H$_2$CO

It is appropriate to make a few remarks on the capabilities and generality of this dipole moment measuring technique based on Stark microwave spectroscopy. The only requirement for a molecule to be investigated by this approach is that it have a rotationally resolved electronic transition with at least a moderate fluorescence quantum yield. Pure rotational transitions can be observed in high resolution over a broad frequency range. The upper limit is simply determined by the availability of appropriate radiation sources. For example, as shown in Fig. 3.9, we have been able, using the same laser set-up as described in Section 3.7, to observe the $2_{12} \leftarrow 1_{11}$ rotational transition in $5_2$ level of H$_2$CO at 140.48208(2) $GHz$ using a backward wave oscillator (BWO). This allows us to measure higher J rotational transitions, in cases where it would not be possible to measure low J transitions. In addition small molecules with extremely large rotational spacings can be studied using this microwave radiation source. This BWO has a range of $118 - 178$ $GHz$ with an output power of about 17 $dBm$ (50 $mW$). The frequency is stabilized by a phase lock loop using the Hewlett-Packard model $83751A$ frequency synthesizer.
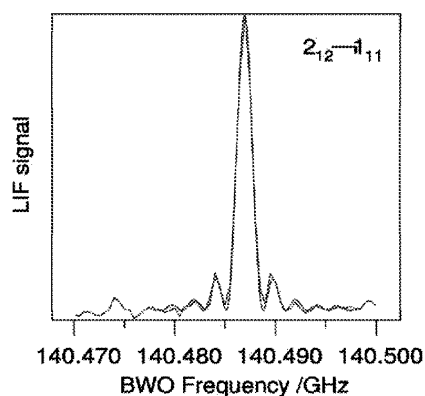


**Figure 3.9:** The microwave induced $2_{1\ 2} \leftrightarrow 1_{1\ 1}$ rotational transition in the $5_2$ vibrational state of H$_2$CO at 140 482.08(2) $MHz$. The microwave radiation is generated using a BWO synthesizer.

### 3.2.6 Stimulated Emission Pumping on $\tilde{X}^1A_1$ $2_14_6$ of $H_2CO$

The fluorescence detected microwave spectroscopy technique is not limited to overtone excitation in $H_2CO$ which can only access vibrational levels with $-CH$ stretch character. It is actually possible to access other vibrational levels with different vibrational character, using the Stimulated Emission Pumping (SEP) technique [6, 7]. In order to prepare planned pump/dump-microwave-probe experiments, as described in Fig. 3.10, preliminary Stimulated Emission Pumping experiments have been done on the $2_14_6$ level of formaldehyde. The fluorescence is separated from other laser radiations using colored filters.
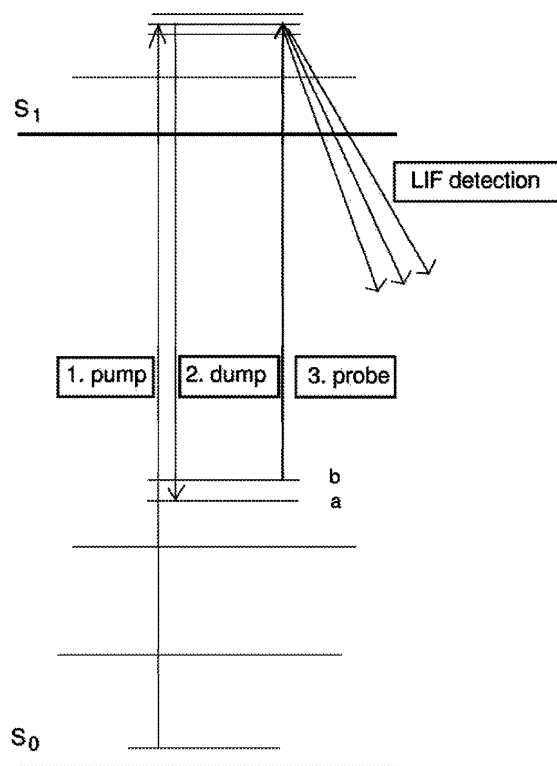


**Figure 3.10:** The excited state $a$ is prepared by a pump-dump sequence of two laser pulses (SEP). A probe laser pulse can enable the detection of the population transferred from state $a$ to state $b$ by microwave radiation.

A rovibronic transition $4_0^1$ in the $\tilde{A} \leftarrow \tilde{X}$ electronic system is excited with a first laser, populating the $\tilde{A}$ $4^1$ state which fluoresces. A second laser, when in resonance with a rovibronic transition of the $\tilde{X}$ $2_14_6$ state, induces dips in the fluorescence, as shown in Fig. 3.11. In this way single rovibrational states of $2_14_6$ are prepared, with the ultimate goal of inducing pure rotational transitions and detecting via the $2_1^0 4_6^1$ rovibronic transition. While we have not added the microwave step to the pump/dump/probe scheme of the SEP experiment, these spectra show that is possible to get sufficient signal to enable the microwave transition in $2_14_6$ to be attempted.
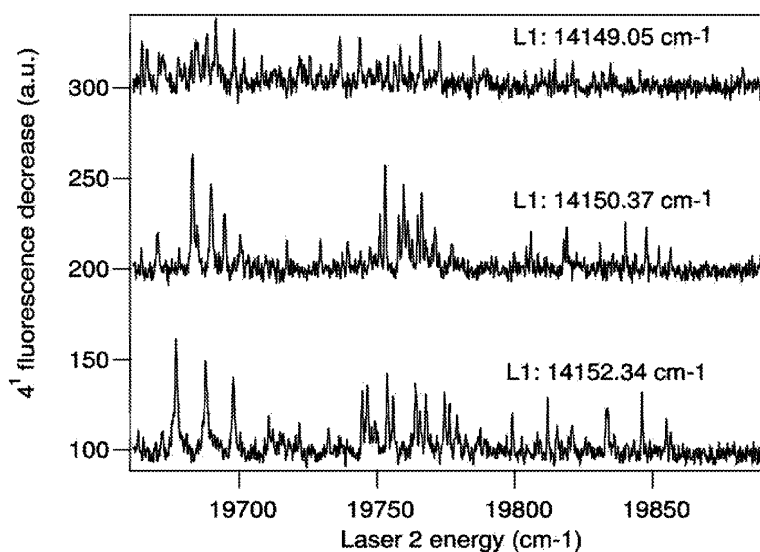
**Figure 3.11:** SEP spectra of the $2_1 4_6$ vibrational state of H$_2$CO. The $L_1$ pump laser excites the $4^1$ vibronic state. The three spectra are performed scanning the dump laser $L_2$ at three $L_1$ pump laser fixed frequencies. In this figure dips in the fluorescence are reversed to appear as bumps. There is neither microwave radiation nor probe laser here.

## 3.3 Results and analysis

We will now see how we can extract the dipole moment of a vibrationally excited state of H$_2$CO from the series of scans we took at different Stark voltages, as displayed in Fig. 3.8. We will first extract the center frequency of the microwave transition as a function of the Stark electric field, and derive from this the Stark shift from the zero field transition frequency. We will see then how the dipole moment is extracted from the Stark shifts.

### 3.3.1 Transition center frequency as a function of the Stark electric field.

The raw data is relatively noisy because of pulse-to-pulse fluctuations in the intensity of the two lasers, and for this reason the signal is digitally filtered. Since the 0.1 $MHz$ microwave step is smaller than the typical 3 $MHz$ line width, this improves the signal to noise ratio without introducing significant distortion. The data are Fourier transformed into the frequency domain and high frequency noise is removed using a low pass filter. The filter cutoff frequency corresponds to a period of five data points. Inverse Fourier transformation back to the time domain provides the experimental signal that we then analyze spectroscopically.

The present microwave transition occurs between $M = 1$ of $|1_{11}\rangle$ and $M = 1$ of $|1_{10}\rangle$. The $|1_{11}\ M = 0\rangle \leftrightarrow |1_{10}\ M = 0\rangle$ transition has no intensity when the static and microwave fields are parallel, as it can be seen in Table $10 - 1$ of Ref. [8] for a $\Delta J = 0\ \Delta M = 0$ transition. The spacing of these two levels increases with the Stark electric field, and the transition is shifted to

higher frequency, as seen in Fig. 3.12.
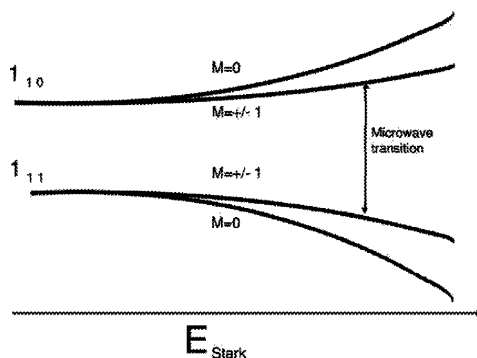


**Figure 3.12:** Schematic energy level diagram showing the Stark shift in the microwave a-type transition $1_{11} \leftrightarrow 1_{10}$ of $H_2CO$. The $M = 0$ to $M = 0$ transition has no intensity.

For every Stark voltage, the microwave transition is fitted with a damped sine-square line shape function associated with the coherent Rabi oscillations in a two-level system, as expressed in Eq. 2.14 with $t = 300$ ns and different $\mu_b$ values. The shift of the center transition frequency as a function of the Stark voltage for the $5_2 \, 1_{11} \leftrightarrow 5_2 \, 1_{10}$ transition is displayed in Fig. 3.8. $E_{mw}$, the microwave radiation electric field amplitude, is not well known, both because of the possibility of interference effects inside the metal cell (since the radiation wavelength is comparable to electrode dimension) and because the coupling of the coaxial adapter to the electrodes is frequency dependent. We therefore consider $\mu_{ij} \cdot E_{mw}$, the transition moment times
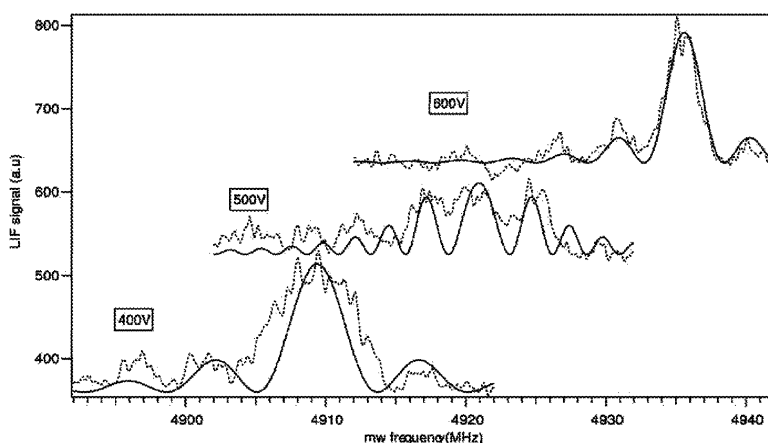


**Figure 3.13:** Dependence of the microwave power on the frequency and its consequence on a two-level transition line shape, as seen in the transition $1_{11} \leftrightarrow 1_{10}$ of $5_1$ of $H_2CO$. The difference of Stark frequency shift due to a 100 $V$ increase in the Stark voltage is sufficient to modify both the pattern of the standing waves inside the cell and the coupling between the coaxial cable and the electrodes.

the amplitude of the microwave electric field, as an adjustable parameter that we fix to fit to the experimental data. The peak intensity of the calculated lines is therefore scaled to agree with that of the signal. Then, both the center frequency of the transition, $\nu_{ij}$, and $\mu_{ij} \cdot E_{mw}$ are adjusted for best agreement with the experimental data. $\nu_{ij}$ has been determined very precisely to give a zero-field transition frequency of $\nu_0 = 27,484.33(10)$ $MHz$. The time delay between the infrared state-selection pulse and the UV detection pulse fixes both the line width and the frequency of the damped oscillations in the wings of the line. The $t = 300$ $ns$ laser time delay gives a theoretical line width of 3 $MHz$, but the flight time of molecules through laser beams and collisional dephasing further shorten the microwave transition time, resulting in a slightly broader observed line shape. It is interesting to note, as shown in Fig. 3.13, that the frequency shift due to the Stark electric field is sufficient to change both the coupling coaxial cable-electrodes and the pattern of the standing waves inside the cell. This modifies significantly the damped sine-square line shape of the microwave transition since the microwave power fixes the number of Rabi oscillations occurring during the time between the excitation and detection laser pulses. The three transitions displayed in Fig. 3.13 do not correspond to the same number of Rabi oscillations between the $1_{11}$ and $1_{10}$ of $5_1$. It is useful to realize that an integer number of coherent Rabi oscillations between the two rotational levels during the time between the two laser pulses is equivalent to no transfer of population at all. In this special case, no transition can be observed.

Fits of the microwave transition give the following transition center frequency to within 100 $kHz$ for the different excited vibrational states and for different Stark fields. These are listed in Table 3.1.

| $1_1$ Symmetric C-H stretch | | $5_1$ Asymmetric C-H stretch | | $5_2$ Asymmetric C-H stretch | |
|---|---|---|---|---|---|
| $E_{dc}(volt/cm)$ | $\nu(MHz)$ | $E_{dc}(volt/cm)$ | $\nu(MHz)$ | $E_{dc}(volt/cm)$ | $\nu(MHz)$ |
| 0.0 | 4945.51 | 0.0 | 4887.15 | 0.0 | 4912.72 |
| 99.76 | 4946.89 | 99.76 | 4888.60 | 99.76 | 4914.08 |
| 199.52 | 4950.86 | 199.52 | 4892.43 | 199.53 | 4917.98 |
| 299.28 | 4957.67 | 299.29 | 4895.37 | 299.30 | 4924.59 |
| 399.05 | 4966.91 | 399.09 | 4908.87 | 349.19 | 4929.18 |
| 498.81 | 4978.98 | 598.65 | 4935.47 | 399.10 | 4934.36 |
| 598.57 | 4993.56 | 698.45 | 4952.62 | 448.98 | 4939.96 |
| 698.33 | 5011.02 | 798.24 | 4972.60 | 488.88 | 4946.30 |
| 798.09 | 5030.83 | 898.02 | 4995.10 | 548.76 | 4953.39 |
| 897.85 | 5053.14 | 997.82 | 5020.30 | | |
| 997.62 | 5078.05 | | | | |

**Table 3.1:** Stark effect data for excited vibrational states of $H_2CO$. $1_{11} \leftrightarrow 1_{10}$ transition center frequencies are indicated along with the Stark field applied for the $1_1$, $5_1$ and $5_2$ states of $H_2CO$.

### 3.3.2 Extracting the dipole moment from Stark shifts.

The Stark shift results from the interaction of the $|1_{11}\ M = 1\rangle$ and $|1_{10}\ M = 1\rangle$ levels with one another through the dipole moment matrix element $\langle 1_{11}\ M = 1|\mu_a|1_{10}\ M = 1\rangle$ (since the $b$ component of the dipole moment is zero by symmetry), and from the $a$-type interaction of the $|1_{11}\ M = 1\rangle$ and $|1_{10}\ M = 1\rangle$ levels with the surroundings energy levels. This is shown schematically in Fig. 3.14.
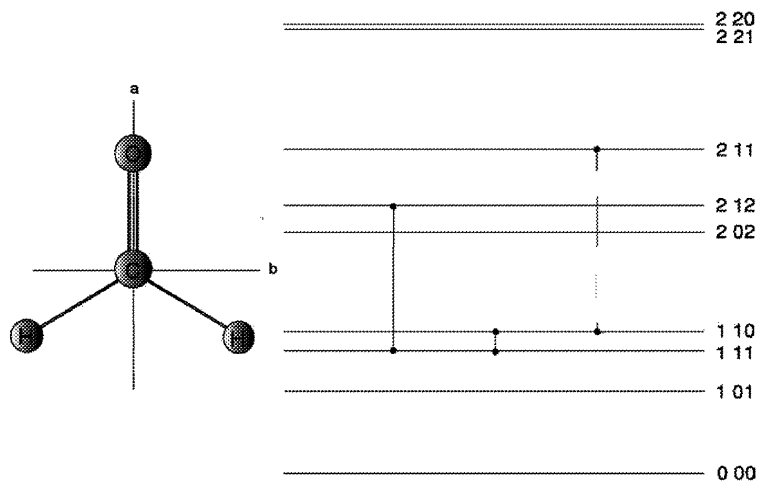


**Figure 3.14:** Interaction of the different rovibrational levels of $H_2CO$ through the $a$ component of the dipole moment in the molecule-fixed frame. The Stark shift of the $|1_{10}\rangle$ and $|1_{11}\rangle$ levels is expressed by Eq. 3.1 and Eq. 3.2. The dashed lines represent interactions between states due to the $a$ component of the dipole moment.

According to the exact expression for a two-level interaction given in Eq. 2.11, to which must be added the interaction with the $|2_{11}\rangle$ and $|2_{12}\rangle$ levels according to Eq. 2.8, we can write the energy of the $|1_{10}\rangle$ and $|1_{11}\rangle$ levels as

$$\nu_{1_{10}} = \left(\frac{\nu_{1_{10}}^0 + \nu_{1_{11}}^0}{2}\right) + \left[\left(\frac{\nu_{1_{10}}^0 - \nu_{1_{11}}^0}{2}\right)^2 + \left(\frac{\mu E f M K}{2}\right)^2\right]^{1/2} - \frac{3}{20}\frac{\mu^2 E^2 f^2}{\nu_{2_{11}}^0 - \nu_{1_{10}}^0} \quad (3.1)$$

$$\nu_{1_{11}} = \left(\frac{\nu_{1_{10}}^0 + \nu_{1_{11}}^0}{2}\right) + \left[\left(\frac{\nu_{1_{10}}^0 - \nu_{1_{11}}^0}{2}\right)^2 + \left(\frac{\mu E f M K}{2}\right)^2\right]^{1/2} - \frac{3}{20}\frac{\mu^2 E^2 f^2}{\nu_{2_{12}}^0 - \nu_{1_{11}}^0} \quad (3.2)$$

where $f$ is the appropriate conversion factor $0.503411\ MHz/\left(D.\frac{V}{cm}\right)$. This can be expressed as:

$$\Delta\nu = (\nu_{1_{10}} - \nu_{1_{11}}) = \left[(\nu_{1_{10}}^0 - \nu_{1_{11}}^0)^2 + (\mu.E.fMK)^2\right]^{1/2} - \frac{3}{20}\mu^2 E^2 f^2 \left[\frac{1}{(\nu_{2_{11}}^0 - \nu_{1_{10}}^0)} - \frac{1}{(\nu_{2_{12}}^0 - \nu_{1_{11}}^0)}\right]$$
$$(3.3)$$

The interaction term with the $|2_{11}\rangle$ and $|2_{12}\rangle$ levels contributes less than 100 $kHz$ to the

Stark shift, even at the largest field strengths. We fit the observed Stark shift $\Delta\nu$ by adjusting $\mu$ for each value of the Stark electric field $E$.

We repeat this procedure for all the microwave transitions recorded at different electric fields, and get a value of $\mu_a$ for the vibrational states $5_1$, $5_2$ and $1_1$. The value for the first state $5_1$ is a check to ensure that our calibration is correct (see Section 3.2.4), since it has been previously measured in Ref. [5]. We do not have to include any hyperfine correction, as $^{12}C$ has no nuclear spin. Moreover, as we are using states with $J = 1$, the centrifugal distortion correction should be negligible as explained for water in Appendix C.

The uncertainty in the dipole moment value can be expressed as

$$\frac{\Delta\mu}{\mu} = \sqrt{\left(\frac{\Delta d}{d}\right)^2 + \left(\frac{\Delta V}{V}\right)^2 + \left(\frac{\Delta\nu}{2\nu}\right)^2 + \left(\frac{\Delta C}{2C}\right)^2}$$

where the first term under the square root comes from the uncertainty in the electrode spacing, the second from the non-linearity of the power supply, the third from the uncertainty in determining the line center from our fitting procedure, and the fourth from the uncertainty of the Stark coefficients. In the H$_2$CO experiment, the dominant uncertainty terms are $\left(\frac{\Delta V}{V}\right)$ and $\left(\frac{\Delta d}{d}\right)$. The calibration procedure is explained in Section 3.2.4. We estimate the uncertainty of a single dipole moment value to be $\left(\frac{\Delta\mu}{\mu}\right) = 0.24\%$. We then average several spectra, recorded for several Stark voltages, to get the final uncertainty on the dipole moment. This gives a dipole moment of $2.2944(50)D$ for $1_1$ and of $2.2936(47)D$ for $5_2$.

## 3.4 Discussion: the dipole moment function of H$_2$CO.

Table 3.2 summarizes the dipole moment measured during this work along with those previously recorded for other vibrational states. Figure 3.15 displays the evolution of the dipole moment upon vibration for the 6 normal modes of H$_2$CO.

We anticipate from Section 1.3 that the formaldehyde dipole moment should exhibit linear dependence with vibrational quantum numbers, $v_i$, increasing for stretching modes and decreasing for bending modes. A brief glance at Table 3.2, however, shows this not to be the case. While the carbonyl stretching mode $\nu_2$ fits this simple description, with $\mu$ exhibiting nearly linear increases for the $0_0$, $2_1$ and $2_2$ states, the $\nu_5$ mode behavior is so nonlinear that the moment for the $5_2$ state lies between those of the $0_0$ and $5_1$ states. It is not possible to fit the twelve moments in Table 3.2 with well determined values for $\mu_e$ and the six $a_i$ coefficients from Eq. 3.4. Since the effects of cubic potential constants and $\frac{\partial^2\mu}{\partial q_i^2}$ are incorporated into the $a_i$ coefficients, the inability of Eq. 3.4 to fit the observed H$_2$CO moments most likely arises from either the breakdown of the assumption of isolated, non interacting modes that is implicit in this expression or from a dipole moment surface that cannot be well described by a Taylor's

| vib. state | $\mu$ (D) | Ref. | $(\mu - \mu_0)$ $(D)$ |
|:---:|:---:|:---:|:---:|
| 0 | 2.3316(5) | [9] | 0.0 |
| $1_1$ | 2.2944(50) | This work | -0.0372 |
| $2_1$ | 2.3469(15) | [10] | +0.0153 |
| $2_2$ | 2.3605(20) | [11] | +0.0289 |
| $3_1$ | 2.3250(25) | [5] | -0.0066 |
| $4_1$ | 2.3086(5) | [9] | -0.0230 |
| $4_4$ | 2.2723(86) | [12] | -0.0593 |
| $5_1$ | 2.2841(47) | [9] | -0.0475 |
| $5_2$ | 2.2936(47) | This work | -0.0380 |
| $6_1$ | 2.3285(5) | [9] | -0.0031 |
| $2_1 4_4$ | 2.2825(33) | [13] | -0.0491 |
| $2_2 4_2$ | 2.322(47) | [13] | -0.0094 |

**Table 3.2:** Collection of the experimentally measured dipole moments for the ground electronic state of $H_2CO$.

series expansion truncated at the second derivatives

$$\langle \mu \rangle_v = \mu_e + \sum_i^{3N-6} a_i(\nu_i + \frac{1}{2}) \qquad (3.4)$$

$$\text{with} \quad a_i = \frac{\partial^2 \mu}{\partial q_i^2} - \sum_j (1 + \delta_{ij}) \frac{k_{iij}}{\omega_j} \frac{\partial \mu}{\partial q_j} \qquad (3.5)$$

While we usually consider the normal mode approximation to be reasonably accurate for low vibrational quantum numbers in molecules the size of $H_2CO$, this certainly need not be the case. One consequence of mixing between normal modes is a perturbation in the dipole moments of the mixed states relative to the predictions of a simple linear model. In fact, dipole moment measurements have been used as a diagnostic of vibrational state mixing in OCS [14] and $NH_3$ [15, 16]. While at least some of the non-linear evolution of the dipole moment in $H_2CO$ with $\nu_5$ excitation is likely to arise from vibrational state mixing, it can also arise from higher-order terms in the dipole moment surface. Having independent information on either one of these two contributions would make it possible to determine the other. A rational approach to this problem would combine *ab initio* calculations of the dipole moment surface and vibrational wave functions with experimental Stark effect measurements of the kind reported here. Accurate calculations of dipole moments to compare with those listed in Table 3.2, as well as those of several different isotopomers in the ground [9] and excited states [12, 17, 18] would be an excellent starting point. We hope that our dipole moment data for highly excited vibrational states will stimulate new theoretical calculations, and that the combination of these efforts will significantly improve our understanding of molecular electronic structure and vibrational state mixing of $H_2CO$.
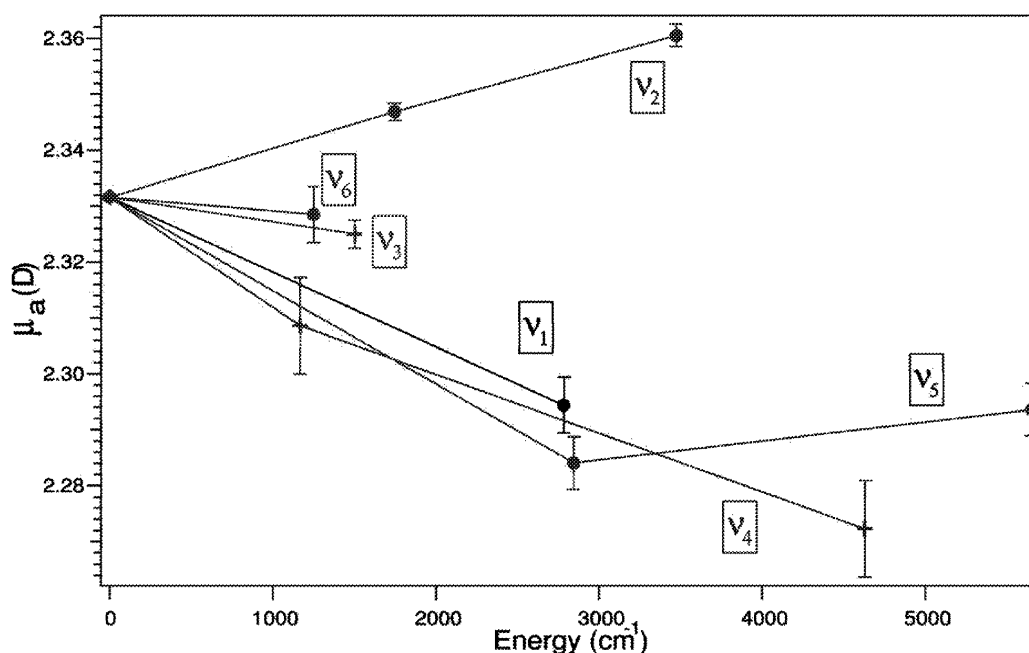
**Figure 3.15:** Evolution of the dipole moment upon vibration for the different normal modes of H₂CO.

## 3.5 Summary

We have used fluorescence detected microwave spectroscopy to determine the only missing fundamental dipole moment, $\mu_{1_1} = 2.2944(50)$, and to measure the dipole moment of the first overtone of the asymmetric CH stretch, $\mu_{5_2} = 2.2936(47)$ of H₂CO. We have shown that a simple perturbative dipole moment function could not explain the evolution of the dipole moment upon vibration mainly because of vibrational state mixing and higher-order terms in the dipole moment surface.

## References

[1] D. J. Clouthier and D. A. Ramsay. The spectroscopy of formaldehyde and thioformaldehyde. *Annual Review of Physical Chemistry*, 34:31–58, 1983.

[2] C. B. Moore and J. C. Weisshaar. Formaldehyde photochemistry. *Annual Review of Physical Chemistry*, 34:525–555, 1983.

[3] A. S. Pine. Doppler-limited spectra of C − H stretching fundamentals of formaldehyde. *Journal of Molecular Spectroscopy*, 70(2):167–178, 1978.

[4] V. A. Job, Sethuram.V, and K. K. Innes. 3500-$a^1a_2$ - $x^1a_1$ transition of formaldehyde-$h_2$ $d_2$ and HD vibrational and rotational analyses. *Journal of Molecular Spectroscopy*, 30(3):365, 1969.

[5] M. Allegrini, J. W. C. Johns, and A. R. W. McKellar. Study of coriolis-coupled $\nu_4$, $\nu_6$, and $\nu_3$ fundamental bands and $\nu_5$ -$\nu_6$ difference band of $H_2CO$ - measurement of dipole-moment for $\nu_5 = 1$. *Journal of Molecular Spectroscopy*, 67(1-3):476–495, 1977.

[6] C. Kittrell, E. Abramson, J. L. Kinsey, S. A. McDonald, D. E. Reisner, R. W. Field, and D. H. Katayama. Selective vibrational-excitation by stimulated-emission pumping. *Journal of Chemical Physics*, 75(5):2056–2059, 1981.

[7] P. H. Vaccaro, A. Zabludoff, M. E. Carrerapatino, J. L. Kinsey, and R. W. Field. High-precision dipole-moments in $\tilde{A}^1a_2$ formaldehyde determined via stark quantum beat spectroscopy. *Journal of Chemical Physics*, 90(8):4150–4168, 1989.

[8] C.H. Townes and A.L. Schawlow. *Microwave Spectroscopy*. Dover Publications, New York, 1975.

[9] B. Fabricant, D. Krieger, and J. S. Muenter. Molecular-beam electric resonance study of formaldehyde, thioformaldehyde, and ketene. *Journal of Chemical Physics*, 67(4):1576–1586, 1977.

[10] J. W. C. Johns and A. R. W. McKellar. Stark spectroscopy with CO laser - dipole-moment of $H_2CO$ in $v_2 = 2$ state. *Journal of Chemical Physics*, 63(4):1682–1685, 1975.

[11] M. Allegrini, J. W. C. Johns, and A. R. W. McKellar. Stark spectroscopy with co laser - $\nu_3$ fundamental band of $H_2CO$. *Journal of Molecular Spectroscopy*, 66(1):69–78, 1977.

[12] J. W. C. Johns and A. R. McKellar. Stark spectroscopy with CO laser - $\nu_2$ fundamentals of $H_2CO$ and $D_2CO$. *Journal of Molecular Spectroscopy*, 48(2):354–371, 1973.

[13] P. H. Vaccaro, J. L. Kinsey, R. W. Field, and H. L. Dai. Electric-dipole moments of excited vibrational levels in the $\tilde{X}^1a_1$ state of formaldehyde by stimulated-emission spectroscopy. *Journal of Chemical Physics*, 78(6):3659–3664, 1983.

[14] L. S. Masukidi, J. G. Lahaye, and A. Fayt. Intracavity co laser stark spectroscopy of the $\nu_3$ band of carbonyl sulfide. *Journal of Molecular Spectroscopy*, 148(2):281–302, 1991.

[15] M. D. Marshall, K. C. Izgi, and J. S. Muenter. Ir-microwave double resonance studies of dipole moments in the $\nu_1$ and $\nu_3$ states of ammonia. *Journal of Chemical Physics*, 107(4):1037–1044, 1997.

[16] Y. Y. Kwan and E. A. Cohen. Coriolis interaction between $v_t$ and $2v_n$ for axially-symmetric molecules of group $c_3v$ - application to stark effect of $NH_3$ in $v_4$ 1 state. *Journal of Molecular Spectroscopy*, 58(1):54–75, 1975.

[17] J. W. C. Johns and A. R. W. McKellar. $\nu_3$ fundamental band of HDCO. *Journal of Molecular Spectroscopy*, 64(2):327–339, 1977.

[18] D. Coffey, C. Yamada, and E. Hirota. Laser stark spectroscopy of formaldehyde-$d2$ - coriolis coupled $v_4$ and $v_6$ fundamentals. *Journal of Molecular Spectroscopy*, 64(1):98–108, 1977.

# Chapter 4

# Photodissociation-detected microwave spectroscopy of rovibrationally excited HOCl.

This chapter describes an experiment in which we measure dipole moments of single rovibrational states of HOCl with 4 quanta in the OH stretch vibrational mode. As explained in Chapter 2, a single rovibrational state is populated with a laser transition, a cw microwave source induces a pure rotational transition from a rovibrational state to another rovibrational state and the microwave transition is detected by photofragment LIF. This work is an extension of the Double Resonance Overtone Photofragment Spectroscopy (DROPS) technique that has been used to study the unimolecular dissociation dynamics of small molecules [1, 2, 3, 4, 5].

## 4.1 Motivation.

HOCl is an interesting molecule for both theoretical and experimental reasons because its relatively simple structure and well separated vibrational modes make the high-energy dynamics easy to access by OH overtone excitation. Numerous studies have produced potential energy surfaces and accurate spectroscopic constants for levels below the dissociation threshold. The spectroscopy and state-to-state unimolecular reaction dynamics of HOCl near the dissociation threshold has been investigated extensively, a good review of which can be found in Ref. [5]. From a practical point of view, HOCl plays an important role in the catalytic depletion of the stratospheric ozone, acting as a reservoir for active chlorine [6], and thus its spectroscopy and dynamics are important for atmospheric studies.

When referring to vibrational states of HOCl we use the notation $(n_{OH}, n_\theta, n_{OCl})$ to indicate the number of quanta in the OH stretching, HOCl bending and OCl stretching modes

respectively. These states are zeroth-order eigenstates of an approximate Hamiltonian which is separable in the above mentioned coordinates.

## 4.2 Experimental procedure.

We describe here Stark effect measurements on a pure rotational transition in HOCl containing four quanta of OH stretching excitation ($\nu_{OH} = 4$), at about $14,000\ cm^{-1}$.
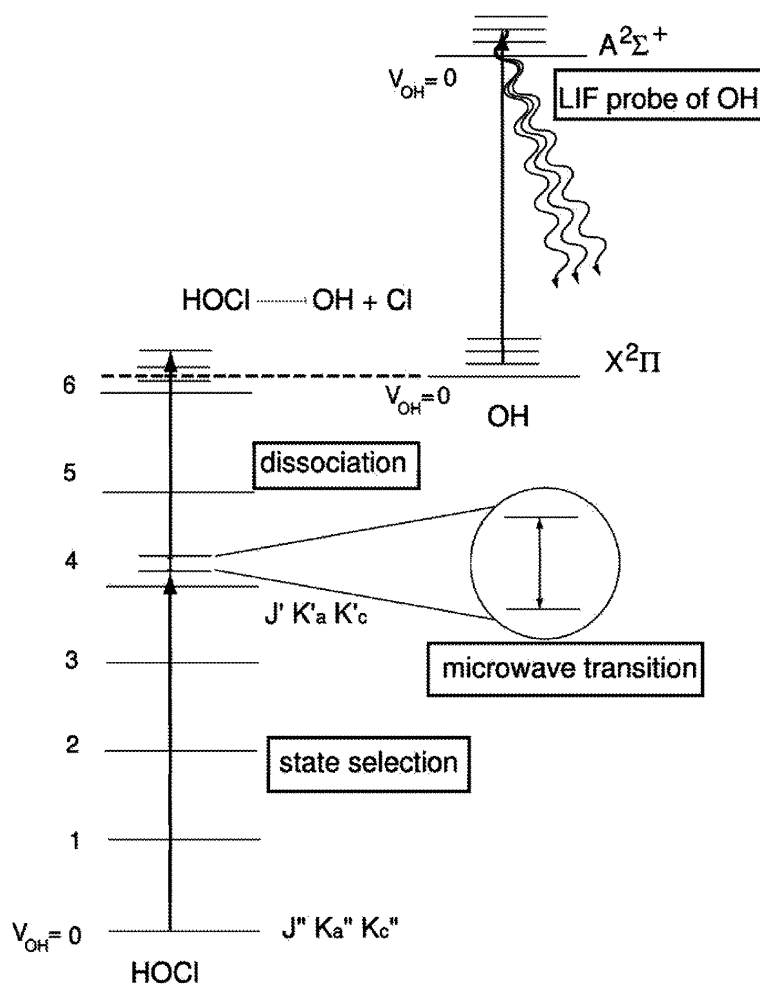


**Figure 4.1:** Energy level diagram for the experiment. A first laser pulse populates a rovibrational state with 4 quanta of OH stretch. As shown in the inset a microwave radiation then induces a pure rotational transition between two rotational levels of this excited vibrational state. A second laser pulse makes a vibrational overtone transition to a dissociative rovibrational state, and a third laser probes the OH fragments by LIF.

The experimental procedure involved is quite similar to those described in Section 3.2 or in Ref. [7] and Ref. [8]. As for $H_2CO$, there is a state-selection step followed by a microwave transition. However, since there is no fluorescing electronic state that we can easily access for detection of the microwave transition, we use vibrational overtone excitation to a predissociative

level followed by LIF of the unimolecular dissociation fragments (see Section 2.2.3). Figure 4.1 shows a schematic energy level diagram for the experiment, and Fig. 4.2 gives an overview of the experimental set-up. Following the procedure described by Barnes and Sinha [9], HOCl is



**Figure 4.2:** Experimental set-up used for $\nu_{OH} = 4$ of HOCl. Three pulsed $Nd : YAG$ pumped dye lasers generate respectively the state-selection pulse, the dissociation pulse and the OH electronic excitation pulse. The three laser beams are focused in a quasi-static cell of HOCl in between a pair of electrodes. Microwave radiation is generated and introduced inside the cell at the focal point of the lasers. A power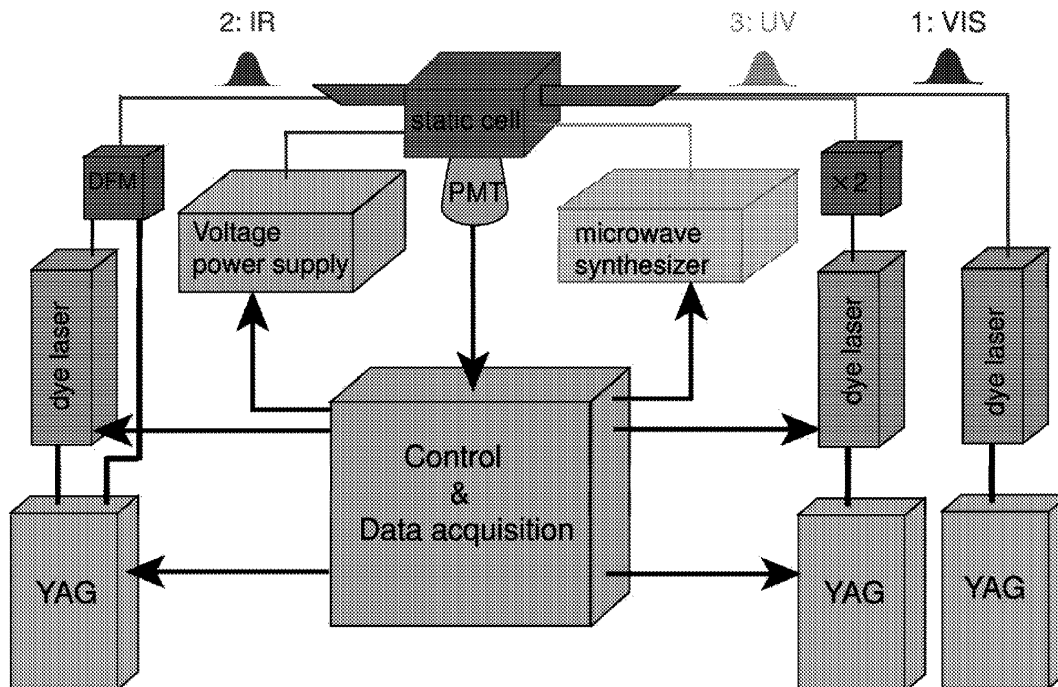 supply provides the Stark voltage at the electrodes. A photomultiplier tube records the OH fluorescence. CAMAC control units control the scanning of the lasers, of the microwave synthesizer and the data acquisition of the LIF.

prepared *in situ* by flowing $H_2O$ and $Cl_2$ at a pressure of several mTorr through a glass column packed with glass beads and yellow HgO. HOCl is produced by the reaction:

$$HgO + H_2O + 2Cl_2 \rightarrow 2HOCl + HgOCl_2$$
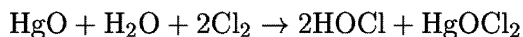
and slowly flows through a gas cell at a total pressure of approximately 20 mTorr.

The state-selection step is made by a Nd:YAG pumped dye laser, using $LDS751$ dye, which produces 50 $mJ$/pulse at about $14,000$ $cm^{-1}$ to induce the (400) $16_{1\ 16} \leftarrow$ (000) $15_{1\ 15}$ rovibrational $a$-type transition of HOCl.

The microwave radiation is generated by a Hewlett-Packard $83751A$ synthesizer and a DBS $2640X218$ frequency doubler and enters the cell via a semi-rigid coaxial cable, where it is coupled to the Stark electrodes using a K-band waveguide to coaxial converter.

As for the detection step, after a 500 $ns$ delay, IR laser pulses excite the (600) $18_{0,18} \leftarrow$ (400) $17_{0,17}$ transition [10, 4], putting the molecule in a state above the barrier for dissociation

into OH + Cl. These IR pulses are generated by difference frequency mixing the output of a Nd:YAG pumped dye laser, operating on $DCM$ dye, with the single mode Nd:YAG radiation at 1.064 $\mu m$ in a $LiNbO_3$ crystal. Approximately 20 $ns$ later, UV laser pulses from frequency doubled Nd:YAG pumped dye laser are used to probe the nascent OH fragments from the unimolecular dissociation of HOCl. The $Q_1(1)$ transition of OH in the $\tilde{A} \leftarrow \tilde{X}$ electronic band is used for OH LIF detection. This transition offers the greatest efficiency for the product state distribution produced here [2], since the most highly populated level of OH has $N = 1$.

The microwave signal between (400) $17_{0,17} \leftarrow 16_{1,16}$ is found to be at $27,484.33(10)$ $MHz$, as can be seen in Fig.4.3.



**Figure 4.3:** Microwave induced pure rotational transition $17_{0\ 17} \leftrightarrow 16_{1\ 16}$ in $v_{OH} = 4$ of HOCl. The $2*16+1 = 33$ M-components of the transition are degenerate. The dashed curve is the experimental data, and the solid curve is a Rabi two-level line shape for a 500 $ns$ delay between the visible and infrared laser pulses. It has a FWHM of 1.8 $MHz$.

It is useful to comment on the choices of transitions we made for the different steps of our experiment and how they are related to the limitations inherent to this technique.

The dissociation barrier for HOCl is at $19,290.3$ $cm^{-1}$, which is 160 $cm^{-1}$ above the (600) level [2]. This means that at least an equivalent amount of rotational energy must be added to reach dissociative states, and this corresponds to the $J = 16$ for $K = 0$ [1, 2]. The height of the HOCl dissociation barrier prohibits us from reaching low $J$, $K$ transitions in both the (400) and (600) states and therefore limits us to studying high $J$ states if we use excitation to the (600) level for detecting the microwave transition. Because of the limited frequency range of our microwave synthesizer, suitable transitions occur when the $J$ state in the $K = 1$ manifold is accidentally nearly degenerate with the $J + 1$ state in the $K = 0$ manifold. Thus, our limited frequency range, the dissociation requirement, large $A$ rotational constants, and the nearly symmetric top nature of HOCl severely restricts the number of available transitions. One

could imagine using excitation to vibrational states well above the dissociation threshold as a detection step, however the unimolecular dissociative lifetime decreases when going to higher predissociative states [4, 5], which broadens and weakens the transitions and prohibits us from reaching low $J$, $K$ levels.

In spite of all these requirements which restrict the number of feasible transitions, two possible microwave transitions were found. The first is (400) $15_{1,15} \leftarrow$ (400) $16_{0,16}$ calculated to be around 5.5 $GHz$ and the second one is (400) $17_{0,17} \leftarrow$ (400) $16_{1,16}$ calculated to be around 27.5 $GHz$. Because collisional dephasing further shortens the microwave transition time, one would observe a slightly broader line shape for the lower frequency transition. Because the collision induced population transfer between the two rotational states is likely to be slower in the higher transition frequency case, we chose to focus on (400) $17_{0,17} \leftarrow$ (400) $16_{1,16}$.

We first recorded the (400) $17_{0,17} \leftarrow 16_{1,16}$ transition at $27,484.33(10)$ $MHz$ in the absence of a Stark field. The transition line shape is displayed as a dashed line in Fig. 4.3 along with a fit of a two-level transition probability using Eq. 2.14 for a 500 $ns$ measurement time (solid line). The pure rotational transition occurs during the time-delay between the visible and the infrared laser pulses, which fixes the time available to generate the microwave signal. The longer this time, the narrower will be the microwave absorption line until either the pulse delay exceeds the transit time of HOCl molecules across the laser beams or until collisions become significant. This represents a second limitation to the time available for the microwave measurement. The



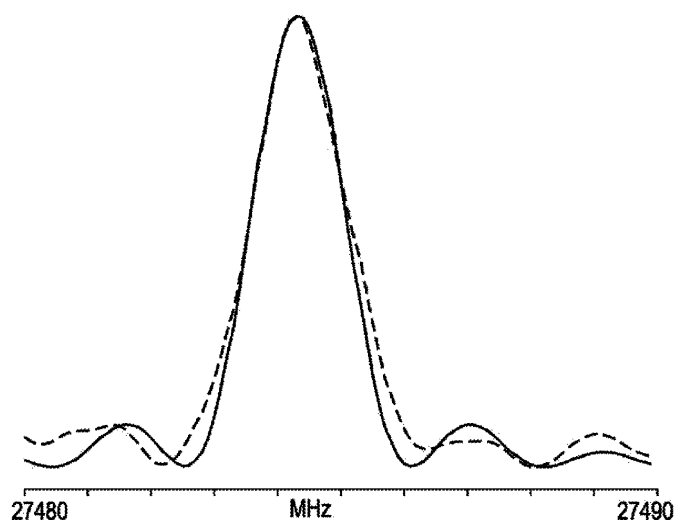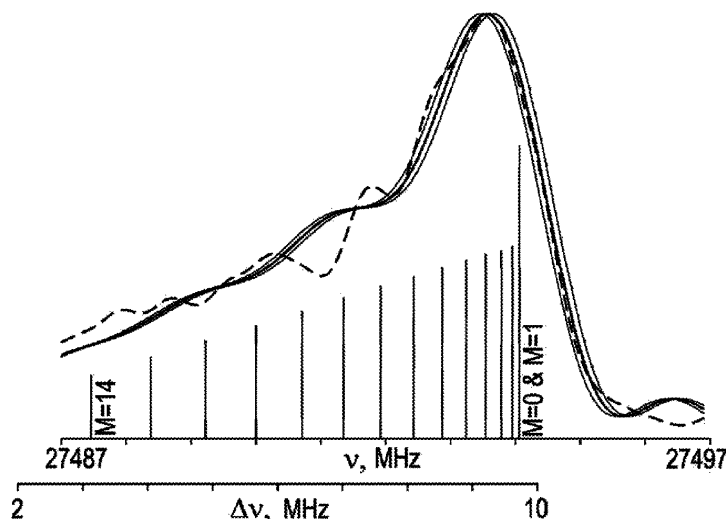**Figure 4.4:** Microwave induced pure rotational transition $17_{0,17} \leftrightarrow 16_{1,16}$ in $v_{OH} = 4$ of HOCl in a 1400 $volts/cm$ Stark field. The dashed curve shows experimental data, while the three solid curves are calculated line shapes. The heavy solid line has $\mu_b$ adjusted to 0.001 $D$ larger than the optimal value, so the high frequency edge of the solid and dashed curves are resolved. The two lighter solid lines use dipole moments differing by ±0.5% from the optimum value. The frequency axes display absolute and relative positions of the Stark shifted signal. Note that the experimental data do not extend to low enough frequency to include the weakest two Stark components.

delay has been optimized at 500 $ns$ between the visible and the IR pulses, which produces a 1.8 $MHz$ FWHM line width. Moreover the pressure is optimized at $15 - 20$ $mtorr$ to minimize collision broadening. To ensure power broadening is not an issue, microwave scans were recorded using from 9 $dBm$ to $-7$ $dBm$.

The second step of the experiment is to generate a Stark field to split the zero field microwave transition into its $M$ components. The Stark field is produced using a Fluke 410B power supply which is calibrated using a Hewlett-Packard 3456$A$ digital voltmeter and a previously calibrated high-voltage probe. The electrode spacing is determined with precision gauge blocks.

When applying this external Stark electric field the previous zero field microwave transition splits up into 17 unresolved Stark components, as the $M$-degeneracy is lifted. Figure 4.4 shows a spectrum for $E_{Stark} = 1400$ $V/cm$ as a dashed line. Data of this type were recorded for Stark fields from 1000 $V/cm$ to 2000 $V/cm$ in 100 $V$ increments.


## 4.3 Results and Analysis

Figure 4.3 displays the pure rotational transition $16_{1,16} \leftarrow 17_{0,17}$ at zero external electric field. This transition clearly shows the damped sine-square dependence associated with Rabi oscillations in a two-level system, as expressed in Eq. 2.14. Since the two rotational levels have been deliberately chosen to be accidentally close so that they fall within the range of our microwave generator, we can use the treatment discussed in Section 2.1.2 for two nearby levels, and consider to a first approximation a two-level system. Since HOCl is nearly a symmetric top, we can write in a first approximation the two rotational states as Wang linear combinations of symmetric top basis wavefunctions, and the transition dipole moment matrix element can be written as:

$$\mu_{J,K,M \to J-1,K+1,M} = \mu_b^v \sqrt{\frac{(J^2 - M^2)(J - K)(J - K - 1)}{2J^2(2J - 1)(2J + 1)}} \tag{4.1}$$

where $\mu_b^v$ is the $b$ component of the dipole moment of the vibronic state $v$. In the absence of a Stark field, the transition is a superposition of 33 degenerate $M$-components, each having its own matrix element. When the spatial degeneracy is removed by the Stark field, as displayed in Fig. 4.4, the signal consists of 17 components, each one (except $M = 0$) being a doubly-degenerate two-level transition since we have a second-order Stark effect (see Section 2.1.2) and $\Delta M = 0$ selections rules (see Appendix A). In Figure 4.4, the dashed line represents experimental data.

Using the expression for the Stark effect derived in Section 2.1.2 that is dominated by the matrix element of Eq. 4.1, we get from Eq. 2.11, the frequency shift of each $M$-component as a

function of the Stark field

$$\Delta\nu = W(J,K,M,E_{Stark}) - W(J-1,K+1,M,E_{Stark}) \tag{4.2}$$
$$= \frac{\mu_b^2 E_{Stark}^2}{\nu_0} \frac{(J^2 - M^2)(J-K)(J-K-1)}{J^2(2J-1)(2J+1)}$$

As the Stark splitting is smaller than the line width, we do not see 17 separated components but a modified lineshape. The $M$ components with the most intensity and largest frequency shift form a sharp edge on the high frequency side of the microwave signal that accurately defines the Stark shift.

The frequency shift given by Eq. 4.2 accounts for more than 90% of the total observed Stark shift due to the accidental degeneracy of the two levels involved. This makes the frequency shift primarily sensitive to the $b$-component of the permanent dipole moment, $\mu_b$. However, a complete data analysis must take into account other contributions to the Stark effect.

First we must account for up to the fourth order terms in the $16_{1,16} - 17_{0,17}$ interaction by expanding the two-level system solution of Eq. 2.11:

$$W = \frac{w_1 + w_2}{2} \pm \left[ \left( \frac{w_1 - w_2}{2} \right)^2 + \mu^2 E^2 \right]^{\frac{1}{2}} \tag{4.3}$$

$$\simeq \frac{w_1 + w_2}{2} \pm \frac{w_1 - w_2}{2} \left[ 1 + \frac{1}{2} \left( \frac{2\mu E}{w_1 - w_2} \right)^2 \mp \frac{1}{4.2!} \left( \frac{2\mu E}{w_1 - w_2} \right)^4 \pm \ldots \right] \tag{4.4}$$

We have also to consider real asymetric rotor dipole moment matrix elements (tabulated in appendix V of Ref. [11] or calculated using SPFIT/SPCAT set of programs) and not simply Wang linear combinations of symmetric top basis wavefunctions as in Eq. 4.1. Moreover, we must consider additional $\mu_b$ matrix elements from all the states lying around the $16_{1,16}$ and $17_{0,17}$ levels, as long as their contribution is not negligible. We thus considered the following interactions:

$$16_{1,16} \leftrightarrow 17_{2,15}$$
$$16_{1,16} \leftrightarrow 15_{0,15}$$
$$16_{1,16} \leftrightarrow 15_{2,13}$$
$$17_{0,17} \leftrightarrow 18_{1,18}$$

Note that we did not include $16_{1,16} \leftrightarrow 16_{2,15}$ and $17_{0,17} \leftrightarrow 17_{1,16}$. Indeed the Stark shift induced on states with $\Delta M = 0$, $\Delta J = 0$ is proportional to $M^2$ [11], thus the shift on the $M = 0,1,2$ components of $16_{1,16}$ and $17_{0,17}$ induced respectively by $16_{2,15}$ and $17_{1,16}$ is negligible.

The $a$-component of the permanent dipole moment $\mu_a$ of HOCl does not make a significant contribution to this Stark effect both because $\mu_a$ is very small (0.36 D in the ground state [12])

and because the $a$-type terms all have large energy denominators. We can then calculate the Stark shift for every $M$ value in terms of a single parameter $\mu_b$.

We also take into account the slight lifting of the $M = \pm 1$ degeneracy by the chlorine hyperfine structure ($I(^{35}Cl) = \frac{3}{2}$, $Q = -8.165.10^{-30}$ $m^2$) as explained in Section 2.1.4. If the nuclear quadrupole moment of the Cl atom makes negligible contributions to the zero field transition, the Stark effect and hyperfine energies have comparable magnitude, and we are therefore in the intermediate field regime. We can carry out a Stark hyperfine calculations using an uncoupled basis set $|J, I, M_J, M_I\rangle$ and the nuclear quadrupole tensor of the ground vibrational state [13]. The relative intensities for a given $M$-component, of the $((2 * \frac{3}{2} + 1)(2 * 16 + 1) = 122)$ Stark hyperfine components are derived in Appendix 1 of Ref. [11], and the Stark hyperfine components are superposed to the $M$-components. Note that if we were able to examine transitions for low $J$ values, where the nuclear quadrupole structure would have been resolved, we could have measured the nuclear quadrupole constant which contains a useful description of the electron distribution at the chlorine nucleus.

The total expression for the Stark shift, resulting from the different expressions above, indicates that the low $M$ values exhibit both the largest frequency shifts and intensities, and henceforth the shape of the spectrum in Fig. 4.4, where the stick diagram represents the calculated shift and intensity of each $M$-transition. The frequency and shift distribution of Fig. 4.4 forms a sharp and well-defined high frequency edge on the signal. Using the expression for the total Stark shift along with the intensity expression given by Eq. 2.14, with $t = 500$ $ns$ (which is fixed by the lasers timing) and a value of $\mu_b$, we can calculate the lineshape of the transition. The three solid lines in Fig. 4.4 represent the calculated curves for different values of $\mu_b$. The peak intensity of the calculated curves is scaled to agree with the $M = 0$ peak intensity of the experimental signal, by adjusting the microwave radiation amplitude $E_{mw}$. The Stark shift $\nu_{ij}$ and the dipole moment $\mu_b$ are also adjusted to get the best agreement between the observed and simulated signal. $E_{mw}$, the microwave radiation electric field amplitude, is not well known because of the possible standing waves and interference effects that can occur and because the coupling of the coaxial adapter to the electrode is not known and should be frequency dependent. We therefore consider $E_{mw}$ as an adjustable parameter that we fix to fit the experimental data. The radiation field $E_{mw}$ primarily determines the slope of the low frequency side of the simulated signal. The time delay $t = 500$ $ns$, determines both the linewidth and the frequency of the damped oscillations in the wings of the line. $\mu_b$ is fixed by the clean and near vertical high frequency edge of the signal. A small amount of excess linewidth, arising from unresolved Cl quadrupole hyperfine splittings and residual Doppler width can be observed on Fig.4.3. These broadening mechanisms partially wash out the damped sine-squared oscillations.

First, $\nu_{ij}$ has been determined very precisely from Fig. 4.3 to give a zero-field transition frequency of $\nu_0 = 27,484.33(10)$ $MHz$. Then, for each electric field $E_{Stark}$ used, the calculated

| $E_{dc}(volt/cm)$ | $\mu_b(D)$ | $\nu_{M=0}(MHz)$ |
|---|---|---|
| 983.7 | 1.592(15) | 27489.51 |
| 1180.2 | 1.555(10) | 27491.44 |
| 1377.0 | 1.561(8) | 27494.08 |
| 1475.4 | 1.562(7) | 27495.54 |
| 1573.8 | 1.569(6) | 27497.20 |
| 1672.2 | 1.562(5) | 27498.73 |
| 1770.8 | 1.561(5) | 27500.45 |
| 1869.0 | 1.563(4) | 27502.34 |
| 1967.7 | 1.563(4) | 27504.29 |

**Table 4.1:** Stark fields, dipole moment fit to the data and calculated frequencies for the $M = 0$ components of the $17_{0,17} \leftrightarrow 16_{1,16}$ transition in $v_{OH} = 4$ of HOCl.

and observed signals are displayed together and $\mu_b$ is varied until the high frequency edge of the two waveforms is superimposed. For calculated signal represented by the heavy solid line, the value of $\mu_b$ is $0.001D$ larger than optimum so the two calculated and experimental waveforms can be distinguished at the high frequency edge. The two lighter solid lines use dipole moments differing by $\pm0.5\%$ from the optimum value. The dipole moments obtained in this way are listed in Table 4.1, along with $E_{Stark}$ values and calculated frequencies for the $M = 0$ component.

The experimental accuracy listed with the dipole moments are based on maximum Stark shifts deviating from the calculated values by no more than $100\ kHz$. As in the case of $H_2CO$, the uncertainty on each individual dipole moment determination is given by

$$\frac{\Delta\mu_b}{\mu_b} = \sqrt{\left(\frac{\Delta d}{d}\right)^2 + \left(\frac{\Delta V}{V}\right)^2 + \left(\frac{\Delta\nu}{2\nu}\right)^2 + \left(\frac{\Delta C}{2C}\right)^2}$$

In this experiment, the critical uncertainties are both the determination of the Stark shift $\left(\frac{\Delta\nu}{\nu}\right) \simeq 0.5\%$ and the electrode spacing with $\left(\frac{\Delta d}{d}\right) = 0.6\%$. This large uncertainty on the electrode spacing comes from the dispersion of the results when measuring the spacing with gauge blocks or determining it from the known dipole moment of $5_1$ of $H_2CO$. We measured the dipole moment from several microwave spectra and for several Stark voltages, as reported in Table 4.1. A weighted average of the individual dipole moment values obtained in this way gives $\mu_b = 1.562(9)\ D$, where the $\pm0.009\ D$ final uncertainty includes both statistical and calibration uncertainties on the individual dipole moments we average on.

Since we measured the dipole moment using a high $J$ transition, it is important to address the centrifugal distortion problem. Reference [14] reports a value of $1.4708(60)D$ for $\mu_b$ of HOCl in the ground vibrational state using the $17_{1,17} - 18_{0,18}$ transition, a value $1.4707(60)D$ using the $20_{0,20} - 19_{0,19}$ transition, and a value of $1.472(36)D$ using the $1_{0,1} - 0_{0,0}$ transition. $\mu_b$ is

reported to be $1.463(30)D$ in Ref. [12] for the same $1_{0,1} - 0_{0,0}$ transition. The uncertainty in low $J$ transition is greater because the signal is weaker. Even if it is difficult to say something because of the large uncertainty on the small $J$ transitions, it seems that the rotational contribution to the dipole moment affects the third decimal of the dipole moment. Although there is no reason that the rotational contribution should be the same for $v_{OH} = 0$ and for $v_{OH} = 4$, this gives an order of magnitude, which is on the same order than our measurement uncertainty. Since it is not possible to calculate to a satisfactory accuracy the centrifugal distortion, we must keep in mind that the dipole moment value we get for $v_{OH} = 4$ is related to the $16_{1,16} \leftarrow 17_{0,17}$ transition.

The dipole moment data that we have obtained for vibrationally excited states of HOCl are limited to $\mu_b$ components. While we have devoted substantial effort to both microwave double resonance and Stark induced quantum beat experiments to measure $\mu_a$, the combination of spectroscopic and HOCl dissociation requirements has made it impossible to obtain $\mu_a$ values for vibrationally excited states of this molecule. Moreover a strong hyperfine constant completely washes out the quantum beat oscillations.

## 4.4 Discussion: The dipole moment function of HOCl.

We can use the geometry of HOCl and a bond moment model to interpret $\mu_b$. The a inertial axis is just 2 degrees from the $O - Cl$ bond axis, and this angle varies by only $0.2^o$ for the excited states in question. We can thus consider that the inertial frame does not move with vibration and that the inertial contribution is negligible for HOCl, due to the mass of the chlorine atom (see Fig.4.5). From the rotational constants for the three vibrational states, we can verify that the HOCl angle changes by $0.4^o$ in going from $v_{OH} = 0$ to $v_{OH} = 4$. Thus the $O - Cl$ bond moment has a negligible projection on the b axis. The OH bond lies at a $15^o$ angle relative to the b axis, making $\mu_b = \mu_{OH} \cos(15^o)$. Thus, to a quite good approximation, the $\mu_b$ values reported here represent OH bond moments, that we can determine by making this small correction. Together with the previously published dipole moments for HOCl, $\mu_b = 1.472(36)$ [12] for the ground state and $\mu_b = 1.515(5)$ for $v_{OH} = 2$ [7], we summarize the results for HOCl in Fig. 4.6. As shown in this Figure 4.6, $\mu_{OH}$ appears to vary linearly with vibrational energy. As explained in Section 1.3, such behavior is expected even in the presence of mechanical $(\omega_e x_e)$ and electrical $(\frac{d^2\mu}{dR^2})$ anharmonicities, if the energy is localized to the extent that the vibrational excitation can be treated like a single oscillator. The linear dipole moment behavior that we observe in HOCl is thus evidence for local mode behavior [15, 16]- that is, that the OH stretching mode is not significantly mixed with other modes for energies up to $14,000 \ cm^{-1}$. This is consistent with our earlier observation of just small, local perturbations in $v_{OH} = 6$ rotational energy levels structure [2].
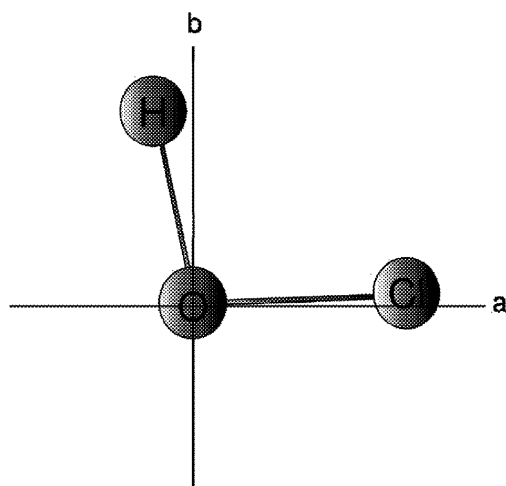
**Figure 4.5:** Position of the inertial axis system for HOCl. The $a$ axis is very close to the O − Cl bond. Due to the high mass of the Cl nucleus compared to the H nucleus, the molecule-fixed frame almost does not tilt with OH stretch vibrational excitation when the OH bond length is elongated due to vibrational anharmonicity.

However, the magnitude of the dipole moment is expected to eventually decrease, since the dipole moment of very highly excited OH stretching states of HOCl must approach the $1.2974\ D$ moment of OCl [17]. It is not clear at what point the OH bond moment in HOCl will turn over, but it must do so at sufficiently high levels of excitation.

## 4.5   Summary

We used photodissociation-detected microwave spectroscopy to measure the $b$ component of the dipole moment of HOCl with four quanta of OH stretch to be $\mu_b = 1.562(9)D$. Comparing it with previous dipole moment measurements [12, 7], we showed that $\mu_b$ appears to vary linearly with vibrational energy and that he OH stretching mode is not significantly mixed with other modes for energies up to $14,000\ cm^{-1}$.

## References

[1] M. R. Wedlock, R. Jost, and T. R. Rizzo. Direct measurement of eigenstate-resolved unimolecular dissociation rates of HOCl. *Journal of Chemical Physics*, 107(23):10344–10347, 1997.

[2] A. Callegari, J. Rebstein, J. S. Muenter, R. Jost, and T. R. Rizzo. The spectroscopy and intramolecular vibrational energy redistribution dynamics of HOCl in the $v_{(oh)} = 6$
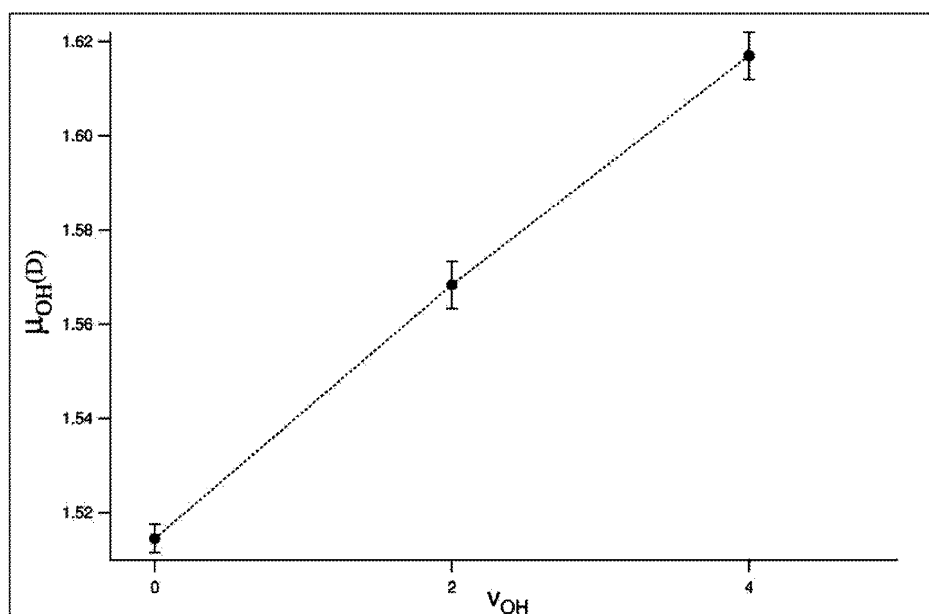
**Figure 4.6:** $\mu_{OH}$ dipole moment data for HOCl plotted as a function of vibrational energy. The three moments plotted here are from comparably high $J$ transitions and centrifugal distortion is not an issue in this comparison.

region, probed by infrared-visible double resonance overtone excitation. *Journal of Chemical Physics*, 111(1):123–133, 1999.

[3] A. Callegari, J. Rebstein, R. Jost, and T. R. Rizzo. State-to-state unimolecular reaction dynamics of HOCl near the dissociation threshold: The role of vibrations, rotations, and ivr probed by time- and eigenstate-resolved spectroscopy. *Journal of Chemical Physics*, 111(16):7359–7368, 1999.

[4] A. Callegari, R. Schmied, P. Theule, J. Rebstein, and T. R. Rizzo. Eigenstate-resolved unimolecular dissociation dynamics of HOCl at $v_{OH} = 7$ and 8. *Physical Chemistry Chemical Physics*, 3(12):2245–2252, 2001.

[5] A. Callegari and T. R. Rizzo. State-to-state unimolecular reaction dynamics of highly vibrationally excited molecules. *Chemical Society Reviews*, 30(4):214–225, 2001.

[6] L. Froidevaux, M. Allen, and Y. L. Yung. A critical analysis of ClO and $O_3$ in the mid-latitude stratosphere. *Journal of Geophysical Research-Atmospheres*, 90(D7):2999–3029, 1985.

[7] J. S. Muenter, J. Rebstein, A. Callegari, and T. R. Rizzo. Photodissociation detection of microwave transitions in highly excited vibrational states. *Journal of Chemical Physics*, 111(8):3488–3493, 1999.

[8] A. Callegari, P. Theule, R. Schmied, T. R. Rizzo, and J. S. Muenter. The dipole moment of HOCl in $v_{OH} = 4$. *Journal of Molecular Spectroscopy*, submitted, 2003.

[9] R. J. Barnes and A. Sinha. State selected unimolecular dissociation of HOCl. *Journal of Chemical Physics*, 107(9):3730–3733, 1997.

[10] B. Abel, A. Charvat, S. F. Deppe, and H. H. Hamann. State-resolved intramolecular dynamics in highly excited HOCl. *Berichte Der Bunsen-Gesellschaft-Physical Chemistry Chemical Physics*, 101(3):329–338, 1997.

[11] C.H. Townes and A.L. Schawlow. *Microwave Spectroscopy*. Dover Publications, New York, 1975.

[12] G. Modugno, P. DeNatale, M. Bellini, M. Inguscio, G. DiLonardo, L. Fusina, and T. VanderAuwera. Precise measurement of molecular dipole moments with a tunable far-infrared stark spectrometer: Application to HOCl. *Journal of the Optical Society of America B-Optical Physics*, 13(8):1645–1649, 1996.

[13] A. M. Mirri, F. Scappini, and G. Cazzoli. Microwave spectrum, structure and electric quadrupole coupling constants of HOCl. *Journal of Molecular Spectroscopy*, 38(2):218, 1971.

[14] H. E. G. Singbeil, W. D. Anderson, R. W. Davis, M. C. L. Gerry, E. A. Cohen, H. M. Pickett, F. J. Lovas, and R. D. Suenram. The microwave and millimeter-wave spectra of hypochlorous acid. *Journal of Molecular Spectroscopy*, 103(2):466–485, 1984.

[15] M. S. Child and R. T. Lawton. Local mode degeneracies in the vibrational-spectrum of $H_2O$. *Chemical Physics Letters*, 87(3):217–220, 1982.

[16] M. S. Child and L. Halonen. Overtone frequencies and intensities in the local mode picture. *Advances in Chemical Physics*, 57:1–58, 1984.

[17] D. Yaron, K. Peterson, and W. Klemperer. On the dipole-moment functions of ClO and OH. *Journal of Chemical Physics*, 88(8):4702–4710, 1988.

# Chapter 5

# Stark induced quantum beat spectroscopy of rovibrationally excited $H_2O$/HDO.

This chapter describes experiments in which we measure dipole moments of single rovibrational states of $H_2O$ and HDO in the time domain. The technique of Stark induced quantum beat spectroscopy used here is complementary to the Stark microwave technique discussed in Chapters 3 and 4.

## 5.1 Motivation

The dipole moment surface (DMS) of the ground electronic state of water directly affects the absorption spectrum from the microwave through the near-UV portions of the spectrum, and this makes it particularly important for understanding energy deposition in the Earth's atmosphere. Water accounts for about 70% of the atmospheric absorption of incoming solar radiation [1] and is the most important greenhouse gas, trapping reradiated energy. Thus water plays a crucial role in the Earth's energy balance, and its spectrum is an essential part of atmospheric models. The fact that the best models cannot account for up to 30% of solar radiation incident on the Earth [2] stresses the importance of a quantitative understanding of the water absorption spectrum and the need for an accurate water DMS.

Difficulties in line strength calculation along with experimental difficulties associated with measuring accurate absorption cross sections [3, 4, 5] call attention to the need for improving the DMS for water [6], particularly for configurations far from equilibrium, which strongly affect the overtone and combination band transitions occurring at short wavelengths. Dipole surfaces can be improved both by generating new *ab initio* data points for DMS development, and by

measuring dipole moments of highly excited rovibrational states (*i.e.* for configurations far from equilibrium) to use as critical benchmarks for judging current and newly constructed surfaces. It is for this purpose that we developed this technique for measuring dipole moments of highly excited rovibrational states of $H_2O$.

Single deuterated water, HDO, is a simpler molecule than $H_2O$, since the high frequency normal modes consist of vibrational motion largely localized in the OH and OD bonds [7, 8]. Moreover, it does not exhibit tunneling associated with the identical H atoms in $H_2O$ [9]. Moreover HDO and $H_2O$ have the same DMS. For these reasons it is useful to measure dipole moments for highly excited rovibrational states of both $H_2O$ and HDO to compare them with those obtained from calculated DMS's, with the goal of improving the latter.

This chapter describes the measurements we made for vibrational states with 4, 5 and 8 quanta in the OH stretch of these two molecules. The evolution of the dipole moment function with vibration will be discussed. We will also compare our experimental data with high level *ab initio* calculations.

## 5.2 Experimental procedure

We discuss the application of this technique to the specific case of $H_2O$ and HDO excited with 4, 5 and 8 quanta of O-H stretching vibration [10, 11, 12]. The principles of the technique have been described in Section 2.2.2.

### 5.2.1 $v_{OH}$ = 4 and 5 of $H_2O$/HDO.

Figure 5.1 represents the energy level diagram for our dipole moment experiments of the $v_{OH} = 4$ level of $H_2O$. For both $H_2O$ and HDO, a linearly polarized nanosecond laser pulse $P_1$ excites at time $\tau_1$ a $J = 1$ rotational level of an excited vibrational state. The laser polarization is oriented at $45^o$ with respect to the Stark electric field, creating a wave packet that is a coherent superposition of the $J = 1$, $M = 0$ and $M = \pm 1$ states (quadratic Stark effect, see Section 2.2.2). At time $\tau_2$, a second linearly polarized nanosecond laser pulse $P_2$ projects the wave packet from the vibrationally excited state to the $\tilde{A}^1B_1$ dissociative electronic state. Pulses $P_1$ and $P_2$ are polarized parallel to one another, at $45^o$ to the Stark electric field, using Fresnel rhombs. A third nanosecond laser pulse $P_3$, polarized parallel to the Stark field ($\Delta M = 0$ selection rules), excites at time $\tau_3$ the $Q_1(1)$ line in the $\Delta v = 0$ band of the $\tilde{A} \leftarrow \tilde{X}$ transition of the resulting OH/OD photofragments. A PMT records the total LIF signal. $P_1$ and $P_2$ are counter-propagating and focused into the cell. $P_2$ and $P_3$ are superimposed using a dichroïc mirror. The three $J = 1$ rotational levels are excited using different initial states. The scheme for the $v_{OH} = 5$ level is the same apart from the different frequency of $P_1$.

$P_1$ is produced by a Nd:YAG pumped dye laser, (using $LDS750$ dye for $v_{OH} = 4$, $Rh\,610+$
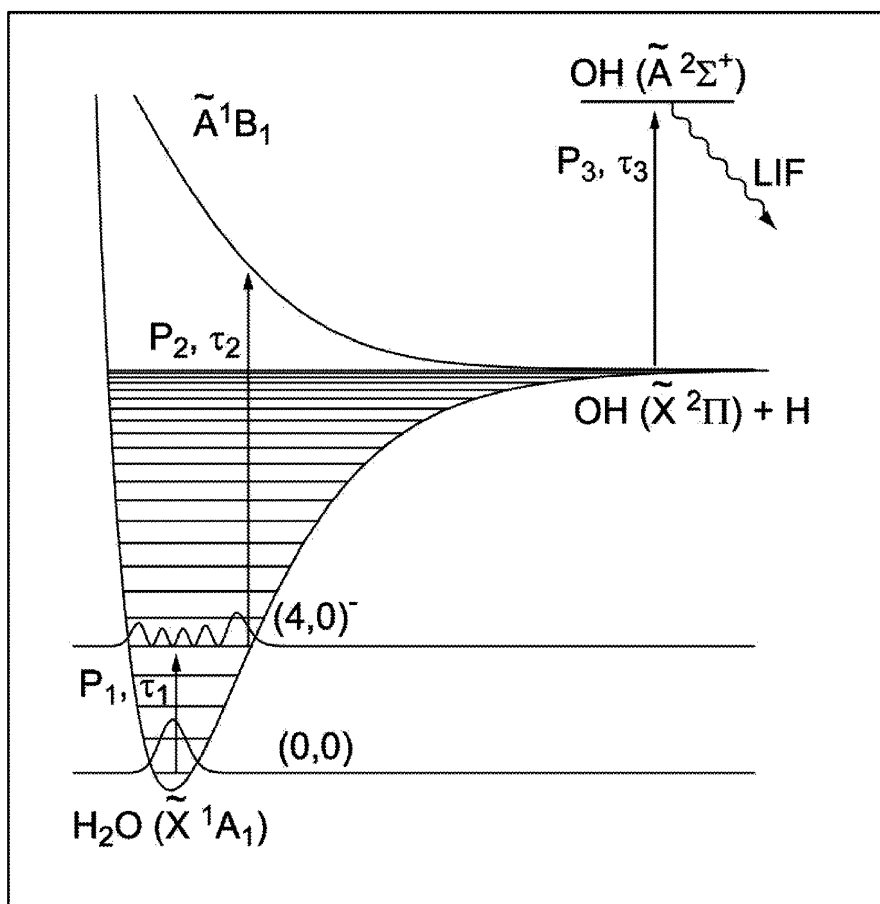
**Figure 5.1:** Energy level diagram for $v_{OH} = 4$ of H$_2$O and HDO. A first laser populates a rovibrational state with 4 quanta in the OH stretch. A second laser brings the molecule to a purely repulsive electronic state. A third laser probes by LIF the OH fragments.

$Rh$ 640 for $|5,0\rangle^-$ and $|4,0\rangle^-|2\rangle$ [1]) and $P_2$ is the fourth harmonic of a Nd:YAG laser (266 $nm$) obtained by doubling the second harmonic in KDP. $P_3$ is produced by doubling a Nd:YAG pumped dye laser, using *Rhodamine* 640. The three lasers are overlapping and focused in the center of the cell, halfway between the two Stark electrodes surfaces and about 10 $mm$ from

---

[1]This local mode notation refers to the number of quanta in each identical OH oscillator of H$_2$O. $|n_1, n_2\rangle$ denotes the state with $n_1$ quanta of stretch in bond 1 and $n_2$ quanta in bond 2. This notation is completed by appending the number of bending quanta $n_b$ present: $|n_1, n_2\rangle|n_b\rangle$. In the absence of bending excitation, it is common to drop the appended zero from the notation. If the two local oscillators are not coupled, the $|n_1, n_2\rangle$, $|n_2, n_1\rangle$ pair of states is degenerate, but any interaction between the oscillators removes the degeneracy and the resulting eigenstates are symmetric $|+\rangle$ (or $|s\rangle$) and asymmetric $|-\rangle$ (or $|a\rangle$) linear combinations of the $|n_1, n_2\rangle$, $|n_2, n_1\rangle$ basis functions:

$$|+\rangle = \frac{1}{\sqrt{2}} (|n_1, n_2\rangle + |n_2, n_1\rangle) \tag{5.1}$$

$$|-\rangle = \frac{1}{\sqrt{2}} (|n_1, n_2\rangle - |n_2, n_1\rangle) \tag{5.2}$$

their top edges. The electrodes are parallel stainless steel metal plates separated by quartz spacers. The plates were machined and then flattened using cold diamond grinding. The quartz spacers are made from plane parallel windows (CVI, $PW1 - 1037 - UV$) with a wedge $\leq 10$ seconds of arc, a $\lambda/10$ surface quality and a thickness tolerance of $\pm 0.010$". The thickness has been measured with a precision sensor head in a temperature stabilized environment and the averaged measurements give a spacing of $9.7285 \pm 5.10^{-4}$ $mm$. The effect of fringing fields in this geometry was investigated with the SIMION computer program [13] and found to be negligible. The voltage between the electrodes is set by an $HNC20000$ Heinzinger high voltage power supply controlled by a Hewlett-Packard $59303A$ D/A converter. To calibrate the power supply, we use a Hewlett-Packard $3456A$ digital voltmeter and a high-voltage probe previously calibrated on a very stable power supply (Standford Research Sytems PS350/5000V-25W, 0.05 % accuracy). The calibration is periodically performed to check for long term drift. The overall uncertainty for the electric field is estimated to be 0.1%. The $H_2O$ sample is slowly pumped through the
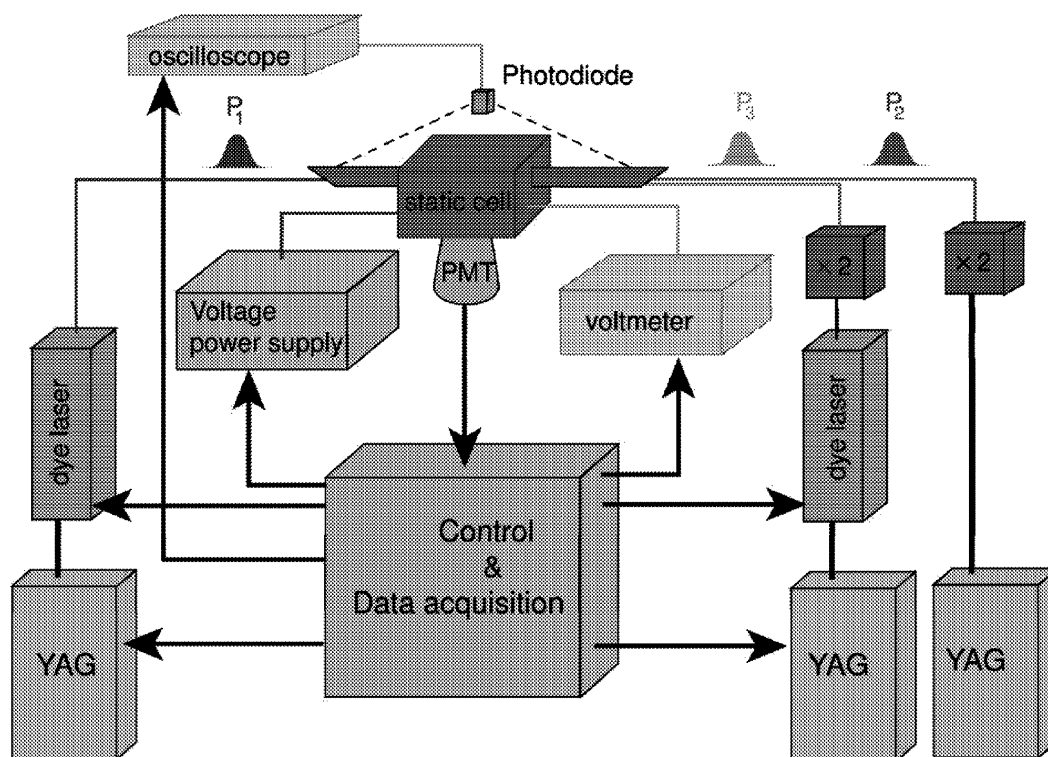


**Figure 5.2:** Experimental set-up used for $v_{OH} = 4$ and 5 of $H_2O$ and HDO.

cell at $15 - 20$ $mTorr$ pressure . HOD is obtained by mixing $H_2O$ and $D_2O$.

The pump-probe delay $\Delta t = \tau_2 - \tau_1$ is measured using a fast photodiode taking the reflections of the counter propagating pump and probe lasers at the Brewster angle windows of the cell. To maintain the Brewster angle, the windows must be rotated to follow the rotation of the polarization. The photodiode signal is sent to a Hewlett-Packard $54615B$ oscilloscope. The

Stark voltage is measured using a Hewlett-Packard 3456$A$ digital voltmeter measuring the output of the D/A converter. The oscilloscope and the digital voltmeter are GPIB controlled and the timing pulses, data acquisition, and control signals are generated with CAMAC electronics. The whole experiment is controlled by a LabView program running on a PC, as shown in Fig. 5.2. To acquire a quantum beat spectrum, the lasers are tuned to the desired frequencies, and the initial Stark voltage and voltage increment of the power supply are set. For a given Stark voltage, the computer then averages the LIF signal for a fixed number of laser shots (typically 20), acquires the $\Delta t$ from the fast photodiode and measures the Stark voltage at the output of the D/A converter from the voltmeter. It then steps the Stark field at the GPIB controlled D/A converter. The Stark voltage is stepped through the whole voltage scan range twice, once in each direction, to reduce possible non-linearity. The quantum beat signal is averaged for a fixed number of these double scans.

The resolution of the quantum beat frequency measurement increases as the delay time $\Delta t$ increases, so we carry out the measurement with a $\Delta t$ that is fixed at the largest value possible. For H₂O and HOD, the optimum $\Delta t$ is about 400 $ns$, determined by the combination of the collisional dephasing time in the gas phase sample, the time of flight of the excited molecules through the volume of the three overlapping laser beams, the breakdown voltage, and the Stark coefficients. $\tau_3 - \tau_2$ is fixed at 20 $ns$ to maximize the OH LIF detection efficiency. We verified that a longer delay does not modify the quantum beat spectrum and therefore that the third laser does not contribute to the beat, since it is polarized parallel to the Stark field.

Using this experimental set-up, quantum beat spectra of the $|4,0,0\rangle$, $|5,0,0\rangle$ vibrational states of HDO[2], and $|4,0\rangle^-$, $|5,0\rangle^-$ and $|4,0\rangle^-|2\rangle$ of H₂O have been recorded. Figure 5.3 shows an example of a quantum beat spectrum. For H₂O, the transition frequencies are taken from Ref. [14] and Ref. [15]. For HDO the transitions are taken from Ref. [16] and Ref. [17].

The fact it is possible to modulate the OH or OD photofragment population with the Stark field, as shown in Fig. 5.3, demonstrates that the photofragments keep the coherence of the wavepacket of the $|J_e\ M_e\rangle$ states during the photodissociation. This new way of detecting quantum beats extends the number of molecules to which we can apply our Stark induced quantum beat technique.

### 5.2.2   v$_{OH}$ = 8 of H₂O/HDO.

For $v_{OH} = 8$, the experimental procedure is slightly different. As shown in Fig. 5.4, we need two Nd:YAG pumped dye lasers to access the $v_{OH} = 8$ level by a $v_{OH} = 4 \leftarrow v_{OH} = 0$, $v_{OH} = 8 \leftarrow v_{OH} = 4$ scheme. The dissociation photon, $P_3$, is now the third harmonic of a Nd:YAG laser at 355 $nm$. The delay between the two first lasers is set at 10 $ns$ and $\Delta t$ is now $\tau_3 - \tau_2$. $P_1$, $P_2$ and $P_3$ are linearly polarized parallel to one another, at $45°$ to the Stark field.

---

[2]HDO vibrational energy levels are labeled as $(n_{OH}, n_{bend}, n_{OD})$.
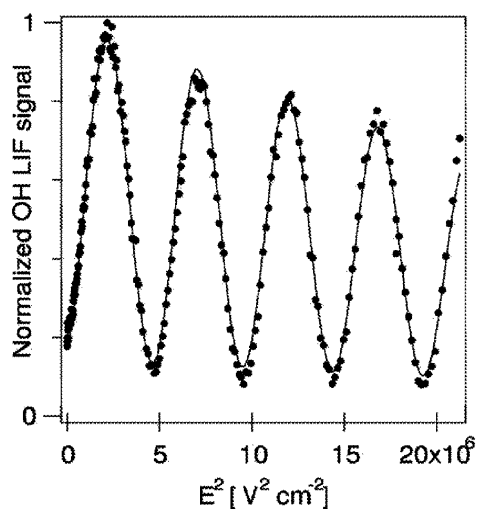
**Figure 5.3:** Quantum beat spectrum for $1_{1\ 0}$ of $v_{OH} = 4$ of $H_2O$. The wavepacket is the superposition of the $M$-states of the $1_{10}$ rotational state of the $v_{OH} = 4$ intermediate vibrational level of $H_2O$. The spatial orientation of the wavepacket at $t = t_{pobe}$ is reflected by the amount of LIF of the OH fragments, as shown in Fig. 5.1. Scanning the Stark field, changes the orientation of the wavepacket at $t = t_{pobe}$ and thus modulates the LIF. The period of these oscillations is related to the dipole moment of this vibrational state.
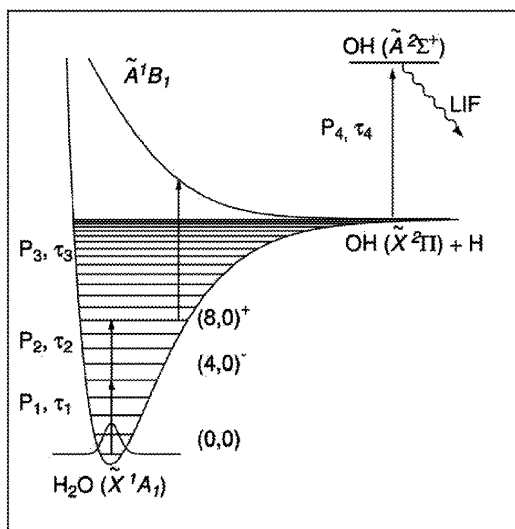


**Figure 5.4:** Energy level diagram for $v_{OH} = 8$ of $H_2O$. Two laser pulses populates a rovibrational state with 8 quanta in the OH stretch. A third laser brings the molecule to a purely repulsive electronic state. A fourth laser probes by LIF the OH fragments.

Using this set-up, quantum beat spectra have been measured for $|8, 0, 0\rangle$ of HDO and $|8, 0\rangle^+$ of $H_2O$. For $H_2O$, transition frequencies taken from [18] are used together with others that we measure ourselves, as there is not much spectroscopic data in this energy region, especially for symmetric states. For HOD, we relied solely on our measurements, the absolute frequencies of which were verified on our wavemeter which is in turn calibrated by an opto-galvanic lamp.

## 5.3  Results and Analysis

### 5.3.1  An asymmetric molecule: HDO.

**Experimental Stark coefficients**

We will first extract, for every rovibrational state, the second-order Stark coefficient $C^2$ (that we will note henceforth $C$) from the experimental LIF signal as a function of the Stark electric field E (see Section 2.2.2). The simple $1 + k sin(2\pi C E^2 t + \phi)$ form of the quantum beat must be generalized to account for limitations of actual experiments, as dephasing processes and imperfect laser polarizations affect the signal waveform. To account for these effects, we write the $E$ field dependent LIF signal $S(E)$, as:

$$S(E) = (k_1 - k_2 E^2)[1 + k_3 sin(2\pi C E^2 t + \phi)] \tag{5.3}$$

The constant $k_1$ scales the signal amplitude, $k_2$ describes any systematic $E$ field dependence of the amplitude and $k_3$ specifies the quantum beat contrast. $C$ is the desired second order Stark coefficient and $\phi$ is the phase factor. $k_1$ depends solely on experimental conditions. Some $J_{K_a K_c}$ states exhibit small positive values for $k_2$, as is the case for the $1_{10}$ levels data, while other rotational levels exhibit small negative $k_2$ values. Even for ideal conditions, $k_3$ can vary from zero to one and $\phi$ can be a multiple of $90^o$ depending on polarizations and on the transitions used in the experiment. These five parameters are fitted to each set of $S(E)$ data points to obtain $C$ for the rovibrational state under study. The solid line in Fig. 5.3 displays the fit obtained from the experimental data points. There are no significant correlations among the fitted parameters.

The procedure is applied to the three $J = 1$ rovibrational states investigated and the corresponding values of the Stark coefficients $C$ are reported in Table 5.1.

All of the fundamental information provided by these measurements is contained in these experimental Stark coefficients, which can be compared directly with theoretical *ab initio* calculations based on potential energy and dipole moment surfaces. While at present wavefunctions for HDO with sufficient accuracy do not exist to calculate theoretical Stark coefficients, the theoretical machinery to do so exists, and our measurements provide a benchmark for future calculations. As described further in this chapter, most of our comparison with theory is concentrated on the $H_2O$ isotopomer.

| vib. state | $J_{K_a K_c}$ | $C_{obs} Hz(v/cm)^{-2}$ |
|---|---|---|
| $\lvert 4,0,0 \rangle$ | $1_{01}$ | 0.546(1) |
| $\lvert 4,0,0 \rangle$ | $1_{11}$ | 0.557(2) |
| $\lvert 4,0,0 \rangle$ | $1_{10}$ | 0.798(1) |
| $\lvert 5,0,0 \rangle$ | $1_{01}$ | 0.583(1) |
| $\lvert 5,0,0 \rangle$ | $1_{11}$ | 0.561(3) |
| $\lvert 5,0,0 \rangle$ | $1_{10}$ | 0.821(1) |
| $\lvert 8,0,0 \rangle$ | $1_{01}$ | 0.657(1) |
| $\lvert 8,0,0 \rangle$ | $1_{11}$ | 0.582(2) |
| $\lvert 8,0,0 \rangle$ | $1_{10}$ | 0.886(1) |

**Table 5.1:** Experimental Stark coefficients for different $J = 1$ rovibrational states of HDO. Experimental Stark coefficients are directly derived from the frequency modulation of the OD LIF when the external electric field is scanned.

## Vibrational dipole moment components

While every eigenstate has its own specific Stark coefficient, dipole moments derived from these coefficients have traditionally been considered as molecular properties having well defined values for specific vibrational states. This common assumption implicitly assumes that rotational and vibrational motions can be separated (*i.e.* that the wavefunction can be written as the product of a rotational term and a vibrational term). Obtaining values for $\mu_n$, the dipole moment operator averaged over the vibrational motion of the vibrational state $\lvert n \rangle$, remains desirable, as these moments provide intuitive descriptions of the structural dependence of molecular charge distributions upon vibration. To extract vibrationally dependent moments from Stark coefficients of rovibrational states, we start by writing the second order energy correction for the rovibrational state $\lvert \alpha J K_a K_c \rangle$ using the perturbation expression developed in Section 2.1.2:

$$\Delta W_{\alpha, J, K_a, K_c} = \sum_{X=a,b,c} \sum_{\alpha' J' K_a' K_c'} \frac{\lvert \langle \alpha' J' K_a' K_c' \lvert \mu_X \lvert \alpha J K_a K_c \rangle \rvert^2 E^2}{W^0_{\alpha J K_a K_c} - W^0_{\alpha' J' K_a' K_c'}}$$

$$= (A_{\alpha J K_a K_c} + B_{\alpha J K_a K_c} M^2) E^2$$

(5.4)

where $X$ stands for the $a$, $b$ or $c$ axis in the appropriate molecule-fixed axis frame, $\alpha$ represents all the other quantum numbers (electronic and vibrational motion) and $\langle \alpha' J' K_a' K_c' \lvert \mu_X \lvert \alpha J K_a K_c \rangle$ represents the dipole moment matrix elements connecting $\lvert \alpha J K_a K_c \rangle$ to all possible states $\lvert \alpha' J' K_a' K_c' \rangle$ through the $X$ component of the dipole moment vector. These Stark connections are represented in Fig. 5.5. The left hand arrows represent dipole matrix elements involving states connected by the $a$ component of the dipole moment while the right hand arrows represent dipole matrix elements involving states connected by the $b$ component of the dipole moment.

In a conventional analysis, $\lvert \alpha J K_a K_c \rangle$ is separated into the product of vibronic and rotational functions, $\lvert \alpha J K_a K_c \rangle = \lvert \alpha \rangle \lvert J K_a K_c \rangle$, and only angular coordinates are explicitly consid-
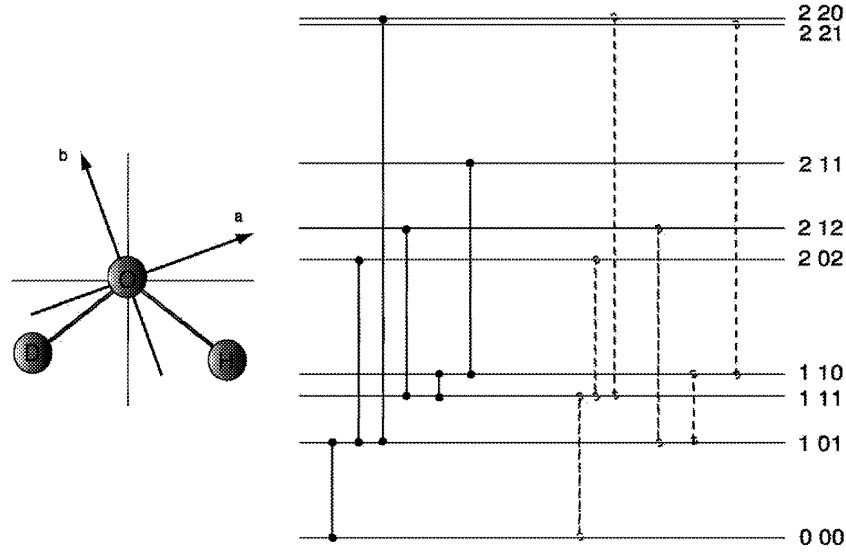
**Figure 5.5:** Interaction of the different rovibrational levels in HDO through the $a$ and $b$ components of the dipole moment in the molecule-fixed frame. The Stark shift a level undergoes is expressed by Eq. 5.4. The vertical lines represents the dipole moment matrix elements of Eq. 5.4. The full vertical lines represent dipole matrix elements involving states connected by the $a$ component of the dipole moment. The dashed vertical lines represent dipole matrix elements involving states connected by the $b$ component of the dipole moment.

ered in calculating the $\langle \alpha' J' K_a' K_c' | \mu_X | \alpha J K_a K_c \rangle$. Since we are dealing only with the ground electronic state, we have $\langle \alpha' | \mu_X | \alpha \rangle = \langle n' | \mu_X | n \rangle$. The vibrational state dependence remains incorporated in the permanent moment, $\langle \mu_X^n \rangle = \langle n | \mu_X | n \rangle$. These assumptions permit the dipole moment matrix elements to be written in the general form:

$$|\langle \alpha' J' K_a' K_c' | \mu_X | \alpha J K_a K_c \rangle|^2 = \sum_{X=a,b,c} \sum_{J' K_a' K_c'} \langle \mu_X^n \rangle^2 S_{J,K_a,K_c,J',K_a',K_c'} \qquad (5.5)$$

where $\langle \mu_X^n \rangle$ is the projection of the vibrationally averaged dipole moment on the $n^{th}$ principal axis and $S_{J,K_a,K_c,J',K_a',K_c'}$ [19] is calculated from direction cosine matrix elements. The direction cosine matrix elements for an asymmetric rotor are calculated from the set of rotational constants of the vibrational state $|n\rangle$ using $SPFIT/SPCAT$ set of programs [20].

Inserting Eq. 5.5 in Eq. 5.4, we get for the rovibrational state $|nJK_aK_c\rangle$

$$\Delta W_{nJK_aK_c} = \sum_{X=a,b,c} \langle \mu_X^2 \rangle^\alpha . E^2 \sum_{J' K_a' K_c'} \frac{(S_{J,K_a,K_c,J',K_a',K_c'})^2}{W_{J,K_a,K_c} - W_{J',K_a',K_c'}} \qquad (5.6)$$

$$= \sum_{X=a,b,c} \langle \mu_X^2 \rangle^\alpha (A_{JK_aK_c}^X + B_{JK_aK_c}^X M^2) E^2 \qquad (5.7)$$

and for a given rovibrational state $|nJK_aK_c\rangle$, the Stark coefficient between $M = 0$ and $M = 1$

can be written as

$$C_{n,J,K_a,K_c} E^2 = \frac{1}{h} \left( W_{n,J,K_a,K_c}^{M=1} - W_{n,J,K_a,K_c}^{M=0} \right) \tag{5.8}$$

$$= \frac{1}{h} \left( B_{JK_aK_c}^a \langle \mu_a^n \rangle^2 + B_{JK_aK_c}^b \langle \mu_b^n \rangle^2 \right) \cdot E^2 \tag{5.9}$$

We use Eq. 5.8 and experimentally determined energies (see Section 5.2) to fit $\langle \mu_a^n \rangle^2$ and $\langle \mu_b^n \rangle^2$ (or more simply $\mu_a^2$ and $\mu_b^2$) to the experimental $C_{n,J,K_a,K_c}$ Stark coefficients for the three $J = 1$ levels measured for the vibrational states investigated[3]. The resulting $\mu_a$ and $\mu_b$, as well as the total dipole moments, $\mu_T = \sqrt{\mu_a^2 + \mu_b^2}$, and their standard deviations, are listed in Table 5.2. Since we only measure the absolute value of the dipole moment components, the sign is given using the convention set in Fig. 1.2 and the orientation of the molecule-fixed axis we chose in Fig. 5.5.

| vibrational state | $\mu_a(D)$ | $\mu_b(D)$ | $\mu_T(D)$ |
|---|---|---|---|
| (000) | -0.6591(2)[21] | -1.7304(5) | 1.8517(5) |
| (001) | -0.6412(2)[21] | -1.7528(5) | 1.8664(5) |
| (004) | -0.5867(9) | -1.822(1) | 1.914(1) |
| (005) | -0.572(1) | -1.8292(9) | 1.917(1) |
| (008) | -0.571(1) | -1.828(1) | 1.915(1) |

**Table 5.2:** Components of the dipole moment in the molecule-fixed frame for different vibrational states of HDO. The last column gives the magnitude of the total dipole moment. This magnitude is independent of the frame used to express the dipole moment.

The uncertainty on each individual Stark coefficients is written as:

$$\frac{\Delta C}{C} = \sqrt{4 \left( \frac{\Delta V_{2\pi}}{V_{2\pi}} \right)^2 + 4 \left( \frac{\Delta V_{volt.}}{V_{volt.}} \right)^2 + 4 \left( \frac{\Delta d}{d} \right)^2 + \left( \frac{\Delta t}{t} \right)^2}$$

where $\left( \frac{\Delta V_{2\pi}}{V_{2\pi}} \right) \simeq 0.3\%$ is the uncertainty on the fit of the oscillation using expression 5.3, $\left( \frac{\Delta V_{volt.}}{V_{volt.}} \right)$ is the uncertainty on the Stark voltage, $\left( \frac{\Delta d}{d} \right)$ the uncertainty on the electrode spacing and $\left( \frac{\Delta t}{t} \right)$ the uncertainty on the pump-probe delay measurement. These three last uncertainties can be evaluated to $\simeq 0.01\%$, and thus we can say to a good approximation that the dominant uncertainty on the Stark coefficients is on the fit of the oscillations:

$$\frac{\Delta C}{C} \simeq 2 \left( \frac{\Delta V_{2\pi}}{V_{2\pi}} \right) \simeq 0.6\%$$

One should note that the uncertainty on the dipole moment components come from both the uncertainty of the Stark coefficients as well as that of energy levels, the former being dominant.

---

[3] See Appendix C for a discussion on the rotational contribution to the dipole moment.

## 5.3.2   A symmetric molecule $H_2O$.

In contrast with HOD, $H_2O$ has two indistinguishable hydrogen atoms that can be permuted, and thus belongs to the $C_{2V}(M)$ molecular symmetry group [22]. Because the complete molecular Hamiltonian has $C_{2V}(M)$ symmetry, every eigenfunction will generate an (reducible or irreducible ) representation of the $C_{2V}(M)$ group of the molecular Hamiltonian. While $H_2O$ is better described in a local mode basis, it is convenient to take into account the permutation operation by introducing a tunneling effect between nearly degenerate OH stretch vibrational modes and to work in a local $C_s$ basis. Each local mode O-H stretch has a constant vibrational action, and the tunneling can bee seen as the swapping of the local mode wavefunction from one bond to another.

In this section, we will present the treatment we used to take into account the indistinguishability of the hydrogen atoms in $H_2O$ in order to extract from the experimental Stark coefficients the components of the vibrational dipole moment, both in the $C_{2V}(M)$ symmetrized basis and in a $C_s$ local basis. This treatment makes use of a Hamiltonian developed by Lehmann [9]. We will use this Hamiltonian to calculate the dipole moment matrix elements we need to extract the vibrationally averaged dipole moment components from the Stark coefficients.

### Experimental Stark coefficients

We extract the Stark coefficients for $H_2O$ following the same procedure explained for HDO in Section 5.3.1[4]. The results are summarized in Table 5.3. The uncertainty calculation is the same as for HDO.

### Identical hydrogen atoms and tunneling

***Local mode properties***   Generally, highly excited vibrational states of symmetric molecules are better described by a local mode basis set than by the more traditional normal modes [23, 24]. As said previously, for a molecule like water with two identical OH bonds, one starts by specifying the number of quanta in each identical OH oscillator, (e.g. $|m, n\rangle$ denotes the state with $m$ quanta of stretch in bond 1 and $n$ quanta in bond 2). For water, this notation is completed by appending the number of bending quanta $b$ present, $|m, n\rangle|b\rangle$. In the absence of bending excitation the appended zero is dropped from the notation. If the two local oscillators are not coupled, the $|m, n\rangle$ pair of states is degenerate, but any interaction between the oscillators removes the degeneracy and the resulting eigenstates are symmetric ($s$) and asymmetric ($a$)

---

[4] See Appendix C for a discussion on the rotational contribution to the dipole moment.

| $\lvert n, 0^{\pm}\rangle \lvert b\rangle$ | $J_{K_a K_c}$ | $C_{obs} Hz(v/cm)^{-2}$ |
|---|---|---|
| $\lvert 4, 0^{-}\rangle$ | $1_{01}$ | 0.4372(8) |
| $\lvert 4, 0^{-}\rangle$ | $1_{11}$ | 0.3160(9) |
| $\lvert 4, 0^{-}\rangle$ | $1_{10}$ | 0.5097(10) |
| $\lvert 4, 0^{-}\rangle \lvert 2\rangle$ | $1_{01}$ | 0.3153(26) |
| $\lvert 4, 0^{-}\rangle \lvert 2\rangle$ | $1_{11}$ | 0.2137(39) |
| $\lvert 4, 0^{-}\rangle \lvert 2\rangle$ | $1_{10}$ | 0.6306(27) |
| $\lvert 5, 0^{-}\rangle$ | $1_{01}$ | 0.4277(7) |
| $\lvert 5, 0^{-}\rangle$ | $1_{11}$ | 0.3032(7) |
| $\lvert 5, 0^{-}\rangle$ | $1_{10}$ | 0.5077(4) |
| $\lvert 8, 0^{+}\rangle$ | $1_{01}$ | 0.4953(16) |
| $\lvert 8, 0^{+}\rangle$ | $1_{11}$ | 0.4250(10) |
| $\lvert 8, 0^{+}\rangle$ | $1_{10}$ | 0.6657(38) |

**Table 5.3:** Experimental Stark coefficients for different $J = 1$ rovibrational states of $H_2O$. Experimental Stark coefficients are directly derived from the frequency modulation of the OH LIF when the external electric field is scanned.

linear combinations of the $\lvert m, n\rangle$ basis functions:

$$\lvert s\rangle \quad = \quad \lvert m, n\rangle^{+} = \frac{1}{\sqrt{2}}(\lvert m, n\rangle + \lvert n, m\rangle) \tag{5.10}$$

$$\lvert a\rangle \quad = \quad \lvert m, n\rangle^{-} = \frac{1}{\sqrt{2}}(\lvert m, n\rangle - \lvert n, m\rangle) \tag{5.11}$$

Much has been written about the local mode representation and several criteria exist for judging the transition from normal to local mode behavior [23, 24]. One of the simplest is the magnitude of the $s - a$ splitting between pairs of states, $\left(i.e. \quad W_{\lvert m,n\rangle^{-}} - W_{\lvert m,n\rangle^{+}}\right)$. Small $s - a$ splittings indicate highly localized vibrations. The $s - a$ splitting for the $H_2O$ vibrational states studied in this work are: $W(\lvert 4, 0\rangle^{-}) - W(\lvert 4, 0\rangle^{+}) = 2.7 \ cm^{-1}$, $W(\lvert 5, 0\rangle^{-}) - W(\lvert 5, 0\rangle^{+}) = 0.4 \ cm^{-1}$ and $W(\lvert 8, 0\rangle^{-}) - W(\lvert 8, 0\rangle^{+}) \simeq 0 \ cm^{-1}$ [14, 15]. It is convenient and useful to consider the $s - a$ splittings as arising from tunneling between the two local mode basis states involved. The rapid decrease in the separation between the $s$ and the $a$ states is then seen to arise from the increasing difficulty of transferring n quanta from one bond to the other as $n$ increases. In the harmonically coupled anharmonic oscillator model of local modes [25], the coupling between the $\lvert n, 0\rangle$ and $\lvert 0, n\rangle$ states is of order $n$, so for example the resulting $s - a$ splitting of the $\lvert 5, 0\rangle^{\pm}$ states of water is very small because it arises from a fifth order perturbation. For any process occurring on a time scale that is fast relative to the tunneling between the $s$ and the $a$ states, water is more accurately described as an asymmetric molecule having only one bond excited. The $s - a$ splittings in the vibrational states studied here are small relative to rotational spacings, indicating that rotational motion is faster than tunneling, and the conventional semi-rigid rotor model based on the separability of vibration and rotation is not appropriate. Lehmann [9] has

constructed a Hamiltonian that starts with the $|n, 0\rangle$ and $|0, n\rangle$ states and simultaneously treats local mode tunneling and molecular rotation. The lower symmetry of the $|n, 0\rangle$ and $|0, n\rangle$ basis states affects experimental observations in a variety of ways. For example, any spectroscopic experiment that does not resolve the $s - a$ splitting will not exhibit the $3 : 1$ ortho-para intensity ratios because the two hydrogen atoms are now dynamically inequivalent. In the case of Stark effect measurements, we will show that it is more effective to focus on the dipole moment components of the $|n, 0\rangle$ and $|0, n\rangle$ local states, which do not exhibit $C_{2v}$ symmetry, rather than on the moments of the $s$ and $a$ states. We will use this local mode basis following the treatment developed by Lehmann [9], as explained below.

**The Lehmann Hamiltonian[9]**   Treating each OH local mode as independent and the two bonds as inequivalent, since only one of them is excited, neglects tunneling motion between the two OH. A correct treatment of water rotational-vibrational motion must include tunneling, which re-establishes the equivalence of the two bonds and hence requires that the wavefunctions be properly symmetrized with respect to the permutation symmetry of the molecular Hamiltonian. This is done by introducing a coupling term $\lambda$ in the local mode Hamiltonian. Following Lehmann's treatment, we write:

$$\mathbf{H} = [G_0 + AJ_{x_1}^2 + BJ_{y_1}^2 + CJ_{z_1}^2]|1\rangle\langle 1| + [G_0 + AJ_{x_2}^2 + BJ_{y_2}^2 + CJ_{z_2}^2]|2\rangle\langle 2|$$
$$+\lambda[|1\rangle\langle 2| + |2\rangle\langle 1|] \tag{5.12}$$

In this expression $G_0$ is the vibrational energy of the local mode basis states, $|1\rangle = |n, 0\rangle$ and $|2\rangle = |0, n\rangle$ , and $\lambda$ defines the interaction that removes the degeneracy between these states. The $J_1$ and $J_2$ angular momentum operators are defined in the inertial coordinate systems of the $|1\rangle$ and $|2\rangle$ basis states, respectively. The rotational constants in the $x_1$, $y_1$, $z_1$ and $x_2$, $y_2$, $z_2$, coordinate systems are equal to one another by symmetry and the two coordinate systems are mirror images, rotated by an angle $\theta_f$ in opposite directions from the $C_{2v}$ axis system, with $x_i = a_i$ and $y_i = b_i$ ($i = 1, 2$). Lehmann rewrites this Hamiltonian in terms of projections onto the vibrational eigenstates, giving

$$\mathbf{H} = [G_0 + \lambda + A_s J_x^2 + B_s J_y^2 + C_s J_z^2]|s\rangle\langle s| \tag{5.13}$$
$$+[G_0 + \lambda + [A_a J_x^2 + B_a J_y^2 + C_a J_z^2]|a\rangle\langle a|$$
$$+2d_{sa}\{J_x + J_y\}[|s\rangle\langle a| + |a\rangle\langle a|]$$

with

$$A_s = A_a = A\cos 2\theta_f + B\sin 2\theta_f \tag{5.14}$$

$$B_s = B_a = A\sin 2\theta_f + B\cos 2\theta_f \tag{5.15}$$

$$C_s = C_a = C \tag{5.16}$$

$$d_{sa} = (A - B)\sin 2\theta_f \tag{5.17}$$

The angular momentum operators are now referred to the $C_{2v}$ inertial axis system appropriate for the $|s\rangle$, $|a\rangle$ eigenstates. The anti-commutator $\{J_x, J_y\}$ mixes rotational levels having the same $J$ and $K_c$, but from local mode combinations of opposite symmetry and, not surprisingly, the size of the mixing term increases with increasing frame rotation.

***Permanent and transition dipole moments.*** Not only does the $d_{sa}$ term mix rotations and vibrations, it also scrambles permanent with transition dipole moment matrix elements. It is useful to consider how the dipole matrix element taken between purely vibrational wavefunctions transforms going from the local mode basis (and the corresponding molecule-fixed frame) to the $C_{2v}$ symmetrized basis. In our notation, a double subscript indicates the identity of the vibrational states and a superscript indicates the Cartesian axis over which the dipole is projected. Hence, for example, $\mu_{11}^b$ indicates the projection of $\langle 1|\vec{\mu}|1\rangle$ on the b-axis of the molecule, that is, the dipole moment operator vibrationally averaged over the local mode state $|1\rangle$, projected over the tilted inertial frame. Similarly, $\mu_{sa}^x$ indicates the projection of the $\langle s|\vec{\mu}|a\rangle$ transition dipole on the $x$ axis appropriate for the $C_{2v}$ symmetry of the $s$ and $a$ states. With the above notation,

$$\mu_{11}^x = \mu_{11}^a \cos\theta_f - \mu_{11}^b \sin\theta_f \tag{5.18}$$

$$\mu_{11}^y = \mu_{11}^a \sin\theta_f + \mu_{11}^b \cos\theta_f \tag{5.19}$$

and similarly for $\mu_{22}^x$ and $\mu_{22}^y$.

From the definitions of the $s$ and $a$ wavefunctions in Eq. 5.10 and Eq. 5.11, and the symmetry of the $\langle n,0|$ and $\langle 0,n|$ states we have:

$$\mu_{11}^y = \mu_{22}^y \tag{5.20}$$

$$\mu_{11}^x = -\mu_{22}^x \tag{5.21}$$

$$\mu_{ss}^y = \frac{1}{2}(\mu_{11}^y + \mu_{12}^y + \mu_{22}^y + \mu_{21}^y) = \mu_{11}^y + \mu_{12}^y \tag{5.22}$$

$$\mu_{aa}^y = \frac{1}{2}(\mu_{11}^y - \mu_{12}^y + \mu_{22}^y - \mu_{21}^y) = \mu_{11}^y - \mu_{12}^y \tag{5.23}$$

$$\mu_{sa}^y = \frac{1}{2}(\mu_{11}^y - \mu_{12}^y - \mu_{22}^y + \mu_{21}^y) = 0 \tag{5.24}$$

$$\mu_{as}^y = \frac{1}{2}(\mu_{11}^y + \mu_{12}^y - \mu_{22}^y - \mu_{21}^y) = 0 \tag{5.25}$$

$$\mu_{sa}^x = \frac{1}{2}(\mu_{11}^x - \mu_{12}^x - \mu_{22}^x + \mu_{21}^x) = \mu_{11}^x \tag{5.26}$$

$$\mu_{as}^x = \frac{1}{2}(\mu_{11}^x + \mu_{12}^x - \mu_{22}^y - \mu_{21}^x) = \mu_{11}^x \tag{5.27}$$

Since $\mu_{12}^y$ is of the same order as transition moment for an $n^{th}$ overtone transition, it is equal to zero in the pure local mode limit. So to a good approximation, $\mu_{ss}^y = \mu_{aa}^y = \mu_{11}^y = \mu_{22}^y$, while the $\mu_{sa}^x = \mu_{as}^x$ transition moment equals $\mu_{sa}^x = \mu_{as}^x = \mu_{11}^x = -\mu_{22}^x$.

Therefore, to a good approximation, the permanent dipole moment in the $C_{2v}$ symmetrized basis (by symmetry the permanent dipole has only one component, the one along the $C_{2v}$ axis) is equal to the $y$ component of the permanent dipole moment in the local basis, whereas the transition dipole moment in the $C_{2v}$ symmetrized basis, connecting the symmetrized $a$ and $s$ eigenstates, is equal to the $x$ component of the permanent dipole moment in the local basis. Tunneling from $|n, 0\rangle$ to $|0, n\rangle$ reverses the sign of $\mu^x$. A permanent moment in the local mode basis states becomes a transition moment between the eigenstates when tunneling occurs.

## Vibrational state dipole moments

***Dipole moment matrix elements and local basis dipole moments.*** To continue with the full analysis we need to know the parameters of the Lehmann Hamiltonian (band origins, rotational constants, and coupling term $d_{sa}$). Even though rotational assignments of the transitions exist, the rotational states have never been analyzed by fitting to an effective Hamiltonian, since the presence of many local perturbations precludes the usual full analysis. However, at least a limited rotational constants determination is required to calculate dipole moment matrix elements. For each symmetrized local mode doublet $|n, 0\pm\rangle|b\rangle$ we use the SPFIT/SPCAT suite of programs [20] to fit $G_0$, $\lambda$, $A$, $B$, $C$, and $d_{sa}$ in Eq. 5.13 to experimental energy levels. In addition, we include $D_J \hat{J}^4$, $D_{JK} \hat{J}^2 \hat{J}_z^2$, and $D_K \hat{J}_z^4$ centrifugal distortion terms in the Lehmann Hamiltonian so nine parameters are used to describe each $s,a$ pair of states. There is no obvious perturbation in the low $J$, $K$ levels of these vibrational states, and we use a limited set of rotational levels for the fit, typically $J \leq 6$, $K_a \leq 3$. There is very little data for the $|8, 0^\pm\rangle$ states [18], and some of the $|8, 0^+\rangle$ energies had to be determined from laser frequency measurements made in this work. All of the $|8, 0^\pm\rangle$ data is consistent with this pair of states being degenerate and $\lambda$ was fixed at zero in this fit. The vibration and rotation results from these fits, listed in Table 5.4, should be considered as effective values because of both the limited data set used and the inevitable presence of small perturbations.

From this fitting procedure it is also possible, using SPCAT program, to obtain for each pair of tunneling states the coefficients $c_{ij}$ that relate the dipole moment matrix elements $\mu_{ij}$ of Eq. 5.4 to the permanent dipole moment $\mu_{ss}^y = \mu_{aa}^y$ and the transition dipole moment $\mu_{sa}^x = \mu_{as}^x$:

$$\mu_{ij} = c_{ij}^x \mu_{sa}^x + c_{ij}^y \mu_{ss}^y \tag{5.28}$$

The dependence of the transition dipole moment $\mu_{ij}$ of each of the rovibrational states on both the $\mu_y$ permanent moment and the $\mu_x$ transition moment arises from the $d_{sa}$ induced mixing of rotational levels across the $s$ and $a$ pair of vibrational states. The specific $\mu_{ij}$ required to analyze $J = 1$ Stark effects are shown schematically in Fig. 5.6, which uses the $|4, 0^-\rangle$ state as an example. The b-type connections for the three different $J = 1$ levels are drawn vertically within the $|4, 0^-\rangle$ manifold, while the a-type interactions are shown as diagonal lines connecting

| param. $cm^{-1}$ | $|4, 0^{\pm}\rangle$ | $|4, 0^{\pm}\rangle|2\rangle$ | $|5, 0^{\pm}\rangle$ | $|8, 0^{\pm}\rangle$ |
|---|---|---|---|---|
| $G_0$ | 13829.5951 | 16821.0975 | 16898.9081 | 25120.2784 |
| $\lambda$ | 1.3376 | 0.3217 | 0.3548 | 0.00 |
| $d_{sa}$ | 1.12 | 0.674 | 1.88 | 2.16 |
| A | 24.6618 | 30.351 | 24.6031 | 21.478 |
| B | 13.8079 | 13.910 | 13.8562 | 12.902 |
| C | 8.6533 | 8.3435 | 8.4713 | 7.931 |
| $D_J$ | $-0.629.10^{-3}$ | $0.441(3).10^{-3}$ | $-0.207.10^{-3}$ | $-0.610$ |
| $D_{JK}$ | $3.27.10^{-3}$ | $8.62(3).10^{-3}$ | 0.0236?? | $3.30.10^{-3}$ |
| $D_K$ | $-0.0263$ | 0.173(4) | 0.0533 | $-0.0188$ |
| $\theta_f$ | 5.8 | 1.911(13) | 9.6 | 13.4 |

**Table 5.4:** Spectroscopic constants for the studied vibrational states of $H_2O$. The constants are derived by fitting experimental energy levels of $H_2O$ to the Lehmann Hamiltonian as expressed in Eq. 5.13.

rotational levels between the $|4, 0^+\rangle$ and the $|4, 0^-\rangle$ states. In the absence of rotation-tunneling mixing, the b-type matrix elements would only depend on $\mu_y$ and the a-type matrix elements would depend solely on $\mu_x$. However, the mixing induced by $d_{sa}$ causes the vertical dashed lines in Fig. 5.6 to have a contribution of about 10% from $\mu_x$ and the diagonal Stark connections to have roughly 10% $\mu_x$ content.

We now combine Eq. 5.28 with Eq. 5.18 and Eq. 5.19 to give $\mu_{ij}$ in terms of $\mu_a$ and $\mu_b$:

$$\mu_{ij} = c_{ij}^x(\mu_{11}^a \cos\theta_f - \mu_{11}^b \sin\theta_f) + c_{ij}^y(\mu_{11}^a \cos\theta_f + \mu_{11}^b \sin\theta_f) \tag{5.29}$$

The $c_{ij}^x$, $c_{ij}^y$ and $\theta_f$ are known from fitting experimental term values to the Hamiltonian, we thus have the necessary dipole moments matrix elements in terms of $\mu_a$ and $\mu_b$ and can write:

$$\mu_{ij} = c_{ij}^a \mu_{11}^a + c_{ij}^b \mu_{11}^b \tag{5.30}$$

**Stark coefficients and local basis dipole moments.** These expressions are combined with the definition of second order Stark effect and Eq. 5.4 to give:

$$C_i E^2 = \frac{\Delta W}{h} = \frac{1}{h}\sum_j \frac{|c_{ij}^x \mu_{sa}^x + c_{ij}^y \mu_{ss}^y|^2.E^2}{W_i - W_j} \tag{5.31}$$

$$= \frac{1}{h}\sum_j \frac{|c_{ij}^x(\mu_{11}^a \cos\theta_f - \mu_{11}^b \sin\theta_f) + c_{ij}^x(\mu_{11}^a \cos\theta_f + \mu_{11}^b \sin\theta_f)|^2.E^2}{W_i - W_j} \tag{5.32}$$

$$= \frac{1}{h}\sum_j \frac{|c_{ij}^a \mu_{11}^a + c_{ij}^b \mu_{11}^b|^2.E^2}{W_i - W_j} \tag{5.33}$$

We use Eq. 5.33 and experimentally determined energies $W_i$ and $W_j$ to fit $\mu_a$ and $\mu_b$ to the experimental $C_i$ Stark coefficients of the three $J = 1$ rotational levels measured for each pair
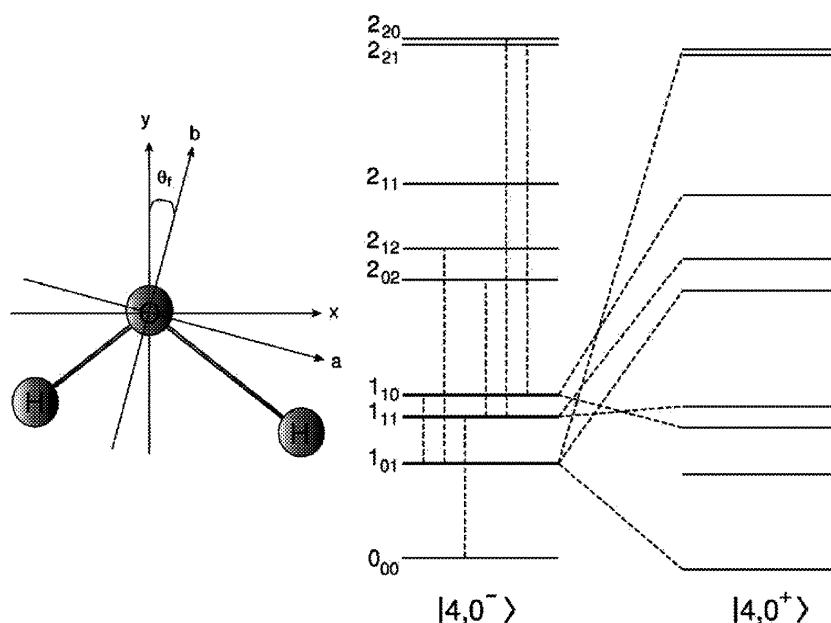
**Figure 5.6:** Interaction of the different rovibrational levels in $H_2O$ through the $a$ and $b$ components of the dipole moment in the molecule-fixed frame. The Stark shift a level undergoes is expressed by Eq. 5.4. The dashed lines represent the dipole moment matrix elements of Eq. 5.4. The left hand dashed lines represent dipole matrix elements involving states connected primarily by the $a$ component of the dipole moment expressed in the local basis. The right hand dashed lines represent dipole matrix elements involving states connected primarily by the $b$ component of the dipole moment. $\mu_a$ mainly connects rovibrational states between the symmetric and asymmetric vibrational states, $|40^+\rangle$ and $|40^-\rangle$ respectively while $\mu_b$ mainly connects rovibrational states with the same vibrational symmetry.

of vibrational states investigated. The resulting $\mu_a$ and $\mu_b$ are listed in column 2 of Table 5.5 along with their standard deviations. Total dipole moments, $\mu_T = \sqrt{\mu_a^2 + \mu_b^2}$, are also listed in Table 5.5. The $v = 0$ and $v = 1$ dipole moments are taken from Ref. [21].

As shown in Eq. 5.33, the Stark effect depends on the square of the sum of two terms, having coefficients of $c_{ij}^x$ and $c_{ij}^y$ and this causes interference between the permanent moment $\mu_y$, and the transition moment $\mu_x$. Since the coefficients $c_{ij}$ can have either the same or opposite sign, the interference can be, accordingly, constructive or destructive. In the absence of $d_{sa}$ mixing, $c_{ij}^y$ would be identically equal to zero for a-type transitions (diagonal connections in Fig. 5.6) and $c_{ij}^x$ would equal zero for b-type transitions (vertical connections in Fig. 5.6) and there would be no interference effects.

To show the extent to which this analysis is necessary for a proper description of the dipole properties of these tunneling states, we also present the results of a conventional analysis that treats the $s$, $a$ pair of states in the semi-rigid rotor approximation, as described by the Watson Hamiltonian [26]. This treatment includes all of the Stark effect terms indicated in Fig. 5.6, both pure rotational $b$-type and vibration-rotation a-type connections, but the matrix elements

| vibrational state | | $\mu(D)$ | semi-rigid rotor | $\mu_x$ $\mu_y$ for $s$ and $a$ |
|---|---|---|---|---|
| (000) | $\lvert 0,0\rangle\ \mu_b$ | -1.85498(9)[21] | -1.8554(4) | |
| (010) | $\lvert 0,0\rangle\lvert 1\rangle\ \mu_b$ | -1.82332(20)[21] | -1.8238(4) | |
| (100) | $\lvert 1,0^+\rangle\ \mu_b$ | -1.86006(22)[21] | -1.8603(4) | |
| (001) | $\lvert 1,0^-\rangle\ \mu_b$ | -1.87744(8)[21] | -1.878(2) | |
| (301) | $\lvert 4,0^-\rangle\ \mu_a$ | 0.299(3) | 0.26(3) | 0.102(3) |
| (301) | $\lvert 4,0^-\rangle\ \mu_b$ | -1.926(2) | -1.94(2) | -1.946(2) |
| (301) | $\lvert 4,0^-\rangle\ \mu_T$ | 1.949(2) | 1.957(3) | 1.947(2) |
| (221) | $\lvert 4,0^-\rangle\lvert 2\rangle\ \mu_a$ | 0.37743(51) | 0.22696(64) | 0.31719(56) |
| (221) | $\lvert 4,0^-\rangle\lvert 2\rangle\ \mu_b$ | -1.8001(22) | -1.8183(64) | -1.8116(22) |
| (221) | $\lvert 4,0^-\rangle\lvert 2\rangle\ \mu_T$ | 1.8392(23) | 1.8324(71) | 1.8392(23) |
| (401) | $\lvert 5,0^-\rangle\ \mu_a$ | 0.354(3) | 0.35(8) | 0.030(3) |
| (401) | $\lvert 5,0^-\rangle\ \mu_b$ | -1.909(1) | -1.91(4) | -1.942(4) |
| (401) | $\lvert 5,0^-\rangle\ \mu_T$ | 1.942(1) | 1.942(74) | 1.942(6) |
| (800) | $\lvert 8,0^+\rangle\ \mu_a$ | 0.600(7) | 0.60(1) | 0.158(7) |
| (800) | $\lvert 8,0^+\rangle\ \mu_b$ | -1.846(5) | -1.84(1) | -1.935(5) |
| (800) | $\lvert 8,0^+\rangle\ \mu_T$ | 1.941(5) | 1.935(16) | 1.941(8) |

**Table 5.5:** Dipole moments for different vibrational states of $H_2O$. The vibrational states are indicated in the first column, both in normal mode notation and in local mode notation. The second column gives the dipole moment components in the local basis derived by fitting the experimental Stark coefficients to Eq. 5.33. The third column gives the dipole moment components if we use a semi-rigid rotor model in which the rovibrational coupling $d_{sa}$ that mixes the symmetric and the asymmetric states of $H_2O$ is ignored. The last column gives $\mu_x$ and $\mu_y$, the $x$ and $y$ components of the dipole moment between the $s$ and $a$ pairs of states in the symmetrized basis. They have been derived by fitting the experimental Stark coefficients directly to Eq. 5.31.

for these interactions were calculated in the conventional fashion using molecular properties obtained by fitting low energy rotational energy levels to the Watson Hamiltonian. This approach produces dipole moment components in agreement with the more detailed analysis, and thus qualitatively correct, but the quality of the fits is much worse, as indicated by standard deviations a factor of ten larger than the more rigorous results.

## 5.4   Discussion

In this section, we will use the dipole moments we measured for the different vibrationally excited states of the OH stretch of HDO and $H_2O$ to understand how the dipole moment is evolving upon vibrational excitation. We will see how adding quanta to an OH stretch vibration changes both the charge distribution along the bonds and the dipole moment vector, both in magnitude and in direction. We will show that the charge redistribution is not the only factor responsible for the evolution of the dipole moment. We will also compare the dipole moments

of HDO, $H_2O$ and HOCl.

We will use a simple bond dipole moment model, where the dipole moment vector is expressed as the sum of dipole moment vectors along the different chemical bonds. This simple approach is quite useful in getting physical understanding of charge distribution, but is only qualitative. To go to a higher level of theory we will use *ab-initio* calculation. Dipole moment matrix elements are generated using ab-initio PES and DMS and used to build calculated Stark coefficients that we can compare to our experimental Stark coefficients. We will see then that the *ab initio* calculation can be improved to match better the experimental results.

## 5.4.1 The dipole moment function of $H_2O$ and HDO.

Table 5.6 summarizes the dipole moments measured during this work along with the ones previously recorded for $v = 0$ and $v = 1$ in Ref. [21] and Ref. [27]. Equation 5.34 gives the

| vibrational state | | $\mu(D)$ |
|---|---|---|
| (000) | $|0,0\rangle$ | $\mu_b = -1.85498(9)$ |
| (010) | $|0,0\rangle|1\rangle$ | $\mu_b = -1.82332(20)$ |
| (100) | $|1,0^+\rangle$ | $\mu_b = -1.86006(22)$ |
| (001) | $|1,0^-\rangle$ | $\mu_b = -1.87744(8)$ |
| (301) | $|4,0^-\rangle$ | $\mu_a = 0.299(3)$ |
| | | $\mu_b = -1.926(2)$ |
| | | $\mu_t = 1.949(2)$ |
| (221) | $|4,0^-\rangle|2\rangle$ | $\mu_a = 0.37743(51)$ |
| | | $\mu_b = -1.8001(22)$ |
| | | $\mu_t = 1.8392(23)$ |
| (401) | $|5,0^-\rangle$ | $\mu_a = 0.354(3)$ |
| | | $\mu_b = -1.909(1)$ |
| | | $\mu_t = 1.942(1)$ |
| (800) | $|8,0^+\rangle$ | $\mu_a = 0.600(7)$ |
| | | $\mu_b = -1.846(5)$ |
| | | $\mu_t = 1.941(5)$ |

**Table 5.6:** Summary of the known dipole moment components of $H_2O$, either measured in this work or in previous work [27]. The vibrational states are indicated both in normal mode and local mode notations.

perturbative expression for the dipole moment function as a function of the vibrational quantum numbers (as is discussed in Section 1.3), which we can fit to the experimental $\mu_b$. Table 5.7 gives the fitted parameters $a_i$ if we use only $v = 0$ and $v = 1$ as it has been done in previous work [27], and if we use all the experimentally available data for $\mu_b$ and $\mu_a$. The experimental

data for $\mu_b$ are displayed in Fig. 5.7 along with the two fits.

$$\langle \mu \rangle_v = \mu_e + \sum_i^{3N-6} a_i(\nu_i + \frac{1}{2}) \tag{5.34}$$

$$\text{with} \quad a_i = \frac{\partial^2 \mu}{\partial q_i^2} - \sum_j (1 + \delta_{ij}) \frac{k_{iij}}{\omega_j} \frac{\partial \mu}{\partial q_j} \tag{5.35}$$

| parameters | $\mu_b$ fit [27] | $\mu_b$ fit | $\mu_a$ fit |
|---|---|---|---|
| $\mu_e$ | -1.8570 | -1.893(22) | 0.0(0) |
| $a_1$ | -0.0051 | 0.011(30) | -0.156(75) |
| $a_2$ | 0.0317 | 0.029(13) | 0.046(10) |
| $a_3$ | -0.0225 | 0.0057(35) | 0.0748(54) |

**Table 5.7:** Parameters of the perturbative dipole moment function for $H_2O$. These parameters have been obtained by fitting Eq. 5.34 to the experimental dipole moments. The parameters in the first column have been obtained fitting $\mu_b$ to the experimental dipole moments for the $v = 0$ and $v = 1$. The parameters in the last two columns have been obtained fitting $\mu_b$ to all the experimental dipole moments of vibrationally excited states.
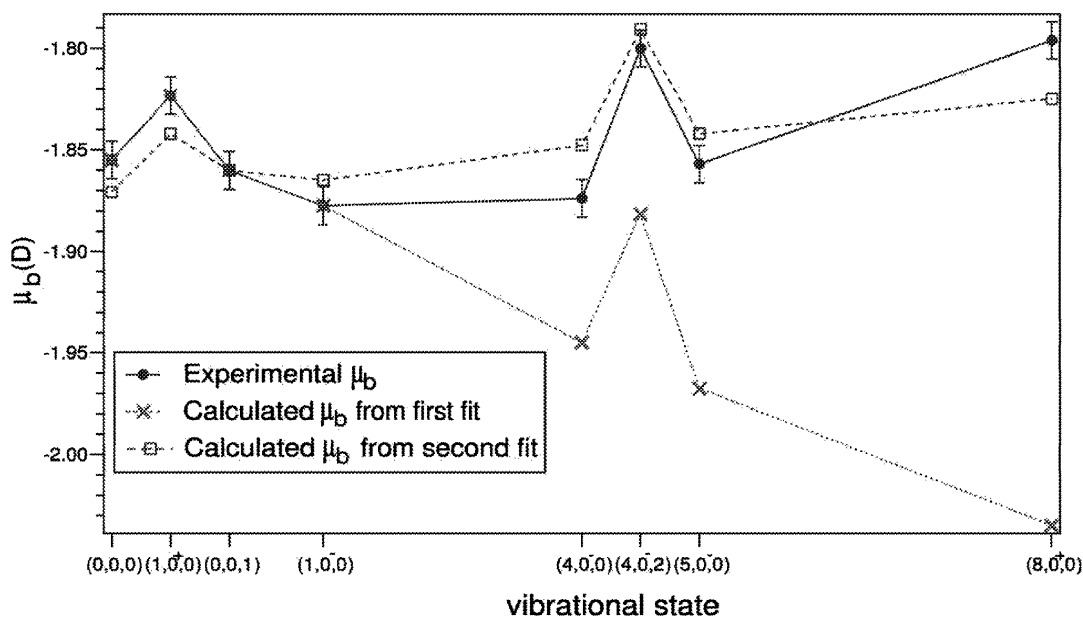


**Figure 5.7:** Evolution of the $b$ component of the dipole moment upon vibration for the different vibrational states of $H_2O$. Experimental dipole moments are plotted along with $\mu_b$ calculated using the dipole moment function with parameters coming first from a fit of the experimental dipole moments of $v = 0$ and $v = 1$, and second from a fit of all the known dipole moments.

It can be seen in Fig. 5.7 that the perturbation approach works fairly well for $\mu_b$ of the

$v = 0$ and $v = 1$ vibrational states. The $a_i$ parameters from the first fit [27] give small residuals for $\mu_b$ of $v = 0$ and $v = 1$, and therefore truncating the dipole moment function to the first and second derivatives (see Eq. 5.35) is sufficient to reproduce the experimental data. However they dramatically fail in predicting $\mu_b$ of higher excited vibrational states. Moreover the second fit which considers $\mu_b$ until $v = 8$ gives large residuals. This, as for $H_2CO$, brings into question the adequacy of the perturbation approach, the inability of Eq. 5.34 to fit the observed $H_2O$ moments arising from either the breakdown of the assumption of isolated, non interacting modes or from a dipole moment surface that cannot be well described by a Taylor's series expansion.

A similar treatment can be applied to HDO. Table 5.8 gives the parameters for a fit of the observed dipole moments to Eq. 5.34 for this molecule. Similar conclusions on the adequacy of the perturbation approach can be drawn by considering the residuals as can be seen in Fig. 5.8.

| parameters | $\mu_b$ fit | $\mu_a$ fit |
|---|---|---|
| $\mu_e$ | -1.738(18) | -0.655(14) |
| $a_3$ | -0.0133(37) | 0.0119(28) |

**Table 5.8:** Parameters of the perturbative dipole moment function for the OH stretch mode of HDO.

## 5.4.2 Inertial and electrical contribution to dipole moment change

The goal of this section is to discuss how we must interpret this evolution with vibration, or how the electronic charge distribution is evolving when the H atom is pulled away from the O atom. From the dipole moment measurements carried out for HOCl (see Chapter 4) and for $H_2O$ and HDO, we can sketch the evolution of the $a$ and $b$ components of the dipole moment vector, displayed in Fig. 5.9.

### The inertial contribution

In practice, for both HDO and $H_2O$, we start from a local mode state $|n, 0\rangle$ with $n$ quanta of vibration in bond 1 and 0 quanta in bond 2. In the case of HDO, bond 1 is the OD bond and bond 2 is the OH that is stretched during the vibrational excitation, as shown in Fig. 5.11. In the case of $H_2O$, if we temporarily neglect tunneling and treat the problem in the local mode basis, bond 1 is the OH bond which is not excited and bond 2 is the OH that is stretched during the vibrational excitation. We will denote them $OH_1$ and $OH_2$ respectively, as shown in Fig. 5.11. In this local mode basis, we will use the usual semi-rigid rotor approach and factor out rotational and vibrational wavefunctions in the appropriate molecule-fixed Eckart frame
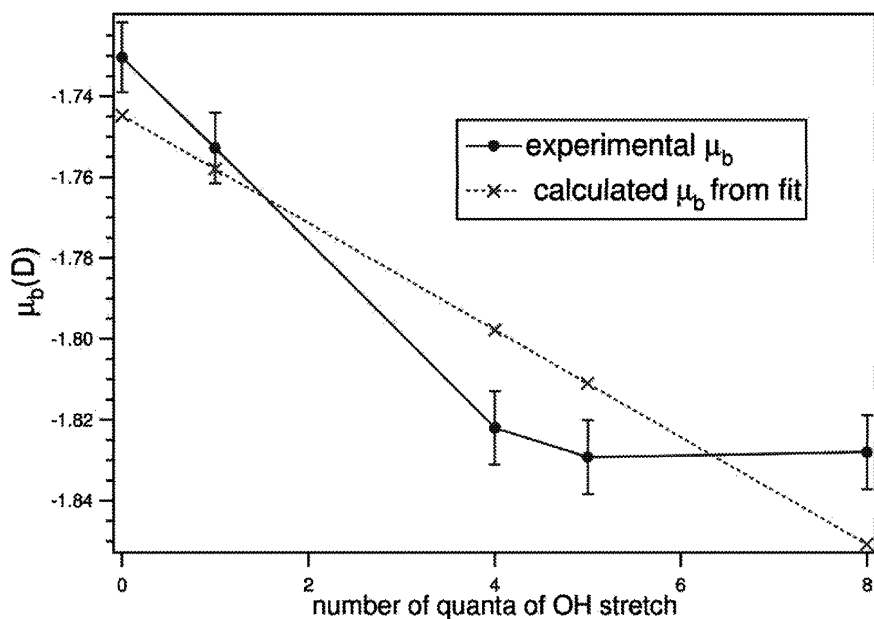
**Figure 5.8:** Evolution upon vibration of the $b$ component of the dipole moment of HDO for the different OH stretch vibrational states. The calculated values come from using the perturbative dipole moment function with parameters coming from fitting experimental data.

averaged over a vibrational period.

Treating the two bonds as inequivalent because of anharmonicity causes the excited bond to have a longer vibrationally averaged length. An important consequence of the excited bond elongation is an asymmetric mass distribution that results in the molecule-fixed frame axes tilting away from the $C_{2v}$ frame appropriate for the ground state of $H_2O$, or from the position of the molecule-fixed axes of ground state HDO, as shown schematically in Fig. 5.11. Therefore, two different vibrational states have different orientation of the molecule-fixed axes. Furthermore, the bond elongation alters the molecular charge distribution, as the electronic charge is redistributing around the atoms and along the bond when the atoms are displaced from equilibrium, producing a change in both the magnitude and the direction of the molecular dipole moment. Therefore the OH bond is stretched, the dipole moment vector rotates in the plane of the molecule and changes in magnitude. Even if the dipole vector was not changing from one vibrational state to another, the difference in orientation of the molecule-fixed axes of the two vibrational states makes the projection on the $a$ and $b$ axes different for the same vector. This is of particular importance when calculating transition dipole moments, and thus intensities of transitions [28], since the dipole moment operator is integrated over two rovibrational wavefunctions which are not expressed in the same frame. This frame rotation is of crucial importance, and great care must be taken to take it correctly into account when treating the
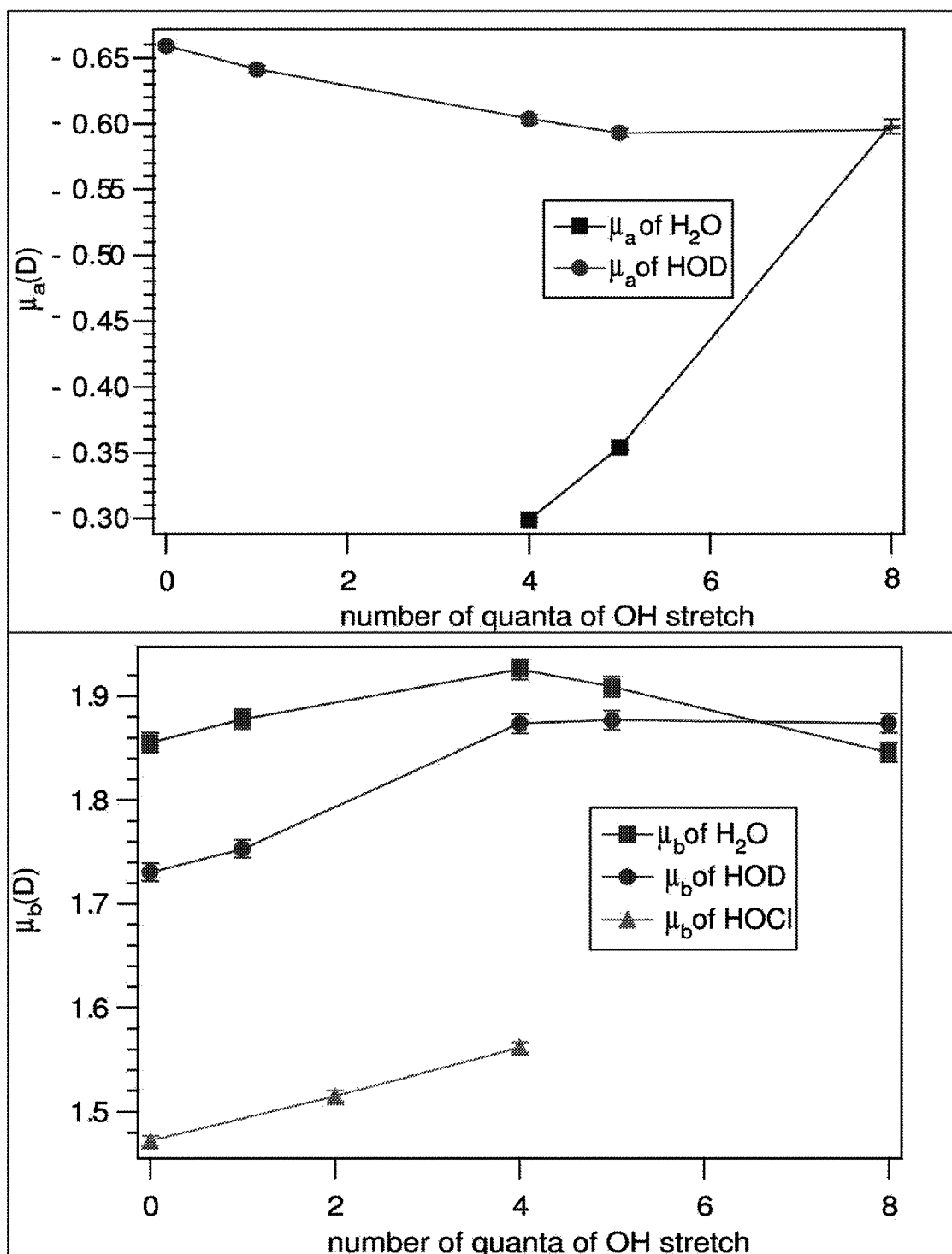
**Figure 5.9:** Evolution of $\mu_a$, $\mu_b$, the a and b components of the dipole moment vector on an averaged Eckart frame, upon OH stretch excitation for $H_2O$, HDO and HOCl.
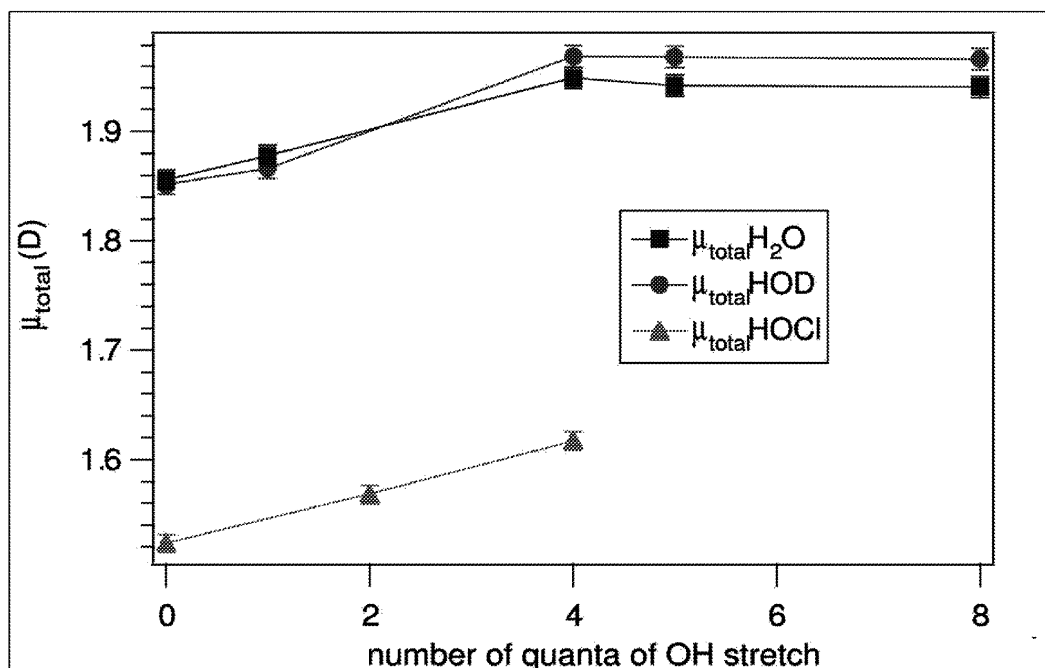
**Figure 5.10:** The figure displays the evolution of the magnitude of the dipole moment vector upon OH stretch excitation for $H_2O$, HDO and HOCl. For HOCl the evolution is linear with OH stretch excitation up to the energy we measured. For $H_2O$ and HDO the evolution upon OH stretch excitation of the magnitude of dipole moment is first linear, then levels off and slightly decreases at higher excitation.

kinetic operator term of the vibration-rotation molecular Hamiltonian, as explained in Ref. [29] and Ref. [30]. Both the frame rotation and the charge redistribution thus affect the projections of the molecular dipole on the new molecule-fixed axes.

In order to get a sense of the relative magnitude of these two contributions we turn briefly to a simple bond moment model for the dipole moment of a $|n, 0\rangle$ basis state. In a bond moment model, the dipole moment vector is considered to be the sum of the two dipole moment vectors lying along the two bonds, $\vec{\mu} = \vec{\mu_1} + \vec{\mu_2}$. In water, for example, the vibrational ground state has $O - H$ bond lengths of 0.958 $\mathring{A}$ and a bond angle of $\theta = 103.5^o$, and the 1.855 $D$ molecular dipole moment is reproduced by two $O - H$ bond moments of 1.499 $D$. We assume the unexcited $O - H$ bond of the $|n, 0\rangle$ state retains these properties (i.e. we take $r_1 = 0.958$ $\mathring{A}$ and $\mu_{OH} = 1.499$ $D$). We determine $r_2$ and $\theta$ from the excited state $A$ and $B$ rotational constants, and estimate $\mu(OH_2)$ using $r_2$ and an assumed dipole derivative. Using the $|4, 0\rangle$ state as an example, the $A$ and $B$ rotational constants give $r_2 = 1.033$ $\mathring{A}$, and $\theta = 102.9^o$, while $r_1$ remains at its 0.958 $\mathring{A}$ ground state value and $\mu_1$ at 1.499 $D$ . The 0.075 $\mathring{A}$ bond extension and a linear bond dipole moment function having a typical 1 $D/\mathring{A}$ derivative give a rough estimate of 1.574 $D$ for the excited bond moment $\mu_2$. Thus, the new molecular dipole is larger and has rotated counterclockwise by $\theta_\mu = 1.8^o$. This situation is summarized in Fig. 5.11, where the excited $O - H_2$ bond, having a greater length and larger bond moment, is on the right. The dot-dash line axes, labeled $x$
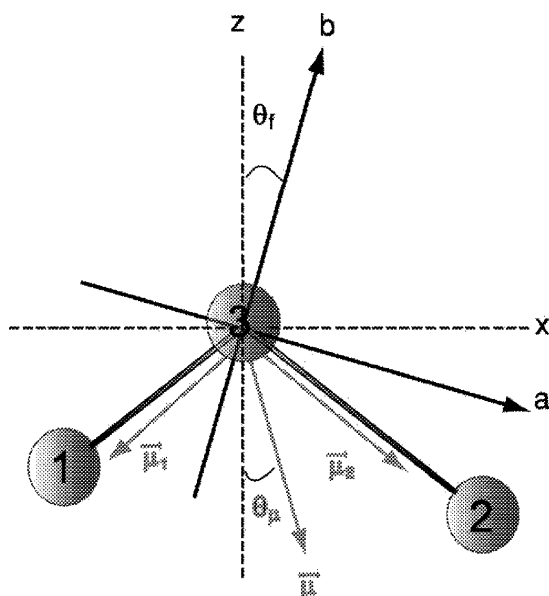
**Figure 5.11:** Tilt of the molecule-fixed frame in a triatomic molecule when a bond is elongated. Because of mechanical anharmonicity, the excited bond, in a local basis, is longer. For both $H_2O$ and HDO atoms 2 and 3 are H and O respectively. Atom 1 is H for $H_2O$ and D for HDO. The molecule-fixed frame (*i.e.* the average on a vibration period of the Eckart frame) makes an angle $\theta_f$ with the $z$ axis. For $H_2O$ the $z$ axis corresponds to the equilibrium configuration $C_{2v}$ axis. In a bond model, the dipole moment vector $\vec{\mu}$ of a triatomic molecule can be decomposed as the sum of two dipole moment vectors $\vec{\mu}_1$ and $\vec{\mu}_2$ lying along respectively bond 1 and 2.

and $z$, are appropriate for the $C_{2v}$ ground state. However, because of the longer $r_2$ bond length and the corresponding asymmetric mass distribution, the axes of the molecule-fixed Eckart frame averaged on a vibrational period, labeled $a$ and $b$ and drawn with solid lines, are slightly translated and rotated through an angle $\theta_f = 7.2^o$ relative to the $C_{2v}$ axes. The direction of this rotation brings the $a$ molecule-fixed axis closer to the extended bond, $r_2$. The two bond moments project onto the molecule-fixed axis of the distorted vibrational state to produce $a$ and $b$ components of the total dipole moment. The numerical values used here to represent the $|0,4\rangle$ state give a magnitude for these components of $\mu_a = 0.298$ $D$ and $\mu_b = 1.893$ $D$, and a total moment of $\mu_T = 1.916$ $D$. The difference in magnitude between $\theta_f = 7.2^o$ and $\theta_\mu = 1.8^o$ clearly indicates that the large $a$ component of the moment results primarily from the molecule-fixed frame rotation.

We have thus shown that the molecule-fixed frame rotation from one vibrational state to another is the primary factor in the change of the dipole moment components with vibrational excitation and that the pure electronic charge density redistribution around the nuclei and along the bonds is of less importance. From this we conclude that the relevant quantity to investigate is the dipole moment change along the extended OH bond, where the charge is redistributing when the H atoms is moved away the O atom. Moreover, the relative balance between the $a$ and $b$ components of the dipole moment vector is very sensitive to the orientation of the molecule-

fixed axis, whereas the magnitude of the dipole moment vector $\mu_T$ is insensitive to this tilt, and really gives information on the electrical anharmonicities (*i.e.* the electronic charge density redistribution). Moreover the a-component of the dipole moment is very sensitive to how well the problem of the rotation of the molecule-fixed frame is treated.

Another important point is that by its nature our measurement gives the projections of the dipole moment vector, $\mu_a$ and $\mu_b$, directly in the molecule-fixed system that separates the best vibration and rotation and defines the total angular momentum of the rovibrational state of interest. The angle that the dipole moment vector makes with the molecule-fixed axes associated with the vibrational state, are free of the inertial axis tilt, and is a direct indication of the rotation of the vector in the plane due to the charge redistribution.

## The electrical contribution

We will derive from our experimental $\mu_a^n$ and $\mu_b^n$, the real change of the electronic charge density along the elongated OH bond. For doing so, we need to know the position of each atom in the molecule-fixed frame of the measured vibrational state, by calculating firstly the geometry (length of the two bonds and angle) of the molecule in the vibrational state of interest and secondly the position of the molecule-fixed axes for this given geometry.

*Geometry from the rotational constants* The bond dipole model is only qualitative, not only because of the assumptions employed, but also because different results obtain if $A$ and $C$ were used instead of $A$ and $B$ to determine $r_2$ and $\theta_f$. The substantial inertial defect, also called the mass defect, exhibited by $H_2O$ or HOD means that simplistic structural interpretations of rotational constants can only give qualitative results [21]. The inertial defect is a measure of the vibrational and electronic dynamics of the problem, since it comes from the fact that if for each instantaneous position of the atoms of a perfectly planar and rigid molecule during the vibrational motion, the eigenvalues of the inertial tensor have the relation $I_c = I_a + I_b$. However integrating the inverse of an inertial tensor eigenvalue over the vibrational motion (which is what a rotational constant is) is not equivalent of taking the inverse of the integrated eigenvalues, and the inertial defect, $\Delta = I_c - (I_a + I_b)$ is non zero. It is a measure of the dynamics (Coriolis interactions, non-planarity and fluxional behavior) of the system, and it prevents us from obtaining any structural determination from the rotational constants.

The length of bond 1 ($r(OH_1)$ for $H_2O$ and $r(OD)$ for HDO) and $\theta$ angle are kept fixed to the ground state value (*i.e.* $r_1 = 0.95864$ Å for $H_2O$ and $r_1 = 0.957$ Å for HDO), and $r_2$ and $\theta$ are fitted to the experimental rotational constants. We therefore calculated the geometry of $H_2O$ or HDO for all the vibrational states investigated from both the $A$ and $C$ rotational constants and from the $A$ and $B$ rotational constants. Although the results are different from the two different sets of constants, the evolution of the parameters with vibrational quantum

number and therefore the qualitative conclusions we can draw are consistent within each set of rotational constants.

For $v_{OH} = 4$ and 5 of HDO, the experimental rotational constants are taken from Ref. [16] and Ref. [17], and for $v_{OH} = 8$ they are obtained by fitting our measured energy levels to an asymmetric rotor model. The rotational constants for HDO are tabulated in Table 5.9. For $H_2O$, as explained in Section 5.3.2, the rotational constants are obtained from a limited rotational analysis of experimental data from Ref. [14] and Ref. [15] for $v_{OH} = 4$ and 5, and from Ref. [18] and from our own measurements for $v_{OH} = 8$. They are tabulated in Table. 5.10.

| parameters | $|0,0,0\rangle$[31] | $|0,0,1\rangle$[21] | $|0,0,4\rangle$[16] | $|0,0,5\rangle$[17] | $|0,0,8\rangle$ |
|---|---|---|---|---|---|
| A | 23.256(95) | 22.37611(3) | 19.443(1) | 18.5142(5) | 16.741(3) |
| B | 9.084(36) | 9.09259(1) | 9.0577(3) | 9.0444(1) | 8.926(1) |
| C | 6.398(29) | 6.328(1) | 6.0903(2) | 6.01268(1) | 5.749(2) |

**Table 5.9:** $A$, $B$ and $C$ rotational constants for HDO for the vibrational states for which the dipole moments have been measured.

| constants | $|0,0,0\rangle$[32] | $|1,0^-\rangle$[32] | $|4,0^-\rangle$[14] | $|4,0^-\rangle|2\rangle$[15] | $|5,0^-\rangle$[15] | $|8,0^+\rangle$[18] |
|---|---|---|---|---|---|---|
| A | 27.88068 | 26.64805 | 24.6618 | 29.8210 | 24.6031 | 21.478 |
| B | 14.52169 | 14.43130 | 13.8079 | 13.94560 | 13.5966 | 12.902 |
| C | 9.27746 | 9.13817 | 8.6533 | 8.3943 | 8.4713 | 7.9310 |

**Table 5.10:** $A$, $B$ and $C$ rotational constants for $H_2O$ for the vibrational states for which the dipole moments have been measured.

The structure determination from the rotational constants has been done from both the $A$ and $C$ rotational constants and from the $A$ and $B$ rotational constants, and the resulting geometries are tabulated in Table. 5.11 for HDO, and Table. 5.12 for $H_2O$.

From Table 5.11 and Table 5.12, it is clearly seen that as we excite the OH vibration, the OH bond gets longer and the molecule is closing. This means that, going to high excited vibrational states, the wavefunctions spans region of the space much different from the equilibrium values.

***Projection of the moment along the OH stretch.*** Using a simple bond dipole model, we calculate from the experimental dipole moment vector the contribution of the dipole moment vector located on the stretched OH.

According to Fig. 5.12, we will define $\theta_{br_1}$ as the tilt angle of the inertial frame with respect to the resting bond $r_1$, that we will use as a reference, $\theta_{\mu r_1}$ and $\theta_{\mu b}$ as the rotation angles of the dipole moment vector with respect to the resting bond $r_1$ and the $b$ axis respectively. The last angle $\theta_{\mu b}$ expresses the rotation of the dipole moment vector in the molecular plane only due to

| vib.states | | $r_2(\mathring{A})$ | $\theta(^{o})$ |
|---|---|---|---|
| $|0,0,0\rangle$ | A/B | 0.9653 | 105.463 |
| | A/C | 0.9899 | 107.542 |
| $|0,0,1\rangle$ | A/B | 0.9805 | 104.784 |
| | A/C | 1.0058 | 106.900 |
| $|0,0,4\rangle$ | A/B | 1.0449 | 102.797 |
| | A/C | 1.0619 | 104.124 |
| $|0,0,5\rangle$ | A/B | 1.0686 | 102.076 |
| | A/C | 1.0809 | 103.017 |
| $|0,0,8\rangle$ | A/B | 1.1271 | 101.064 |
| | A/C | 1.1420 | 102.044 |

| vib.states | | $r_2(\mathring{A})$ | $\theta(^{o})$ |
|---|---|---|---|
| $|0,0,0\rangle$ | A/B | 0.9503 | 105.105 |
| | A/C | 0.9795 | 106.269 |
| $|1,0^-\rangle$ | A/B | 0.9730 | 104.007 |
| | A/C | 0.9953 | 104.930 |
| $|4,0^-\rangle$ | A/B | 1.028 | 102.614 |
| | A/C | 1.049 | 103.312 |
| $|4,0^-\rangle|2\rangle$ | A/B | 1.9549 | 108.065 |
| | A/C | 1.0704 | 112.087 |
| $|5,0^-\rangle$ | A/B | 1.0480 | 102.461 |
| | A/C | 1.0693 | 103.803 |
| $|8,0^+\rangle$ | A/B | 1.123 | 97.986 |
| | A/C | 1.138 | 98.300 |

**Table 5.11:** Molecular geometries averaged on a vibrational period for different vibrational states of HDO. The bond length $r_2$ and the bending angle $\theta$ have been derived from the experimentally determined rotational constants.

**Table 5.12:** Molecular geometries averaged on a vibrational period for different vibrational states of $H_2O$. The bond length $r_2$ and the bending angle $\theta$ have been derived from the experimentally determined rotational constants.

electronic charge redistribution, as the inertial tilt is not accounted for. Atom 1 is D for HDO, and $H_1$ for $H_2O$.

Using the geometry of the molecule drawn from the rotational constants, we calculate the position of each atom in the inertial frame, and then project the experimental dipole moment along the $r_2$ bond for HOCl, HDO and $H_2O$. The evolution of the projection on the extended OH bond is displayed in Fig. 5.13.
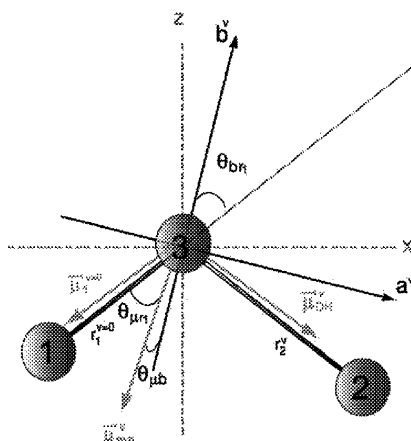
**Figure 5.12:** In a bond dipole model, the dipole moment vector $\vec{\mu}$ of a triatomic molecule can be decomposed as the sum of two dipole moment vectors $\vec{\mu}_1$ and $\vec{\mu}_2$ lying along respectively bond 1 and 2. Each bond dipole moment is written as the product of a charge and a distance $\vec{\mu}_i = \delta_i.\vec{r}_i$. We can also project the total dipole moment vector of every vibrational state along the elongated OH bond 2. We define here a set of different angles. $\theta_{\mu r_1}$ is the angle between total dipole moment vector and bond 1. $\theta_{br_1}$ is the angle between bond 1 and the $b$ axis of the molecule-fixed frame; it represents the tilt of the molecule-fixed frame due to vibrational anharmonicity. $\theta_{\mu b}$ is the angle between the total dipole moment vector and the $b$ axis of the molecule-fixed frame; it represents the true rotation of the dipole moment vector, since the inertial contribution is taken into account in the tilt of the molecule-fixed frame and since the dipole moment components are directly measured in the molecule-fixed frame of the corresponding vibrational state.
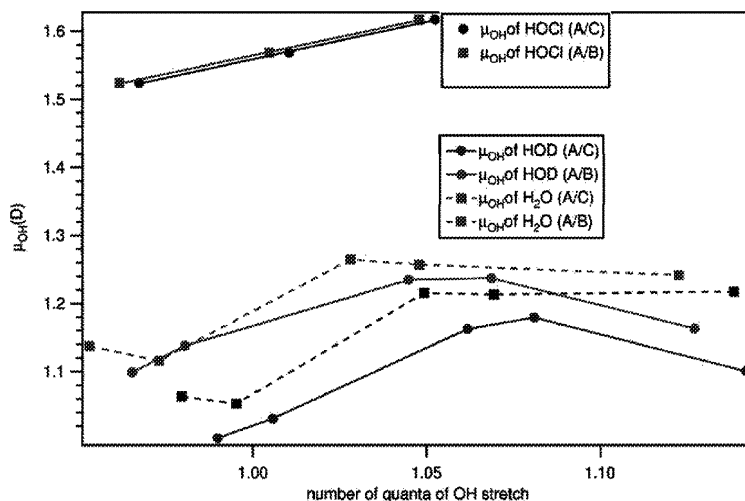


**Figure 5.13:** Evolution of the projection of the dipole moment along the extended OH bond for HOCl, HDO and $H_2O$. The projection is derived using molecular geometry determined from rotational constants. Because of the inertial defect, it is not equivalent to use $A$ and $B$ or $A$ and $C$ sets of rotational constants. Depending on which set we used, we do not exactly find the same bond lengths and bending angle, and therefore not the same projection of the dipole moment. However, the qualitative evolution is consistent. It is seen that the dipole moment projection increases with vibrational excitation to level off and to initiate a decrease for the highest measured energy.

***Single bond charge redistribution.*** We write the dipole moment as:

$$\vec{\mu}^v = \vec{\mu}_1^v + \vec{\mu}_2^v \tag{5.36}$$

$$= \delta_1^v \vec{r}_1^v + \delta_2^v \vec{r}_2^v \tag{5.37}$$

We calculate $\mu_1^{v=0}$ and $\mu_2^{v=0}$ the components of the dipole moments along bond $r_1$ and bond $r_2$ for the vibrational ground state, and we fix the magnitude $\mu_1^{v=n} = \mu_1^{v=0}$ of the dipole moment vector along bond $r_1$. Using the geometry of the molecule drawn from the rotational constants, we calculate what should be the magnitude of $\delta_2^v$ to fit our experimental dipole moment vector components, $\mu_a$ and $\mu_b$, along the molecule-fixed frame. Multiplying $\delta_2^v$ by $r_2^v$ calculated from the rotational constants, we can get $\mu_2^v$. The first derivative of the dipole moment can be derived as:

$$\frac{d\mu_2}{dr}\Big|_{r=r_2} = \frac{\mu_2^v - mu_0^v}{r_2^v - r_2^0} \tag{5.38}$$

Tables. 5.13 and Table 5.14 display the rotation angles of the inertial frame and of the dipole moment vector due to electrical redistribution for HDO and $H_2O$ respectively.

| A/C | | | | | |
|---|---|---|---|---|---|
| | $|0,0,0\rangle$ | $|0,0,1\rangle$ | $|0,0,4\rangle$ | $|0,0,5\rangle$ | $|0,0,8\rangle$ |
| $\theta_{br_1}$ | 16.659 | 19.476 | 21.812 | 22.635 | 26.307 |
| $\theta_{\mu b}$ | 20.852 | 19.311 | 17.858 | 17.531 | 17.619 |
| $\theta_{\mu r_1}$ | 37.511 | 38.787 | 39.670 | 40.166 | 43.926 |
| $\mu_2$ | 1.494 | 1.522 | 1.561 | 1.547 | 1.441 |
| $\frac{d\mu_2}{dr}\big|_{r=r_2}$ | 0.000 | 1.724 | 0.927 | 0.583 | -0.348 |
| A/B | | | | | |
| | $|0,0,0\rangle$ | $|0,0,1\rangle$ | $|0,0,4\rangle$ | $|0,0,5\rangle$ | $|0,0,8\rangle$ |
| $\theta_{br_1}$ | 17.27 | 17.79 | 20.49 | 21.62 | 25.04 |
| $\theta_{\mu b}$ | 20.85 | 19.31 | 17.86 | 17.53 | 17.62 |
| $\theta_{\mu r_1}$ | 38.12 | 37.10 | 38.35 | 39.15 | 42.66 |
| $r_2$ | 0.9653 | 0.9805 | 1.0449 | 1.0686 | 1.1271 |
| $\mu_2$ | 1.511 | 1.541 | 1.577 | 1.556 | 1.462 |
| $\frac{d\mu_2}{dr}\big|_{r=r_2}$ | 0.000 | 1.965 | 0.830 | 0.432 | -0.307 |

**Table 5.13:** Rotation of the dipole moment vector of HDO in the molecular plane. $\theta_{\mu b}$ expresses its rotation with respect to the $b$ axis of the molecule-fixed frame. This rotation is only due to charge redistribution. The mechanical contribution, *i.e.* the tilt of the molecule-fixed frame with vibrational anharmonicity, is expressed in $\theta_{br_1}$. We thus have the relation $\theta_{\mu r_1} = \theta_{br_1} + \theta_{\mu b}$. $\mu_2$ is bond moment along the elongated bond 2. We also calculate its derivative with respect to the $r_2$ bond length. The evolution of these quantity is using molecular geometry derived from both the A/C and the A/B sets of rotational rotational constants.

| A/C | | | | | |
|---|---|---|---|---|---|
| | $|0,0,0\rangle$ | $|0,0,1\rangle$ | $|0,0,4\rangle$ | $|0,0,5\rangle$ | $|0,0,8\rangle$ |
| $\theta_{br_1}$ | 38.620 | 40.855 | 46.831 | 47.930 | 60.767 |
| $\theta_{\mu b}$ | 0.000 | 0.000 | 8.826 | 10.595 | 18.013 |
| $\theta_{\mu_1}$ | 38.620 | 40.855 | 38.005 | 37.435 | 42.754 |
| $\mu_2$ | 1.446 | 1.437 | 1.520 | 1.529 | 1.397 |
| $\frac{d\mu_2}{dr}\big|_{r=r_2}$ | 0.000 | -0.246 | 0.808 | 0.743 | -0.2767 |
| **A/B** | | | | | |
| | $|0,0,0\rangle$ | $|0,0,1\rangle$ | $|0,0,4\rangle$ | $|0,0,5\rangle$ | $|0,0,8\rangle$ |
| $\theta_{br_1}$ | 36.995 | 39.388 | 36.828 | 37.100 | 25.04 |
| $\theta_{\mu b}$ | 0.000 | 0.000 | 8.826 | 10.595 | 18.013 |
| $\theta_{\mu_1}$ | 36.995 | 39.3884 | 36.828 | 37.100 | 42.134 |
| $\mu_2$ | 1.446 | 1.4734 | 1.549 | 1.537 | 1.412 |
| $\frac{d\mu_2}{dr}\big|_{r=r_2}$ | 0.000 | 1.790 | 1.468 | 1.010 | -0.209 |

**Table 5.14:** Rotation of the dipole moment vector of $H_2O$ in the molecular plane. $\theta_{\mu b}$ expresses its rotation with respect to the $b$ axis of the molecule-fixed frame. This rotation is only due to charge redistribution. The mechanical contribution, (*i.e.* the tilt of the molecule-fixed frame with vibrational anharmonicity) is expressed in $\theta_{br_1}$. We thus have the relation $\theta_{\mu r_1} = \theta_{br_1} + \theta_{\mu b}$. $\mu_2$ is bond moment along the elongated bond 2. We also calculate its derivative with respect to the $r_2$ bond length. The evolution of this quantity is determined using molecular geometry derived from both the A/C and the A/B sets of rotational rotational constants.

Figure 5.14 displays the evolution of the dipole moment along the extended OH bond if the electronic charge is constrained to redistribute only along this bond. We can see that the contribution to bond 2 to the dipole moment is increasing as bond 2 is elongated, to reach a plateau between $v_{OH} = 4$ and $v_{OH} = 5$, and then to decrease, as $\mu_2$ cannot increase indefinitely and has to decrease when the H atom goes to infinity.

***Second bond charge redistribution.*** In the previous model we do not take into account the fact that the change in charge accounting for the dipole moment along bond 2 can redistribute to or from bond 1. In this model we now allow the charge to redistribute between bond 2 to bond 1, as former is elongated, we write the dipole moment as

$$\vec{\mu}^v = \vec{\mu}_1^v + \vec{\mu}_2^v = \delta_1^v \vec{r}_1^v + \delta_2^v \vec{r}_2^v \qquad (5.39)$$

Figure 5.16 displays how $\mu_2$ evolves, both for HDO and $H_2O$, when it is possible for the difference of charge $\delta_2$ to be redistributed along bond 1. Only results for the set of $A/B$ rotational constants is displayed since the other set shows a similar trend.
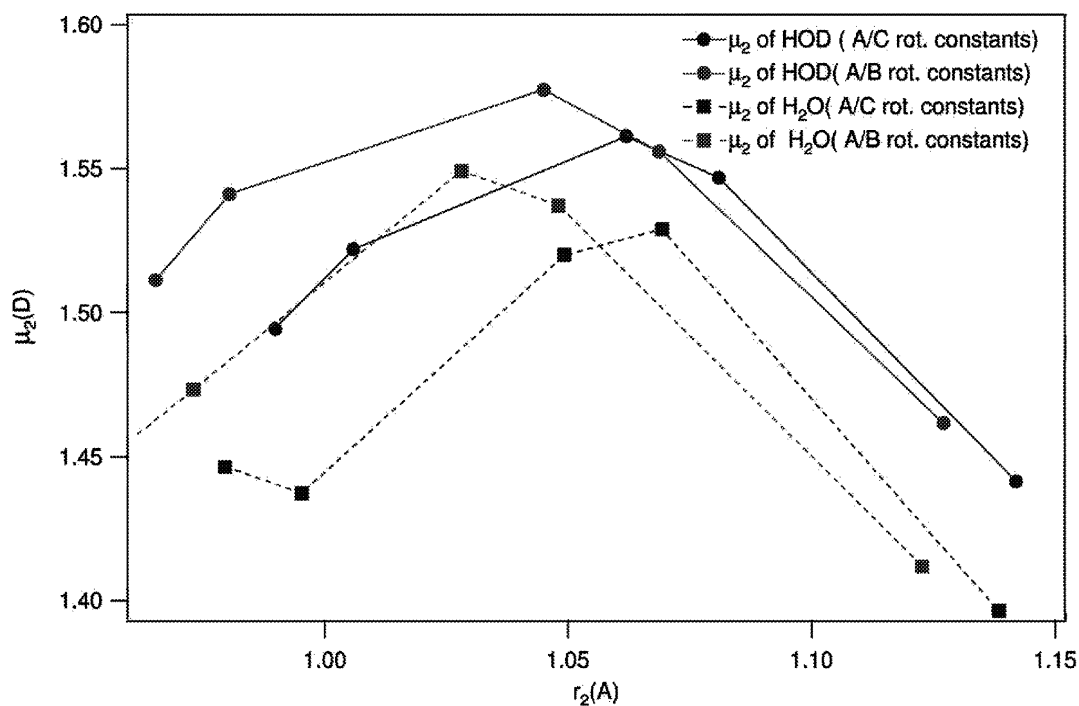
**Figure 5.14:** Evolution of the bond dipole moment $\mu_2$ along the extended OH bond while no charge redistribution is allowed between bond 1 and 2. $\mu_2$ is derived from molecular geometry determined from both the A/C and the A/B sets of rotational rotational constants. The agreement is only qualitative because of the strong inertial defect in $H_2O$. The bond dipole moment $\mu_2$ is first increasing with OH stretch vibrational excitation due to increase charge separation. When the $O$ and $H$ atoms are sufficiently far enough, the electronic charge are redistributing both along the OH chemical bond and around the nuclei. The bond dipole moment $\mu_2$ is then increasing.
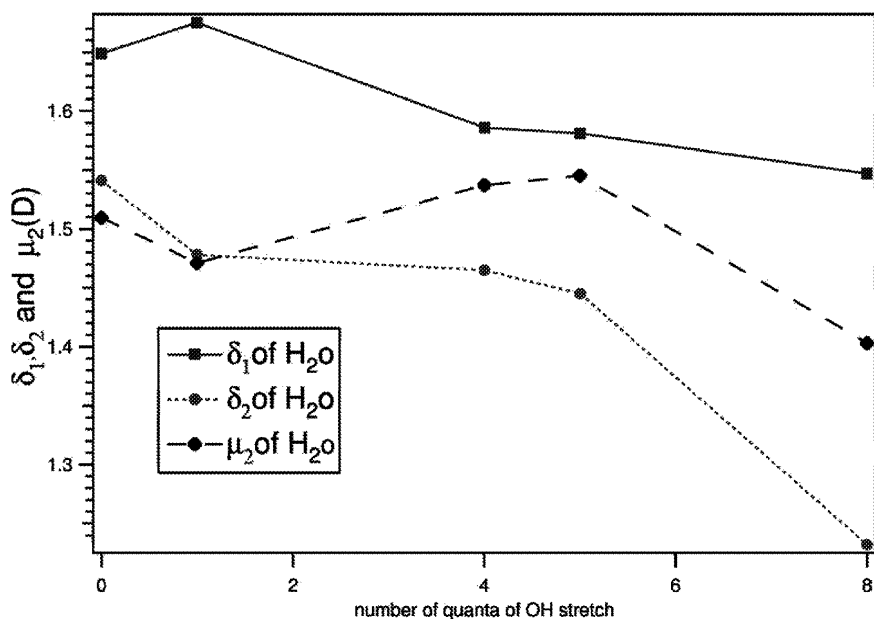
**Figure 5.15:** Charge redistribution along bond 1 and bond 2 as bond 2 is elongated for H$_2$O. $\delta_2$ (dotted line), the difference of charge along bond 2, is decreasing when bond length 2 is increasing, since a part of the electronic charge along bond 2 is taken back by the atoms. $\delta_1$ (full line), the difference of charge along bond 1, is slightly decreasing since a part of the electronic charge is taken back by the O atoms and thus transferred to the unstretched bond 1.
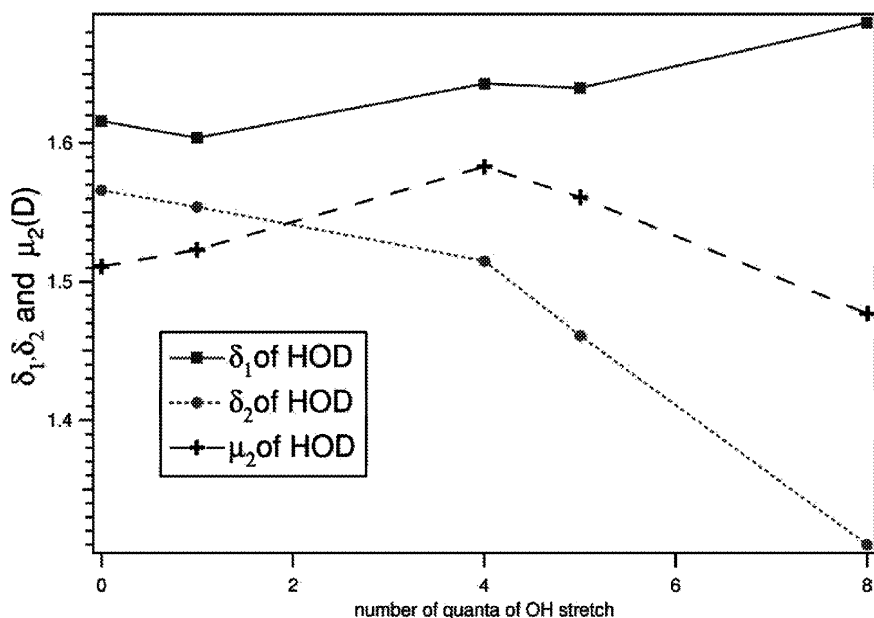


**Figure 5.16:** Charge redistribution along bond 1 and bond 2 as bond 2 is elongated for HDO, $\delta_2$ (dotted line), the difference of charge along bond 2 is decreasing when bond length 2 is increasing since a part of the electronic charge along bond 2 is taken back by the atoms. $\delta_1$ (full line), the difference of charge along bond 1, is almost constant, thus the electronic charge transferred from the stretched bond to the unstretched bond, bond 1, is smaller.

The first thing we can learn from this is that the contribution $\mu_2$ to the total dipole moment from bond 2 is quite similar to the one in the previous model, and that there is little change in $\delta_1$ compared to the change in $\delta_2$. This means that the charge redistribution upon bond elongation mainly takes place along the stretched bond. The charge redistribution from the elongated bond to the other bond is smaller. It is moreover important to note that the sum $\delta_1 + \delta_2$ need not be conserved since it represents rather a difference of charge, or a difference to homogeneous charge distribution along the bond than a point charge.

Looking closer, we can see that as expected, the difference of charge $\delta_2$ along bond 2 is decreasing, and a part of this difference of charge is transferred to bond 1. For HDO, it is clear that as $\delta_2$ is decreasing, $\delta_1$ is increasing. At $v_{OH} = 8$, $\mu_1^{v=8} = \delta_1^{v=8}*r_1^{v=8} = 0.957*1741 = 1.666\ D$ has almost reached the value of the dipole moment of the OD fragment. Therefore, in full agreement with our intuitive model of the covalent bond elongated, a part of the electronic charge is taken back by the O atoms and thus transferred to the remaining bond, and the electrons shared in the covalent bond are recovered when the H atom goes to infinity. The situation for $H_2O$ is not so clear, as if $\delta_2$ is decreasing, $\delta_1$ seems to decrease as well, since the two H atoms are equivalent and tunneling occurs.

### 5.4.3 Comparison with ab-initio calculations.

**Calculated Stark coefficients**

Following the same procedure we used in Section 5.3.2 to get experimental Stark coefficients from dipole moment matrix elements, it is possible to calculate the theoretical Stark coefficients using Eq. 5.40 for an asymmetric rotor in which the relevant matrix elements are calculated from an *ab initio* PES and DMS. We have for the Stark shift

$$\Delta W^{(2)}_{\alpha JK_aK_cM} = \sum_{X=a,b,c} \sum_{\alpha' J' K_a' K_c'} \frac{|\langle \alpha' J' K_a' K_c' M' | \mu_X | \alpha JK_aK_cM \rangle|^2 E^2}{W^0_{\alpha JK_aK_c} - W^0_{\alpha' J' K_a' K_c'}} \tag{5.40}$$

$$= (A_{\alpha JK_aK_c} + B_{\alpha JK_aK_c}M^2)E^2 \tag{5.41}$$

Considering all the rovibrational levels $|\alpha' J' K_a' K_c'\rangle$ that lie close in energy to $|\alpha JK_aK_c\rangle$ and have a strong transition dipole moment $\langle \alpha' J' K_a' K_c' M' | \mu_X | \alpha JK_aK_cM \rangle$ (*i.e.* elements of terms with $\frac{\mu_{ij}^2}{W_{ij}} > 10^{-4}$), we can calculate the Stark coefficient $C_{\alpha JK_aK_c}$ of the rovibrational state $|\alpha JK_aK_c\rangle$. A Stark coefficient $C_{\alpha JK_aK_c}$ is the difference of energy $\Delta W^{(2)}_{\alpha JK_aK_cM_2} - \Delta W^{(2)}_{\alpha JK_aK_cM_1}$ between the two $|\alpha JK_aK_cM_1\rangle$ and $|\alpha JK_aK_cM_2\rangle$ states coherently populated. In order to calculate these theoretical Stark coefficients, we use experimental energy values. A compilation of all the numerous existing experimental energy levels, mainly from Camy-Peyret and Flaud [33] and more recent works [34, 35], can be found at http://www.tampa.phys.ucl.ac.uk/jonny/waterlevels.html, or in Ref. [36]. Some of the $(80)^+$ terms values were missing and have been measured using our wavemeter calibrated with an opto-galvanic lamp.

The *ab initio* transition dipole moment matrix elements were calculated by Prof. Jonathan Tennyson's group at University College of London. In the variational procedure employed for the calculations reported here, the accuracy of the wavefunction of the individual rotation-vibration states is determined by the potential energy surface (PES). The calculation of accurate dipole matrix elements relies on having both accurate wavefunctions and an accurate dipole moment surface (DMS), it is therefore necessary to consider the accuracy of both the PES and DMS when considering the reliability of any calculated dipole moment matrix elements. Tennyson and co-workers chose a PES and DMS and used the variational program DVR3D [37] to calculate these dipole moment matrix elements. The calculations have been performed with various combinations of Partridge and Schwenke's PES [38], a newly fitted PES [39], the DMS of Partridge and Schwenke [40] and the revised DMS of Schwenke and Partridge [38]. Each combination gives surprisingly similar results, with different $C_{\alpha J K_a K_c}$ values agreeing with each other to within 1%. The $C_{\alpha J K_a K_c}$ values obtained from the most recent PES [39] and the revised DMS [38] are considered the most accurate and are listed in Table 5.15 [5]. What we call theoretical Stark coefficients are "half theoretical", since the denominators are determined from experimental energy values. Because of the high energy of the vibrational states investigated here, the Stark coefficients, both experimental and calculated, are sensitive to the PES and DMS at configurations far from equilibrium, and therefore, these comparisons should provide stringent tests of vibrational wavefunctions and dipole moment surfaces. For example the $(8,0)^+$ wavefunction, which is halfway to dissociation of the OH bond, span a large volume of the DMS and PES since it has classical turning points extending from $-0.25$ Å to $+0.6$ Å along the $r_2$ coordinate.

The calculated Stark coefficients differ from our measured values by up to $-25.69\%$ for the $1_{10}$ rotational level of the $|4,0^-\rangle|2\rangle$, or by $-9.2\%$ for the $1_{11}$ rotational level of the $|4,0^-\rangle$. These states that are the most sensitive to $\mu_a$, because of the a-type $1_{11} - 1_{10}$ interaction, and $1_{10}$ of $|4,0^-\rangle|2\rangle$ is extremely sensitive to $\mu_a$ since this level is almost degenerate with $1_{11}$ of

---

[5] **Note for water $|40^+2\rangle$:** it has been found during the analysis of water $|4,0^+2\rangle$ that the lines assigned in Ref. [34] as $^RP_0(2)$ at $16795.04477$ $cm^{-1}$ and $^PP_2(2)$ at $16728.92213$ $cm^{-1}$ did not match correctly the combination difference with the ground state, and that therefore the $|4,0^+2\rangle$ $1_{11}$ was not correctly determined. After a new fit of the lines mentioned above and subsequent analysis, a new assignement has been proposed by Olga Naumenko (*Institute of Atmospheric Optics, Russian Academy of Sciences, Tomsk, Russia*) from the work of Ref. [41], defining $1_{11}$ from two lines $^PP_2(2)$ at $16728.92213$ $cm^{-1}$ and $^RR_0(0)$ at $16864.6174$ $cm^{-1}$, an assignement confirmed from both combination differences and intensity arguments (from line intensities calculated by Schwenke). This assignement has also been proposed independently by Nikolai Zobov (*Institute of Applied Physics, Russian Academy of Science, Nizhnii Novgorod, Russia*). We thus take the energy of the $|4,0^+2\rangle$ $1_{11}$ level to be $16864.6207$ $cm^{-1}$. The position in energy of $|4,0^+2\rangle$ $1_{11}$ is a crucial issue, since an accidental resonance occurs with $|4,0^-2\rangle$ $1_{10}$ at $16865.017813$ $cm^{-1}$, making the interaction term between the those two levels, and thus the Stark coefficient calculated for $|4,0^-2\rangle$ $1_{10}$, very sensitive to $\mu_a$. Therefore, this accidental resonance will magnify any mistake on the a component of the dipole moment, as it is clearly seen in Table 5.15.

| $\lvert n,0^{\pm}\rangle\lvert b\rangle$ | $J_{K_a K_c}$ | $C^{obs}\left(Hz.(V/cm)^{-2}\right)$ | $C_1^{calc}$ | $\left(\frac{calc_1-obs}{obs}\right)(\%)$ |
|---|---|---|---|---|
| $\lvert 4,0^-\rangle$ | $1_{01}$ | 0.4372(8) | 0.4413 | 0.95% |
| $\lvert 4,0^-\rangle$ | $1_{11}$ | 0.3160(9) | 0.2871 | -9.2% |
| $\lvert 4,0^-\rangle$ | $1_{10}$ | 0.5097(10) | 0.5060 | 0.72% |
| $\lvert 4,0^-\rangle\lvert 2\rangle$ | $1_{01}$ | 0.3153(26) | 0.31996 | 1.46% |
| $\lvert 4,0^-\rangle\lvert 2\rangle$ | $1_{11}$ | 0.2137(39) | 0.2164 | 1.26% |
| $\lvert 4,0^-\rangle\lvert 2\rangle$ | $1_{10}$ | 0.6306(27) | 0.4686 | -25.68% |
| $\lvert 5,0^-\rangle$ | $1_{01}$ | 0.4277(7) | 0.4343 | 1.50% |
| $\lvert 5,0^-\rangle$ | $1_{11}$ | 0.3032(7) | 0.2849 | -6.1% |
| $\lvert 5,0^-\rangle$ | $1_{10}$ | 0.5077(4) | 0.4996 | -1.6% |
| $\lvert 8,0^+\rangle$ | $1_{01}$ | 0.4953(16) | 0.5058 | 2.1% |
| $\lvert 8,0^+\rangle$ | $1_{11}$ | 0.4250(10) | 0.4154 | -2.3% |
| $\lvert 8,0^+\rangle$ | $1_{10}$ | 0.6657(38) | 0.6667 | 0.20% |

**Table 5.15:** Comparison between observed and calculated Stark coefficients for $H_2O$. Stark coefficients are in units of $(Hz.(V/cm)^{-2})$. Observed Stark coefficients are directly determined from the modulation frequency of the OH LIF by the Stark electric field. Calculated Stark coefficients $C_1^{calc}$ are constructed using Eq. 5.40, experimental energy levels and ab-initio dipole moment matrix elements calculated using the SPZBT PES and the new Partridge and Schwenke DMS.
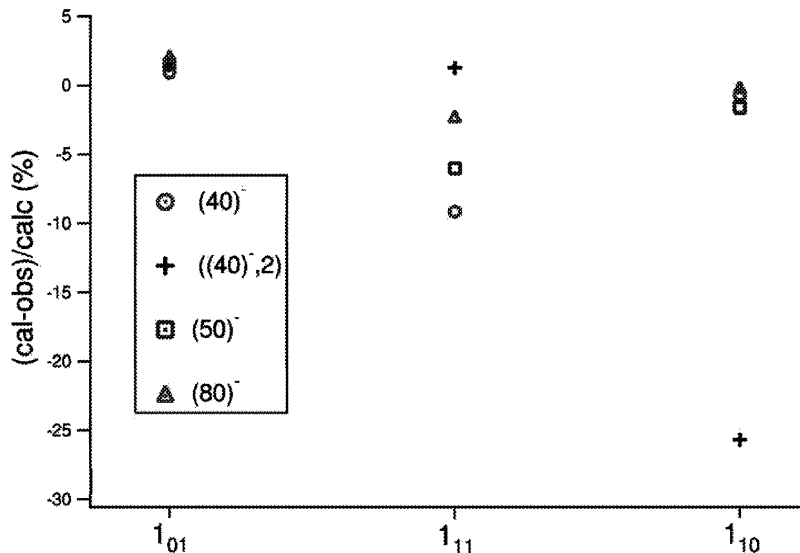


**Figure 5.17:** Comparison between observed Stark coefficients and calculated Stark coefficients reported in Table 5.15 for the $J = 1$ rovibrational levels of different vibrational states of $H_2O$. There is a systematic discrepancy between calculated and observed Stark coefficients for the $1_{11}$ level because the a-type $\lvert 4,0^-\rangle\, 1_{11} - \lvert 4,0^+\rangle\, 1_{10}$ interaction is dominant in the Stark coefficients since these two rovibrational levels are close in energy. Moreover, the highest discrepancy is observed between for $\lvert 4,0^-2\rangle\, 1_{10}$ since $\lvert 4,0^-2\rangle\, 1_{10}$ and $\lvert 4,0^+2\rangle\, 1_{11}$ are very close in energy. This indicates that the origin of the discrepancy is mainly due to the a component of the dipole moment.

$|4, 0^+\rangle|2\rangle$ (see Fig. 5.6). Moreover as the $s - a$ splitting decreases when going to more quanta of OH stretch, the difference in energy between the $1_{11}$ level of the $|-\rangle$ state and the $1_{10}$ level of the $|+\rangle$ state increases and the $\mu_a$ contribution becomes smaller, since the energy denominator of this corresponding term in the Stark effect expression increases. This causes the difference between the observed and calculated Stark coefficients to go from 9.2% to 2.25% when going from $|4, 0^-\rangle$ to $|8, 0^+\rangle$. These discrepancies do not arise from coincidental connections to other close-lying vibrational states, since the nuclear motion calculations explicitly include all these interactions.

These systematic differences listed in Table 5.15 can arise from either the dipole moment surface or the wavefunctions, since Stark effect is described as a summation of dipole moment matrix elements squared over the energy difference. As we took highly accurate experimental energy levels, this cannot be the source of the discrepancy. A dipole moment matrix element is the integral of the dipole moment vector operator, coming from the *ab initio* dipole moment surface, over the wavefunctions of two states, which come from solving, in the Born-Oppenheimer approximation, the nuclear Schrödinger equation of the vibration-rotation molecular Hamiltonian [29] using potential energy coming from ab-initio potential energy surfaces. This focuses attention both on limitations of the ab-initio surfaces used and on calculated wavefunctions.

Four different calculations using two different potential and two different dipole surfaces give very similar results. The two potential surfaces used are completely independent from one another, while the two dipole surfaces are different analytical fits of the same set of dipole moment calculations. This might suggest that the source of discrepancy with experiment is related to the DMS. New ab initio calculations made by Polyanski et al.[6], yet unpublished, with large augmented basis sets (aug-cc-pV6Z) suggest that the Partridge and Schwenke dipole surfaces systematically underestimate the water dipole moment for molecular configurations far from equilibrium, and these are precisely the geometries probed in the current experiments as one bond is extended. This is an important issue since these are the molecular geometries that contribute to short wavelength atmospheric water absorption, which is pertinent to atmospheric modeling.

The systematic underestimation of the a-component of the dipole moment could give us some hints to the source of the problem. We have already said that *ab initio* calculations of dipole moments converge differently than those of energies, since they do not obey the variational principle, and calculations that give comparable energies can give different moments, with various methods and basis sets producing transition moments that differ by as much as a factor of two. This problem is mainly due to the fact that experimentally we just have access to the average values of observables, that is the integration of the operator over two wavefunctions (that is $\int \psi_i \vec{H} \psi_j$ or $\int \psi_i \vec{\mu} \psi_j$). If we can, following the variational principle, determine wavefunctions by making the calculated averaged energies converge better and better to ex-

perimental energy levels, this does not ensure that the spatial distribution of the wavefunction is correct. If the spatial extension of the wavefunctions has not been correctly determined by the variational principle, this will be seen in overtone transitions intensities, or in Stark coefficients, calculations for which we need dipole moment matrix elements. When going to high excited vibrational levels, the wavefunction probability density is increasing at the inner and outer turning points. Therefore the more excited the molecule is, the larger configuration space the wavefunction spans, and the more important the spatial distribution of the wavefunction in region of large amplitude motion is. The increased probability density in those regions of the configuration space far from equilibrium makes the dipole moment matrix elements, and thus the Stark coefficients, very sensitive to the wavefunctions spatial distribution in those regions far from equilibrium. Since $\mu_a$ connects two wavefunctions with different spatial distribution and orientation it is reasonable to suspect the spatial overlap of these two wavefunctions to be in cause. The spatial overlap being directly related to the two molecule-fixed frames orientations, we suspect those frames to not be correctly oriented.

All these considerations above point up the necessity of very accurate PES and DMS precisely in the regions far from equilibrium and make these experimental results critical benchmarks to test and correct PES and DMS, as well as the spatial orientation and amplitude distribution of the wavefunctions in these regions. The difference between observed and calculated Stark coefficients is interesting because it may allow us to correct the dipole moment matrix elements calculations. We shall now try to investigate this difference.

### The instantaneous inertial frame model

As we saw previously, the inertial defect, and the uncertainty of the geometry of the molecule it leads to, prevent us from doing more than qualitative models, which, if they confirm our intuition and give physical meaning to the quantities we measure, do not allow us to explain where a few percentages difference between observed and calculated Stark coefficients is coming from. To discriminate among the different assumptions we made above, we will use a simple model [6] that takes better into account the dynamics of the problem.

For doing so, we will try to reproduce our experimental dipole moments, using the *ab-initio* dipole moment surface of Partridge and Scwhenke [42, 38] to test the DMS and the tilt

---

[6] This instantaneous inertial frame model has been made at a time we were considering that the molecule-fixed frame the dipole moment vector is expressed in, was the principal inertial axis system instead of the Eckart frame averaged over a vibrational period. This is not correct. However, the arguments relative to the orientation of the wavefunctions with respect to one another and with respect to the DMS are still valid and relevant. Moreover, this work leads to a deeper reinvestigation of the relative orientation of the different axis systems. In the end it turned out that the origin of the difference between experimental and calculated Stark coefficients really was a problem of correctly orientating the molecule-fixed frame with respect to the DMS. For these reasons, this section on the instantaneous inertial frame model is left in this Chapter.

|   | experimental | calculation 1 | calculation 2 |
|---|---|---|---|
| A | 19.4426 | 19.4427 | 19.7213 |
| B | 9.0577 | 9.0509 | 9.3646 |
| C | 6.0934 | 6.0941 | 5.9658 |

**Table 5.16:** $H_2O$ rotational constants derived from the instantaneous inertial frame model. For every instantaneous position of the nuclei during the vibrational motion, instantaneous rotational constants are determined from the instantaneous inertia tensor. Instantaneous rotational constants are then averaged over the vibrational motion and compared to experimental rotational constants. Calculated 1 rotational constants are determined using $r_1 = 0.9375\text{Å}$ and $\theta = 100.20°$. Calculated 2 rotational constants are determined using $r_1 = 0.957\text{Å}$ and and physically reasonable $\theta(r_2)$.

of the molecule-fixed frame. We will approximate the OH stretch ($r_2$) as Morse oscillator, and the unexcited bond ($r_1$) as an harmonic oscillator in its fundamental state (*i.e.* $r_1$ is fixed). The bending angle $\theta_{132}$ will be either fixed or considered as undergoing harmonic motion whith average value determined from the Partridge and Schwenke Potential Energy Surface (PES) [40, 38], following the minimum energy path when $r_2$ is stretched. We introduce thus a $\theta(r_2)$ dependence.

Since the time scale for tunneling is larger than the time scale of rotation, we can separate these motions, by defining at each instantaneous position $r_2$ an instantaneous position of the inertial frame and instantaneous angular momentum. We can calculate the expectation value of any operator $\hat{O}$ by integrating over the Morse oscillator variable $r_2$, that is:

$$\overline{O} = \int \psi^*_{Morse}(r_2)\hat{O}(r_2)\psi^*_{Morse}(r_2)dr_2 \tag{5.42}$$

At each $r_2$ position, the relation $I_c^{r_2} = I_a^{r_2} + I_b^{r_2}$ holds, and if we take $\hat{O} = \frac{1}{r^2}$ we can define a set of instantaneous rotational constants $A^{r_2}$, $B^{r_2}$ and $C^{r_2}$. If we take $r_1 = 0.9375\text{Å}$ and $\theta = 100.20°$ we find a very good agreement with experimental rotational constants (calculation 1), as can be seen in Table 5.16. However, if we take physically reasonable values of $r_1 = 0.957\text{Å}$ and $\theta(r_2)$, the agreement is not so good (calculation 2). While we can reproduce better the inertial defect, and thus dynamics, it is still not perfect.

If we now set $\hat{O} = \mu_a$, $\hat{O} = \mu_b$ or $\hat{O} = \sqrt{\mu_a^2 + \mu_b^2}$, we can integrate the dipole moments over the Morse wavefunction. The Morse potential and wavefunctions parameters are determined by fitting the first experimental levels of HOD and $H_2O$ to the expressions given in Ref. [43]:

$$E_n = D - \left(\frac{a^2\hbar^2}{2\mu}\right)\left(\frac{\sqrt{2\mu D}}{a\hbar} - (m + \frac{1}{2})\right)^2 \tag{5.43}$$

where $\mu$ is the OH reduced mass, $D$ the dissociation limit and $a$ the inverse of a length. We can

write the Morse wavefunction as

$$|m\rangle = x^{(K-m-\frac{1}{2})} L_m(x)^{(2K-2m-1)} \exp -\frac{x}{2} \qquad (5.44)$$

$$\text{with:} \quad x = 2K \exp -a(r - r_{eq})$$

where $L_m(x)$ are the Laguerre polynomials.

***Results for HDO.*** As HDO is a much better localized oscillator, most of the work has been done on this molecule. By fitting vibrational levels up to $v_{OH} = 6$ we find the Morse parameters for HDO to be $a = 2.096(10)$ $\mathring{A}^{-1}$ and $D = 47566.3 \pm 274$ $cm^{-1}$, and by fitting levels up to $v_{OH} = 8$ we find $a = 2.125(10)$ $\mathring{A}^{-1}$ and $D = 46575 \pm 200$ $cm^{-1}$.

Despite much effort in changing the different parameters of the system ( $\theta(r_2)$ from the *ab-initio* PES, the enharmonicity of the Morse potential, or the $r_1$ length), it is not possible to reproduce the vibrational dependence of $\mu_b$ that we observe experimentally. Although the magnitude is reasonably reproduced, the partition of $\vec{\mu}$ between $\mu_a$ and $\mu_b$ is not. The results of the expectation values for $\mu_a$ and $\mu_b$ are not very sensitive to the Morse potential parameters, but are sensitive to the $\theta(r_2)$ dependence. As an example of the results such calculations can give, Table. 5.17 gives a set of $\mu_a$, $\mu_b$ and $\mu_T$ ($\langle \mu_t \rangle_{av.} \neq \sqrt{\mu_a^2 + \mu_b^2}$) obtained for $a = 2.132$ $\mathring{A}^{-1}$, $D = 45995$ $cm^{-1}$ and $r_1 = 0.957 \mathring{A}$, $\theta = -44.975$ $r_2 + 147.463$, along with experimental moments and dipole moment components corresponding to $r_2$ fixed to the average value of the corresponding Morse wavefunction. This corresponds to a single point on the DMS, that is, the *ab initio* moment of a rigid rotor whose inertial frame is correctly rotated in the DMS.

From the results above, it seems that probing the DMS at geometries relevant to the bond 2 extension gives better results for the magnitude of the dipole moment. The magnitude of the dipole moment is the same whatever the frame we take, independent of the tilt. Moreover, it is possible to reproduce the increase in $\mu_b$ if we rotate the inertial frame to the angle corresponding to the extended bond. If we now integrate over the region far around the expectation value we took as $r_2$ in the rigid rotor model, we see it is not possible to reproduce the increase in $\mu_b$. This could be a problem of spatial extension or orientation of the wavefunction. Figure 5.18 shows the sequence of positions of the inertial frame and the trend of $\mu_a$ and $\mu_b$ for different regions of the PES the wavefunction is spanning into when bond 2 is vibrating. In a classical picture the instantaneous inertial frame can see as tilting back and forth from step 1 to step 4 as the bond is vibrating, the bond length spanning the positions in between the inner and outer turning points of the PES. Step 4 is only reached for $v_{OH} = 8$, and most of the motion is between step 1 and 2. The two turning points are not equivalent, if the outer turning point increases $\mu_b$, the inner turning point decreases it. While it is not possible to reproduce exactly the experimental results, since the $\mu_a$ and $\mu_b$ calculated are dependent on the angular dependence $\theta(r_2)$ and anharmonicity of the Morse potential we choose, different calculations give the same conclusions.

|  |  | exp. | inst. frame | rigid rotor |
|---|---|---|---|---|
| (0,0,0) | $\mu_a$ | -0.6591(2) | -0.6707 | -0.663 |
|  | $\mu_b$ | -1.7304(5) | -1.7470 | -1.759 |
|  | $\mu_t$ | 1.8517(5) | 1.881 | 1.880 |
| (0,0,1) | $\mu_a$ | -0.6412(2) | -0.6639 | -0.646 |
|  | $\mu_b$ | -1.7528(5) | -1.7562 | -1.792 |
|  | $\mu_t$ | 1.8664(5) | 1.873 | 1.905 |
| (0,0,4) | $\mu_a$ | -0.5867(9) | -0.3504 | -0.604 |
|  | $\mu_b$ | -1.822(1) | -1.7391 | -1.866 |
|  | $\mu_t$ | 1.914(1) | 1.8784 | 1.966 |
| (0,0,5) | $\mu_a$ | -0.572(1) | -0.0106 | -0.590 |
|  | $\mu_b$ | -1.8292(9) | -1.7655 | -1.881 |
|  | $\mu_t$ | 1.917(1) | 1.8694 | 1.971 |
| (0,0,8) | $\mu_a$ | -0.571(1) | +0.4088 | -0.396 |
|  | $\mu_b$ | -1.828(1) | -1.5429 | -1.917 |
|  | $\mu_t$ | 1.915(1) | 1.8279 | 1.958 |

**Table 5.17:** Experimental dipole moment components for vibrationally excited states of HDO compared to calculated dipole moment components using ab-initio DMS along with the instantaneous frame model or with a rigid rotor model. In a rigid rotor model, the bending angle and bond length are fixed to their average value.

It seems that the DMS does not underestimate the dipole moment. However if the spatial extension of the wavefunction, and most particularly the tilt of the angle, is not correctly accounted for (which is probably the case in this instantaneous inertial frame model), the repartition between the $a$ and the $b$ component of the dipole moment is not reproduced. The magnitude of the total dipole moment, which is insensitive to the frame tilt, is not far off, even though it is decreasing in our model.

***Results for* H$_2$O.** When comparing qualitatively H$_2$O to HDO, and only considering the inertial contribution and the direction of frame tilt (see Fig. 5.19), we can understand the difference of sign of $\mu_a$ and the increase of $\mu_b$ in HDO, and corresponding decrease in H$_2$O. However, the same kind of calculations does not reproduce the experimental $\mu_a$ and $\mu_b$. Table 5.18 displays the experimental dipole moments along with the point in the DMS corresponding to a rigid rotor with $r_1 = r_e$, $\theta_1 = \theta_e$ and $r_2 = \langle \psi^v_{Morse} | r_2 | \psi^v_{Morse} \rangle$. The Morse parameters are taken to be for H$_2$O $a = 2.14$ $\mathring{A}^{-1}$ and $D = 47,500$ $cm^{-1}$. The $\theta$ angular dependence (in degrees) is taken to be $\theta(r_2) = -44.957 \, r_2 + 147.5$.

Note that in the rigid rotor model, an angular dependence other than $\theta_1 = \theta_e$ can give magnitudes similar to the observed ones but different between the $a$ and $b$ components of the dipole moments. The angular dependence is therefore a very critical parameter.
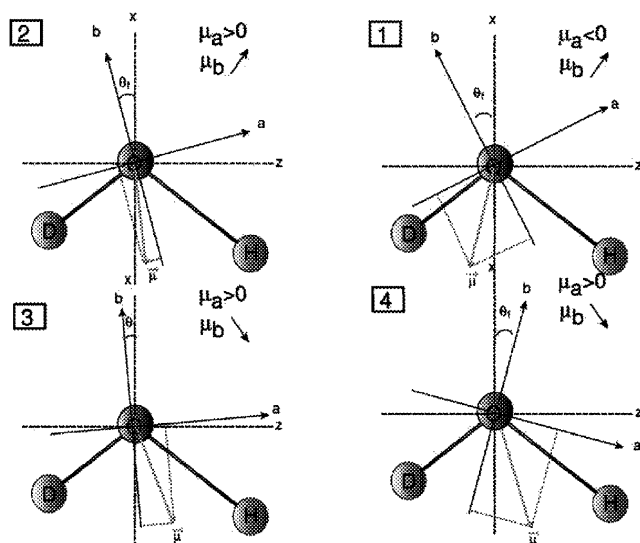
**Figure 5.18:** Position of the inertial frame and $\mu_a$ and $\mu_b$ trends for different position of $r_2$. During a bond 2 vibrational period, the molecule-fixed frame takes different orientation according to the position of the different nuclei. The molecule-fixed frame tilt being the main contribution to the dipole moment change, we can see that the configurations spanned by the molecule-fixed frame axis can be divided in several regions. In these different regions, $\mu_a$ is either positive or negative and $\mu_b$ either increases or decreases. Region 4 is only reached close to the outer turning point of $|0,0,8\rangle$.
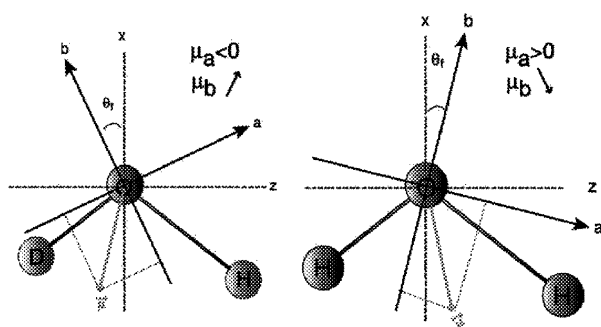


**Figure 5.19:** Comparison, between $H_2O$ and HDO, of the position of the inertial frame and the evolution trends for $\mu_a$ and $\mu_b$ when bond 2 length, $r_2$, is stretched during the bond 2 vibrational motion in a local basis. For both $H_2O$ and HOD, a stretched $r_2$ tilts the $b$ axis away from the $x$ axis in a clockwise direction. However, if for $H_2O$ $\mu_a$ starts to increase and $\mu_b$ to decrease, if for HDO $\mu_a$ starts to decrease and $\mu_b$ to increase.

|  |  | exp. | instant.fr. | rigid rotor |
|---|---|---|---|---|
| $|4,0^-\rangle$ | $\mu_a$ | 0.291 | 0.455 | 0.542 |
|  | $\mu_b$ | -1.874 | -1.809 | -1.644 |
|  | $\mu_T$ | 1.896 | 1.865 | 1.879 |
| $|5,0^-\rangle$ | $\mu_a$ | -0.344 | 0.523 | -0.603 |
|  | $\mu_b$ | -1.857 | -1.776 | -1.603 |
|  | $\mu_T$ | 1.889 | 1.851 | 1.870 |
| $|8,0^+\rangle)$ | $\mu_a$ | -0.584 | 0.611 |  |
|  | $\mu_b$ | -1.796 | -1.672 |  |
|  | $\mu_T$ | 1.889 | 1.761 | 1.816 |

**Table 5.18:** Experimental dipole moment components for vibrationally excited states of $H_2O$ compared to calculated dipole moment components using an *ab initio* DMS along with the instantaneous model or with a rigid rotor model. In a rigid rotor model, the bending angle and bond length are fixed to their average value.

Once again, while this level of modeling is not sufficient to reproduce the experimental dipole moment components and to make strong conclusions, it may seem that as for HDO the DMS does not underestimate dramatically the magnitude of the dipole moment. However, the inertial tilt is a very critical issue, which greatly affects a lot the repartition between the $a$ and $b$ components of the dipole moment. It therefore seems worth directing our effort to this inertial frame tilt issue, using a more sophisticated model.

## New calculated Stark coefficients

To use general dipole surfaces, the $DVR3D$ programs [37] needs to use internal coordinates for the wavefunction which are the same as those used to represent the dipole surface [28]. A closer reinvestigation of the code making this dipole moment rotation has been led by Pr. Tennyson. It has been found that the majority of the discrepancy shown in Table 5.15 was caused by the use of an incorrect embedding of the body-fixed axis system. This embedding is close to, but not the same as, the bisector embedding [37] used to compute the wavefunctions. As shown in Table 5.19, the use of the correct embedding significantly reduces these errors with respect to our measurements.

Dipole matrix elements have been computed using several combinations of PES and DMS. In particular the spectroscopically determined PES's of Partridge and Schwenke (PS) [40] and Shirin *et al* (SPZBT) [39] have been used. Calculations were performed using the ab initio DMS reported by PS [40] and their subsequent refit of the same ab initio data which we call newPS [42]. The calculations were performed using the new version of the $DVR3D$ program suite (unpublished) and well converged wavefunctions. This led to new sets of dipole moment

matrix elements, generated by the same *ab initio* DMS and PES. These new dipole moment matrix elements are used to get new calculated Stark coefficients, reported as $calc_2$, $calc_3$ and $calc_4$, which are compared with our observed Stark coefficients. $calc_2$ Stark coefficients come from Partridge and Schwenke's PES and DMS [42]. $calc_3$, $calc_4$, $calc_5$ Stark coefficients come from Shirin's SPZBT PES [39] and respectively Tennyson's DMS and the new [42] and old [40] fits of Partridge and Schwenke's DMS. Table 5.19 displays the quantity $\left(\frac{calc_{i=2,3,4,5}-obs}{obs}\right)$ (%) for the different combinations of *PES* and *DMS*. It can be seen in Table 5.19 that the agreement

| $\lvert n, 0^{\pm}\rangle \lvert b\rangle$ | $J_{K_aK_c}$ | $\left(\frac{calc_2-obs}{obs}\right)$ (%) | $\left(\frac{calc_3-obs}{obs}\right)$ (%) | $\left(\frac{calc_4-obs}{obs}\right)$ (%) | $\left(\frac{calc_5-obs}{obs}\right)$ (%) |
|---|---|---|---|---|---|
| $\lvert 4, 0^-\rangle$ | $1_{01}$ | 0.515 | 0.867 | 0.454 | 0.438 |
| $\lvert 4, 0^-\rangle$ | $1_{11}$ | 0.875 | 1.27 | 1.79 | 1.92 |
| $\lvert 4, 0^-\rangle$ | $1_{10}$ | 0.965 | 1.45 | 1.01 | 1.02 |
| $\lvert 4, 0^-\rangle\lvert 2\rangle$ | $1_{01}$ | 1.45 | 1.86 | 1.52 | 1.85 |
| $\lvert 4, 0^-\rangle\lvert 2\rangle$ | $1_{11}$ | -1.07 | -0.733 | -1.05 | -1.07 |
| $\lvert 4, 0^-\rangle\lvert 2\rangle$ | $1_{10}$ | -0.021 | 0.895 | 0.386 | 0.313 |
| $\lvert 5, 0^-\rangle$ | $1_{01}$ | 1.00 | 1.40 | 1.05 | 0.999 |
| $\lvert 5, 0^-\rangle$ | $1_{11}$ | 0.893 | 1.33 | 0.902 | 0.85 |
| $\lvert 5, 0^-\rangle$ | $1_{10}$ | 1.46 | 1.89 | 1.50 | 1.45 |
| $\lvert 8, 0^+\rangle$ | $1_{01}$ | 1.31 | 1.69 | 1.22 | 1.31 |
| $\lvert 8, 0^+\rangle$ | $1_{11}$ | 1.94 | 2.37 | 1.53 | 1.92 |
| $\lvert 8, 0^+\rangle$ | $1_{10}$ | 2.44 | 2.86 | 2.17 | 2.43 |

**Table 5.19:** Comparison between experimental and calculated Stark coefficients from different ab-initio PES and DMS. $calc_2$ Stark coefficients come from Partridge and Schwenke's PES and DMS . $calc_3$, $calc_4$, $calc_5$ Stark coefficients come from Shirin's SPZBT PES and respectively Tennyson's DMS and the new and old fits of Partridge and Schwenke's DMS.

between observed and calculated Stark coefficients is now much better, around 1%. A closer look at Table 5.19 shows a slight but systematic overestimation of the experimental Stark coefficients. Moreover, the Stark coefficients for $v_{OH} = 8$ seem to be slightly worse than those for lower $v_{OH}$. We hope that new calculations will be able to get an even better agreement to our observed Stark coefficients.

## 5.5   Summary

We showed in this Chapter how its has been possible to measure the dipole moments for the $\lvert 0, 0, 4\rangle$, $\lvert 0, 0, 5\rangle$ and $\lvert 0, 0, 8\rangle$ states of HDO and for the $\lvert 4, 0^-\rangle$, $\lvert 4, 0^-\rangle\lvert 2\rangle$, $\lvert 5, 0^-\rangle$, and $\lvert 8, 0^+\rangle$ states of $H_2O$. We demonstrated that the evolution of the dipole moment with vibrational excitation could not be described by the usual perturbative dipole moment function and that the tilt of the molecule-fixed frame accounted for the most part of the dipole moment rotation

in the molecule plane. Moreover, we saw that the charge redistribution mainly occurs along the vibrationally excited bond, and that the dipole moment along the OH bond increases, levels off, and then turns around for OH bond lengths far from equilibrium. We also compared our measured Stark coefficients with those calculated from *ab initio* PES and DMS. We showed that it was possible to improve the calculation of transition dipole moments by correctly rotating the molecular frame of the rovibrational wavefunctions. We tested several *ab initio* PES and DMS and showed that the agreement with experimental data is good.

# References

[1] P. F. Bernath. The spectroscopy of water vapor: Experiment, theory and applications. *Physical Chemistry Chemical Physics*, 4(9):1501–1509, 2002.

[2] M. D. Chou. Atmospheric solar heating in minor absorption bands. *Terrestrial Atmospheric and Oceanic Sciences*, 10(3):511–528, 1999.

[3] L. P. Giver, C. Chackerian, and P. Varanasi. Visible and near-infrared $h_2o$-o-16 line intensity corrections for *hitran* − 96. *Journal of Quantitative Spectroscopy & Radiative Transfer*, 66(1):101–105, 2000.

[4] W. Y. Zhong, J. D. Haigh, D. Belmiloud, R. Schermaul, and J. Tennyson. Note on 'the impact of new water vapour spectral line parameters on the calculation atmospheric absorption' by wenyi zhong *et al.* (july a, 2001, 127, 1615-1626). *Quarterly Journal of the Royal Meteorological Society*, 128(582):1387–1388, 2002.

[5] W. Y. Zhong and J. D. Haigh. Shortwave radiative forcing by stratospheric water vapor. *Geophysical Research Letters*, 30(3):art. no.–1113, 2003.

[6] O. L. Polyansky, A. G. Csaszar, S. V. Shirin, N. F. Zobov, P. Barletta, J. Tennyson, D. W. Schwenke, and P. J. Knowles. High-accuracy ab initio rotation-vibration transitions for water. *Science*, 299(5606):539–542, 2003.

[7] R. A. Toth. Measurements of hdo between 4719 and 5843 $cm^{-1}$. *Journal of Molecular Spectroscopy*, 186(2):276–292, 1997.

[8] R. A. Toth. Line positions and strengths of hdo between 6000 and 7700 $cm^{-1}$. *Journal of Molecular Spectroscopy*, 186(1):66–89, 1997.

[9] K. K. Lehmann. The interaction of rotation and local mode tunneling in the overtone spectra of symmetrical hydrides. *Journal of Chemical Physics*, 95(4):2361–2370, 1991.

[10] F. F. Crim. Bond-selected chemistry: Vibrational state control of photodissociation and bimolecular reaction. *Journal of Physical Chemistry*, 100(31):12725–12734, 1996.

[11] R. L. Vanderwal, J. L. Scott, and F. F. Crim. State resolved photodissociation of vibrationally excited water - rotations, stretching vibrations, and relative cross-sections. *Journal of Chemical Physics*, 94(3):1859–1867, 1991.

[12] R. L. Vanderwal, J. L. Scott, F. F. Crim, K. Weide, and R. Schinke. An experimental and theoretical-study of the bond selected photodissociation of HOD. *Journal of Chemical Physics*, 94(5):3548–3555, 1991.

[13] David A. Dahl. Simion $3d$ version 6.0. Technical report, Idaho National engineering Laboratory.

[14] J. Y. Mandin, J. P. Chevillard, C. Camy-Peyret, J. M. Flaud, and J. W. Brault. The high-resolution spectrum of water-vapor between 13200 and 16500 $cm^{-1}$. *Journal of Molecular Spectroscopy*, 116(1):167–190, 1986.

[15] C. Camy-Peyret, J. M. Flaud, J. Y. Mandin, J. P. Chevillard, J. Brault, D. A. Ramsay, M. Vervloet, and J. Chauville. The high-resolution spectrum of water-vapor between 16500 and 25250 $cm^{-1}$. *Journal of Molecular Spectroscopy*, 113(1):208–228, 1985.

[16] O. Naumenko, E. Bertseva, and A. Campargue. The $4v_{OH}$ absorption spectrum of HDO. *Journal of Molecular Spectroscopy*, 197(2):122–132, 1999.

[17] E. Bertseva, O. Naumenko, and A. Campargue. The 5 $v_{OH}$ overtone transition of HDO. *Journal of Molecular Spectroscopy*, 203(1):28–36, 2000.

[18] N. F. Zobov, D. Belmiloud, O. L. Polyansky, J. Tennyson, S. V. Shirin, M. Carleer, A. Jenouvrier, A. C. Vandaele, P. F. Bernath, M. F. Merienne, and R. Colin. The near ultraviolet rotation-vibration spectrum of water. *Journal of Chemical Physics*, 113(4):1546–1552, 2000.

[19] C.H. Townes and A.L. Schawlow. *Microwave Spectroscopy*. Dover Publications, New York, 1975.

[20] H. M. Pickett. The fitting and prediction of vibration-rotation spectra with spin interactions. *Journal of Molecular Spectroscopy*, 148(2):371–377, 1991.

[21] S. L. Shostak, W. L. Ebenstein, and J. S. Muenter. The dipole-moment of water .1. dipole-moments and hyperfine properties of $H_2O$ and HDO in the ground and excited vibrational-states. *Journal of Chemical Physics*, 94(9):5875–5882, 1991.

[22] Philip R. Bunker and Per Jensen. *Molecular Symmetry and Spectroscopy*. NRCC, Ottawa,Ont., second edition, 1998.

[23] M. S. Child and R. T. Lawton. Local mode degeneracies in the vibrational-spectrum of $H_2O$. *Chemical Physics Letters*, 87(3):217–220, 1982.

[24] M. S. Child and L. Halonen. Overtone frequencies and intensities in the local mode picture. *Advances in Chemical Physics*, 57:1–58, 1984.

[25] M. S. Child and R. T. Lawton. Local and normal vibrational-states - a harmonically coupled anharmonic-oscillator model. *Faraday Discussions*, 71:273–285, 1981.

[26] M.R. Aliev and J.K.G. Watson. *High-order effects in the vibration-rotation spectra of semi-rigid molecules, Molecular Spectroscopy: Modern Research*, volume III, pages 2–67. Academic Press, Orlando, Fla., 1985.

[27] S. L. Shostak and J. S. Muenter. The dipole moment of water .2. analysis of the vibrational dependence of the dipole moment in terms of a dipole moment function. *Journal of Chemical Physics*, 94(9):5883–5890, 1991.

[28] C. R. Lesueur, S. Miller, J. Tennyson, and B. T. Sutcliffe. On the use of variational wave-functions in calculating vibrational band intensities. *Molecular Physics*, 76(5):1147–1156, 1992.

[29] C. Camy-Peyret and J. M. Flaud. *Vibration-rotation dipole moment operator for asymmetric rotors, Molecular Spectroscopy: Modern Research*, volume III, pages 69–110. Academic Press, Orlando, Fla., 1985.

[30] H. Meyer. The molecular hamiltonian. *Annual Review of Physical Chemistry*, 53:141–172, 2002.

[31] F. C. Delucia, R. L. Cook, P. Helminge, and W. Gordy. Millimeter and submillimeter wave rotational spectrum and centrifugal distortion effects of HDO. *Journal of Chemical Physics*, 55(11):5334, 1971.

[32] J. M. Flaud. *Etude vibrorotationnelle de la molécule* $H_2O$. Thèse de doctorat, Université Pierre et Marie Curie, Paris, Paris, 1975.

[33] J. M. Flaud, C. Camy-Peyret, and R.A. Toth. *Water vapor line parameters from microwave to medium infrared*. Pergamon, Oxford, UK, 1981.

[34] M. Carleer, A. Jenouvrier, A. C. Vandaele, P. F. Bernath, M. F. Merienne, R. Colin, N. F. Zobov, O. L. Polyansky, J. Tennyson, and V. A. Savin. The near infrared, visible, and near ultraviolet overtone spectrum of water. *Journal of Chemical Physics*, 111(6):2444–2450, 1999.

[35] H. Naus, W. Ubachs, P. F. Levelt, O. L. Polyansky, N. F. Zobov, and J. Tennyson. Cavity-ring-down spectroscopy on water vapor in the range 555 − 604 *nm*. *Journal of Molecular Spectroscopy*, 205(1):117–121, 2001.

[36] J. Tennyson, N. F. Zobov, R. Williamson, O. L. Polyansky, and P. F. Bernath. Experimental energy levels of the water molecule. *Journal of Physical and Chemical Reference Data*, 30(3):735–831, 2001.

[37] J. Tennyson, J. R. Henderson, and N. G. Fulton. *dvr3d* - for the fully pointwise calculation of ro-vibrational spectra of triatomic-molecules. *Computer Physics Communications*, 86(1-2):175–198, 1995.

[38] D. W. Schwenke. Beyond the potential energy surface: *Ab initio* corrections to the born-oppenheimer approximation for $H_2O$. *Journal of Physical Chemistry A*, 105(11):2352–2360, 2001.

[39] S. V. Shirin, O. L. Polyansky, N. F. Zobov, P. Barletta, and J. Tennyson. Spectroscopically determined potential energy surface of $h_2o - o - 16$ up to 25 000 $cm^{-1}$. *Journal of Chemical Physics*, 118(5):2124–2129, 2003.

[40] H. Partridge and D. W. Schwenke. The determination of an accurate isotope dependent potential energy surface for water from extensive ab initio calculations and experimental data. *Journal of Chemical Physics*, 106(11):4618–4639, 1997.

[41] P. F. Coheur, S. Fally, M. Carleer, C. Clerbaux, R. Colin, A. Jenouvrier, M. F. Merienne, C. Hermans, and A. C. Vandaele. New water vapor line parameters in the 26000 − 13000 $cm^{-1}$ region. *Journal of Quantitative Spectroscopy & Radiative Transfer*, 74(4):493–510, 2002.

[42] D. W. Schwenke and H. Partridge. Convergence testing of the analytic representation of an *ab initio* dipole moment function for water: Improved fitting yields improved intensities. *Journal of Chemical Physics*, 113(16):6592–6597, 2000.

[43] I. A. Watson, B. R. Henry, and I. G. Ross. Local mode behavior - the morse oscillator model. *Spectrochimica Acta Part A-Molecular and Biomolecular Spectroscopy*, 37(10):857–865, 1981.

# Chapter 6

# Conclusion and perspective.

In this work, electric dipole moments of highly excited vibrational states of $H_2CO$, HOCl, HDO, and $H_2O$, have been measured using either frequency or time domain techniques based on Stark effect. The results are summarized in Table 6.1.

| | HOCl (400) |
|---|---|
| $\mu_b$ $(D)$ | 1.562(9) |

| | $H_2CO$ | |
|---|---|---|
| | $1_1$ | $5_2$ |
| $\mu_a(D)$ | 2.2944(5) | 2.2936(30) |

| | HDO | | |
|---|---|---|---|
| | (004) | (005) | (008) |
| $\mu_a(D)$ | 0.5867(9) | 0.572(1) | 0.571(1) |
| $\mu_b(D)$ | 1.822(1) | 1.8292(9) | 1.828(1) |

| | $H_2O$ | | | |
|---|---|---|---|---|
| | $\lvert 4,0^-\rangle$ | $\lvert 4,0^-\rangle\lvert 2\rangle$ | $\lvert 5,0^-\rangle$ | $\lvert 8,0^+\rangle$ |
| $\mu_a(D)$ | 0.299(3) | 0.37743(51) | 0.354(3) | 0.600(7) |
| $\mu_b(D)$ | 1.926(2) | 1.80005(222) | 1.909(1) | 1.846(5) |

**Table 6.1:** List of all the dipole moments measured in this work for different vibrationally excited states of HOCl, $H_2CO$, HDO and $H_2O$.

The values that we have determined must be added to the list of dipole moment measurements for these molecules in their ground and first excited vibrational states, and to the very

few measurements performed on highly excited vibrational states. Due to the rarity of dipole moment data for highly excited vibrational states, and to the importance of dipole moment for transition intensities, intermolecular forces and collisions, these measurements are extremely valuable, particularly for probing regions of the dipole moment surface at geometries far from equilibrium. Highly excited molecules are of special importance for chemical and energy transfer processes in atmospheric sciences, combustion studies, planetology, and more generally in the whole quantitative spectroscopy field, where transitions intensities are at least as important as line positions. For example, geometries far from equilibrium contribute to short wavelength atmospheric water absorption [1, 2], since the sun, a 5500 K star, has its peak emission in the visible. Thus, these measurements are, albeit indirectly, very important for helping understanding global climatology, since substantial controversies exist concerning the solar radiation budget [3]. Moreover, experimental Stark coefficients can be compared to those determined from *ab initio* dipole moment and potential energy surfaces, and this comparison provides a correction method for these ab-initio surfaces and establishes critical benchmarks for future improvements.

The techniques used here to measure dipole moments can be compared with other existing methods such as direct intensity measurements, the most common measurement technique of quantitative spectroscopy, or *ab initio* calculations from which intensity data is derived. In terms of accuracy and insensitivity to sample conditions, the methods used in this work are by far superior to other approaches. However they have severe limitations:

- They are heavy experiments to carry out, requiring the simultaneous use of several lasers in addition to microwave generators for the frequency domain experiments. The experiments are non trivial and slow to implement. This constraint prevents a fast and extensive study of dipole moments of numerous excited states.

- Substantial spectroscopic work has to be done before applying this technique to determine the energies of the rotational levels of the investigated excited vibrational state. One must be able to identify the rovibrational levels that one wants to study and determine the laser frequencies needed for each step of the multiple laser experiment. In general, the higher the energy of the vibrational state in question, the smaller the chance that spectroscopic work has already been done on it. Because dipole moments are derived from Stark coefficients by taking into account all the interaction with all the other nearby rovibrational states the positions in energy of these interacting states must be known to a sufficient accuracy. Since all levels are not spectroscopically accessible by the same technique (CRDS, FTIR or double-resonance), several techniques must be combined to get all the required information. Fortunately the vibrational mixing may play in our favor and allow energy of the dark states to be determined. The limited amount of high resolution spectroscopic data on highly excited vibrational states available in the literature restricts

the molecules that can be studied without paying the price of a difficult and extensive spectroscopy study.

- To access highly excited states, we are limited to OH, CH or NH stretch overtones since strong anharmonicity is required to relax harmonic oscillator selection rules. Moreover, it is not obvious that double or triple resonance can be always done, since the Franck-Condon factors put severe limitations on the detection step which is based on an electronic transition. Furthermore, detection techniques based on photodissociation or unimolecular dissociation product detection have the usual limitations associated with dissociation experiments, mainly the finite dissociation rate and distribution of products among many different states. Moreover fluorescence detection of the vibrationally excited molecule itself or of the dissociation fragments is obviously limited by the fluorescence quantum yield. This adds additional constraints to the molecules that can been studied, even if these constrains are strongly correlated with the previous ones. Furthermore, in the case of quantum beat experiments, molecules with a large nuclear hyperfine constant exhibit hyperfine structure, that can wash out the quantum beat oscillations, since each $J$ level is split in $(2J + 1)(2I + 1)$ $M_F$ components, and the energy difference for all the $M_F$ components is not the same. This being said, it is possible to make Stark or Zeeman induced quantum beat experiments on $M_F$ levels to get other parameters like nuclear hyperfine constant and spin-orbit matrix elements [4]. However this is more easily done in a molecular jet than in a static cell, since the $J = 1$ states are more populated and split in fewer $M_F$ components.

- Since we want to compare our experimental Stark coefficients with calculated Stark coefficients to test currently existing dipole moment surfaces and wavefunctions, and provide benchmarks for future improvements, we must focus on molecules for which dipole moments surfaces and potential energy surfaces are available at a sufficient accuracy. This reduces again the number of molecules that are worth being studied by this approach.

From the remarks above, we can conclude that direct dipole moments measurements data are of crucial importance for quantitative spectroscopy and the techniques that we have developed offer the necessary accuracy needed for testing and improving calculated DMS's and PES's. However, in practice they are not straightforward to carry out and have several limitations which restrict their application to a limited number of molecules and vibrational states. This means that such dipole moment measurements must be carefully targeted. The molecule we can plan to study must be chosen, in addition to its broader scientific interest, according to the previously mentioned criteria as well as the spectroscopic data available.

The techniques applied in this thesis are complementary to traditional spectroscopic techniques, such as photoacoustic spectroscopy, FTIR, ICLAS, CRDS and double-resonance overtone

spectroscopy techniques which can provide accurate energy levels positions for excited rovibrational states. This is the preliminary step to any dipole moment study. In addition to the energy level position these techniques provide, they also give information on intensities. However all these techniques are very sensitive to experimental fluctuations of the sample or of the laser power, which gives large uncertainties on the measurements, sometimes larger than the dipole moment changes [5]. Moreover, all the dipole moments measured from intensity analysis are transition dipole moments, the dipole moment operator matrix element between two different rovibrational eigenstates, and not permanent dipole moments, (*i.e.* the average of the dipole moment on a period of rotation-vibration of a single rovibrational eigenstate). One must account for the fact that in transition dipole moments, the two wavefunctions linked by the dipole moment operator are not necessarily expressed in the same frame, and deriving a permanent dipole moment from transition dipole moment measurements is a not straightforward operation [6]. However, all these considerations and limitations must be balanced against the quantity of measurement one can get during a given period of time. Even if they are time consuming, measurements of permanent dipole moments of excited vibrational states by the techniques developed and employed here are extremely useful, because of the increased accuracy. Therefore these techniques should be used as a check of dipole moment from line intensity analysis of selected systems rather than to make a wide survey of the dipole moments of highly excited rovibrational states.

However, we must keep in mind that because all the experimental limitations associated with line strength measurements, dipole moment surfaces from theoretical calculations can be superior to empirical surfaces derived from these line strength measurements [7]. Moreover ab-initio calculations can be made for a large number of geometric configurations, sometimes unreachable by experiment, in an small amount of time, and in this sense are very promising [8]. *Ab initio* calculations are intimately linked to experimental spectroscopic work, and improving our understanding of molecular physics requires a feedback between theory and experiment. On one hand, *ab initio* calculations need experimental input for validation, correction and improvement, and one the other hand they can provide a large amount of useful data for spectroscopists. However, even if at low energy the agreement with experimental energy and dipole moment is relatively good [9], when going to higher energy the discrepancy between experimental and calculated energy levels tends to increase. Until this work, almost no data was available for checking dipole moment surfaces at geometries far from equilibrium, and this work demonstrates that improvements can be made on dipole moment surfaces. Our dipole moment measurement techniques must be conceived as a check and a way of improving DMS's and wavefunctions and thus as a complement to *ab initio* calculations which remain faster and more useful than experiment for constituting a database that can be used for atmospheric modeling, for example. In this way, the work done must be considered as being a guide for calculations, in order to improve their

validity. For example, the work made on $H_2O$ has definitely improved dipole moment matrix element calculations as seen in Section 5.4.3. Despite the small discrepancy that remains between calculated and observed Stark coefficients, we hope that in the future these experimental data will lead to further improvements of transition dipole moments and thus transition intensities for $H_2O$.

With this in mind, it seems to me that water is the key molecule that fulfill the necessary criteria and for which our results can lead to serious improvements of *ab initio* methods. In addition to the huge interest for atmospheric sciences, a wealth of spectroscopic data are available for this molecule. As a simple triatomic molecule there are sophisticated and reliable PES's and DMS's available. To test these surfaces more critically, it will be very useful to go to still higher excited vibrational states, such as $|9, 0^+\rangle$, $|10, 0^+\rangle$ and $|11, 0^+\rangle$. These states can be accessed in the same way as $|8, 0^+\rangle$, by double-resonance from $|0, 0, 0\rangle$ to $|4, 0^-\rangle$ or $|5, 0^-\rangle$, and photodissociated using the third harmonic of a Nd:YAG laser. The spectroscopy of these vibrational states has not been investigated, and will have to be done prior to Stark measurements. However, since double-resonance will be used to access them and because the intermediate energy level positions ($|4, 0^-\rangle$ or $|5, 0^-\rangle$) are known, the assignment should be straightforward. There are no additional difficulties than for our measurements on $|8, 0^+\rangle$ for getting Stark coefficients that can be compared to those from ab-initio calculations. However, the spectroscopy of the dark states $|9, 0^-\rangle$, $|10, 0^-\rangle$ and $|11, 0^-\rangle$ is not known, and they are measured either by FTIR, ICLAS or CRDS, we shall not be able to extract dipole moment components. In addition to those states with more OH stretch quanta of vibration, it will be desirable to get states with quanta of bending other than $|4, 0^-, 2\rangle$, in order to test how well the bending motion is accounted for. Populating these states with bending character requires more laser power, and $|4, 0^-, 2\rangle$ constituted the experimental limit, but power improvements, as using a Bethune cell in another laser amplifier stage for example, can make measurements on those states possible.

Because of complications due to tunneling effects in $H_2O$, it seems to me that water DMS can be better tested using HDO Stark coefficients. However it has not been possible at this time to compare our experimental Stark coefficients for HDO with calculated ones from *ab initio* transition dipole moments. This comparison may be particularly useful, since it could allow a true test of the DMS without being concerned of how well wavefunctions take into account tunneling. Therefore, it is useful to carry experiments on $H_2O$ along with experiments on HDO, which does not introduce additional difficulties since the energy levels positions are not so different. However the signal intensity is twice smaller.

It is probably possible to get vibrational levels higher than $|11, 0^+\rangle$, by using $|5, 0^-\rangle$ as

the intermediate levels, which probably constitutes the highest intermediate levels we can fore-see to use, but the photodissociation laser may not be an harmonic of a Nd:YAG laser, and introducing a tunable photodissociation laser is one experimental step further. This work on excited vibrational states higher than $v_{OH} = 8$ both on $H_2O$ and HDO is relatively feasible and extremely useful, both in term of energy levels positions determination and in term of dipole moment measurements, for improving both the PES and DMS.

In addition to $H_2O$ and HDO, quantum beat oscillations have been measured on $H_2CO$, which like water, has been extensively studied. This is the molecule with the most dipole moment data available and thus the most susceptible to give a complete picture of dipole moment dependence on vibration, not only on CH stretch vibrational motion, but on different vibrational modes. We have shown that SEP quantum beat spectroscopy is feasible (see Section 3.2.6). Because of the wealth of data currently available on $H_2CO$, the possibility to access by SEP vibrational states different than CH stretch overtones [10], and because it is a relatively simple system, it is in my sense a molecule that is worth studying in order to test and improve *ab initio* DMS's.

Another molecule, that could be worth studying is $NH_3$, because of its umbrella motion, similar to the tunneling motion in $H_2O$. Stark effects observed in $NH_3$ arise from transition moments connecting the two halves of the tunneling doublets of $NH_3$ (like $\mu_a$ in $H_2O$ is related to the transition moment connecting the $|s\rangle$ and $|a\rangle$ states). This transition moment is conventionally interpreted as the permanent moment of $NH_3$ in the pyramidal geometry of either the left or right handed basis state. Inversion of ammonia basis states changes the sign of the $NH_3$ moment, just as tunneling from $|n, 0\rangle$ and $|0, n\rangle$ reverses the sign of $\mu_x$. Double-resonance experiments on $v_{NH} = 4$ and 5 have been attempted following the experimental scheme of Ref. [11] on $v_{NH} = 1$. An overtone transition populated the $v_{NH} = 4$ state, and an electronic transition was used to excite the $2^4$ $\tilde{A}^1A"_2$ electronic levels, and we tried to detect $NH_2$ chemiluminescence. Unfortunately the Franck-Condon factors of the second step are almost zero, and we did not transfer enough molecules from $v_{NH} = 4$ to the electronic excited state to detect the overtone transition. Moreover Franck-Condon favorable vibronic states were out of reach of our laser wavelength range. Nevertheless another alternative for the detection step would be to make a one photon forbidden, two photon allowed transition to populate the Rydberg state $\tilde{C}'A'_1$ [12], that fluoresces on the $\tilde{A}^1A"_2$ at 650 $nm$ to give the so-called Schuster bands. This experimental scheme may allow one to study the dipole moment of the $v_{NH} = 4$ and 5 states.

Those techniques can be extended to larger molecules, with the limitations mentioned above, as long as the rotational structure can be resolved. Nevertheless the overall goal that has to be kept in mind is that those experiments must be thought as means to improve our physical understanding of charge distribution in molecules with vibrational motion in order to test and improve *ab initio* DMS and PES, and both theoretical and experimental work must be

carried out together to finally get reliable PES and DMS. Reliable *ab initio* PES's and DMS's will allow one to make a large transition intensity database that can be used, one level further, by quantitative spectroscopists.

# References

[1] P. F. Bernath. The spectroscopy of water vapor: Experiment, theory and applications. *Physical Chemistry Chemical Physics*, 4(9):1501–1509, 2002.

[2] W. Y. Zhong, J. D. Haigh, D. Belmiloud, R. Schermaul, and J. Tennyson. Note on 'the impact of new water vapour spectral line parameters on the calculation atmospheric absorption' by wenyi zhong *et al.* (july a, 2001, 127, 1615-1626). *Quarterly Journal of the Royal Meteorological Society*, 128(582):1387–1388, 2002.

[3] M. D. Chou. Atmospheric solar heating in minor absorption bands. *Terrestrial Atmospheric and Oceanic Sciences*, 10(3):511–528, 1999.

[4] H. Bitto and J. R. Huber. Molecular quantum beat spectroscopy. *Optics Communications*, 80(2):184–198, 1990.

[5] R. Schermaul, R. C. M. Learner, D. A. Newnham, R. G. Williams, J. Ballard, N. F. Zobov, D. Belmiloud, and J. Tennyson. The water vapor spectrum in the region $8600 - 15000$ $cm^{-1}$: Experimental and theoretical studies for a new spectral line database. i. laboratory measurements. *Journal of Molecular Spectroscopy*, 208(1):32–42, 2001.

[6] C. Camy-Peyret and J. M. Flaud. *Vibration-rotation dipole moment operator for asymmetric rotors, Molecular Spectroscopy: Modern Research*, volume III, pages 69–110. Academic Press, Orlando, Fla., 1985.

[7] B. Galabov, T. Dudev, S. Ilieva, and J. R. Durig. Creation of intensity theory in vibrational spectroscopy: Key role of ab initio quantum mechanical calculations. *International Journal of Quantum Chemistry*, 70(2):331–339, 1998.

[8] G. Chambaud. Potential surfaces and spectroscopy. *Journal De Chimie Physique Et De Physico-Chimie Biologique*, 95(8):1892–1924, 1998.

[9] O. L. Polyansky, A. G. Csaszar, S. V. Shirin, N. F. Zobov, P. Barletta, J. Tennyson, D. W. Schwenke, and P. J. Knowles. High-accuracy ab initio rotation-vibration transitions for water. *Science*, 299(5606):539–542, 2003.

[10] P. H. Vaccaro, J. L. Kinsey, R. W. Field, and H. L. Dai. Electric-dipole moments of excited vibrational levels in the $\tilde{X}^1 a_1$ state of formaldehyde by stimulated-emission spectroscopy. *Journal of Chemical Physics*, 78(6):3659–3664, 1983.

[11] A. Bach, J. M. Hutchison, R. J. Holiday, and F. F. Crim. Vibronic structure and photodissociation dynamics of the $\tilde{A}$ state of jet-cooled ammonia. *Journal of Chemical Physics*, 116(21):9315–9325, 2002.

[12] M. N. R. Ashfold, C. L. Bennett, R. N. Dixon, P. Fielden, H. Rieley, and R. J. Stickland. Fluorescence excitation and emission-spectroscopy of the $\tilde{C}'a_1'$ rydberg state of ammonia - assignment of the schuster bands of ammonia. *Journal of Molecular Spectroscopy*, 117(2):216–227, 1986.

# Appendix A: Stark effect

We will review in Appendix A the different expressions used to express the modification induced in the spectrum of a molecule by an external electric field following the treatment exposed in Ref. [1]. We will first see how the application of an external Stark electric field breaks the inversion symmetry of a molecule + external charges system, and we will then derive the mathematical expression of the second order correction to the energy of a symmetric rotor. The asymmetric rotor case is not treated but can be found in Ref. [1]. The results are cited in Section 2.1.2.

## Dipole moment and inversion operators

### The zero-field molecular Hamiltonian

The inversion operator $E^*$, which has the effect of permuting in a molecule the spatial coordinates of all particles (both nuclei and electrons) through the origin of the space-fixed axis system (usually the center of mass) commutes with the molecular Hamiltonian, $i.e$ $[H_0, E^*]$, and the eigenfunctions $|\psi_n^0\rangle$ of the zero-field Hamiltonian $H_0$ can be labeled by their behavior under the inversion operator and thus have a defined total parity, either even or odd:

$$E^*|\psi_n^0\pm\rangle = \pm|\psi_n^0\pm\rangle \tag{1}$$

The electric dipole moment operator is of odd parity, that is $E^*T_p^1(\mu) = -T_p^1(\mu)$ where $T_p^1(\mu)$ is the space-fixed $p^{th}$ component of the molecular dipole moment vector operator. Its expectation value for a molecular eigenstate of defined parity is thus zero:

$$\langle T_p^1(\mu)\rangle_n = \langle\psi_n^0|T_p^1(\mu)|\psi_n^0\rangle = 0 \tag{2}$$

Therefore, no single eigenstate of defined parity can give nonzero expectation value for any *space-fixed* component of the electric dipole moment. Permanent dipole moments of molecules only referred to *body-fixed* system of coordinates. The space-fixed components of the dipole moment will average to zero for a freely rotating molecule (or since the Heisenberg uncertainty principle prohibits a freely rotating molecule from being oriented along a preferential direction in space).

If we now take the case of two degenerate states of opposite parity $|\psi_+^0\rangle$ and $|\psi_-^0\rangle$, they form a new set of mixed parity:

$$\begin{cases} |\psi_a^0\rangle &= \frac{1}{\sqrt{2}}(|\psi_+^0\rangle + |\psi_-^0\rangle) \\ |\psi_b^0\rangle &= \frac{1}{\sqrt{2}}(|\psi_+^0\rangle - |\psi_-^0\rangle) \end{cases} \tag{3}$$

and the expectation value of any $p$ component of the space-fixed dipole moment operator for these states of mixed parity is now:

$$\langle\psi_a^0|T_p^1(\mu)|\psi_a^0\rangle = \langle\psi_b^0|T_p^1(\mu)|\psi_b^0\rangle = \langle\psi_-^0|T_p^1(\mu)|\psi_+^0\rangle \neq 0 \tag{4}$$

This means that no electric dipole moment (and more generally no electric multipole moment of odd order) can exist in the absence of degeneracy. A nonzero expectation value for the space-fixed dipole moment occurs only for degenerate eigenstates. This degeneracy can occur accidentally or for symmetry related reasons, as it is the case for the $K$-degeneracy of purely symmetric top (the $(2J+1)$ degeneracy associated with $M$ does not count, as all the $M$-sublevels have the same parity). In an asymmetric top there are no systematic degeneracies between states of opposite parity, and therefore a zero expectation value for the space-fixed dipole moment.

## Interaction between a molecule and an external electric field: the Stark Hamiltonian

Electrical interactions occur between the collection of charged particles constituting a molecule and a distribution of external charges producing an external electric field which exerts various forces and torques on the molecule. The classical interaction for the electrostatic interaction between a molecule and a surrounding static distribution of charges can be expressed in the following form:

$$V = \sum_n \sum_m \frac{q_m q_n}{|\vec{r_n} - \vec{r_m}|} \tag{5}$$

where $q_m$ and $\vec{r}_m$ represent the charge and position vector of the $m^{th}$ particle in the molecule, and $q_n$ and $\vec{r}_n$ represent the charge and position vector of the $n^{th}$ particle in the external charge distribution. Position vectors are relative to the origin of a space-fixed coordinate system, that is taken to be the molecular centre of mass. If we assume that the external charges are widely separated from the molecules (i.e. $|\vec{r}_n| \gg |\vec{r}_m|$), we can make use of the expressions, see [2]:

$$\frac{1}{|\vec{r_n} - \vec{r_m}|} = \sum_{k=0}^{\infty} \frac{(|\vec{r_m}|)^k}{(|\vec{r_n}|)^{k+1}} P_k(\cos\theta_{n,m}) \tag{6}$$

$$P_k(\cos\theta_{n,m}) = \left(\frac{4\pi}{2k+1}\right) \sum_{p=-k}^{k} Y_p^k(\theta_m, \phi_m)^* . Y_p^k(\theta_n, \phi_n) \tag{7}$$

where $\theta_i$ and $\phi_i$ are the angular coordinates of $\overrightarrow{r_i}$ with respect to the space-fixed axis system, and $\theta_{i,j}$ is the angle formed between $\overrightarrow{r_i}$ and $\overrightarrow{r_j}$. By combining those expressions into Eq. 5, the interaction can be reformulated [2] in terms of the electric multipole moments describing the charge distributions (see Section 1.1) present both inside and outside of the molecular system:

$$V = \sum_{k=0}^{\infty} \sum_{p=-k}^{k} \left(\frac{4\pi}{2k+1}\right) \sum_{m=-k}^{k} q_m |\overrightarrow{r_m}|^k Y_p^k(\theta_m, \phi_m)^* \cdot \sum_{n=-k}^{k} \frac{q_n}{(|\overrightarrow{r_n}|)^{k+1}} Y_p^k(\theta_n, \phi_n) \qquad (8)$$

$$= \sum_{k=0}^{\infty} \sum_{p=-k}^{k} T_p^k(\mathbf{M})^* T_p^k(\mathbf{S}) \qquad (9)$$

$$= \sum_{k=0}^{\infty} (T^k(\mathbf{M}).T^k(\mathbf{S})) \qquad (10)$$

$$= \sum_{k=0}^{\infty} V^{(k)} \qquad (11)$$

where $T_p^k(\mathbf{M})$ and $T_p^k(\mathbf{S})$ are the $p^{th}$ component of a rank $k$ spherical tensors which describe the $k^{th}$ multipole moments of the molecular charge distribution and of surrounding external charge distribution respectively, and $V^k$ represents the contribution to the energy from interactions between the $k^{th}$ electric multipole moments.

The successive terms of $V$ denote the interaction of higher and higher electric multipole moments of the molecule with those of the surrounding distribution of charges. The $k = 0$ term represents the interaction of the electric monopole moment, or the total charge $Q$ of the molecule, with the electric potential $\Phi$, produced by the surrounding charge distribution. The $k = 1$ represents the interaction of the molecular electric dipole moment, $\overrightarrow{\mu}$, with the gradient of the external electric potential or electric field vector, $\overrightarrow{E} = -\nabla\Phi$. The $k = 2$ term represents the interaction of the molecular electric quadrupole moment with the gradient of the external electric field $\nabla\overrightarrow{E} = -\nabla^2\Phi$. A great care is taken in the experiments that the electric field applied to the molecule is extremely uniform and homogeneous, and moreover we study neutral molecules ($Q = 0$), and the terms of order higher than $k = 2$ are much smaller than the $k = 1$ term, so the expansion above collapses to a single term describing the interaction between the molecular electric dipole moment, $\overrightarrow{\mu}$, and the electric field $\overrightarrow{E}$:

$$V = V^{(1)} = -T^1(\overrightarrow{\mu}) \cdot T^1(\overrightarrow{E}) = -\overrightarrow{\mu} \cdot \overrightarrow{E} \qquad (12)$$

The quantum mechanical operator, $\widehat{H}_{Stark}$, describing the interaction of a molecular electric dipole moment and an external electric field, can be formulated from the classical expression (see Eq. 12):

$$\widehat{H}_{Stark} = -\widehat{T}^1(\widehat{\overrightarrow{\mu}}) \cdot \widehat{T}^1(\widehat{\overrightarrow{E}}) = -\widehat{\overrightarrow{\mu}} \cdot \widehat{\overrightarrow{E}} \qquad (13)$$

or:

$$\widehat{H}_{Stark} = -\mu E \cos\theta \qquad (14)$$

where $\theta$ is the angle between the molecular dipole $\vec{\mu}$ and the field $\vec{E}$. $\mu_Z = \mu\cos\theta$ is the $Z$ component of the dipole moment vector in the space-fixed system.

The application of an external Stark electric field breaks the inversion symmetry of the system (molecule + external charges), since the inversion operator does not invert the space-fixed charges that produce the external electric field, and the effective Hamiltonian can be written as:

$$H^{eff} = H_0 + H_{Stark} \qquad (15)$$

$$\text{with} \qquad H_{Stark} = -T^1(\mu).T^1(E) = \vec{\mu}.\vec{E} \qquad (16)$$

where $T^1(\mu)$ and $T^1(E)$ represent the space-fixed molecular dipole moment vector and external electric field vector. Now the expectation value of any $p$ component of the space-fixed dipole moment is non-zero since the parity is no longer a valid symmetry label:

$$\langle\psi_n|T_p^1(\mu)|\psi_n\rangle \neq 0 \qquad (17)$$

where $|\psi_n\rangle$ is now an eigenfunction of the effective molecular Hamiltonian with ill-defined parity. The breakdown of the inversion symmetry that accompanies the application of an external electric field can thus lead to an induced, space-fixed component of the electric dipole moment.

Therefore, for asymmetric rotors, there is no first-order Stark effect (since $\langle\psi_\pm^0|T_p^1(\mu)|\psi_\pm^0\rangle \cdot T^1(E) = 0$ due to the lack of systematic degeneracy between states of opposite parity, and thus no space-fixed permanent dipole moment at zero-field, as we use the zero-field wavefunctions for first-order perturbation theory). The Stark effect will be second-order (see Eq. 17) and can be classically seen in terms of an induction process (polarization) in which the external electric field must induce a moment in the molecular system with which it can subsequently interact. Or, in the language of perturbation theory, the electric field breaks the symmetry and new eigenfunctions are defined that subsequently interact with the Stark Hamiltonian. However, once the electric field is large enough to cause the mixing of states having opposite parity (e.g. the members of an asymmetry doublet) the Stark perturbation can be transformed into a first-order effect, linearly proportional to the magnitude of the electric field. For an asymmetric rotor there is a transition from second-order Stark effect at low field to first-order Stark effect at higher field, this transition being correlated with the size of the asymmetry splitting. Note that a $J_{0,J}$ state, since it is not a member of a $K$-doublet, will show a second-order Stark effect until the field is large enough to mix it with adjacent rotational states of different $J$ or $K_a$.

# Stark effect for a symmetric rotor

## First-order Stark effect for a symmetric rotor

We will now derive the Stark Hamiltonian matrix elements in a basis of a purely symmetric rotor that describes the interaction energy between a molecular electric dipole moment and an external electric field:

$$H_{Stark} = -T^1(\mu) \cdot T^1(E) = -\sum_p (-1)^p T_p^1(\mu) \cdot T_{-p}^1(E) = \vec{\mu} \cdot \vec{E} \qquad (18)$$

where $T^1(\mu)$ and $T^1(E)$ represent the *space-fixed* molecular dipole moment vector and external electric field vector. However the molecular dipole moment is defined in the *molecule-fixed* axis system while the Stark electric field is defined in the *space-fixed* axis system. So, we will first transform the space-fixed dipole moment operator into the molecule-fixed frame:

$$T_p^1(\mu) = \sum_q D_{pq}^{(1)}(\Omega)^* \cdot T_q^1(\mu) \qquad (19)$$

where $D^{(1)}(\Omega)$ is the Wigner rotation matrix of rank 1, that is function of the Euler angles $\Omega$, and that is the operator connecting the space-fixed and the molecule-fixed coordinates. The $q$ index refers to the molecule-fixed system and the $p$ index refers to the space-fixed system. Eq. 18 and Eq. 19 give:

$$H_{Stark} = -\sum_p \sum_q (-1)^p D_{pq}^{(1)}(\Omega)^* T_q^1(\mu) \cdot T_{-p}^1(E) = \vec{\mu} \cdot \vec{E} \qquad (20)$$

and we want to evaluate this operator for rovibronic states in the basis set of symmetric rotor eigenfunctions:

$$|\alpha JKM\rangle = |\alpha\rangle |JKM\rangle = |\alpha\rangle \left(\frac{2J+1}{8\pi^2}\right)^{1/2} D_{MK}^J(\Omega)^* \qquad (21)$$

where $K$ and $M$ are respectively the projection of the total angular momentum $J$ along the molecule-fixed and the space-fixed $z$ axis. $\alpha$ represents all the other quantum numbers (for electronic and vibrational degrees of freedom), and we decompose the rovibronic state into a vibronic state and a rotational state, the latter can be written in terms of Wigner rotation functions. So, we have:

$$\langle \alpha J'K'M' | H_{Stark} | \alpha JKM \rangle = -\sum_p \sum_q (-1)^p \langle J'K'M' | D_{pq}^{(1)}(\Omega)^* | JKM \rangle \qquad (22)$$

$$\langle \alpha | T_q^1(\mu) | \alpha \rangle T_{-p}^1(E) \qquad (23)$$

$\langle \alpha | T_q^1(\mu) | \alpha \rangle$ is the $q$ component of the vibronic molecular dipole moment of the molecule-fixed frame.

It is important at that point to make a very important and useful remark about the nature of the vibronic molecule-fixed frame the vibronic dipole moment $\mu(\alpha)$ is expressed in. If we choose to separate rotational and vibrational motion for non-equilibrium geometries, as it is done in Eq. 22, to get a vibronic molecular dipole moment, we must use the rules proposed by Eckart for separating rovibrational motion. These rules consist in eliminating the vibrational angular momentum $J_{vib}$ in the molecule-fixed system:

$$J_{vib} = \sum_i m_i r_i \times \dot{r}_i = 0 \tag{24}$$

Making the approximation that for a rigid molecule the nuclei do not depart far from the equilibrium configuration, we can get the so-called Eckart equation [3]:

$$J_{vib} = \sum_i m_i r_i^e \times r_i = 0 \tag{25}$$

Equation 25 fixes the orientation of the $(x, y, z)$ molecule-fixed system that gives a minimal $J_{vib}$ and thus minimum Coriolis coupling terms to spoil the separation of rotation and vibration. It is important to understand that **the vibronic dipole moment $\mu(\alpha)$ is expressed in an Eckart frame averaged on a vibration period.** We will refer in the text to the $a$ and $b$ components of the vibronic dipole moment in this specific molecule-fixed frame.

Coming back to the derivation of Eq. 22, the derivation of the $\langle J'K'M'|D_{pq}^{(1)}(\Omega)^*|JKM\rangle$ can be found in Ref. [2] where use have been made of the relation:

$$D_{pq}^{(k)}(\Omega)^* = (-1)^{p-q} D_{-p-q}^{(k)}(\Omega) \tag{26}$$

and of the Clebsch-Gordan series to contract the product of two Wigner rotation functions:

$$D_{-M-K}^{(J)}(\Omega)D_{-p-q}^{(k)}(\Omega) = \sum_{J"} \begin{pmatrix} J & k & J" \\ -M & -p & M+p \end{pmatrix} \begin{pmatrix} J & k & J" \\ -K & -q & K+q \end{pmatrix} D_{M+pK+q}^{(J")}(\Omega)^* \tag{27}$$

which gives the following expression in terms of Clebsch-Gordan coefficients:

$$\langle J'K'M'|D_{pq}^{(1)}(\Omega)^*|JKM\rangle = (-1)^{M'-K'}\sqrt{(2J'+1)(2J+1)} \tag{28}$$
$$\begin{pmatrix} J' & k & J \\ -M' & p & M \end{pmatrix} \begin{pmatrix} J' & k & J \\ -K' & q & K \end{pmatrix}$$

what we can put in Eq. 22 to give:

$$\langle \alpha J'K'M'|H_{Stark}|\alpha JKM\rangle = -(-1)^{M'-K'}\sqrt{(2J'+1)(2J+1)} \tag{29}$$
$$\sum_p \sum_q (-1)^p \begin{pmatrix} J' & 1 & J \\ -M' & p & M \end{pmatrix} \begin{pmatrix} J' & 1 & J \\ -K' & q & K \end{pmatrix}$$
$$\langle \alpha|T_q^1(\mu)|\alpha\rangle T_{-p}^1(E)$$

The symmetry properties of the Wigner 3-j symbols gives the selection rules for which rotational states the interaction Hamiltonian can connect:

$$\Delta J = 0 \text{ (excepted for J=0)}, \pm 1 \quad \Delta K = 0, \pm 1 \quad \Delta M = 0, \pm 1 \tag{30}$$

The $p$ index refers to the polarization of the electric field, either right-handed or left-handed circularly polarized ($p = +1$ or $p = -1$) or linearly polarized ($p = 0$). The quantization axis is defined by the direction of the external Stark electric field and for Stark effect (as well as for rotational transitions with radiation linearly polarized along the quantization axis) we just consider $p = 0$, which simplifies Eq. 29 to:

$$\langle \alpha J'K'M'|H_{Stark}|\alpha JKM\rangle = -(-1)^{M'-K'}\sqrt{(2J'+1)(2J+1)} \tag{31}$$
$$\begin{pmatrix} J' & 1 & J \\ -M' & 0 & M \end{pmatrix} \sum_q (-1)^p \begin{pmatrix} J' & 1 & J \\ -K' & q & K \end{pmatrix} \langle \alpha|T_q^1(\mu)|\alpha\rangle E$$

where only the rotational states of the same vibronic state obeying the selection rules of Eq. 32 can be connected:

$$\Delta J = 0 \text{ (excepted for J=0)}, \pm 1 \quad \Delta K = 0, \pm 1 \quad \Delta M = 0 \tag{32}$$

The Stark Hamiltonian is diagonal in $M$. The summation over $q$ allows the (permanent or transition) dipole moment to have nonzero component along all the three molecule-fixed axes.

Of course if the states connected do not belong to the same vibronic state as we assumed in Eq. 22, we must consider the total symmetry of the rovibronic state and the representation of $\langle \alpha'|T_q^1(\mu)|\alpha\rangle$ must contains an irreducible representation of $A_1$ symmetry for Eq. 31 to be non zero.

Applying the Wigner-Eckart theorem to derive Eq. 31 assumes an explicit separability of rotational motion from other degrees of freedom, $\langle \alpha|T_q^1(\mu)|\alpha\rangle$ is the expectation value for the $q^{th}$ spherical component of the dipole moment of the vibronic state $|\alpha\rangle$, and the dependence on rotational quantum numbers is included in the 3-j components. Of course, this is not strictly true for a non-rigid molecule. An asymmetric rotor can have components of the molecular dipole moment along all three of the body-fixed axes (i.e. $q = 0, \pm 1$). However, for a symmetric top (or for an asymmetric top very close to the symmetric top limit), the dipole moment is directed only along the molecular symmetry axis (i.e $\langle \alpha|T_0^1(\mu)|\alpha\rangle = \mu_0$ and $\langle \alpha|T_{\pm 1}^1(\mu)|\alpha\rangle = 0$) since the symmetry axis is also one of the molecule-fixed axis. Therefore the matrix elements for the Stark Hamiltonian become:

$$\langle \alpha J'K'M'|H_{Stark}|\alpha JKM\rangle = -(-1)^{M'-K'}\sqrt{(2J'+1)(2J+1)}$$
$$\begin{pmatrix} J' & 1 & J \\ -M' & 0 & M \end{pmatrix}\begin{pmatrix} J' & 1 & J \\ -K' & 0 & K \end{pmatrix}\mu_0 E$$
$$= \mu_0 E \frac{MK}{J(J+1)} \tag{33}$$

and we see in Eq. 33 that the Stark Hamiltonian is diagonal in $K$ ($\Delta K = 0$).

## Second-order Stark effect for a symmetric rotor

We can evaluate in the same way the second-order Stark effect. In the second-order perturbation theory, the molecular wave function is changed by the presence of a static electric field, and the resulting energy change is:

$$\Delta E^2 = \sum_{J'K'M'} \frac{\langle JKM|H^{Stark}|J'K'M'\rangle\langle J'K'M'|H^{Stark}|JKM\rangle}{E_{JKM} - E_{J'K'M'}} \tag{34}$$

where we can evaluate the Stark Hamiltonian matrix elements using Eq. 33, which gives:

$$\Delta E^2 = \mu_0^2 E^2 \sum_{J'K'M'} \frac{(2J+1)(2J'+1)(-1)^{M'-K'}(-1)^{M-K}}{E_{JKM} - E_{J'K'M'}} \tag{35}$$

$$\begin{pmatrix} J & J' & 1 \\ M & -M' & 0 \end{pmatrix}\begin{pmatrix} J & J' & 1 \\ K & -K' & 0 \end{pmatrix}\begin{pmatrix} J' & J & 1 \\ M' & -M & 0 \end{pmatrix}\begin{pmatrix} J' & J & 1 \\ K' & -K & 0 \end{pmatrix} \tag{36}$$

$$= \mu_0^2 E^2 \sum_{J'K'M'} \frac{(2J+1)(2J'+1)}{E_{JKM} - E_{J'K'M'}}(2J'+1)^{-2}\langle JM,10|J'M\rangle^2\langle JK,10|J'K\rangle^2$$

$$= \mu_0^2 E^2 \left( \frac{-\left((J+1)^2 - M^2\right)\left((J+1)^2 - K^2\right)}{(2J+3)(2J+1)(J+1)^3} + \frac{\left(J^2 - M^2\right)\left(J^2 - K^2\right)}{(2J+1)J^3(2J-1)} \right) \tag{37}$$

where the last line makes use of the explicit energy eigenvalue for a symmetric top

$$E_{JKM} = BJ(J+1) - (C-B)K^2 \tag{38}$$

# References

[1] C.H. Townes and A.L. Schawlow. *Microwave Spectroscopy*. Dover Publications, New York, 1975.

[2] Richard N. Zare. *Angular Momentum understanding spatial aspects in chemistry and physics*. Wiley-Interscience, New York, 1988.

[3] Philip R. Bunker and Per Jensen. *Molecular Symmetry and Spectroscopy*. NRCC, Ottawa,Ont., second edition, 1998.

# Appendix B: Stark induced molecular quantum beat spectroscopy

Here we describe the theoretical background used for our Stark induced molecular quantum beat experiments following the development derived on p.200 of Ref. [1] that we will adapt to our case of double resonance pump-probe scheme. More mathematically detailed steps will be found in this reference. We will make use in our development of the following schematic process. A
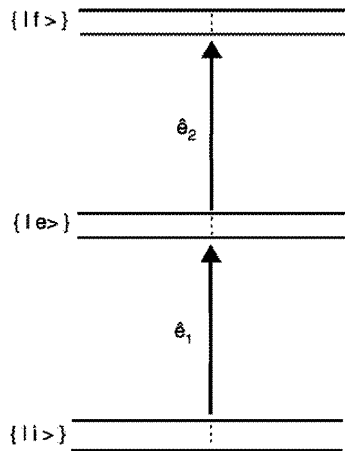


**Figure 1:** Scheme of the double-resonance Stark induced quantum beat technique.

pump radiation of polarization $\vec{e_1}$ transfers by an electric dipole transition molecules in the initial states $|i\rangle$ to the intermediate excited states $|e\rangle$. Then, after a fixed time delay, the pump-probe delay, a probe radiation of polarization $\vec{e_2}$ transfers by an electric dipole transition molecules from the intermediate excited states $|e\rangle$ to the final states $|f\rangle$. We imagine at time $t = 0$ a short pulse of light incident on our sample, and we want to derive an expression for the population at the $|f\rangle$ states at subsequent time $t$. We wish to develop a general expression for an arbitrary pump-probe geometry, for arbitrary polarization $\vec{e_1}$ and $\vec{e_2}$, and for arbitrary sharp angular momentum characterized quantum states $|i\rangle = |\alpha_i J_i M_i\rangle$, $|e\rangle = |\alpha_e J_e M_e\rangle$ and $|f\rangle = |\alpha_f J_f M_f\rangle$.

We will then specialize this expression according to the case we will be interested in. To make this problem tractable we need several assumptions:

- the hyperfine structure is negligible

- the pressure is low enough that we can ignore the effect of collisions and treat our molecules as isolated

- the coherent spectral width of the light pulse is much greater than the energy difference between the excited $|\alpha_e J_e M_e\rangle$ to be prepare coherently. The Fourier transform limited bandwidth corresponding to an excitation pulse of duration $\Delta\tau$ can be written as:

$$\Delta\nu_{coh} = \frac{1}{\eta\Delta\tau} \qquad (39)$$

where $\eta$ is a constant that depends upon the functional form of the excitation pulse in the time domain (e.g. $\eta = \frac{\pi}{4\ln 2}$ for a gaussian pulse shape, and $\eta = 2\pi$ for a Lorentzian profile). If the energy difference is greater than $\Delta\nu_{coh}$, then the two levels are not excited coherently.

- the pump process is sufficiently weak, thus the natural lifetime for the excited system to decay is much less than the average time between two successive photon absorption by the system, and thus we can neglect optical pumping effects.

- the duration of the pulse is short compared to the pump-probe delay. Then the double resonance process may be treated as two independent steps, pump followed by probe.

- the initial state is isotropic, that is, has not been prepared with a preferential population in any of the $M_i$ sublevels nor with special phase relations (coherence) among the M-components.

- the radiative lifetimes of all excited states sublevels are the same and $\tau_e = \Gamma_e^{-1}$, and they are much longer than the pump-probe delay.

Before the light pulse arrives, the wavefunction of the system in some particular initial state is:

$$|\psi(\alpha_i J_i M_i; t < 0)\rangle = |\alpha_i J_i M_i\rangle \exp\left[-i\omega_{M_i} t\right] \qquad (40)$$

At time $t = 0$ the light pulse with polarization $\vec{e}$ causes excitation of the system, and the wavefunction of the excited system then evolves with time according to:

$$|\psi(\alpha_e J_e M_e; t)\rangle \propto \sum_{M_i}\sum_{M_e} \langle\alpha_e J_e M_e|\vec{e}_1 \cdot \vec{\mu}|\alpha_i J_i M_i\rangle|\alpha_e J_e M_e\rangle \exp\left[-i\omega_{M_e} t - \Gamma_e\frac{t}{2}\right] \qquad (41)$$

where $\overrightarrow{\mu}$ is the dipole moment operator and $\Gamma_e$ is the rate of natural radiative decay. Suppose at time $t$ that the excited state is probed to the final state $|\alpha_f J_f M_f\rangle$ by a photon of polarization $\overrightarrow{e_2}$, then the number of molecules into the final states $|\alpha_f J_f M_f\rangle$ is:

$$N_f(t) \quad \propto \quad \sum_{M_i} \sum_{M_f} |\langle \alpha_e J_e M_e; t | \overrightarrow{e_1} . \overrightarrow{\mu} | \alpha_f J_f M_f \rangle|^2 \tag{42}$$

$$\propto \quad \sum_{M_i} \sum_{M_f} \sum_{M_e, M_{e'}} \langle \alpha_e J_e M_e; t | \overrightarrow{e_1} . \overrightarrow{\mu} | \alpha_i J_i M_i \rangle \langle \alpha_i J_i M_i | \overrightarrow{e}^*_1 \cdot \overrightarrow{\mu} | \alpha_e J_e M'_e; t \rangle \tag{43}$$

$$\langle \alpha_e J_e M'_e; t | \overrightarrow{e_2} \cdot \overrightarrow{\mu} | \alpha_f J_f M_f \rangle \langle \alpha_f J_f M_f | \overrightarrow{e_2^*} \cdot \overrightarrow{\mu} | \alpha_e J_e M_e; t \rangle \exp\left[ -i \left( \omega_{M_e} - \omega_{M'_e} \right) t - \Gamma_e t \right]$$

which displays the time behavior of an exponential decay on which are superimposed quantum beats from the interference of the indistinguishable different paths through the sublevels of the intermediate excited state that connect the same initial and final sublevels. Note that in a quantum electrodynamics interpretation, $\overrightarrow{e}.\overrightarrow{\mu}$ corresponds to a photon annihilation operator and $\overrightarrow{e^*}.\overrightarrow{\mu}$ corresponds to a photon creation operator. The sum other $M_i$, $M_e$ and $M_f$ comes from the fact that the pump and probe steps are not $M$-selective, since the lasers line width is much greater than the separation between the different M-levels. The phase of these quantum beats is $\left( \omega_{M_e} - \omega_{M'_e} \right) t$, and there is of course no beats if the $M_e$ and $M'_e$ sublevels are degenerate. There is also no beat between $M_e$ levels prepared from different $M_i$ levels, since the beating is related to the indistinguishability of the different paths, and thus to the coherence of the excitation. The time dependence can display several sets of independent beats, since there can be several sets of indistinguishable different paths. In this case the time dependent signal will be the summation of several independent beats, each one of them having its proper beat frequency. For this reason it is much more convenient to work at $J_e = 1$. Since the exponential decay is much longer than the pump-probe delay used, we will drop the corresponding term and rewrite the number of molecules in the final states as:

$$N_f(t) \propto \sum_{M_e} \sum_{M'_e} P^{pump}_{M_e M'_e} P^{probe}_{M'_e M_e} \exp\left[ -i \left( \omega_{M_e} - \omega_{M'_e} \right) t \right] \tag{44}$$

where the pump and probe matrix elements are:

$$P^{pump}_{M_e M'_e} \quad = \quad \sum_{M_i} \langle \alpha_e J_e M_e; t | \overrightarrow{e_1} \cdot \overrightarrow{\mu} | \alpha_i J_i M_i \rangle \langle \alpha_i J_i M_i | \overrightarrow{e_1}^* \cdot \overrightarrow{\mu} | \alpha_e J_e M'_e; t \rangle \tag{45}$$

$$= \quad \langle \alpha_e J_e M_e; t | \left( \overrightarrow{e_1} \cdot \overrightarrow{\mu} \right) P_i \left( \overrightarrow{e_1}^* . \overrightarrow{\mu} \right) | \alpha_e J_e M'_e; t \rangle$$

and

$$P^{probe}_{M'_e M_e} \quad = \quad \sum_{M_f} \langle \alpha_e J_e M'_e; t | \overrightarrow{e_2} \cdot \overrightarrow{\mu} | \alpha_f J_f M_f \rangle \langle \alpha_f J_f M_f | \overrightarrow{e_2}^* \cdot \overrightarrow{\mu} | \alpha_e J_e M_e; t \rangle \tag{46}$$

$$= \quad \langle \alpha_e J_e M'_e; t | \left( \overrightarrow{e_2} \cdot \overrightarrow{\mu} \right) P_f \left( \overrightarrow{e_2}^* \cdot \overrightarrow{\mu} \right) | \alpha_e J_e M_e; t \rangle$$

with the projection operators:

$$P_i = \sum_{M_i} |\alpha_i J_i M_i\rangle\langle\alpha_i J_i M_i| \tag{47}$$

$$P_f = \sum_{M_f} |\alpha_f J_f M_f\rangle\langle\alpha_f J_f M_f| \tag{48}$$

Since the projection operators $P$ are readily verified to be invariant under rotation (that is $\mathbf{R}^{-1}\mathbf{P}\mathbf{R} = \mathbf{P}$) they are scalars that can be ignored in the tensorial analysis. Moreover, the operators of the form $(\vec{e} \cdot \vec{\mu})\,(\vec{e}^* \cdot \vec{\mu})$ can be written as:

$$(\vec{e} \cdot \vec{\mu})\,(\vec{e}^* \cdot \vec{\mu}) = \sum_{k,q}(-1)^{k-q}\left[e^{(1)} \otimes e^{*(1)}\right]_q^{(k)}\left[\mu^{(1)} \otimes \mu^{*(1)}\right]_{-q}^{(k)} \tag{49}$$

which is the product of the scalar contraction of two tensors, the polarization tensor $E_q^k\,(\vec{e}, \vec{e}^*)$

$$E_q^k\,(\vec{e}, \vec{e}^*) = \left[e^{(1)} \otimes e^{*(1)}\right]_q^{(k)} \tag{50}$$

$$= \sum_{\gamma}(-1)^q(2k+1)^{\frac{1}{2}}e(1,\gamma)e^*(1,q-\gamma)\begin{pmatrix} 1 & 1 & k \\ \gamma & q-\gamma & -q \end{pmatrix}$$

which is concerned with the electric field direction and the tensor $\left[\mu^{(1)} \otimes \mu^{*(1)}\right]_{-q}^{(k)}$ which acts on the molecular wavefunction and thus does not act on the same space than the $E_q^k\,(\vec{e}, \vec{e}^*)$ tensor.

With these relations we can now apply the Wigner-Eckart theorem to the pump $P_{M_e M_e'}^{pump}$ matrix element, giving:

$$P_{M_e M_e'}^{pump} = \langle\alpha_e J_e M_e|\sum_{k,q}\left[(e_1)^{(1)} \otimes (e_1^*)^{(1)}\right]_q^{(k)} P_i \left[\mu^{(1)} \otimes \mu^{(1)}\right]_{-q}^{(k)}|\alpha_e J_e M_e'\rangle \tag{51}$$

$$= \sum_{k,q}(-1)^{k-q}E_q^k\,(\vec{e}_1, \vec{e}_1^*)\,\langle\alpha_e J_e M_e|\left[\mu^{(1)} \otimes \mu^{(1)}\right]_{-q}^{(k)}|\alpha_e J_e M_e'\rangle$$

$$= \sum_{k,q}(-1)^{k-q+J_e-M_e}E_q^k\,(\vec{e}_1, \vec{e}_1^*)\begin{pmatrix} J_e & k & J_e \\ -M_e & -q & M_e' \end{pmatrix}\langle\alpha_e J_e\|\left[\mu^{(1)} \otimes \mu^{(1)}\right]^{(k)}\|\alpha_e J_e\rangle$$

$$= \sum_{k,q}(2k+1)^{\frac{1}{2}}E_q^k\,(\vec{e}_1, \vec{e}_1^*)\,(-1)^{J_e-M_e-q}\begin{pmatrix} J_e & k & J_e \\ -M_e & -q & M_e' \end{pmatrix} \tag{52}$$

$$(-1)^{J_e+J_i}\alpha_e|\langle J_e\|\mu^{(1)}\|\alpha_i J_i\rangle|^2\begin{Bmatrix} 1 & 1 & k \\ J_e & J_e & J_i \end{Bmatrix}$$

where $\langle \alpha_e J_e \| \mu^{(1)} \| \alpha_i J_i \rangle$ is the matrix element of the dipole operator. Similarly, the $P^{probe}_{M'_e M_e}$ matrix element can be expressed using the same machinery as:

$$P^{probe}_{M_e M'_e} = \sum_{k',q'}(2k'+1)^{\frac{1}{2}} E^{k'}_{q'}\left(\vec{e}_2, \vec{e}_2^{\,*}\right)(-1)^{J_e - M'_e - q'}\begin{pmatrix} J_e & k' & J_e \\ -M'_e & -q' & M_e \end{pmatrix}$$

$$(-1)^{J_e + J_f}|\langle \alpha_e J_e \| \mu^{(1)} \| \alpha_f J_f \rangle|^2 \begin{Bmatrix} 1 & 1 & k' \\ J_e & J_e & J_f \end{Bmatrix} \tag{53}$$

and the population of the final state populated by double-resonance can be written as:

$$N_f(t) \;\propto\; |\langle \alpha_i J_i \| r^{(1)} \| \alpha_e J_e \rangle|^2 |\langle \alpha_e J_e \| r^{(1)} \| \alpha_f J_f \rangle|^2 \sum_{k,q}(-1)^q E^k_q(\vec{e_1}\,\vec{e_1}^{\,*})E^k_{-q}(\vec{e_2}\,\vec{e_2}^{\,*}) \tag{54}$$

$$(-1)^{J_i + J_e + J_f + J_e}\begin{Bmatrix} 1 & 1 & k \\ J_e & J_e & J_i \end{Bmatrix}\begin{Bmatrix} 1 & 1 & k \\ J_e & J_e & J_f \end{Bmatrix}\exp\left[-i\left(\omega_{M_e} - \omega_{M'_e}\right)t\right]$$

We will now specialize Eq. 54 to our special case of lineraly-polarized pump-probe scheme (*i.e.* $q = 0$), with $\vec{e_1}$ and $\vec{e_2}$ being unit vectors pointing along the polarization directions of both laser beams, which are the quantization axes of the tensors $E^k_q\left(\vec{e_1}, \vec{e_1}^{\,*}\right)$ and $E^k_q\left(\vec{e_2}, \vec{e_2}^{\,*}\right)$ respectively. The quantization of both tensors differ and we will call $\theta$ the angle that $\vec{e_1}$ makes with $\vec{e_2}$. We can refer the probe polarization tensor to the same axis as that of the pump polarization tensor by carrying out the rotation operation $R(0, \theta, 0)$ (the number into parenthesis being the Euler angles), that is:

$$E^k_q\left(\vec{e_1}, \vec{e_1}^{\,*}\right) = \sum_q D^k_{q0}(0, \theta, 0)E^k_q\left(\vec{e_2}, \vec{e_2}^{\,*}\right) \tag{55}$$

$$= D^k_{00}(0, \theta, 0)E^k_0\left(\vec{e_2}, \vec{e_2}^{\,*}\right)$$

$$= (2k+1)^{\frac{1}{2}}\begin{pmatrix} 1 & 1 & k \\ 0 & 0 & 0 \end{pmatrix}P_k\left(\cos\theta\right)$$

where $P_k\left(\cos\theta\right)$ are the associated Legendre polynomial, which gives by inserting Eq. 55 in Eq. 54 for our linearly polarized pump-probe geometry:

$$N_f(t) \;\propto\; |\langle \alpha_i J_i \| r^{(1)} \| \alpha_e J_e \rangle|^2 |\langle \alpha_e J_e \| r^{(1)} \| \alpha_f J_f \rangle|^2 (-1)^{J_i + J_e + J_f + J_e}$$

$$\sum_{k=0}^{2}(2k+1)\begin{pmatrix} 1 & 1 & k \\ 0 & 0 & 0 \end{pmatrix}^2\begin{Bmatrix} 1 & 1 & k \\ J_e & J_e & J_i \end{Bmatrix}\begin{Bmatrix} 1 & 1 & k \\ J_e & J_e & J_f \end{Bmatrix}$$

$$P_k\left(\cos\theta\right)\exp\left[-i\left(\omega_{M_e} - \omega_{M'_e}\right)t\right] \tag{56}$$

Note that in the summation over $k$ in Eq. 56, the term corresponding to $k = 0$ is isotropic, the term corresponding to $k = 1$ vanishes and the term corresponding to $k = 2$ varies as $\frac{1}{2}(3\cos^2\theta - 1)$. It is convenient to distinguish two cases. In the first, $\vec{e_2}$ is parallel to $\vec{e_1}$, $\theta = 0$, and the number of molecules transferred to the final states is denoted $N_{f\|}$. In the second case, $\vec{e_2}$

is perpendicular to $\vec{e_1}$, $\theta = \frac{\pi}{2}$, and the amount of molecules transferred to the final states is denoted $N_{f\perp}$. We then define two useful quantities, the polarization $P$ and the polarization anisotropy $R$:

$$P = \frac{N_{f\parallel} - N_{f\perp}}{N_{f\parallel} + N_{f\perp}} \tag{57}$$

$$R = \frac{N_{f\parallel} - N_{f\perp}}{I_\parallel + 2N_{f\perp}} \tag{58}$$

and those two quantities are related by

$$P = \frac{3R}{2 + R} \tag{59}$$

$$R = \frac{2P}{3 - P} \tag{60}$$

Using Eq. 56, we can get:

$$R = \frac{\left\{ \begin{array}{ccc} 1 & 1 & 2 \\ J_e & J_e & J_i \end{array} \right\} \left\{ \begin{array}{ccc} 1 & 1 & 2 \\ J_e & J_e & J_f \end{array} \right\}}{\left\{ \begin{array}{ccc} 1 & 1 & 0 \\ J_e & J_e & J_i \end{array} \right\} \left\{ \begin{array}{ccc} 1 & 1 & 0 \\ J_e & J_e & J_f \end{array} \right\}} \tag{61}$$

and $P$ from Eq. 59. Using Eq. 61 and Eq. 59 we can calculate for each set of $J_i$, $J_e$ and $J_f$, the difference between the number of molecules transferred for a parallel and for a crossed pump-probe polarization scheme. We will call this quantity $P$ the contrast. The set of the different initial, intermediate, and final states are indicated by the initial state $J_i$ and of the type $(P, Q$ or $R)$ of rotational transitions involved. For example, $J = 0$ $(R, P)$ indicates an initial state $J_i = 0$, $J_e = 1$ and $J_f = 0$. The contrast for the different possible type of transitions possible is summarized in Table 2, for the first $J$.

Then, we see that taking the real part of Eq. 44, the number of molecules transferred by double resonance excitation, oscillate with a phase $\left(\omega_{M_e} - \omega_{M'_e}\right) t$ and a normalized magnitude of oscillation given by $P$ which depends on the polarization of the pump and probe radiation and on the quantum numbers of the states involved.

# References

[1] Richard N. Zare. *Angular Momentum understanding spatial aspects in chemistry and physics.* Wiley-Interscience, New York, 1988.

| $J_i$ | $(R, R)$ | $(R, Q)$ | $(R, P)$ | $(Q, R)$ | $(Q, Q)$ | $(Q, P)$ | $(P, R)$ | $(P, Q)$ | $(P, P)$ |
|---|---|---|---|---|---|---|---|---|---|
| 0 | 14 | -100 | 100 | 0 | 0 | 0 | 0 | 0 | 0 |
| 1 | 14 | -64 | 45 | -8 | 29 | -100 | 0 | 0 | 0 |
| 2 | 14 | -53 | 32 | -16 | 43 | -64 | 1 | -8 | 14 |
| 3 | 14 | -48 | 27 | -20 | 46 | -53 | 4 | -16 | 14 |
| 4 | 14 | -45 | 24 | -23 | 48 | -48 | 6 | -20 | 14 |
| 5 | 14 | -43 | 22 | -24 | 49 | -45 | 7 | -23 | 14 |
| 6 | 14 | -43 | 21 | -26 | 49 | -43 | 8 | -24 | 14 |
| 7 | 14 | -43 | 20 | -27 | 49 | -41 | 9 | -26 | 14 |
| 8 | 14 | -43 | 19 | -27 | 49 | -40 | 10 | -27 | 14 |
| 9 | 14 | -43 | 19 | -28 | 50 | -40 | 10 | -27 | 14 |
| 10 | 14 | -38 | 18 | -28 | 50 | -39 | 11 | -28 | 14 |

**Table 2:** Contrast for different pump and probe transitions originating from the first $J$ values.

# Appendix C: Rotational contribution to the dipole moment of H₂O and HDO.

Following the derivation of the vibration-rotation dipole moment operator made by Camy-Peyret and Flaud in Ref. [1], the rotational-dependence of the dipole moment [2] can be given by

$$\mu_Z^\nu = \sum_\alpha \varphi_\alpha^\alpha \mu^\nu + \sum_{\alpha,\beta,\gamma} \frac{1}{2}\{\varphi_\alpha, J_\beta J_\gamma\}_{(2)}^{\alpha,\beta\gamma} \tilde{M} \tag{62}$$

$$_{(2)}^{\alpha,\beta\gamma}\tilde{M} = \Theta_\alpha^{\beta\gamma} + C_\alpha^{\beta\gamma} \tag{63}$$

$$\Theta_\alpha^{\beta\gamma} = -\sum_m \frac{B_m^{\beta\gamma}{}^\alpha}{\omega_m} \mu_m \tag{64}$$

$$^\alpha\mu_m = \frac{\partial\mu_\alpha}{\partial Q_m} \tag{65}$$

$$C_\alpha^{\beta\gamma} = s_{111}\sum_\delta \epsilon_{\beta\gamma\delta}(\delta_{\alpha\beta}^\beta\mu_e - \delta_{\alpha\beta}^\gamma\mu_e) \tag{66}$$

$$B_m^{\beta\gamma} = -\frac{\hbar^3}{2(hc)^{3/2}}\frac{(\partial I_{\beta\gamma}/\partial Q_a)_e}{I_\beta I_\gamma \omega_m^{1/2}} \tag{67}$$

This rotational contribution can be decomposed into two terms, as shown in Eq. 63, where $\Theta_\alpha^{\beta\gamma}$ is the coefficient of Watson and $C_\alpha^{\beta\gamma}$ is the term arising from the rotational contact transformation introduced by Clough [3]. $\alpha, \beta, \gamma$ are the principal inertial axis, $\omega_m$ is the vibrational frequency of the mode $m$, $I$ is the inertia tensor, $\delta$ the Kronecker symbol and $\epsilon$ the asymmetric tensor. $s_{111}$ is the term of the contact transformation used to reduce the quartic centrifugal terms of the molecular Hamiltonian [1].

For non-linear $X - Y_2$ molecules like $H_2O$, a much simpler expression can be found in Ref. [1]

147

since there are only five non zero $\overset{\alpha,\beta\gamma}{_{(2)}}\tilde{M}$ terms:

$$\hat{\mu}_Z(\nu, J, K_a, K_c) = \hat{\mu}_Z(\nu) + \frac{1}{2}\overset{x,xx}{_{(2)}}\tilde{M}\{\varphi_x, J_x J_x\} \tag{68}$$

$$+\frac{1}{2}\overset{x,yy}{_{(2)}}\tilde{M}\{\varphi_x, J_y J_y\} + \frac{1}{2}\overset{x,zz}{_{(2)}}\tilde{M}\{\varphi_x, J_z J_z\} \tag{69}$$

$$+\frac{1}{2}\overset{z,xy}{_{(2)}}\tilde{M}\{\varphi_z, J_x J_y\} + \frac{1}{2}\overset{y,xy}{_{(2)}}\tilde{M}\{\varphi_y, J_x J_y\} \tag{70}$$

where we follow Camy-Peyret and Flaud axis designation, that is $x = b$, $y = c$ and $z = a$. The non-zero $\overset{\alpha,\beta\gamma}{_{(2)}}\tilde{M}$ terms can be written as:

$$\overset{x,\alpha\alpha}{_{(2)}}\tilde{M} = -\sum_{m=1,2}\frac{B_m^{\alpha\alpha\,x}}{\omega_m}\mu_m \tag{71}$$

$$\overset{z,xy}{_{(2)}}\tilde{M} = -\frac{B_3^{xz\,z}}{\omega_3}\mu_3 + s_{111}^x \mu_e \tag{72}$$

$$\overset{y,xy}{_{(2)}}\tilde{M} = s_{111}^x \mu_e \tag{73}$$

We take $^x\mu_e = -1.8473\ D$ [3], and the expressions for the several $B_i^{\alpha\beta}$ can be found in Ref. [1]. The $s_{111}$ term can written according to the Watson transformation as:

$$s_{111} = -\frac{T_{004}}{\frac{1}{4}(B_x - B_y)} \tag{74}$$

with the $T_{004} = \frac{1}{16}(T_{xx} + T_{yy} - 2T_{xy})$ being evaluated using planarity relations that give:

$$T_{xx} = -D_J - 2\delta_J \tag{75}$$

$$T_{yy} = -DJ - 2\delta_J \tag{76}$$

$$T_{xy} = -\frac{1}{2}(B_x^e)^2(B_y^e)^2\left[-\frac{T_{zz}}{(B_z^e)^4} + \frac{T_{xx}}{(B_x^e)^4} + \frac{T_{yy}}{(B_y^e)^4}\right] \tag{77}$$

$$T_{zz} = -D_J - D_{JK} - D_K \tag{78}$$

$D_J$, $D_K$, $D_{JK}$ and $\delta_J$ referring to the centrifugal distortion constants of the Watson Hamiltonian. The resulting values for the vibrational states of $H_2O$ are listed in Table 3

The values of the $\overset{\alpha,\beta\gamma}{_{(2)}}\tilde{M}$ coefficients have been calculated from the rotational constants $A$, $B$, $C$, $D_J$, $D_K$, $D_{JK}$, coming from a fit of the first $J$ and $K$ levels, fixing the other parameters to their ground state value. They have to be compared with the values of the first term of Eq. 62. The dipole moment matrix elements from Eq. 62 are between 1 $D$ and $10^{-1}$ $D$ (the smallest being $5.10^{-2}$ $D$). The operators $\{\varphi_\alpha, J_\beta J_\gamma\}$ associated with the $\overset{\alpha,\beta\gamma}{_{(2)}}\tilde{M}$ coefficients can be no more than 4, since they couple only $J = 1$ and $J = 2$, and since a direction cosine matrix element is less than 1. Therefore the order of magnitude of the $\overset{\alpha,\beta\gamma}{_{(2)}}\tilde{M}$ coefficients is conserved after having applied the $\{\varphi_\alpha, J_\beta J_\gamma\}$ operator, which means that the contribution of the second

| | $\lvert 4,0^- \rangle$ | $\lvert 4,0^- \rangle \lvert 2 \rangle$ | $\lvert 5,0^- \rangle$ | $\lvert 8,0^+ \rangle$ |
|---|---|---|---|---|
| $_{(2)}^{x,xx}\tilde{M}$ | $8.21\ 10^{-6}$ | $8.30\ 10^{-6}$ | $8.16\ 10^{-6}$ | $7.4\ 10^{-6}$ |
| $_{(2)}^{x,yy}\tilde{M}$ | $-2.98\ 10^{-8}$ | $3.42\ 10^{-7}$ | $-2.84\ 10^{-7}$ | $-3.70\ 10^{-7}$ |
| $_{(2)}^{y,zz}\tilde{M}$ | $-2.86\ 10^{-5}$ | $3.90\ 10^{-5}$ | $2.84\ 10^{-5}$ | $2.32\ 10^{-5}$ |
| $_{(2)}^{z,xy}\tilde{M}$ | $-3.74\ 10^{-4}$ | $2.42\ 10^{-3}$ | $4.94\ 10^{-4}$ | $0.269$ |
| $_{(2)}^{y,xy}\tilde{M}$ | $-3.72\ 10^{-6}$ | $2.42\ 10^{-3}$ | $4.92\ 10^{-4}$ | $0.269$ |

**Table 3:** This table gives the $_{(2)}^{i,jj}\tilde{M}$ terms of Eq. 62 for different vibrational states of $H_2O$. This tensor $\tilde{M}$ expresses the rotational dependence of the dipole moment. Excepted for the two last terms for $\lvert 8,0^+ \rangle$, it can be seen that the $_{(2)}^{i,jj}\tilde{M}$ terms are much smaller than the uncertainty of the dipole moment measurement.

term of Eq. 62 is much smaller, for $J = 1$, than the contribution of the first term. We can then consider to a good approximation our $J = 1$ rovibrational dipole moments as vibrational dipole moments. A closer look at the values of the $_{(2)}^{\alpha,\beta\gamma}\tilde{M}$ coefficients for $\lvert 8,0^+ \rangle$ shows that we cannot rigorously neglect the terms $\frac{1}{2}_{(2)}^{z,xy}\tilde{M}\{\varphi_z, J_x J_y\}$ and $\frac{1}{2}_{(2)}^{y,xy}\tilde{M}\{\varphi_y, J_x J_y\}$. However, due to the quality of our energy levels fit, that only include the first rovibrational levels and due to the uncertainties on the parameters, a numerical evaluation of $\frac{1}{2}_{(2)}^{z,xy}\tilde{M}$ and $\frac{1}{2}_{(2)}^{y,xy}\tilde{M}$ for $\lvert 8,0^+ \rangle$ would not be accurate to the level required. However, since we want to compare $J = 1$ of a vibrational level with $J = 1$ of another, we decide to keep the $J = 1$ rovibrational dipole moments as vibrational dipole moments for $\lvert 8,0^+ \rangle$ as well, keeping in mind this rotational contribution. We treat HDO in the same way.

# References

[1] C. Camy-Peyret and J. M. Flaud. *Vibration-rotation dipole moment operator for asymmetric rotors, Molecular Spectroscopy: Modern Research*, volume III, pages 69–110. Academic Press, Orlando, Fla., 1985.

[2] T. R. Dyke and J. S. Muenter. Electric dipole-moments of low j states of $H_2O$ and $D_2O$. *Journal of Chemical Physics*, 59(6):3125–3127, 1973.

[3] S. A. Clough, Y. Beers, G. P. Klein, and L. S. Rothman. Dipole-moment of water from stark measurements of $H_2O$, HDO, and $D_2O$. *Journal of Chemical Physics*, 59(5):2254–2259, 1973.

# List of Figures

151

# List of Tables

155

# CURRICULUM VITÆ

---

## Personal

Date and place of birth: October, 1976 - Tarbes, France

Nationality: French

Gender: Male

Marital status: single

Languages: French: native, English: fluent, Spanish: good, Chinese: elementary

---

## Education

| | |
|---|---|
| 1999–2003 | Ph.D, Ecole Polytechnique Fédérale de Lausanne, Switzerland. *Dipole moment measurements in highly vibrationally excited molecules*, Advisor: Prof. T.R. Rizzo. Expected in October 2003. |
| 1998–1999 | DEA (Master of Science), Physics of Matter and Radiation, Joseph Fourier University, Grenoble, France |
| 1996–1999 | Physics Engineering Diploma, Ecole Nationale Superieure de Physique de Grenoble, Grenoble, France |
| 1996–1999 | Two-years university degree, Mathematics and Physics, Université Paul Sabatier, Toulouse, France |

---

## Work and Research Experience

| | |
|---|---|
| 10/1999–11/2003 | Laboratoire de Chimie Physique Moléculaire, EPFL, Switzerland. *Electric dipole moments of highly excited molecular vibrational states*, with Prof. T.R. Rizzo. |
| 03/1999–09/1999 | Grenoble High Magnetic Field Laboratory, Grenoble, France. *The conical intersection of* $NO_2$, *using Cavity Ring Down Spectroscopy in a supersonic molecular beam*, with Prof. R. Jost. |
| 06/1998–09/1998 | Northeastern University, Physics Department, Boston, MA, USA, *colossal magneto-resistance of double-perovskite* $La_{1.2}Sr_{1.8}Mn_2O_7$, with Prof. S. Sridhar. |

## Publications and Awards

- *Dipole moment of highly vibrationnaly excited HDO,by Stark Photofragment Quantum Beat Spectroscopy*, P. Theulé, A. Callegari, J. S. Muenter, and T. R. Rizzo (to be submitted to J. Chem. Phys.)

- *Fluorescence detected microwave Stark effect measurements in excited vibrational states of $H_2CO$*, Patrice Theulé, Andrea Callegari and T. R. Rizzo, J. S. Muenter (accepted, J. Chem. Phys.)

- *The dipole moment of HOCl in $v_{OH} = 4$*, Andrea Callegari, Patrice Theulé, Roman Schmied and T. R. Rizzo, J. S. Muenter; J. Mol. Spect. 221(1), 116-120 (2003)

- Rao Prize 2002, $57^{th}$ Ohio State International Symposium on Molecular Spectroscopy.

- *Stark Photofragment Quantum Beat Spectroscopy: dipole moments of highly vibrationnaly excited $H_2O$*, A. Callegari, P. Theulé, J. S. Muenter, and T. R. Rizzo (to be submitted to J. Chem. Phys.)

- *Dipole Moments of Highly Vibrationally Excited Water*, Andrea Callegari, Patrice Theulé, John S. Muenter, Roman N. Tolchenov, Nikalai F. Zobov, Oleg L. Polyansky, Jonathan Tennyson and Thomas R. Rizzo; Science 297, 993 (2002).

- *Vibrational dependence of unimolecular reaction rates: state-resolved dissociation dynamics of HOCl at $v_{OH} = 6,7$ and 8.* A. Callegari, R. Schmied, P. Theulé, J. Rebstein and T. R. Rizzo, Phys. Chem. Chem. Phys. 3, 2245-2252 (2001).

- *High frequency magneto-impedance of double perovskite $La_{1.2}Sr_{1.8}Mn_2O_7$: secondary transitions at high temperatures*, Patanjali V. Parimi, P. Theulé, Z. Zhai, N. Hakim and S.Sridhar, R. Suryanarayanan, Apostu, G. Dhalenme, and A. Revcolevschi, Phys. Rev. B, 60, 9268 (1999).

## Other interests

Vice-president of the astronomy club of the EPFL (Callista)